PREDICTION OF ELECTROMAGNETIC LAUNCHER BEHAVIOR WITH LUBRICANT INJECTION THROUGH ARMATURE-RAIL INTERFACE MODELING

A Thesis
Presented to
The Academic Faculty

by

Kory A. Swope

In Partial Fulfillment
of the Requirements for the Degree
Master of Science in the
School of Mechanical Engineering

Georgia Institute of Technology
May 2010

PREDICTION OF ELECTROMAGNETIC LAUNCHER BEHAVIOR WITH LUBRICANT INJECTION THROUGH ARMATURE-RAIL INTERFACE MODELING

Approved by:

Dr. Richard F. Salant, Advisor
School of Mechanical Engineering
Georgia Institute of Technology

Dr. Jeffrey L. Streator
School of Mechanical Engineering
Georgia Institute of Technology

Dr. Scott Bair
School of Mechanical Engineering
Georgia Institute of Technology

Date Approved: March 18, 2010

ACKNOWLEDGEMENTS

I would like to especially thank my mother and father for teaching me to work hard and take pride in everything I do.

TABLE OF CONTENTS

Page

ACKNOWLEDGEMENTS iii

LIST OF TABLES vi

LIST OF FIGURES vii

LIST OF SYMBOLS AND ABBREVIATIONS xvi

SUMMARY xix

CHAPTER 1: INTRODUCTION 1

CHAPTER 2: RESEARCH BACKGROUND 4

2.1 Magneto-Hydrodynamic Model 4

2.2 Magneto-Elastohydrodynamic Model 7

2.3 Magneto-Elastothermohydrodynamic Model 10

CHAPTER 3: ARMATURE-RAIL INTERFACE MODELING 15

3.1 Base Case 17

3.1.1 Electromagnetic Field Modeling 18

3.1.2 Thermal Field Modeling 26

3.1.3 Armature Deflection Modeling 28

3.1.4 Lubricant Modeling 42

3.1.5 Results and Discussions 47

3.2 NRL Shot 223 74

3.2.1 Electromagnetic Field Modeling 75

3.2.2 Thermal Field Modeling 80

3.2.3 Armature Deflection Modeling 81

3.2.4 Lubricant Modeling 88
3.2.5 Results and Discussions 90
3.3 NRL Shot 406 118
3.3.1 Lubricant Modeling 119
3.3.2 Results and Discussions 123
3.4 IAP Shot 7 151
3.4.1 Electromagnetic Field Modeling 152
3.4.2 Thermal Field Modeling 156
3.4.3 Armature Deflection Modeling 157
3.4.4 Lubricant Modeling 165
3.4.5 Results and Discussions 167
3.5 GTL-2-4C 194
3.5.1 Electromagnetic Field Modeling 196
3.5.2 Thermal Field Modeling 201
3.5.3 Armature Deflection Modeling 203
3.5.4 Lubricant Modeling 212
3.5.5 Results and Discussions 218
3.6 Modified GTL-2-4C 243
3.6.1 Armature Deflection Modeling 244
3.6.2 Lubricant Modeling 252
3.6.3 Results and Discussions 253
CHAPTER 4: CONCLUSIONS 263
REFERENCES 265

LIST OF TABLES

Page

Table 3.1: Material Properties [2] 16

LIST OF FIGURES

Page

Figure 1.1: Schematic illustrating the EML system..... 1

Figure 3.1: Sketch of the base case armature..... 18

Figure 3.2: COMSOL model used for electromagnetic validation..... 21

Figure 3.3: Comparison of magnetic flux distributions calculated by (a) COMSOL and (b) finite difference method 22

Figure 3.4: Comparison of current distributions calculated by (a) COMSOL and (b) finite difference method 24

Figure 3.5: Magnetic flux density in the direction (a) parallel to the rails (b) transverse to the rails..... 25

Figure 3.6: Temperature field validation calculated by (a) ANSYS and (b) finite difference method 28

Figure 3.7: Transformation of the armature wing to a cantilever beam 29

Figure 3.8: Comparison of armature wing deflection between ANSYS and Euler-Bernoulli models with a shear force 31

Figure 3.9: ANSYS and Greenwood-Williamson model contact pressure for an interference 35

Figure 3.10: ANSYS and Euler-Bernoulli contact deformation for an interference 36

Figure 3.11: Thermal boundary conditions used to validate thermal deflections..... 39

Figure 3.12: Comparison of armature wing deflection between ANSYS and Euler-Bernoulli models for high boundary temperatures 40

Figure 3.13: Interface region used for Equation 3.22 43

Figure 3.14: Mass balance on the pocket 44

Figure 3.15: Schematic of the base case injection system and node points 45

Figure 3.16: Experimental muzzle voltage 47

Figure 3.17: Electric current history 48

Figure 3.18: Magnetic flux density distribution at different times 49

Figure 3.19: Electric current distribution at different times 51

Figure 3.20: Magnetic body force distribution at different times 54

Figure 3.21: Temperature distribution at different times 56

Figure 3.22: *x* direction armature force history 59

Figure 3.23: Armature acceleration history 60

Figure 3.24: Armature velocity history 61

Figure 3.25: Comparison of predicted armature location history with experimental measurements 62

Figure 3.26: History of the amount of lubricant left inside the reservoir. 63

Figure 3.27: Mass flow amount history 64

Figure 3.28: Minimum film thickness history 65

Figure 3.29: Pressures in the fluid at different times 66

Figure 3.30: Distributed forces on the armature leg at different times 68

Figure 3.31: Nondimensional interface gap profiles at different times 71

Figure 3.32: Fluid flow patterns at different times 72

Figure 3.33: Sketch of the NRL shot 223 armature 75

Figure 3.34: Comparison of magnetic flux distributions calculated by (a) COMSOL and (b) finite difference method 76

Figure 3.35: Comparison of current distributions calculated by (a) COMSOL and (b) finite difference method 78
Figure 3.36: Magnetic flux density in the direction (a) parallel to the rails (b) transverse to the rails 79
Figure 3.37: Temperature field validation calculated by (a) ANSYS and (b) finite difference method 80
Figure 3.38: Comparison of armature wing deflection between ANSYS and Euler-Bernoulli models with a shear force 81
Figure 3.39: ANSYS and Greenwood-Williamson model contact pressure for an interference 84
Figure 3.40: ANSYS and Euler-Bernoulli contact deformation for an interference 85
Figure 3.41: Comparison of armature wing deflection between ANSYS and Euler-Bernoulli models for high boundary temperatures 86
Figure 3.42: Schematic of the NRL shot 223 injection system and node points 89
Figure 3.43: Interface configuration after the pocket is emptied 90
Figure 3.44: Experimental muzzle voltage 91
Figure 3.45: Electric current history 92
Figure 3.46: Magnetic flux density distribution at different times 93
Figure 3.47: Electric current distribution at different times 95
Figure 3.48: Magnetic body force distribution at different times 98
Figure 3.49: Temperature distribution at different times 100
Figure 3.50: *x* direction armature force history 103
Figure 3.51: Armature acceleration history 104

Figure 3.52: Comparison of predicted armature velocity history with experimental measurements 105
Figure 3.53: Comparison of predicted armature location history with experimental measurements 105
Figure 3.54: History of the amount of lubricant left inside each reservoir. 107
Figure 3.55: Mass flow amount history 107
Figure 3.56: Minimum film thickness history 108
Figure 3.57: Pressures in the fluid at different times 109
Figure 3.58: Distributed forces on the armature leg at different times 112
Figure 3.59: Nondimensional interface gap profiles at different times 114
Figure 3.60: Fluid flow patterns at different times 115
Figure 3.61: Sketch of the NRL shot 406 armature 119
Figure 3.62: Schematic of the NRL shot 406 injection system and node points 120
Figure 3.63: Schematic of the armature passing over the joint 122
Figure 3.64: Experimental muzzle voltage 124
Figure 3.65: Electric current history 125
Figure 3.66: Magnetic flux density distribution at different times 126
Figure 3.67: Electric current distribution at different times 128
Figure 3.68: Magnetic body force distribution at different times 131
Figure 3.69: Temperature distribution at different times 133
Figure 3.70: *x* direction armature force history 136
Figure 3.71: Armature acceleration history 137

Figure 3.72: Comparison of predicted armature velocity history with experimental measurements 138
Figure 3.73: Comparison of predicted armature location history with experimental measurements 138
Figure 3.74: History of the amount of lubricant left inside the reservoir. 140
Figure 3.75: Mass flow amount history 140
Figure 3.76: Minimum film thickness history 141
Figure 3.77: Pressures in the fluid at different times 142
Figure 3.78: Distributed forces on the armature leg at different times 145
Figure 3.79: Nondimensional interface gap profiles at different times 147
Figure 3.80: Fluid flow patterns at different times 148
Figure 3.81: Sketch of the IAP shot 7 armature 152
Figure 3.82: Comparison of magnetic flux distributions calculated by (a) COMSOL and (b) finite difference method 153
Figure 3.83: Comparison of current distributions calculated by (a) COMSOL and (b) finite difference method 154
Figure 3.84: Magnetic flux density in the direction (a) parallel to the rails (b) transverse to the rails 155
Figure 3.85: Temperature field validation calculated by (a) ANSYS and (b) finite difference method 157
Figure 3.86: Comparison of armature wing deflection between ANSYS and Euler-Bernoulli models with a shear force 158

Figure 3.87: ANSYS and Greenwood-Williamson model contact pressure for an interference 161

Figure 3.88: ANSYS and Euler-Bernoulli contact deformation for an interference 162

Figure 3.89: Comparison of armature wing deflection between ANSYS and Euler-Bernoulli models for high boundary temperatures 163

Figure 3.90: Schematic of the IAP shot 7 injection system and node points..... 166

Figure 3.91: Experimental muzzle voltage 168

Figure 3.92: Electric current history 169

Figure 3.93: Magnetic flux density distribution at different times 170

Figure 3.94: Electric current distribution at different times 172

Figure 3.95: Magnetic body force distribution at different times..... 175

Figure 3.96: Temperature distribution at different times..... 177

Figure 3.97: *x* direction armature force history 180

Figure 3.98: Armature acceleration history 181

Figure 3.99: Comparison of predicted armature velocity history with experimental measurements..... 182

Figure 3.100: Comparison of predicted armature location history with experimental measurements..... 182

Figure 3.101: History of the amount of lubricant left inside each reservoir..... 183

Figure 3.102: Mass flow amount history 184

Figure 3.103: Minimum film thickness history 185

Figure 3.104: Pressures in the fluid at different times..... 186

Figure 3.105: Distributed forces on the armature leg at different times..... 188

Figure 3.106: Nondimensional interface gap profiles at different times 191
Figure 3.107: Fluid flow patterns at different times 192
Figure 3.108: Sketch of the IAT GTL-2-4C rails 195
Figure 3.109: Sketch of the IAT GTL-2-4C armature 196
Figure 3.110: 3D COMSOL steady state electromagnetic forces 197
Figure 3.111: Comparison of magnetic flux distributions calculated by (a) COMSOL and (b) finite difference method 198
Figure 3.112: Comparison of current distributions calculated by (a) COMSOL and (b) finite difference method 199
Figure 3.113: Magnetic flux density in the direction (a) parallel to the rails (b) transverse to the rails 200
Figure 3.114: COMSOL model, light blue is a low temperature boundary, dark blue is a high temperature boundary, and grey or tan is an adiabatic boundary 202
Figure 3.115: Temperature field validation calculated by (a) COMSOL and (b) finite difference method 202
Figure 3.116: Comparison of armature wing deflection between COMSOL and Euler-Bernoulli models with a shear force 204
Figure 3.117: ANSYS and Greenwood-Williamson model contact pressure for an interference 207
Figure 3.118: ANSYS and Euler-Bernoulli contact deformation for an interference 208
Figure 3.119: Comparison of armature wing deflection between COMSOL and Euler-Bernoulli models for high boundary temperatures 210
Figure 3.120: Schematic of the GTL-2-4C injection system and node points 212

Figure 3.121: Control volume and node layout of discretized domain..... 215
Figure 3.122: Experimental muzzle voltage 219
Figure 3.123: Electric current history 220
Figure 3.124: Magnetic flux density distribution at different times 221
Figure 3.125: Electric current distribution at different times 223
Figure 3.126: Magnetic body force distribution at different times 226
Figure 3.127: Temperature distribution at different times..... 228
Figure 3.128: *x* direction armature force history 231
Figure 3.129: Armature acceleration history 232
Figure 3.130: Comparison of predicted armature velocity history with experimental measurements..... 233
Figure 3.131: Comparison of predicted armature location history with experimental measurements..... 233
Figure 3.132: History of the amount of lubricant left inside each reservoir..... 235
Figure 3.133: Mass flow amount history 235
Figure 3.134: Minimum film thickness history 236
Figure 3.135: Pressure in the lubricant at different times..... 237
Figure 3.136: Distributed forces on the armature leg at different times..... 240
Figure 3.137: Nondimensional interface gap profiles at different times 242
Figure 3.138: Schematic of the original GTL-2-4C armature on the left and the modified GTL-2-4C on the right..... 244
Figure 3.139: Comparison of armature wing deflection between COMSOL and Euler-Bernoulli models with a shear force 245

Figure 3.140: ANSYS and Greenwood-Williamson model contact pressure for an interference 248

Figure 3.141: ANSYS and Euler-Bernoulli contact deformation for an interference 249

Figure 3.142: Comparison of armature wing deflection between COMSOL and Euler-Bernoulli models for high boundary temperatures 250

Figure 3.143: *x* direction armature force history 254

Figure 3.144: History of the amount of lubricant left inside each reservoir. 255

Figure 3.145: Mass flow amount history 255

Figure 3.146: Minimum film thickness history 256

Figure 3.147: Pressure in the lubricant at different times 257

Figure 3.148: Distributed forces on the armature leg at different times 259

Figure 3.149: Nondimensional interface gap profiles at different times 262

LIST OF SYMBOLS AND ABBREVIATIONS

a	armature acceleration
B	magnetic flux density
B_0	magnetic flux density at the trailing edge in the film
b	armature width
C_{2D}	correction factor used when simplifying electromagnetic field to 2D
c	specific heat capacity
D	magnetic diffusion coefficient, $D = \frac{1}{\mu_0 \sigma^*}$
dt	duration of a time step
E	modulus of elasticity
EML	Electromagnetic Launch or Electromagnetic Launcher
F	shear force
F_c	cavitation index (1 if no cavitation, 0 if there is cavitation)
F_{emag}	magnetic force on the armature
F_0	concentrated shear force
f_x, f_y	magnetic body force in the x and y directions
G	cavitation factor $G=1+(1-F)\,\Phi$
H	non-dimensional film thickness
h	film thickness
h_b	equivalent armature wing beam height
h_T	local film thickness $h_T = \frac{h}{2} + \frac{h}{2} erf\left(\frac{h}{\sigma\sqrt{2}}\right) + \frac{\sigma}{\sqrt{2\pi}} \exp\left(\frac{-h^2}{2\sigma^2}\right)$
I	electric current

I^*	moment of inertia for bending $I^*(x) = \frac{bh_b(x)^3}{12}$
I'	moment of inertia for asperity contact $I' = \frac{1}{\sqrt{2\pi}} \int_H^\infty (z-H)^{3/2} e^{-z^2/2} dz$
J	electric current density
k	thermal conductivity
L'	inductance gradient
M	bending moment
M_T	thermal moment
P	lubricant pressure
P_c	cavitation pressure
P_{cont}	contact pressure
P_i	pressure at node *i* (inside injection system)
P_{ref}	reference pressure
Q_f	volume flow rate in the lubricant film
$\dot{Q}$	mass flow rate of lubricant
$\dot{Q}_{pre}$	mass flow rate of lubricant at previous time step
$\dot{q}$	viscous heat generation rate
q_{vol}	volume flow rate in the film $q_{vol} = \int_0^h u dy$
q_x	mass flow rate in the film in the x direction $q_x = \int_0^h \rho u dy$
R_{as}	asperity radius (approximated as $10*\sigma$)
T	temperature
t	time
U	armature speed

u, v	fluid velocity, x and y components
v^*	beam deflection
$v^{*},$	beam slope
w	distributed beam load
x, y, z	coordinates
α	coefficient of thermal expansion
η	asperity density (approximated as $(1/ R_{as})^2$)
μ	lubricant viscosity
μ_0	magnetic permeability of the air
μ_a	magnetic permeability of the armature
μ_f	magnetic permeability of the film
μ_r	magnetic permeability of the rail
ν'	Poisson's ratio
ρ	Density
ρ_c	lubricant density
σ	rms surface roughness
σ^*	coefficient of electrical conductivity
$\hat{\sigma}$	non-dimensional rms surface roughness $\hat{\sigma} = \sigma(R_{as})^{1/3}\eta^{2/3}$
Φ	dimensionless lubricant pressure
ψ	stream function
ϕ_n	flow factors *n=f, fs, fp, s, or x*
$(\,)_0$	reference variable
$(\,)_i$	variable corresponding domain *i=a* for armature, *r* for rail, and *f* for film
$\overline{(\,)}$	nondimensional variables

SUMMARY

Electromagnetic launchers are currently being developed for their use as military weapons. These devices launch a projectile to extremely high speeds using very large electric currents. One obstacle facing the development of electromagnetic launchers is damage to the rails and armature during launch. The damage occurs due to current arcing in the armature-rail interface and is denoted as a transition. One solution is to use a lubricant injection system contained inside the armature to provide a conductive lubricant to the interface. The lubricant will ensure good electrical contact, prevent solid-solid contact, and cool the interface to prevent a launch from transitioning. Various different armature designs are currently under development. Each design must be analyzed through armature-rail interface modeling in order to predict the physical behavior and identify causes of transitions.

There have been many studies on the physical behavior of sliding contacts. Some of which are directly applied to electromagnetic launch. In particular the magneto-elastothermohydrodynamic model is the most comprehensive model found for use in simulating electromagnetic launch. It includes calculation of the electromagnetic field, elastic deformation of the armature, calculation of the armature temperature history, and a hydrodynamic study of the lubricant both in the injection system and the armature-rail interface. The magneto-elastothermohydrodynamic model has been applied to only one armature design with limited success due to the assumptions used.

The magneto-elastothermohydrodynamic model is applied to six different armature designs each requiring modifications to be made in order to predict the distinct

behavior of each launcher. Modifications to the model include consideration of turbulent flow in the injection conduit, unique injection configurations, dry-out of the armature-rail interface, two dimensional pressure fields, and analyses of cylindrical bore launcher designs. The results show the model is effective in predicting when a transition will occur and what physical event leads to a transition when compared to experimental launch data. Additionally, experimental observations are used to affirm the simulation of other physical characteristics.

It is found by the simulation that the base case armature is successful in preventing a transition of the shot, which is consistent with the experimental results. The simulation of NRL shot 223 reveals that such a small amount of lubricant is supplied by the reservoirs that the armature-rail interface partially dries out making a transition likely at a time of 4.7 ms; agreeing with the experimentally observed transition at a time of 4.5 ms. It is determined that the transition of NRL shot 406 is not due to a lack of lubricant inside the interface and that the amount of lubricant which leaks from the joint is negligible. IAP shot 7 did not transition in the experiment, however, after a time of about 3.5 ms the muzzle voltage began to rise. The simulation presents a possible explanation, showing that the armature-rail interface is beginning to empty out after 4.2 ms. The simulation of the GTL-2-4C armature shows that the experimentally observed transition is caused by the reservoirs emptying out at about 2.1 ms. The exploratory simulation of a modified GTL-2-4C armature determines that the absence of the slit in the armature trailing edges will not prevent the transition nor extend the successful portion of the shot.

CHAPTER 1

INTRODUCTION

An Electromagnetic Launcher (EML) is a device capable of accelerating a projectile by using an electric current. An EML works in a similar way to a synchronous electric motor. It has two parallel rails made of conductive material attached to a large power source. Between the two rails is the armature, also made of a conductive material. It closes the circuit by acting as a shunt to allow current to pass from one rail to another. When current is supplied to the end of one of the rails, a magnetic field is created such that the magnetic field lines encircle the current path in accordance with the right hand rule (see Figure 1.1). Shunting the current between the rails inside the magnetic field causes a force to be exerted on the armature which results in an acceleration along the rails, until the armature reaches the end of the rails and becomes a projectile.

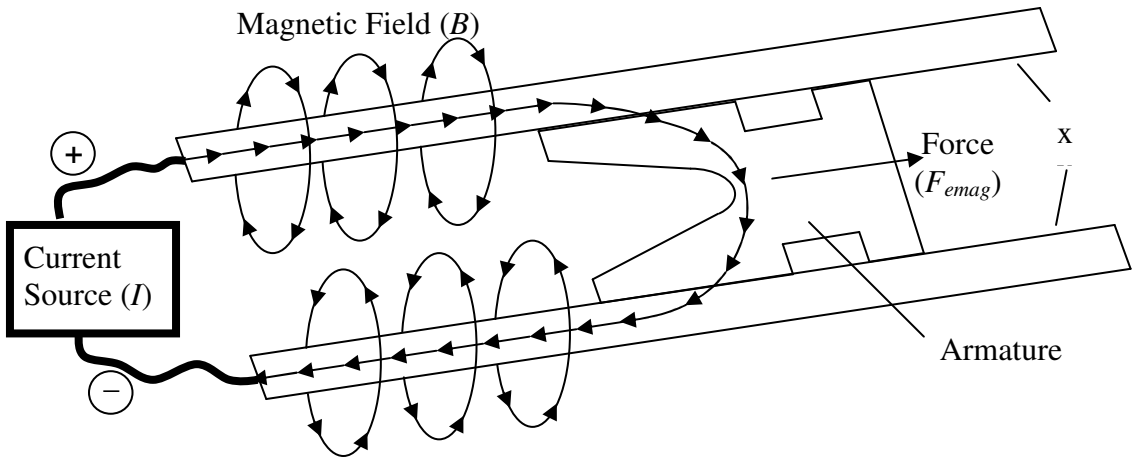

Figure 1.1: Schematic illustrating the EML system (not to scale)

EMLs are a major area of interest for their possible military applications. Conventional, black powder and liquid propellant launchers have projectile speeds limited to about 2.5 km/s by the speed of the expanding gasses from the chemical reaction used to launch the projectile. EML weapons are capable of achieving much higher projectile velocities with an experimentally observed limit of 6-7 km/s [1]. Higher velocities allow for longer range, shorter flight time to the target, and a more direct flight path. Additionally, projectiles can be made smaller since the kinetic energy increases with the square of velocity and only linearly with mass.

One of the difficulties with EMLs is maintaining contact between the armature and the rail until the armature reaches the end of the rails or muzzle. The high sliding velocities can cause wear and melting on both the rails and armature, which depreciates the contact and forces the current to arc inside the gap created. Arcing between the rail and armature creates an increase in voltage measured across the rails at the muzzle of the launcher, called a transition. Transitions have experimentally been shown to coincide with measurable rail damage. Wear also creates problems when firing multiple successive shots. The damage done to the rails makes their surfaces rougher causing following shots to have more extreme current arcing and farther damage to both the rail and armature. One solution to this problem is to use a lubrication system to maintain electrical contact between the rails and armature, reduce the wear and melting of the armature, and provide transition free launches.

Experimental launches using lubrication systems have been conducted to identify if and when a transition occurs for various armature designs. This thesis analyses six armature designs with lubrication systems to predict the physical behavior and identify

the causes of transitions. The analysis models the armature-rail interface and simulates its physical behavior with a magneto-elastothermohydrodynamic model. The magneto-elastothermohydrodynamic model contains analyses of the lubricant between the rail and armature, contact between the rail and armature, electromagnetic and temperature fields, and armature deformation due to pressures, forces, and thermal gradients. This previously developed model has been modified to take account of turbulent flow in the injection conduit, various injection configurations, dry-out of the armature-rail interface, two dimensional pressure fields, and is capable of being extended to simulate armatures without extruded planar geometries.

CHAPTER 2

RESEARCH BACKGROUND

The analytical method presented in this thesis uses an extension of the magneto-elastothermohydrodynamic model developed by Wang [2] in 2009. The model was developed in three stages. First, the magneto-hydrodynamic model analyses the lubrication as it flows from the reservoir, into the armature-rail interface, and leaks out from the trailing edge of the armature. Second, the magneto-elastohydrodynamic model expands the former to consider elastic deformation of the armature due to magnetic and electric field interactions as well as contact and fluid pressure in the armature-rail interface. Finally, the elastothermohydrodynamic model adds the calculation of the temperature field, enabling the use of temperature dependent properties as well as considering the effect of thermal moments and expansion on the armature.

2.1 Magneto-Hydrodynamic Model

The lubricant must be an electrically conductive material to maintain good electrical contact between the rail and armature. For the same reason that the EML exerts forces on the armature, it also exerts Lorentz forces on the lubricant. The magneto-hydrodynamic model considers the armature to act as a hydrodynamic pad bearing. In the model, the effect of the Lorentz forces are merged with a conventional lubricant film

analysis including surface roughness, cavitation, and turbulence in the rail-armature interface.

In 1999 Flegontova and Yuferev presented a way to account for the Lorentz forces in a conducting lubricant arising from the passage of current through a magnetic field and inertial forces caused from acceleration of the armature. They introduced a magnetic pressure which takes the place of the body force in the Navier-Stokes Equation and added an acceleration term. The magnetic pressure term can be added to the hydrodynamic pressure to create the total pressure. The subsequent Reynolds Equation can be found by using the total pressure instead of solely the hydrodynamic pressure and adding the acceleration term [3]. This work is paramount to the magneto-hydrodynamic model especially since the exact magnetic field distribution is not needed to calculate the total pressure in the lubricant, which is sufficient for most studies. However, if cavitation is considered, the magnetic field distribution is needed. As Wang 2009 pointed out, if the hydrodynamic pressure is below the cavitation pressure, cavitation will occur and therefore one must subtract the magnetic pressure from the total pressure to identify if cavitation is occurring [2]. From 1999 to 2001 Drobyshevski et al. used a magneto-hydrodynamic model without cavitation to investigate how an electrically conductive lubricant can eliminate transitions by studying how the formation of an unlubricated gap at the armature-rail interface can lead to current arcing of a solid armature EML [4-7].

As mentioned, if the lubricant pressure drops below a threshold pressure cavitation will occur. The threshold pressure is referred to as the cavitation pressure. Cavitation is an important phenomenon to consider because it can cause transitions in an EML and computationally it sets a lower boundary on the hydrodynamic pressure. A

simplistic solution to the problem of cavitation was used by Oh and Goenka in 1985. They set all pressures in cavitation regions to be zero. While it succeeds in preventing negative pressures, it does not conserve mass [8]. However, in 1992 Payvar and Salant developed a cavitation index method to analyze seals in which cavitation may occur over only a portion of the region of interest [9]. This method both conserves mass and allows one equation to be used for the entire region. The cavitation index method was applied to EMLs by Salant and Wang in 2007 as they determined that configurations with converging gap interfaces and up-stream lubricant injection were the most successful at preventing cavitation [10].

Most EML models approximate the rail and armature surfaces to be smooth while analyzing the lubrication in the rail-armature interface, as done by Ghassemi et al. in 2003, 2005, and 2007 [11-13]. However, in 1978 Patir and Cheng presented an average flow model to account for the effect of roughness on stationary lubricated surfaces. The model uses flow factors developed from numerical simulations of lubricant flow [14]. In 1979 they expanded the model to sliding surfaces by developing the shear flow factor [15]. The flow factors developed by Patir and Cheng are used in many high speed hydrodynamic bearing studies for example, Feng and Kenjo used the flow factors to analyze friction and wear on two hydrodynamic bearings for hard disk drive spindle motors [16]. In 1983 Tripp increased the usability of flow factors by finding a closed form relationship between the flow factors, presented by Patir and Cheng, and the roughness parameters of the surfaces [17].

Due to the high velocities achieved by EML armatures, it can be conceived that lubricant velocities in the rail-armature interface may be high enough to enter into the

turbulent regime. Turbulence is commonly dealt with by increasing the lubricant viscosity using a turbulence factor. Wang considered three turbulent models, the Ng-Pan-Elrod model, Constantinescu's model, and the bulk flow model in 2009. It was determined that all three models employed similar turbulent factors. Constantinescu's model was chosen because it has the smoothest transition between the laminar and turbulent regimes [2]. All of the three models have been shown to obtain good results when applied to seals by Elrod and Ng in 1967 and bearings by Brunetiere et al. in 2002 and 2003 [18-20]. Although it is possible for an EML lubricant to become turbulent as it moves through the armature-rail interface, it has been shown by Stefani et al. in 2001 and 2005 that the laminar model for surface wear in an EML due to melt-lubrication is a closer match to experiments than the turbulent model [21 and 22]. Additionally, in 2009 Wang found that using a turbulent model to analyze an EML with lubricant injection results in fluid pressures high enough to cause yielding of the armature, because armature yielding was not observed in experiments, it was concluded that a laminar model better simulates the lubricant behavior [2].

2.2 Magneto-Elastohydrodynamic Model

The shape of the armature-rail gap has a profound effect on the fluid pressures within the lubricant film. In order to create a good electrical contact at the beginning of a launch, armatures are designed to have an interference fit when inserted between the rails. This deforms the armature elastically and changes the geometry of the gap due to the resulting contact pressure. Additionally, an EML generates extremely high Lorentz

forces on the armature. A significant portion of the Lorentz forces act to accelerate the armature along the rails, however some of the forces act to push the armature into the rails. A Magneto-elastohydrodynamic Model is needed because of the coupled nature of armature deformation, fluid pressure, and contact pressure.

An EML must maintain electrical contact between the armature and rail in order to prevent current arcing. Lubricated EMLs are designed to use the armature-rail interface much like a hydrodynamic pad bearing so at high sliding velocities dry contact does not generate extensive wear and heat which can lead to transitions. However, at the beginning of a launch the armature speed is very low and the contact is dominated by solid-solid contact. In 1966 Greenwood and Williamson developed the Greenwood-Williamson contact model to approximate the contact pressure on a rough surface by assuming a Gaussian distribution of asperity heights [23]. However, the results of the Greenwood-Williamson contact model have been shown by Greenwood and Wu in 2001 to be dependent on the scale at which the surface is measured [24]. In 2001 Streator used the Greenwood-Williamson model along with surface parameters which were less scale dependent to provide a good approximation of the contact pressure of rough surfaces in contact [25].

Deformation of the rail can also change the gap geometry as studied by Rapka et al. in 1995, Jerome in 2003, Johnson and Moon in 2006, and Daneshjoo et al. in 2007 [26-29]. The dynamic resonance of the rails due to a moving pressure wave was studied by Tzeng in 2003, who determined the relationship between critical velocity to cause resonance and the containment size [30]. In 2001 James, T. and James, D. modeled the armature as a cantilever beam to approximate the contact pressure distribution at the

beginning of a launch [31]. A 3D analysis of armature deformation due to Lorentz forces was done by Hopkins et al. in 1999 and Newill et al. in 2003. Their method combined a finite element code, EMAP3D, for electromagnetic field analysis with a structural code, DYNA3D [32 and 33]. In 2003, Zielinski et al. used experimental x-ray data to conclude that large scale plastic deformation of the armature does not occur [34]. Of the literature reviewed, the only one to consider deformation of the armature on a lubricated EML with surface roughness and a non-flat interface was Wang in 2009 [2].

The use of a Magneto-elastohydrodynamic Model requires the calculation of the magnetic field distribution in order to determine the Lorentz forces acting on the armature and their distribution. Few electromagnetic field models applicable to EMLs exist. A 3D model, EMAP3D, was presented in 1995 and 1997 by Hsieh and in 2007 by Thiagarajan and Hsieh. This model calculates the electric field and magnetic field distributions in sliding conductors but does not include an analysis of lubricated interfaces [35-37]. In 1999 Drobyshevski et al. developed a 2D model to approximate the electric and magnetic fields by assuming that the magnetic field was unidirectional between the rails [5]. Assuming a unidirectional magnetic field is an important simplifying assumption because it reduces the Maxwell equations down to one differential equation which governs the magnetic flux density in the armature region. From this magnetic flux density, the electric current and Lorentz force distributions can be calculated. This 2D model was later used by Ghassemi et al. in 2003, 2005, and 2007 as they determined the electromagnetic field, thermal field, and Lorentz force distributions acting on an EML armature and studied the effect of a conductive lubricant in the armature-rail interface [11-13].

The high velocities of an EML armature have an intense effect on the current distributions. This effect called the velocity skin effect tends to concentrate the current density at the trailing edge of the contact. The buildup of high current density at the trailing edge can lead to heating as well as current arcing behind the armature. In 1982 Young and Hughes included the velocity skin effect to obtain closed form solutions for steady state electric and magnetic field distributions in a 2D analysis [39]. A 3D analysis including the velocity skin effect and contact resistance was done in 1995 by Barber and Dreizin for an unlubricated EML [40]. Experimental evidence of the velocity skin effect was shown in 2008 by Engel et al. by analyzing EML efficiency and breech voltage [41].

2.3 Magneto-Elastothermohydrodynamic Model

The extremely high current densities in an EML generate a substantial amount of joule heating within the armature. Additionally, the high velocities give rise to frictional heat generation at the sliding contacts as well as viscous heating within the lubricant film in the interface. Even though the heating occurs over a small amount of time, it has been observed to be high enough to melt the armature material in unlubricated EMLs. James in 1995 and Woods in 1997 used a 2D melt wave model to explain that the velocity skin effect causes the melting to begin at the trailing edge and move to the leading edge of the interface as material is removed and electrical contact is lost [42 and 43]. Lubricated armatures are designed to eliminate melting; however, the temperatures generated can be a major contributor to armature-rail interface gap deformation. Adding the calculation of the temperature field to the magneto-elastohydrodynamic model, the armature

deformation due to thermal expansion and moments as well as temperature dependent material properties can be achieved with the resulting magneto-elastothermohydrodynamic model.

In 1995 and 1999 Powell and Zielinski used a 2D model and Critchley used a 3D finite element model in 1995 to analyze the temperature field in an EML armature due to joule heating [44-46]. Hsieh and Kimused applied a 3D code, EMAP3D, that included frictional heat generation at the interface and joule heating of an unlubricated armature in 1997 [47]. Stefani et al. studied viscous heating in the armature-rail interface of a lubricated EML in 2001 and 2005 [48 and 49]. The previously mentioned work by Ghassemi et al. in 2003 and 2005 includes the effects of both viscous and joule heating. They found that the use of a conductive lubricant in the rail armature interface can prevent the melting of the armature as well as increase the electrical contact area [12 and 13].

The magneto-elastothermohydrodynamic model presented by Wang in 2009 is the most complete model found. It employs the finite difference method to solve the governing differential equations for various physical parameters. This model has been applied to EML with limited success due to some of the simplifying assumptions.

The electromagnetic portion of the model assumes the magnetic field is dominant in one direction to simplify the electric current and magnetic flux fields to 2D. The boundary conditions used were zero magnetic flux on the outer surfaces of the rails, continuity at the interface, current dependent magnetic flux on the inside of the armature trailing edges and inside of the rails behind the armature, and magnetic insulation on all

other boundaries. The current density is then calculated from the magnetic flux density [2].

The thermal portion of the model calculates the temperature field by assuming the heat transfer is two dimensional. Viscous, frictional, and joule heating are all considered. It is assumed that the armature does not melt based on experimental observations. Any portion of the armature which is at the melting temperature is assumed to have an energy below the latent heat of fusion. The model takes the velocity of the armature into account and analyzes the rail, armature, and lubricated regions. The boundary conditions used are continuity over the armature-rail interface and thermal insulation everywhere else [2].

The portion which considers the deformation of the armature uses Euler-Bernoulli beam theory. The armature is modeled as a cantilever beam, fixed at the leading edge of the interface. Two 2D finite element models are used to find two cantilever beam cross sections each being elastically similar to one of the finite element armature models with respect to the armature deformation at the armature-rail interface. The first finite element model uses a point force applied to the trailing edge of the armature. The equivalent cross section of this model is used to analyze the interface deformation due to Lorentz forces, fluid pressures, and contact pressures. The contact pressures are calculated with the Greenwood-Williamson model. The second model uses a distributed temperature field inside the armature; its equivalent cross section is used to analyze the interface deformation due to thermal moments and expansion. In the magneto-elastothermohydrodynamic model, the interface deformation due to forces and pressures is superimposed with those due to thermal moments and expansion [2]. The following assumptions were made:

1. Plane strain
2. The armature is linear-elastic, homogenous, and isotropic
3. The loading and heating is quasi-static
4. Small deformations
5. The rail is rigid and flat
6. Euler-Bernoulli beam theory and the Greenwood-Williamson model are valid

In the hydrodynamic portion of the model the armature is modeled as a hydrodynamic pad bearing with lubricant flowing into the pocket from the initially full reservoir through an injection conduit. The Hagen-Poiseuille equation is used to analyze the lubricant in the injection conduit while the Navier-Stokes and Reynolds Equations are used for the lubricant film in the interface [2]. The following assumptions were used to simplify the problem:

1. The rail is assumed to be rigid, flat, and level
2. The flow is assumed to be laminar, incompressible, and quasi-steady both in the conduit and in the interface
3. The interface is assumed to be sufficiently short, so the change in parameters in the direction of the armature velocity is dominant
4. No-slip boundary conditions are used on the lubricated surfaces
5. Lubricant cavitation in the interface, electromagnetic effects in the lubricant, and temperature dependent viscosity are considered
6. The interface gap profile is given from considering the deformation of the armature

Wang used this magneto-elastothermohydrodynamic model to analyze an armature developed at the Georgia Institute of Technology. The results of the model agreed fairly closely with the experimental data collected. However some of the assumptions made are based on the geometry of the armature and will not be valid for every design. Additionally, based on the results shown, the lubricant flow in the conduit is in the turbulent regime and thus, violates one of the assumptions made while determining the lubricant supplied to the pocket.

CHAPTER 3

ARMATURE-RAIL INTERFACE MODELING

The magneto-elastothermohydrodynamic model developed by Wang is modified to analyze six armature designs. Four of the designs are for rectangular bore EMLs thus, allowing the regions to be simplified to their 2D projections. The other two designs are for round bore EMLs, making 2D approximations more difficult. Every design uses copper rails, an aluminum armature, and gallium as the lubricant. Table 3.1 displays properties for the materials used in this model. The model uses finite difference methods to break the launch down into finite time steps. At each time step the governing equations are also solved with finite difference methods. Highly coupled equations are iterated to a low error while lightly coupled or uncoupled equations only need to be calculated once per time step. The goal of this modeling effort is to predict the behavior of the armature and lubricant. Most prominently, predicting when current arcing transitions happen and explaining what led to the event. Each armature must be analyzed on a case by case basis because different geometries may call for different simplifying assumptions. Below, the overall model is developed for the base case EML. The following EML analyses use the same governing equations as the base case except where modifications are noted.

Table 3.1: Material Properties [2]

Aluminum (Armature)	
σ	1 μm
E	70 GPa
ν	0.33
$\sigma^{*(2)}$	$\frac{3.21\times10^{7}}{1+0.0039(T-27)}$ Mho/m
μ_a	1.2567×10^{-6} N/A^2
k_a	167 W/(m-K)
$c_a^{(2)}$	0.486(T+273)+766 J/(Kg-^{o}C)
Copper (Rail)	
σ	1×10^{-6} m
γ	1 (isotropic)
E	120 GPa
ν	0.33
$\sigma^{*(2)}$	$\frac{4.41\times10^{7}}{1+0.0039(T-27)}$ Mho/m
μ_r	1.2567×10^{-6} N/A^2
k_r	388 W/(m-K)
$c_r^{(2)}$	0.0987(T+273)+355 J/(Kg-^{o}C)
Gallium (Lubricant)	
$\mu^{(1)}$	$2.468\times10^{-4}\left(\frac{\rho}{1000}\right)^{\frac{1}{3}} e^{\frac{79.05\left(\frac{\rho}{1000}\right)}{T+273}}$ Pa-s
ρ	6.0×10^{3} kg/m^3
σ^*	5.75×10^{6} Mho/m
μ_f	1.2567×10^{-6} N/A^2
k_f	41 W/(m-K)
c_f	371 J/(Kg-^{o}C)
Air	
σ^*	0 Mho/m
μ_{air}	1.2567×10^{-6} N/A^2

(1): Units for ρ are kg/m^3.
(2): Unit for T is ^{o}C.

3.1 Base Case

The base case was developed at the Georgia Institute of Technology. A sketch of the base case armature is shown in Figure 3.1. The launcher used is a 0.1 MJ railgun with one meter long rails. The time for the armature to reach the end of the one meter long rails is approximately 1.5 ms [50]. The armature is 1.44 in long with a maximum lubricated surface length of 0.743 in. The nominal width at the trailing edge is 0.561 in which is an interference fit when inserted in between the rails, spaced 0.551 in apart. A reservoir cartridge inserted into the front of the armature provides the lubricant during launch. The reservoir cartridge has an inner diameter of 0.200 in and is initially loaded with a gallium lubricant charge of 0.9 grams. A thin membrane of Mylar seals the reservoir. When the armature accelerates, the Mylar sheet ruptures and allows the lubricant to flow through the two 0.039 in injection conduits to the two pockets. The mass of the aluminum armature and empty cartridge is 8.9 grams.

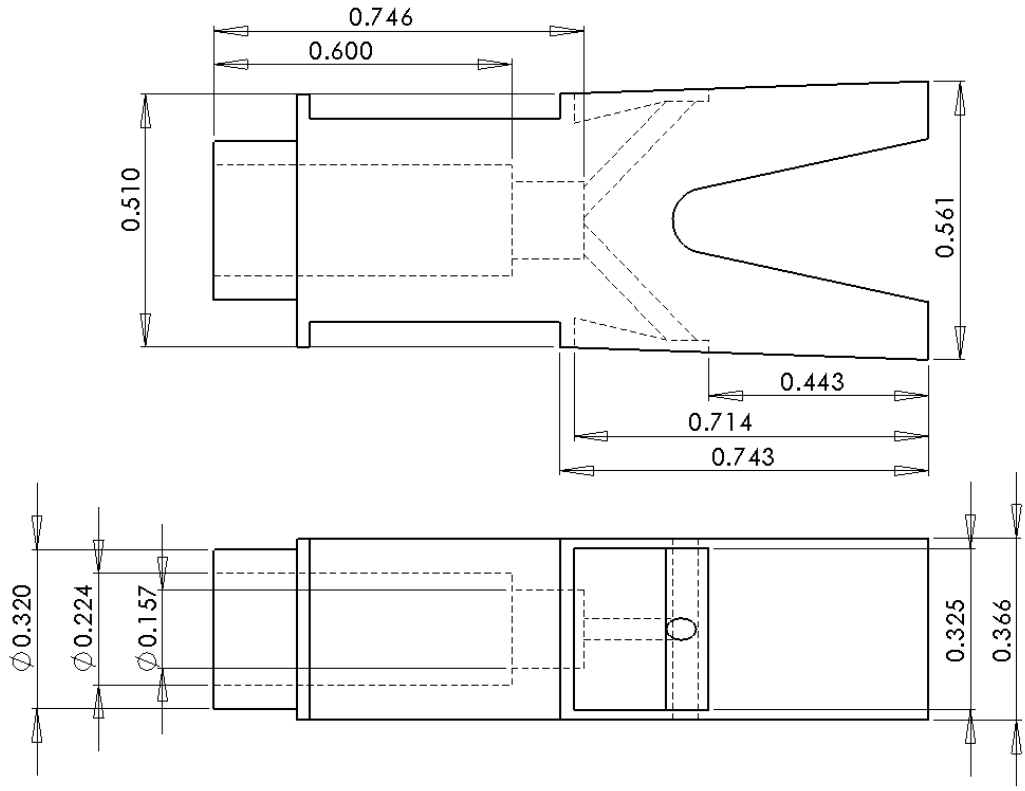

Figure 3.1: Sketch of the base case armature, dimensions are in inches

3.1.1 Electromagnetic Field Modeling

The least coupled physical parameter of interest is the electromagnetic field. The electromagnetic field is affected mainly by the current input and the armature velocity. Passing high currents through a conductor creates a large magnetic field encircling the current path according to the right hand rule. Additionally, the armature velocity creates an induced current by passing a conductor through a magnetic field. Due to the complexities of three dimensional calculations, it is assumed that the magnetic field strength on the armature can be modeled as one dimensional by neglecting the weaker two components of the field. There are three regions for which the magnetic field must be analyzed, the armature, the rails and the lubricant film. The boundary condition of

zero magnetic flux is applied on the outside of the rails, the inside of the rails ahead of the contact region, and the boundary of the armature ahead of the contact. At the armature-rail interface there is continuity between the rail and lubricant as well as between the lubricant and armature. A zero normal gradient was used for the boundary which divides the armature along the line of symmetry allowing for only half the region to be analyzed. For the remaining boundaries, namely, the insides of the rail and armature boundary where it meets the air behind the armature, the magnetic flux density is specified. Equations 3.1-3.3 can be solved numerically to yield the magnetic field strength in the corresponding region. Subscript r, a, and f correspond to properties of the rail, armature, and fluid film respectively [2].

$$\frac{\partial B_r}{\partial t} + U\frac{\partial B_r}{\partial x} = \frac{\partial}{\partial x}\left(\frac{1}{\mu_0 \sigma_r^*}\frac{\partial B_r}{\partial x}\right) + \frac{\partial}{\partial y}\left(\frac{1}{\mu_0 \sigma_r^*}\frac{\partial B_r}{\partial y}\right) \tag{3.1}$$

$$\frac{\partial B_a}{\partial t} = \frac{\partial}{\partial x}\left(\frac{1}{\mu_0 \sigma_a^*}\frac{\partial B_a}{\partial x}\right) + \frac{\partial}{\partial y}\left(\frac{1}{\mu_0 \sigma_a^*}\frac{\partial B_a}{\partial y}\right) \tag{3.2}$$

$$h\frac{\partial B_f}{\partial t} + q_{vol}\frac{\partial B_f}{\partial x} = \frac{\partial}{\partial x}\left(D_f h\frac{\partial B_f}{\partial x}\right) + D_a\frac{\partial B_a}{\partial y} - D_r\frac{\partial B_r}{\partial y} \tag{3.3}$$

Once Equations 3.1-3.3 are solved numerically, the electric current and magnetic force densities can be determined by Equations 3.4-3.7. Because the same equations apply for all three regions when the corresponding properties are used, the subscript i can be either r, a, or f representing the properties of the rail, armature, or fluid film. The force which accelerates the armature is f_x while the force which tends to spread the armatures trailing edges apart and increase the frictional forces is f_y [2].

$$J_{x,i} = \frac{1}{\mu_{0,i}} \frac{\partial B}{\partial y} \tag{3.4}$$

$$J_{y,i} = -\frac{1}{\mu_{0,i}} \frac{\partial B}{\partial x} \tag{3.5}$$

$$f_{x,i} = J_{y,i} B = -\frac{1}{\mu_{0,i}} B \frac{\partial B}{\partial y} \tag{3.6}$$

$$f_{y,i} = -J_{x,i} B = -\frac{1}{\mu_{0,i}} B \frac{\partial B}{\partial x} \tag{3.7}$$

The assumption that magnetic field can be approximated as one dimensional is validated using a 3D analysis in COMSOL. Additionally, the magnetic field and current density distributions will be validated using the COMSOL simulation. The COMSOL model is a steady state model using a combination of the 3D Conductive Media DC module for the electric current distribution and the 3D Magnetostatics module to provide the induced magnetic field. The armature is modeled in a simplified form without the pocket using solid-solid contact along the entire armature-rail interface, see Figure 3.2. Modeling with or without the pocket is acceptable because during launch the velocity skin effect concentrates the magnetic flux, electric current, and magnetic force densities on the trailing edges away from the pocket. The boundary conditions for the Conductive Media DC module are electric insulation for all boundaries except the ends of the rails. One of the rail ends is subjected to an inward current flow and the other is set as ground. For the Magnetostatics module the boundary conditions are magnetic insulation on all the surfaces.

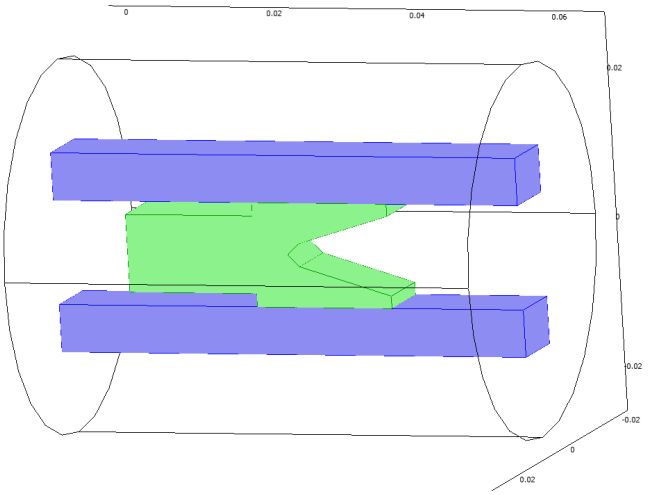

Figure 3.2: COMSOL model used for electromagnetic validation

Figure 3.3 compares the 3D steady state COMSOL simulation magnetic flux density distribution to the 2D finite difference calculations used to analyze the base case. It is important to notice that the COMSOL simulation predicts negative magnetic flux densities on the outer surface of the rails while the finite difference calculations use a zero magnetic flux on these surfaces as a boundary condition. However, the distribution of the magnetic flux density is very similar between the two, especially in the armature region.

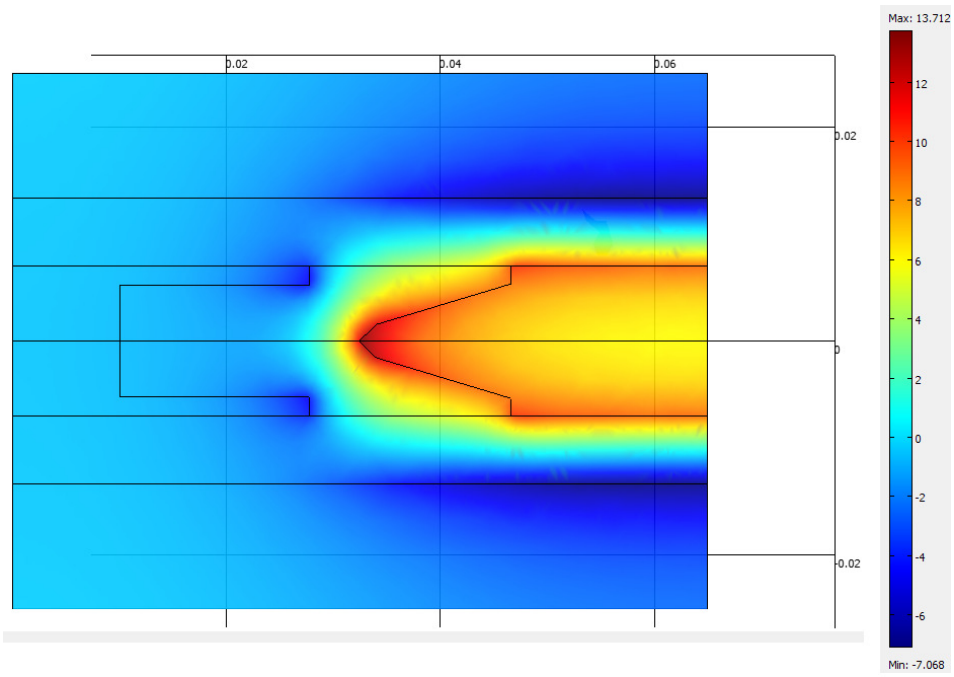

(a)

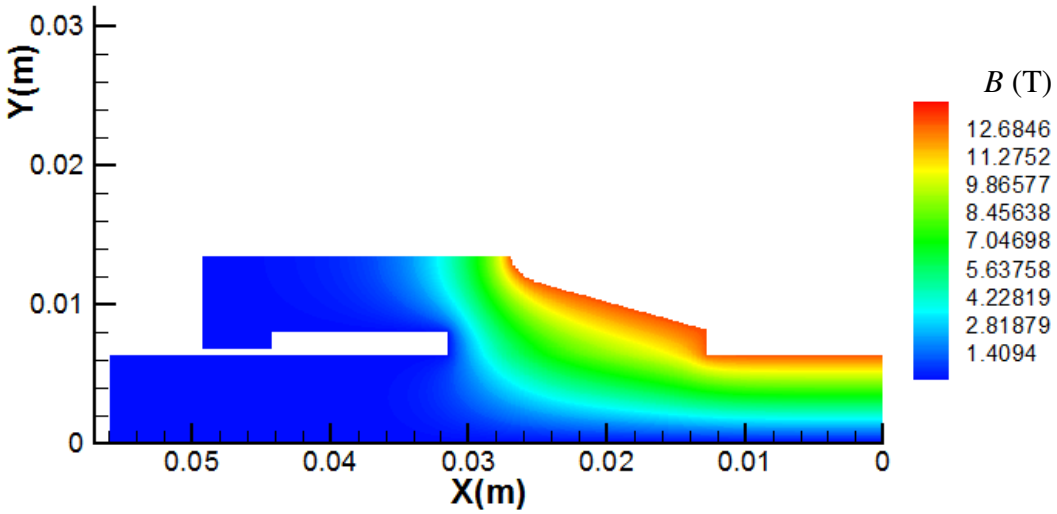

(b)

Figure 3.3: Comparison of magnetic flux distributions calculated by (a) COMSOL and (b) finite difference method, units in T

The magnetic flux boundary condition which must be specified varies from one time step to another in the magneto-elastothermodynamic model. Using Ampere's circuital law, a relation between current and magnetic flux density is developed by Equation 3.8 [51]. When performing the contour integral about the cross section of the rail, the 2D boundary conditions result in zero values for three of the rail boundaries and a constant magnetic flux, $B_{0,}$ on the boundary which faces the armature. However, as shown in Figure 3.3, the boundary conditions used in the 2D simplification are not exactly as portrayed by the 3D analysis. To make the relationship between current and the magnetic flux density on the inside of the rail valid for a 2D simplification, a correction factor is used resulting in Equation 3.9.

$$\oint Bds = \mu_0 I \tag{3.8}$$

$$B_0 = \frac{\mu_0 I}{C_{2D} b} \tag{3.9}$$

The current distributions obtained from both the COMSOL simulation and the finite difference method are displayed in Figure 3.4. The COMSOL simulation shows good concurrence with the finite difference calculations. The electric current density is high at both the trailing edges of the armature wing and the radius between the wings. Also the current density is low toward the front of the armature. Both of these calculations use a steady state model with zero armature velocity. Therefore the velocity skin effect is not observed here, but will be observed when simulating the EML.

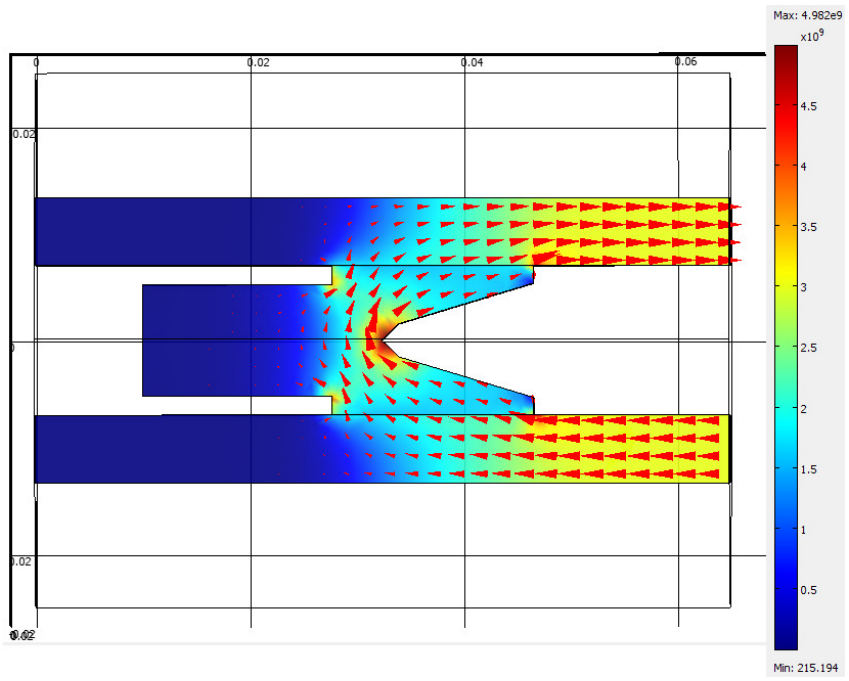

(a)

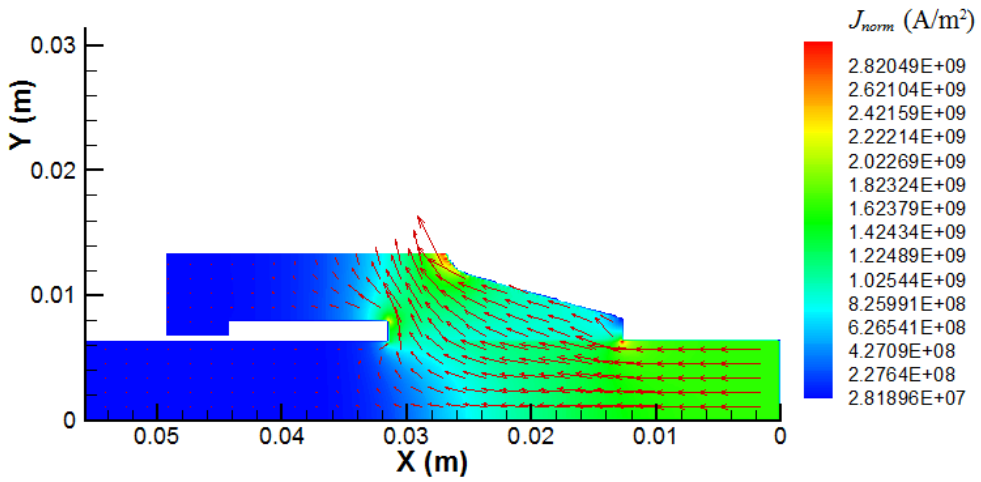

(b)

Figure 3.4: Comparison of current distributions calculated by (a) COMSOL and (b) finite difference method, units in A/m^2

The assumption that the magnetic field can be approximated by only considering the dominant direction of the field is validated in Figure 3.5. The dominant component has a direction into the page. The two other components, parallel and perpendicular to

the rails have much lower magnitudes. Because the magnetic field is weak in these directions, it will not have much effect on the shot and thus will be neglected in order to simplify the computations and modeling efforts.

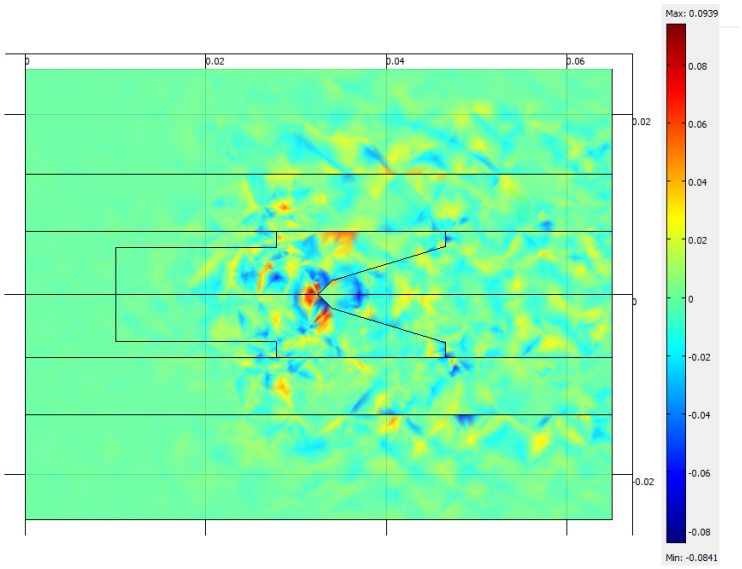

(a)

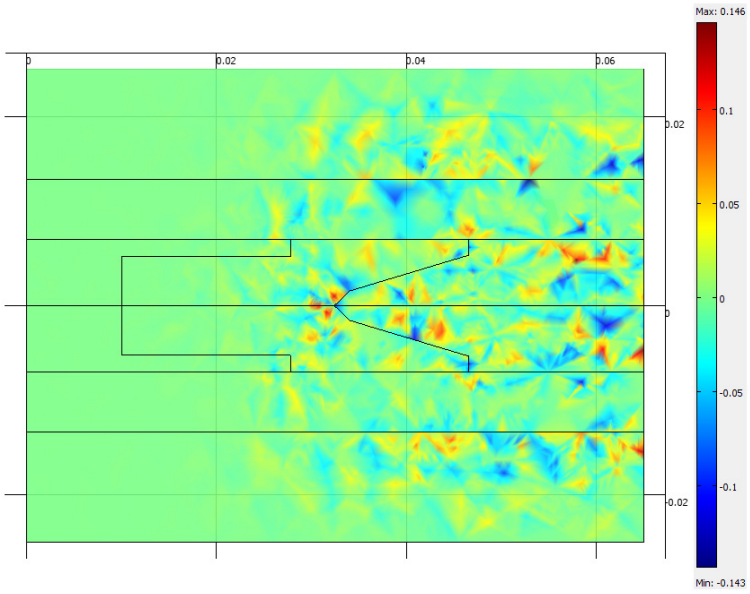

(b)

Figure 3.5: Magnetic flux density in the direction (a) parallel to the rails (b) transverse to the rails, units in T

3.1.2 Thermal Field Modeling

The thermal field is a lightly coupled physical parameter. Even though the thermal field is very important in the magneto-elastothermohydrodynamic model, it changes in a relatively slow and smooth manner allowing the thermal field from the previous time step to be used for current step calculations. Therefore, the thermal field only needs to be calculated at the end of every time step. The heating sources considered are current joule heating, viscous heating, and frictional heating. When considering the heat generated by solid-solid contact, the armature sees a mostly stationary heat source while the rail and lubricant see a moving source. It is expected that the majority of the heat will go to the regions which see a moving heat source. Therefore it is assumed that the lubricant absorbs all of the heat generated by solid-solid contact. Solid-solid contact heating is expected to be small compared to the joule and viscous heating and limited to the beginning of a shot only; as a consequence, the assumption should make little difference in calculating the temperature field. The temperature field in the rail, armature, and lubricant is approximated as two dimensional by neglecting any temperature gradients in the direction of the magnetic flux. Additionally, phase change is not considered. The following three equations can be used to calculate the transient heat diffusion in the rail, armature, and fluid film respectively [2]. Using symmetry, only half of the armature is modeled, with an adiabatic boundary condition on the line of symmetry. Adiabatic boundary conditions are used for the beginning and end of the rail and any boundary which touches the air. The lubricant is assumed to be at ambient temperature when it enters the armature-rail interface.

$$\rho_r c_r \left(\frac{\partial T_r}{\partial t} + U \frac{\partial T_r}{\partial x} \right) = k_r \left(\frac{\partial^2 T_r}{\partial x^2} + \frac{\partial^2 T_r}{\partial y^2} \right) + \frac{J^2}{\sigma_r^*} \tag{3.10}$$

$$\rho_a c_a \frac{\partial T_a}{\partial t} = k_a \left(\frac{\partial^2 T_a}{\partial x^2} + \frac{\partial^2 T_a}{\partial y^2} \right) + \frac{J^2}{\sigma_a^*} \tag{3.11}$$

$$\rho_f c_f \left(h(x) \frac{\partial T_f}{\partial t} + Q_f(x) \frac{\partial T_f}{\partial x} \right) = k_a \frac{\partial T_a}{\partial y} - k_r \frac{\partial T_r}{\partial y} + h \frac{\partial^2 T_f}{\partial x^2} + h \frac{J^2}{\sigma_f^*} + \int_0^h \dot{q} dy + \delta(x) f_f U P_{cont} \tag{3.12}$$

where,
δ = 1 for solid-solid contact, 0 for non-contact
f_f = solid-solid contact friction factor

In order to validate the solution method of the above equations, a simplified steady state case is used. The simplified case applies a high temperature on the boundaries where the current densities and thus joule heating will be the highest, the inside of the armature wing. Continuity is maintained over the armature-rail interface, however, the lubricant is neglected and perfect contact is modeled for the entire interface. The line of symmetry is still taken as adiabatic so only half of the armature needs to be analyzed and all other boundaries are confined to ambient temperature. The finite element software ANSYS is used to validate the finite difference method used. ANSYS PLANE 13 is employed; each element has four nodes with up to four degrees of freedom per node. It is a 2D code capable of considering 2-D magnetic, thermal, electrical, piezoelectric, and structural fields [52]. Figure 3.6 shows agreement between the ANSYS and finite difference methods, modeling with or without the pocket will yield approximately the same temperature field in this case.

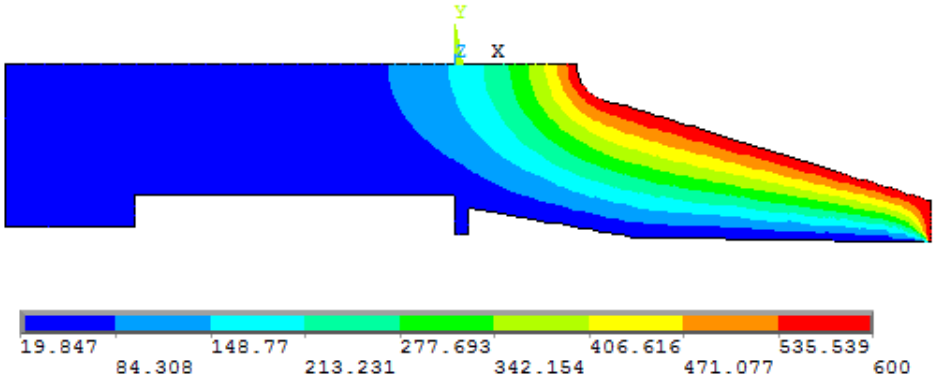

(a)

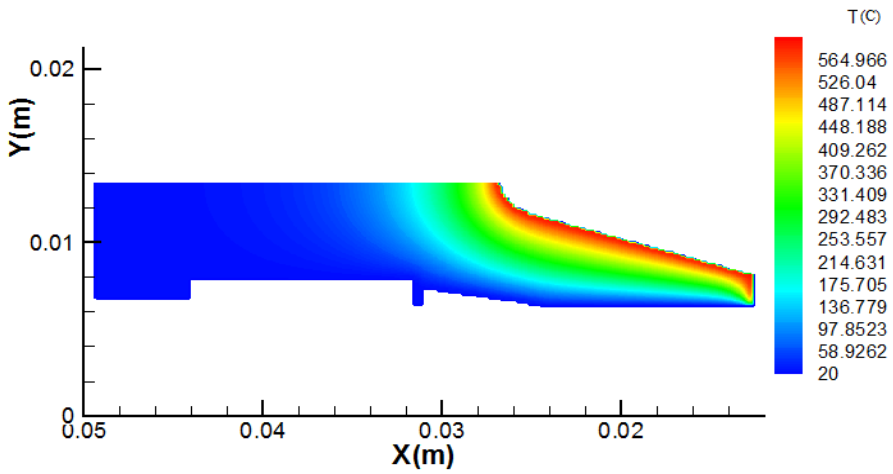

(b)

Figure 3.6: Temperature field validation calculated by (a) ANSYS and (b) finite difference method, units in C

3.1.3 Armature Deflection Modeling

During a launch there are many factors which act to deform the armature. The magneto-elastothermohydrodynamic model includes the elastic deformation of the armature as a result of the contact with the rail, fluid pressure inside the lubricated gap, magnetic forces pushing the wing against the rail, thermal moments, and thermal expansion. The deflection of the armature is very important to the fluid pressure in the interface; also, the fluid pressure is very important to the armature deflection. Due to the

highly coupled nature of these parameters, both must be found simultaneously. Changes in the interface gap height due to damage or wear of the armature and rails is not considered in the model. Therefore, results from the simulation after a transition is predicted should be used cautiously because transitions have been experimentally been shown to coincide with surface damage and wear. The armature wing is approximated as a cantilever beam with a non-constant cross sectional area as shown in Figure 3.7. Euler-Bernoulli beam theory is used to evaluate the elastic deflection of the armature. The magnetic forces in the direction of the rails do not contribute to the armature deformation because they act to accelerate the armature along the rails. The magnetic forces which act perpendicular to the rails as well as the fluid and contact pressures are modeled as distributed loads on the cantilever beam. The deflections resulting from the distributed loads can be found by Equations 3.13-3.17 [2].

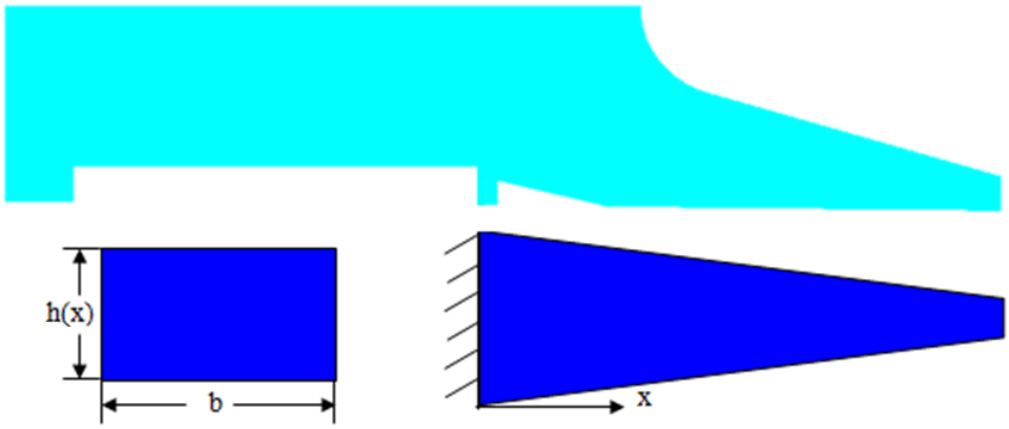

Figure 3.7: Transformation of the armature wing to a cantilever beam

$$-\frac{d^2}{dx^2}\left(EI^*(x)\frac{d^2v^*(x)}{dx^2}\right)=w(x) \tag{3.13}$$

$$F(x) = F_0(x) + \int -w(x)dx = \frac{d}{dx}\left(EI^*(x)\frac{d^2v^*(x)}{dx^2} \right) \tag{3.14}$$

$$M(x) = \int F(x)dx = EI^*(x)\frac{d^2v^*(x)}{dx^2} \tag{3.15}$$

$$v^{*\prime}(x) = \frac{dv^*(x)}{dx} = \int \frac{M(x)}{EI^*(x)}dx \tag{3.16}$$

$$v^*(x) = \int v^{*\prime}(x)dx \tag{3.17}$$

ANSYS is used to determine equivalent cross sectional properties for the approximated cantilever beam such that the approximated beam deforms in the same manner as the ANSYS armature wing model [2]. To obtain a more accurate approximation, two slightly different equivalent cross sections are used and the resulting deformations are superimposed. One cross section is used for all distributed pressures and forces; the other is used for all thermal loads. The ANSYS model utilized to determine the equivalent cross section considering forces and pressures uses PLANE 183. PLANE 183 uses two dimensional eight node elements with two degrees of freedom per node (x and y translations). One half of armature is modeled using a plane strain approximation and symmetry as done for the validation of the thermal field. The armature is constrained so the symmetry line does not deform perpendicular to the rails and the most forward boundary of the armature does not deform along the rails. A shear force is applied at the trailing edge of the armature and the resulting armature deflection is compared to that obtained by the solution to the Euler-Bernoulli equations above. The cross section of the beam in the finite difference model is adjusted until an equivalent cross section is found.

A comparison of the ANSYS and Euler-Bernoulli calculations of armature deflection due to the application of a point force at the armature trailing edge are displayed in Figure 3.8. Error in the deflections at points inside the pocket will not effect the computation of the gap height because deformation of the pocket will have little effect on the lubricant behavior and therefore is not considered. For the remaining regions, the ANSYS simulation and the Euler-Bernoulli solutions only show a small amount of deviation for all of the forces considered.

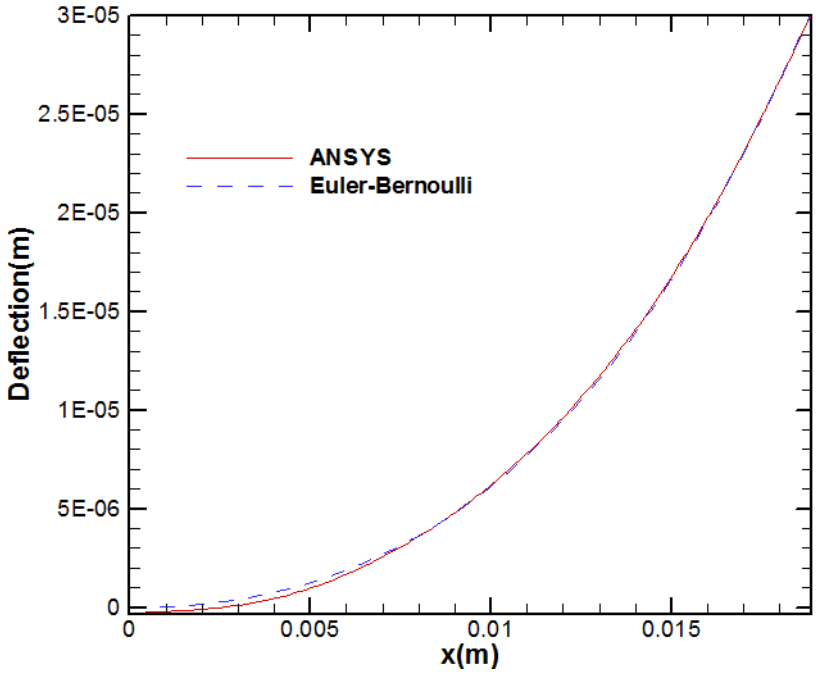

(a)

Figure 3.8: Comparison of armature wing deflection between ANSYS and Euler-Bernoulli models with a shear force of (a) 100 N, (b) 200 N, (c) 500 N, and (d) 1000 N

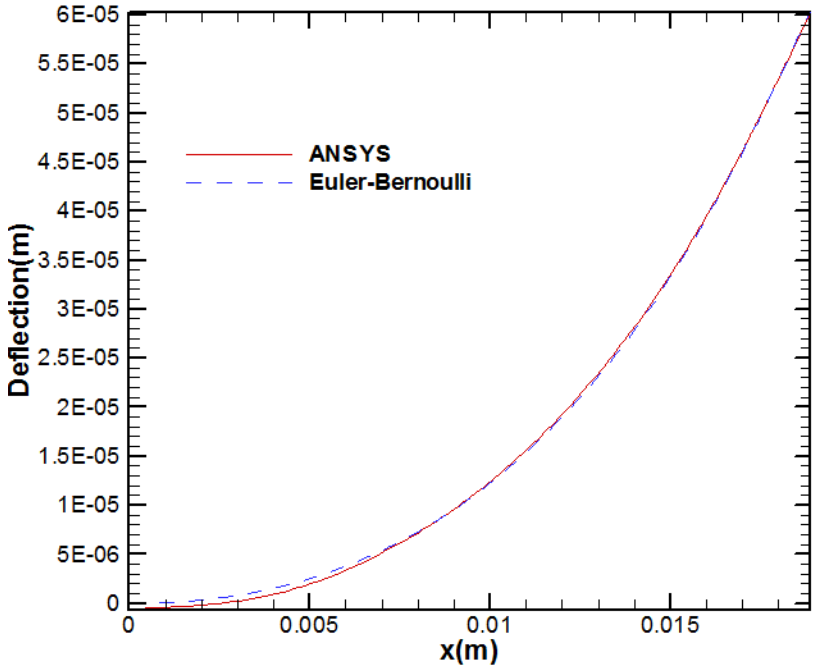

(b)

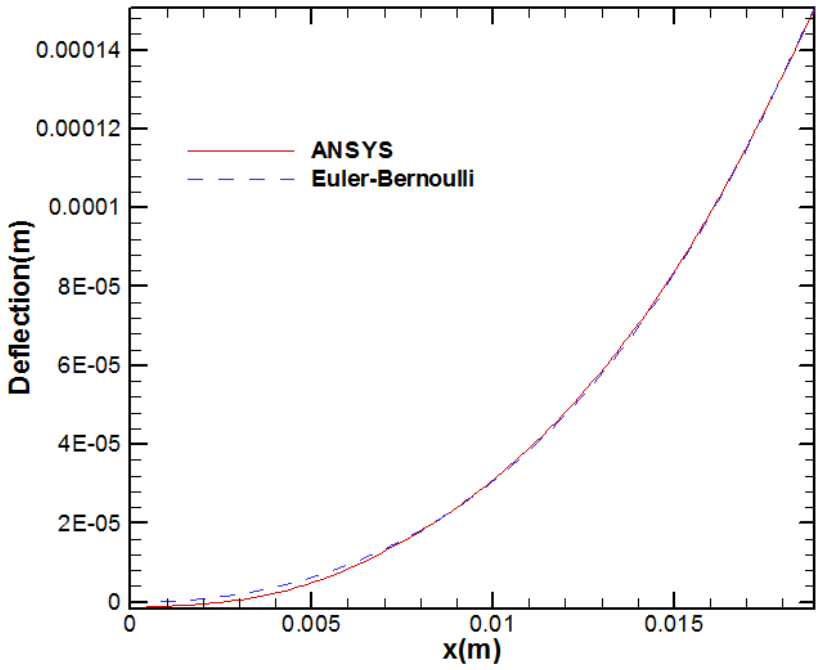

(c)

Figure 3.8 continued

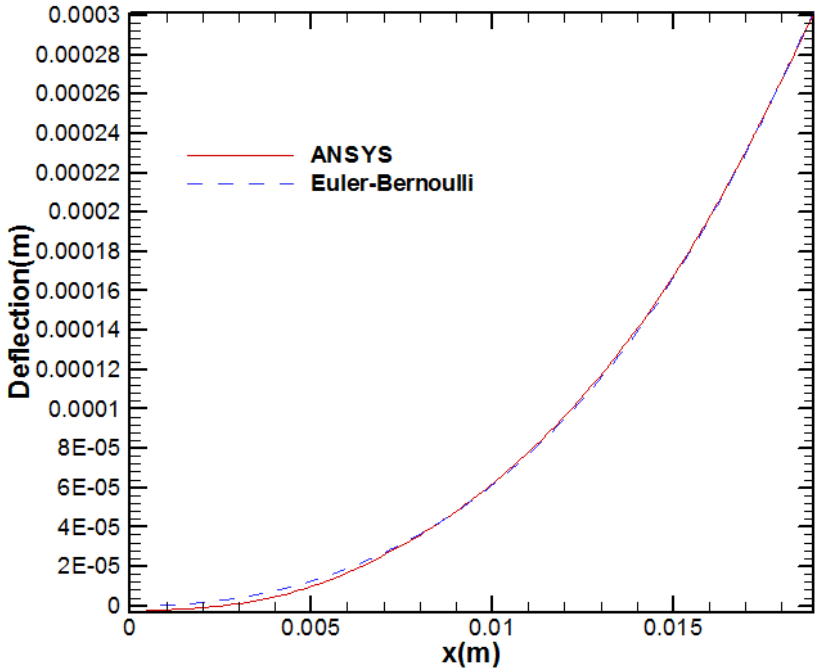

(d)

Figure 3.8 continued

One of the pressures which act to deform the armature is the contact pressure. The contact pressure also gives rise to a frictional force. To estimate the contact pressure between the armature wing and the rail, the Greenwood-Williamson model is employed. The armature is considered to be a rough elastic surface, while the rail is assumed to be rigid, smooth, and flat. As the asperities come into contact, the resulting contact pressure deforms the armature. By assuming a Gaussian distribution of asperity heights, the contact pressure can be found by Equation 3.18. In order to calculate the nondimensional rms roughness the radius of the asperities is assumed to be ten times the rms surface roughness and the asperity density is approximated as one over the square of the asperity radius [2].

$$p_{cont} = \frac{4}{3}\frac{E\hat{\sigma}^{3/2}}{\left(1-\nu'^{2}\right)}I' \tag{3.18}$$

In order to substantiate the contact pressure calculations, ANSYS is again used with the PLANE 183. The cross sections of the armature and rail are modeled and symmetry is used so only half the region is analyzed. The boundary conditions applied to the armature remain the same; however, no shear force is applied to the armature wing tip. Instead, the rail is modeled and selected as the target surface using TARGE169 and the armature is selected as the contact surface with CONTA172. The two conditions on the rail are zero displacement in the direction parallel to the rails and a displacement which brings the inside of the rail into interference with the armature. The actual interference at the beginning of the shot for the base case is 127 μm [2]. Figure 3.9 displays the contact pressure from the leading edge of the armature-rail interface to the trailing edge obtained by the ANSYS simulation and the Greenwood-Williamson model for interferences of 127 μm and 177.8 μm. For the case of 127 μm interference, the armature makes contact only on the trailing edge. Because the armature and rail make a converging gap, as the interference is increased, the contact moves toward the leading edge.

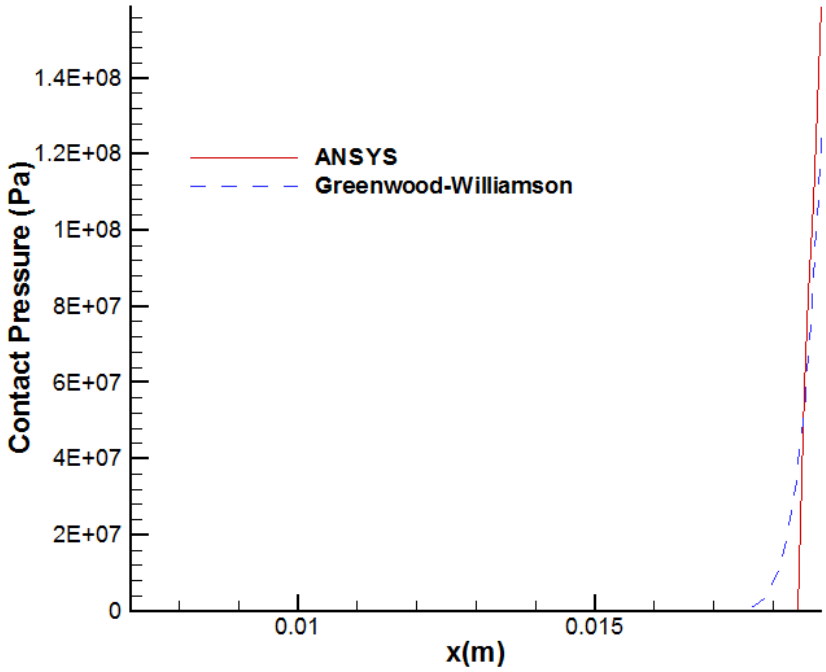

(a)

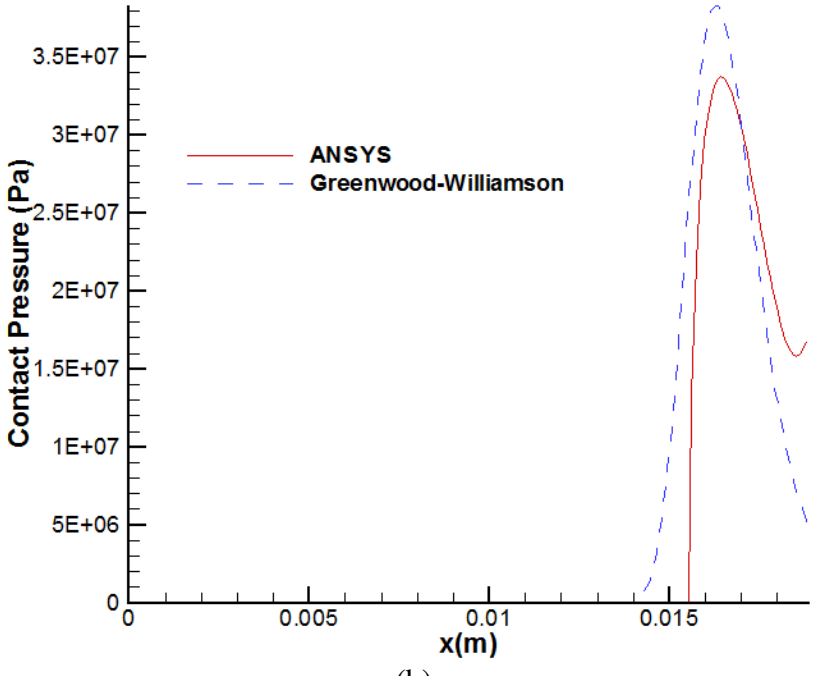

(b)

Figure 3.9: ANSYS and Greenwood-Williamson model contact pressure for an interference of (a) 127 μm and (b) 177.8 μm

It can be seen that there is some difference in the contact pressures calculated by these two models. However, the results are similar in magnitude. Error in the contact pressure is acceptable because it plays a small role in the simulation of a launch. In general as the lubricant fills the interface, the armature is deformed out of contact with the rail making the contact pressure zero for most of a launch. Additionally, the contact occurs over a small enough region that the frictional force due to solid-solid contact is small compared to the net Lorentz force. The most important effect of the contact pressure is the deformation of the armature, compared in Figure 3.10. Although there is some difference in the contact pressures obtained by the two models, the resulting contact deflections using ANSYS and the Euler-Bernoulli model show only little variation. The Euler-Bernoulle model in Figure 3.10 uses the Greenwood-Williamson contact pressures, while the ANSYS model uses the contact pressures calculated by ANSYS.

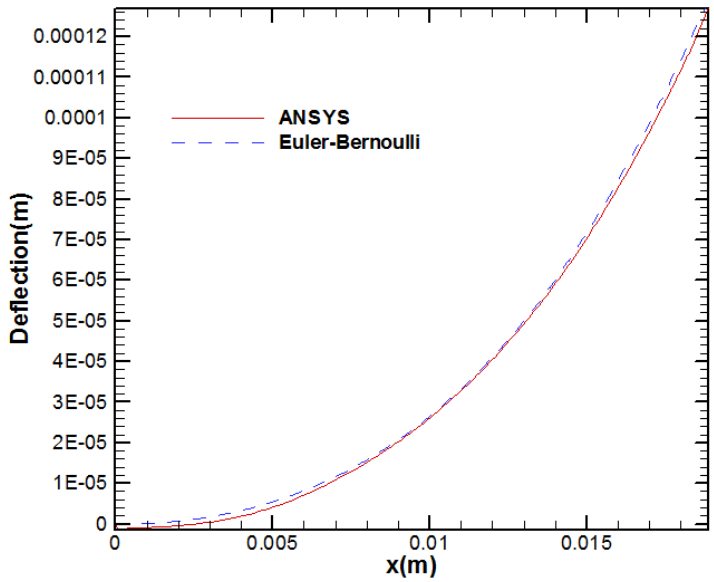

(a)

Figure 3.10: ANSYS and Euler-Bernoulli contact deformation for an interference of (a) 127 μm and (b) 177.8 μm

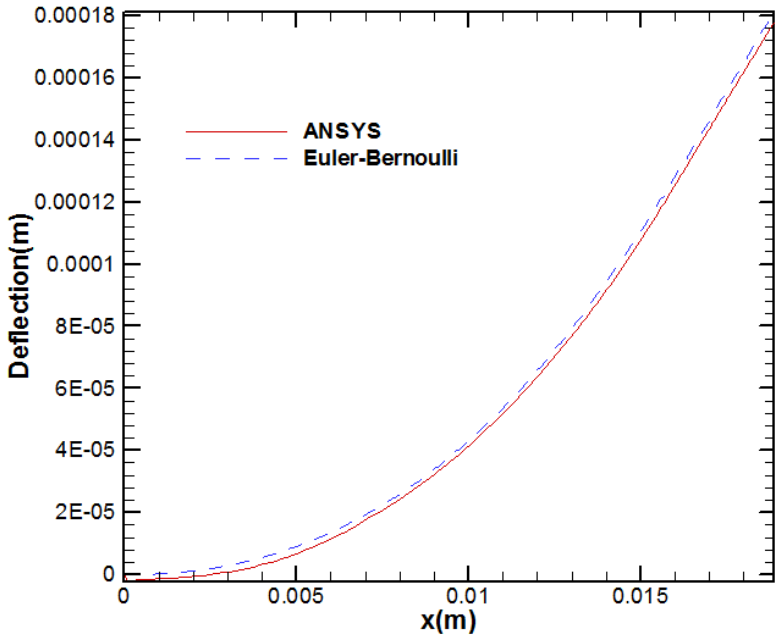

(b)

Figure 3.10 continued

As stated previously, the temperature distribution in the armature can give rise to some significant interface deflections. Using the thermal field calculated above, the thermal moments are calculated from Equation 3.19 and the resulting deflection can be found by Equation 3.20 [2]. The thermal deflection due to moments is superimposed with the thermal expansion toward the rails, calculated by Equation 3.21. Again, deformations are assumed to be elastic and only in the direction perpendicular to the rails. The deflections due to thermal moments and expansion are calculated by using an approximate cantilever beam as done for the deflections due to forces and pressures. However, in order to achieve a more accurate model, a slightly different equivalent cantilever beam cross section is used.

$$M_T = \int_A \alpha E T y dA \tag{3.19}$$

$$\frac{d^2 v^*(x)}{dx^2} = -\frac{M_T}{EI^*} \tag{3.20}$$

$$v^*(x) = \int \alpha (T - T_{ref}) dy \tag{3.21}$$

The process of finding the cross section for the thermal beam is similar to that used above to analyze deflections caused by forces. ANSYS PLANE13 is used as it was to validate the thermal field; boundary conditions are added to constrain the front of the armature from deforming along the rails and the line of symmetry from deforming perpendicular to the rails. To test the validity of superposition of the armature deflections calculated by the two equivalent cantilever beams; a shear force of 200 N is added to the trailing edge of the armature. PLANE13 calculates the thermal field and the resulting structural deflection due to temperature, forces, and pressures. The Euler-Bernoulli model utilizes the thermal field calculated as it was above. The thermal boundary conditions used for the validation are as illustrated in Figure 3.11. The high temperature boundary conditions are applied as in the previous section to the trailing edges of the armature, where the electric current density and therefore joule heating will be greatest during a launch. The high temperature boundary condition is varied from 200 °C to 600 °C in order to ensure the equivalent thermal beam is developed for the range of temperatures most likely to be encountered during a shot.

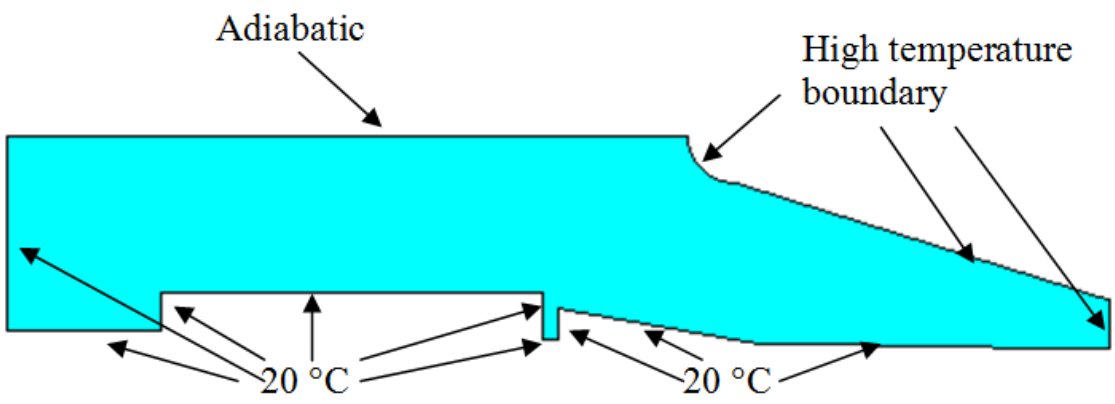

Figure 3.11: Thermal boundary conditions used to validate thermal deflections

Equations 3.19-3.21 are used in conjunction with the thermal beam, fixed at the leading edge of the armature-rail interface, to calculate the thermal deflection for the Euler-Bernoulli model. This deflection is added to the deflection calculated by applying the shear force of 200 N on the trailing edge of the armature and using the previously developed equivalent beam cross section. The thermal beam cross section is adjusted until the ANSYS and Euler-Bernoulli models agree [2]. Figure 3.12 shows that the equivalent thermal beam closely approximates the ANSYS model for high temperature boundary conditions of 200 °C, 300 °C, 400 °C, and 600 °C. There is some small variation between the two methods at the leading edge of the interface and inside the pocket region. However, the deflection in the pocket region is neglected in the simulation because the interface gap height in the pocket is much larger than that of the rest of the interface. Additionally, the deflection at the leading edge of the interface will only be used if the pocket completely fills.

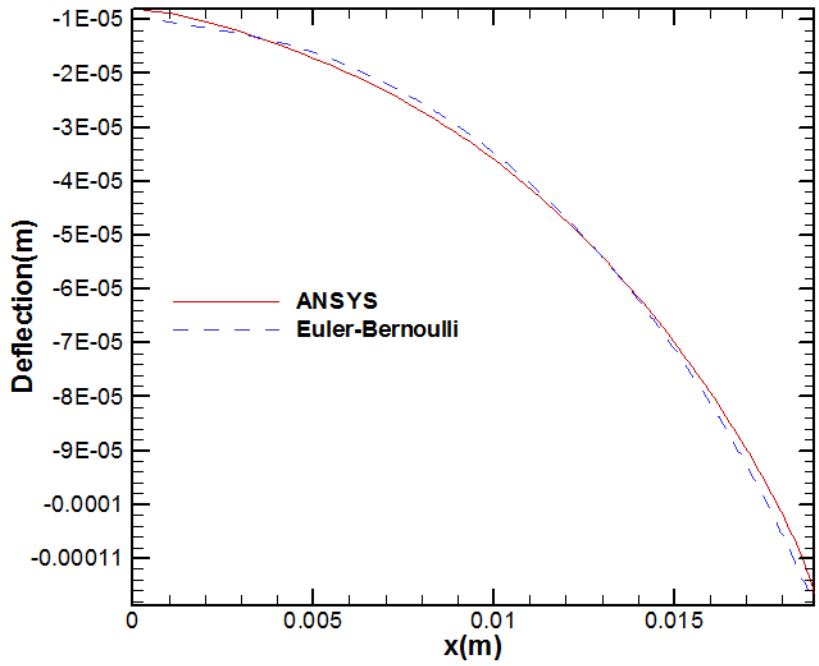

(a)

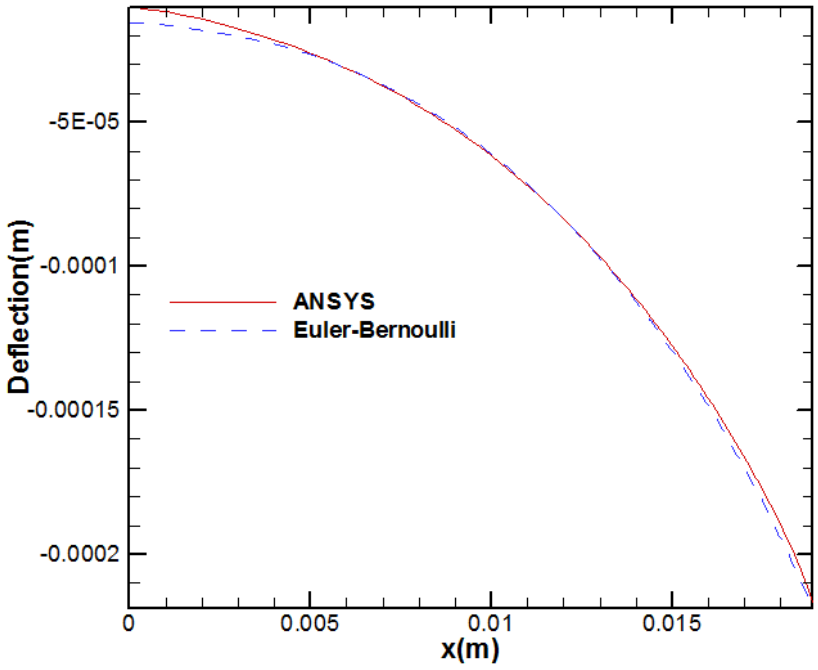

(b)

Figure 3.12: Comparison of armature wing deflection between ANSYS and Euler-Bernoulli models for high boundary temperatures of (a) 200 °C, (b) 300 °C, (c) 400 °C, and (d) 600 °C

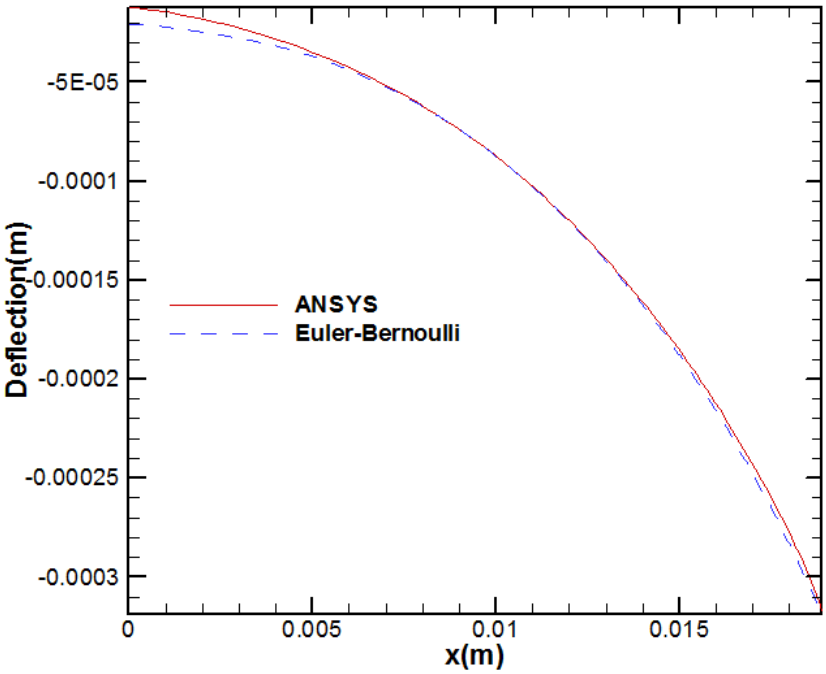

(c)

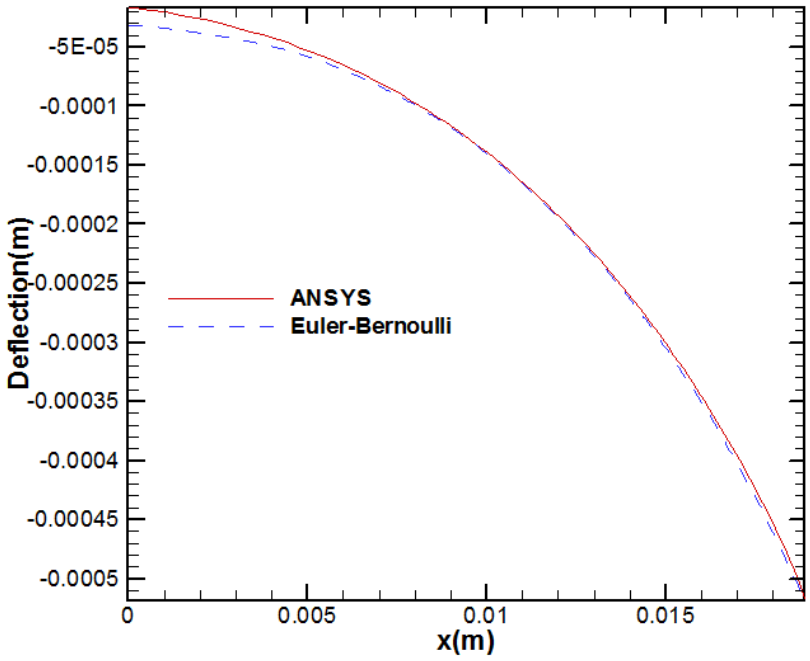

(d)

Figure 3.12 continued

3.1.4 Lubricant Modeling

The lubricant pressure is the parameter which is most sensitive to changes in other parameters, mainly the armature-rail interface gap height. Conjointly, the armature-rail interface gap height is also very sensitive to changes in the lubricant pressure. Therefore, these parameters must be converged simultaneously to obtain the best results. The lubricant flow in the interface is modeled as a one dimensional fluid flow through a small non-uniform height channel. The armature acts like a hydrodynamic pad bearing, increasing the gap height as its velocity increases. The flow field is simplified to two dimensional by assuming that the velocity and pressure gradients along the width of the armature are very small in comparison to those along the length of the rail (the long bearing approximation). The following modified Reynolds Equation is employed to solve for the lubricant pressure inside the armature-rail interface gap. It considers the magnetic, velocity, roughness, cavitation, and squeeze film effects [2].

$$(P_{ref} - P_c)\frac{\partial}{\partial x}(\phi_x h^3 \frac{\partial \Phi F_c}{\partial x}) = a\rho_c \frac{\partial}{\partial x}\left(G^2 h_T^3\right) + 6\mu U(\frac{\partial G h_T}{\partial x} + \sigma \frac{\partial G \phi_s}{\partial x}) + 12\mu \frac{\partial h_T}{\partial t} \quad (3.22)$$

Equation 3.22 is applied to the region of the interface behind the pocket as shown in Figure 3.13. The boundary condition at the trailing edge of the interface is found by calculating the magnetic pressure because the fluid portion of the total pressure will be bound by atmospheric conditions at the trailing edge but the electromagnetic body forces on the lubricant increase the total lubricant pressure. To develop the leading edge boundary condition it is noted that the leading edge of the gap shown in Figure 3.13 coincides with the trailing edge of the pocket in Figure 3.14. Therefore the leading edge

boundary condition for Equation 3.22 is determined by finding the pressure at the trailing edge of the pocket.

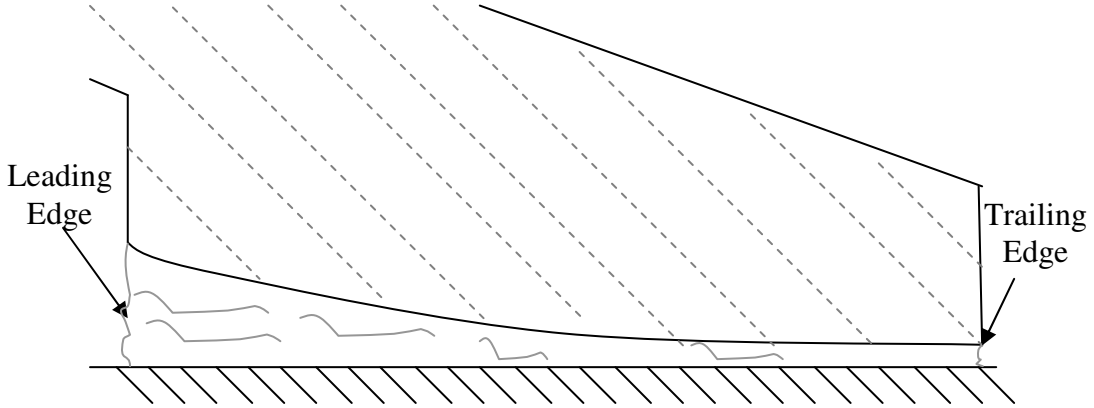

Figure 3.13: Interface region used for Equation 3.22 (not to scale)

The pressure at the trailing edge of the pocket is found by first using a mass balance on the pocket, then determining the length of the column of lubricant inside the pocket assuming the inertia of the lubricant pulls it towards the trailing edge of the pocket due to the acceleration of the armature. Finally, assuming the flow velocity of the lubricant in the pocket is small the pressure at the trailing edge of the pocket is found by using the static Bernoulli equation without head losses. The mass balance diagram is shown in Figure 3.14 below where Q_{out} is the mass of lubricant from the reservoir, Q_l is the leakage from the leading edge, Q_r is the leakage from the rear, and Q_{net} is the amount in minus the amount leaked. The lubricant enters through the conduit from the reservoir at the top of the pocket and is leaked from the leading edge and trailing edge of the pocket. It is assumed that there is no leakage out of the sides of the pocket. If the pocket is not full, there will be no leakage from the leading edge of the pocket either.

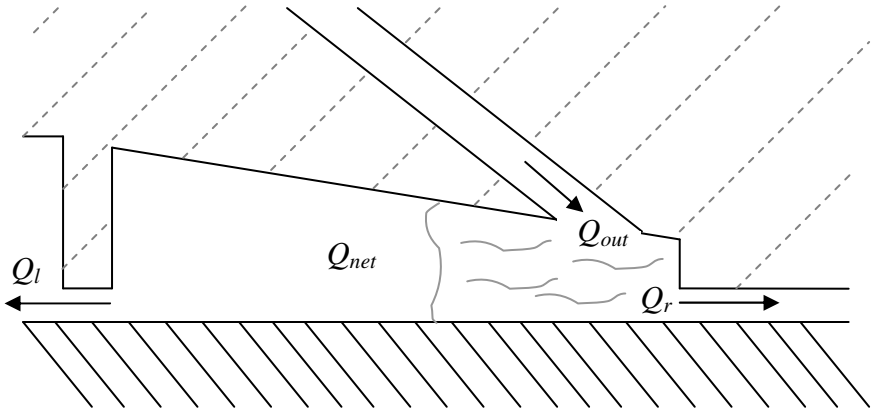

Figure 3.14: Mass balance on the pocket (not to scale)

Experimental results show that the flow inside the conduit is turbulent for most of the shot. Thus the mass flow rate into the pocket is calculated using Bernoulli's equation along with a time dependent term as well as turbulent major and minor losses and a relation between average flow velocity and mass flow rate. The lubricant injection system is modeled as an accelerating piping system. By considering nodes at each point where the pipes change size or branch off and calculating the pressure at each node, the mass flow rate of the lubricant can be found. Due to symmetry, the mass flow rate inside both conduits will be the same.

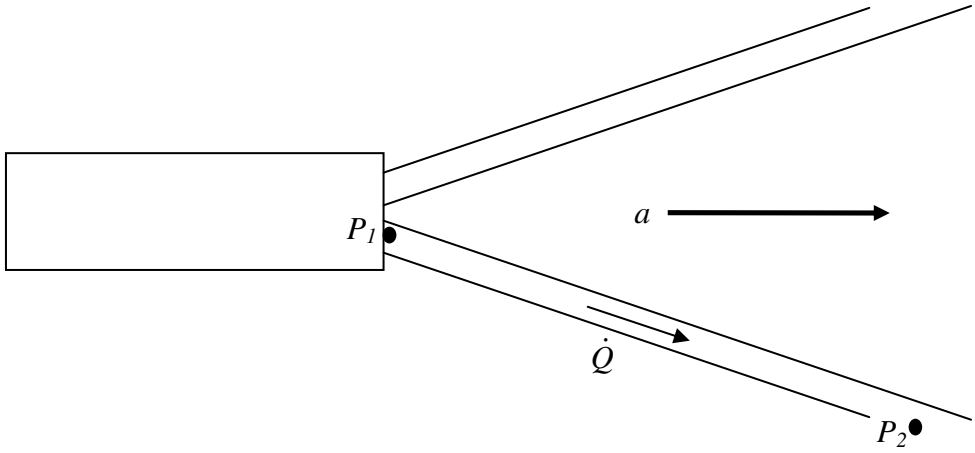

Figure 3.15: Schematic of the base case injection system and node points (not to scale)

The pressure at the first node, P_1, can be calculated by assuming the lubricant velocity inside the reservoir is negligible compared to the lubricant velocity inside the conduit. The pressure at the second node is found in the same way as the inlet boundary condition for Equation 3.22 is found. Equation 3.23 is a quadratic equation which can be solved by taking the largest root to yield the mass flow rate of lubricant through the injection conduit. L_p and R_p represent the length and radius of the injection conduit respectively. The angle the injection pipe makes with respect to the rail is denoted by θ. The friction factor, f, is found to be 0.025 from the moody diagram and the minor loss coefficient, K_e, is caused by the restrictive angled entrance into the conduit and the sharp expansion to the pocket and approximated as 1.8 [53]. The friction factor is relatively insignificant compared to the minor loss coefficient and thus can be roughly approximated using any turbulent flow velocity. The mass flow rate calculated below can be used to find Q_{out} in the mass flow balance.

$$\left(\frac{f\frac{L_p}{2R_p}+K_e+1}{2\rho\pi^2 R_p^{\ 4}}\right)\dot{Q}^2+\frac{L_p}{\pi R_p^{\ 2}dt}\dot{Q}-\left(\frac{L_p\dot{Q}_{pre}}{\pi R_p^{\ 2}dt}+P_1-P_2+\rho a L_p*\cos(\theta)\right)=0 \qquad (3.23)$$

In order to calculate the lubricant velocity the Navier-Stokes Equation in the x direction is solved for the velocity in the x direction using the assumptions of the model. Equation 3.24 yields the x direction component of lubricant velocity by applying no-slip boundary conditions to both the armature and rail surfaces. Viscous heat generation in the lubricant film can be calculated by Equation 3.25 to be used in the calculation of the thermal field presented above. Using Equations 3.24 and 3.26, the stream function for the flow field can be determined as in Equation 3.27.

$$u=\frac{1}{2\mu}\left(\phi_x\frac{\partial P}{\partial x}-\rho a\right)(y-h)\,y+U\left(1-\frac{y}{h}\right)-\frac{3U\sigma\phi_s}{h^3}\,y(y-h) \qquad (3.24)$$

$$\dot{q}=\tau\frac{\partial u}{\partial y}=\left[\frac{\mu U}{h}\left(\phi_f+\frac{2y-h}{h}\phi_{fs}\right)+\frac{2y-h}{2}\phi_{fp}\left(\frac{\partial P}{\partial x}-\rho a\right)\right]* \left[\left(\frac{1}{2\mu}\phi_x\frac{\partial P}{\partial x}-\frac{1}{2\mu}\rho a-\frac{3U\sigma\phi_s}{h^3}\right)(2y-h)-\frac{U}{h}\right] \qquad (3.25)$$

$$u=\frac{\partial\Psi}{\partial y} \qquad v=-\frac{\partial\Psi}{\partial x} \qquad (3.26)$$

$$\Psi=\int_0^y\frac{\rho}{\rho_c}u\,dy=G\left[U\left(y-\frac{y^2}{2h}\right)+\left(\frac{\phi_x}{2\mu}\frac{\partial P}{\partial x}-\frac{\rho a}{2\mu}-\frac{3U\sigma\phi_s}{h^3}\right)\left(\frac{y^3}{3}-\frac{hy^2}{2}\right)\right] \qquad (3.27)$$

3.1.5 Results and Discussions

The Magneto-Elastothermohydrodynamic model presented above for analyzing a shot of the base case armature on the Georgia Institute of Technology launcher is applied. At each time step many physical parameters are calculated. The base case shot simulated has been optimized such that the least amount of lubricant is used to avoid transition. Figure 3.16 shows the muzzle voltage recorded during the shot. It can be seen that a spike in the muzzle voltage occurs at approximately 1.5 ms, the time at which the armature leaves the launcher. This spike is due to the break in the circuit when the shunting armature is removed. The results below support the physical experiments in showing that if there was a smaller initial lubricant charge or a longer rail length, the shot would have transitioned before the armature reached the muzzle.

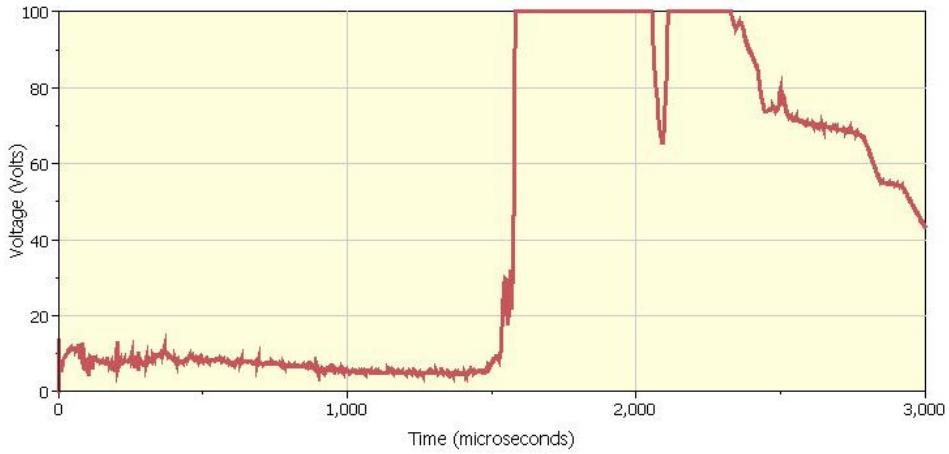

Figure 3.16: Experimental muzzle voltage

The current is supplied by large charged capacitors. The capacitors are discharged in a sequence designed to spread out the application of current over the entire shot. Figure 3.17 shows the electric current used in the simulation which is based on the experimentally recorded current. As shown below, the current increases very quickly to a maximum of about 250 kA at 0.5 ms and gradually decreases to a value around 60 kA by the end of the shot.

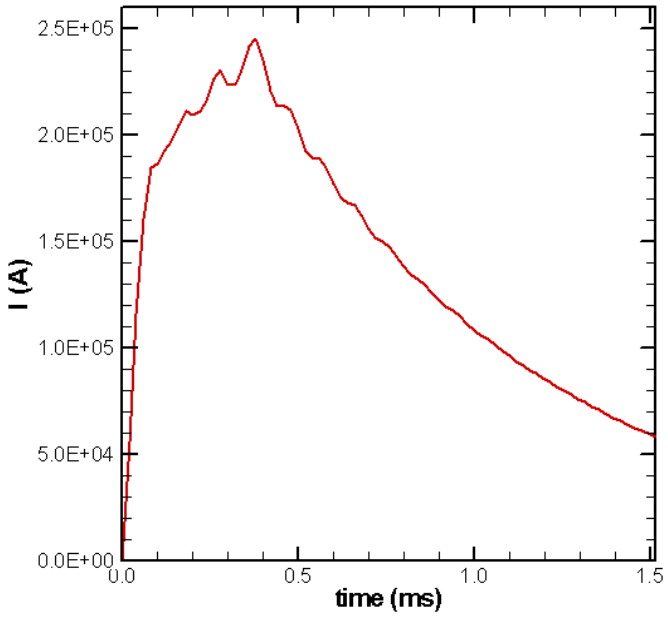

Figure 3.17: Electric current history

The magnetic flux computed resulting from passing an electric current through the rails and armature is shown in Figure 3.18 for different times. Only half the region is calculated and shown below. Symmetry allows the magnetic flux density to be reflected over the upper horizontal boundary of the region shown in order to obtain the entire magnetic flux density. The magnetic flux is most dense at the trailing edges of the

armature where the armature meets the air. The maximum magnetic flux density occurs in conjunction with the maximum current at a time of 0.5 ms.

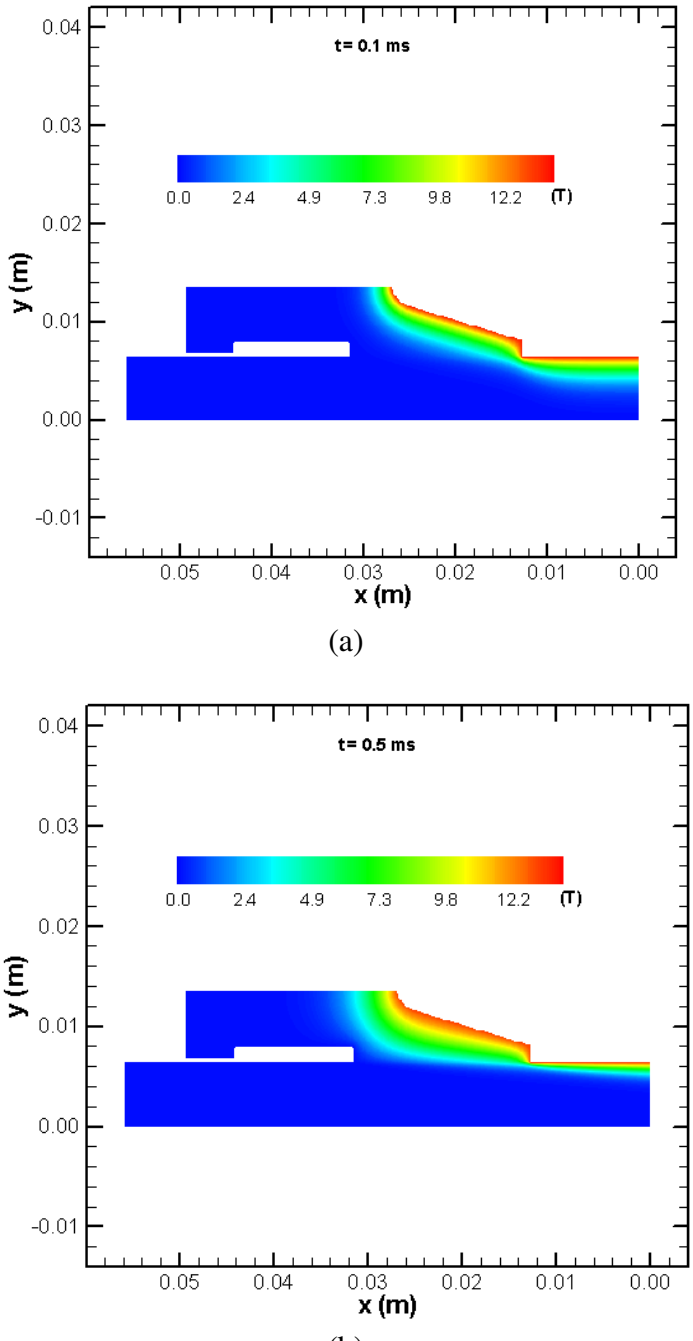

Figure 3.18: Magnetic flux density distribution at different times

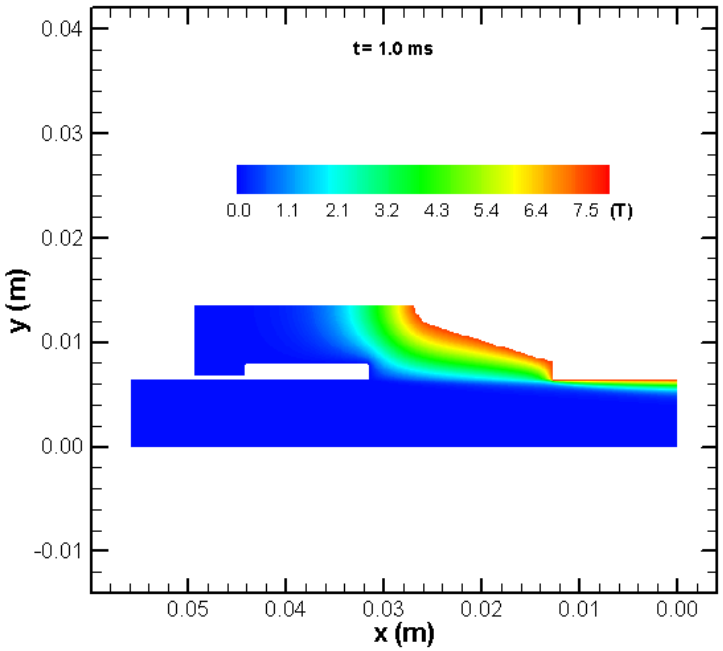

(c)

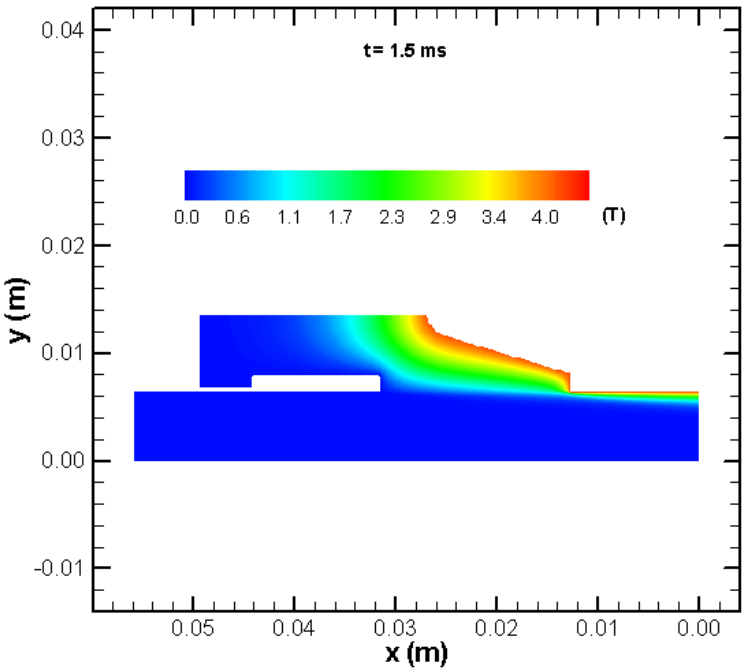

(d)

Figure 3.18 continued

The electric current spreads out over the armature with higher concentrations at the trailing edges of the armature and the inside of the rails. Figure 3.19 presents the electric current distribution at several times. The density for the entire region may again be found through reflection, however, the arrows denoting current path at each reflected point will have the opposite x direction but the same y direction as the parent point. The velocity skin effect can be seen, as the armature speeds up, the current density concentrates farther towards the trailing edge of the armature-rail interface.

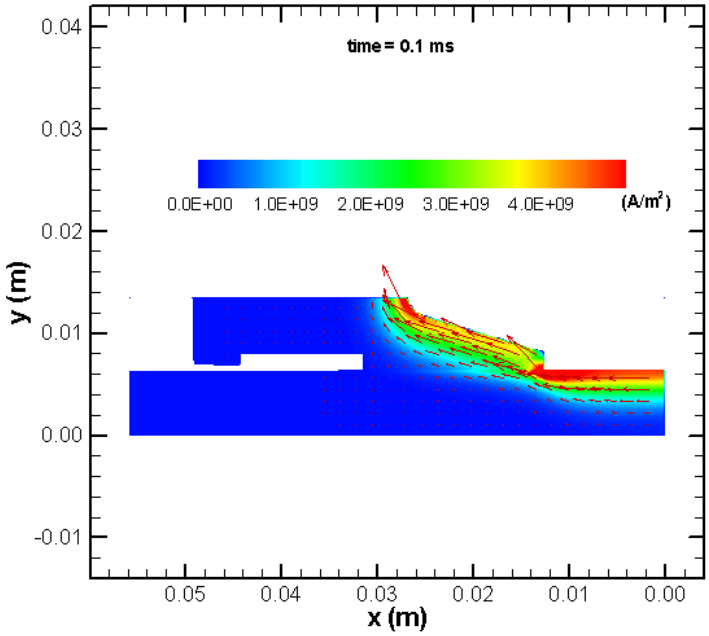

(a)

Figure 3.19: Electric current distribution at different times

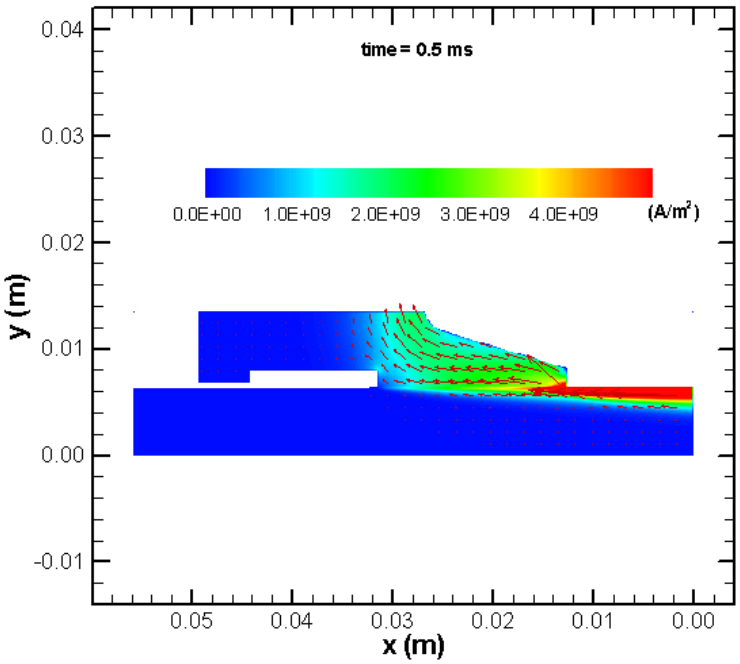

(b)

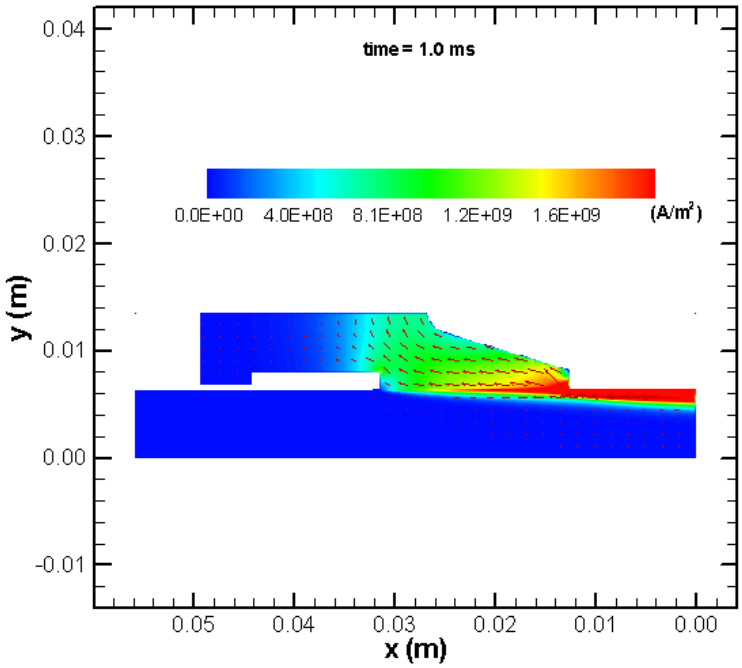

(c)

Figure 3.19 continued

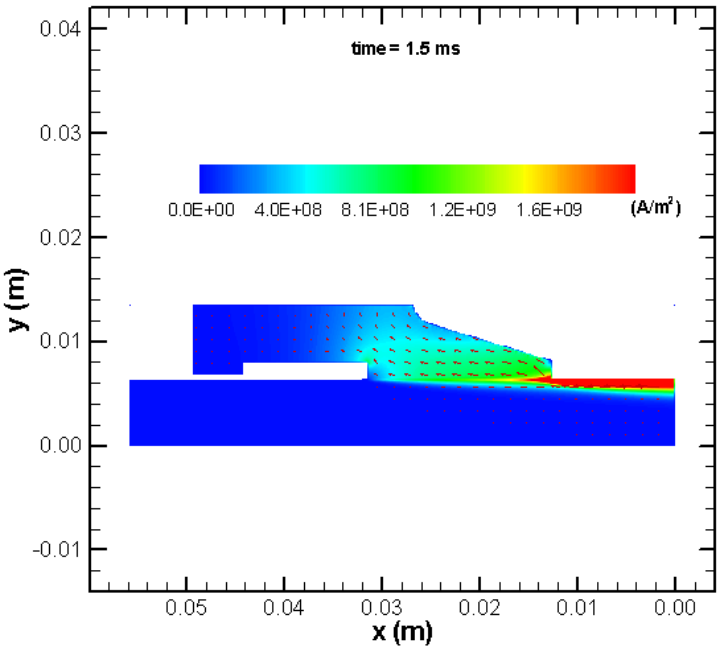

(d)

Figure 3.19 continued

The forces caused by the electromagnetic interactions are illustrated in Figure 3.20. As with the current density figures the arrows do not simply reflect. In this case the x component of force remains the same and the y component is reflected for the half not calculated. The x component of the electromagnetic force is what propels the armature forward. The y component acts to spread the armature's trailing edges apart, pushing them into the rails.

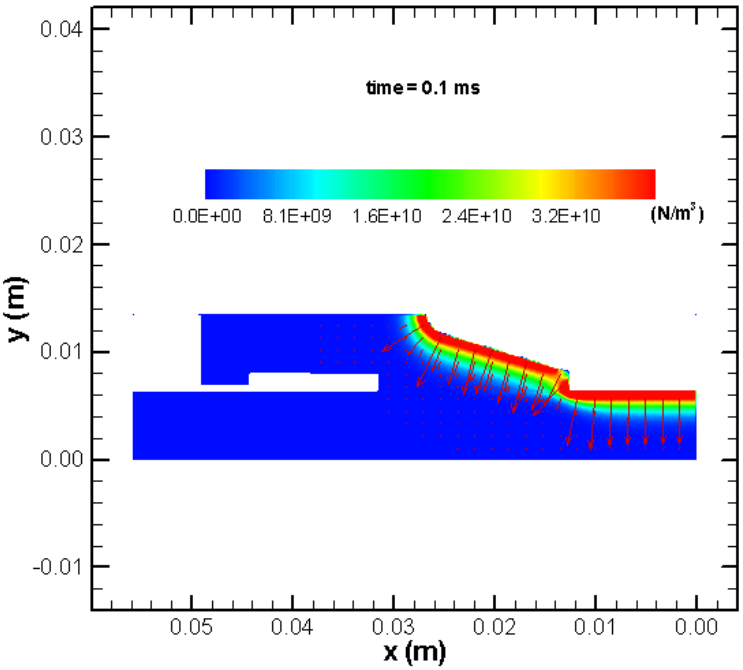

(a)

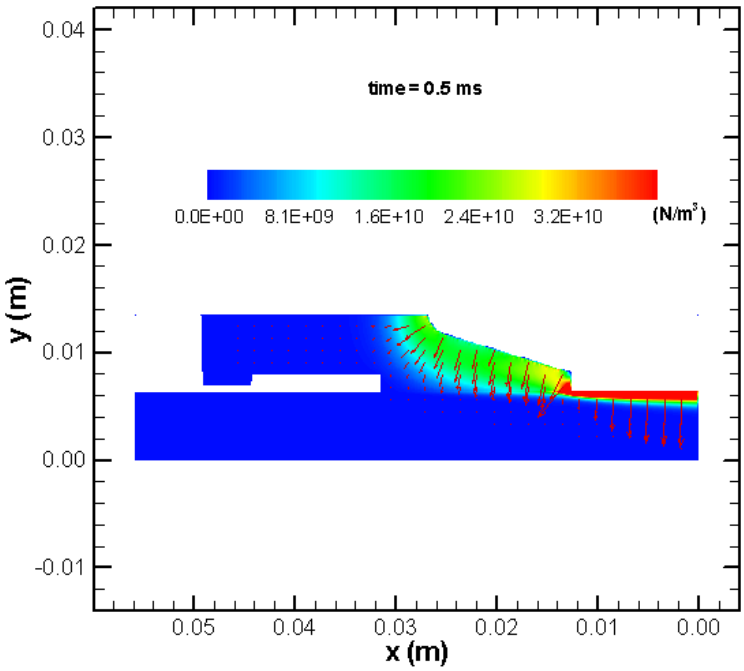

(b)

Figure 3.20: Magnetic body force distribution at different times

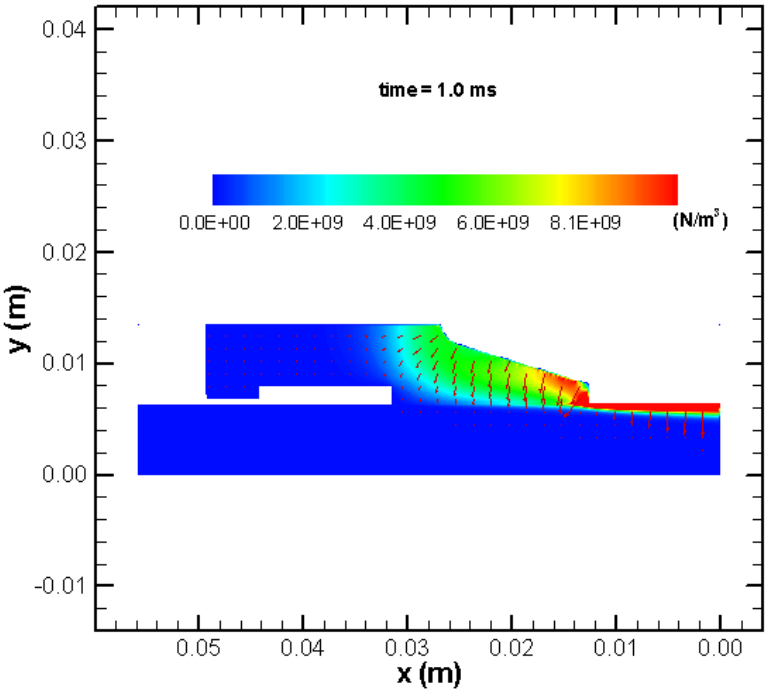

(c)

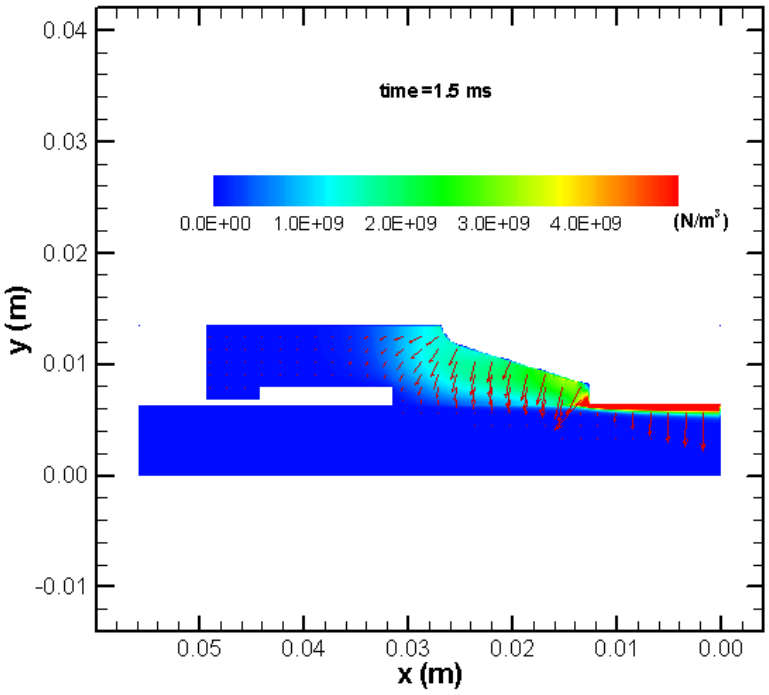

(d)

Figure 3.20 continued

The temperature increase in the armature is caused by joule, viscous, and frictional heating. The temperature field is shown for different times during a shot in Figure 3.21. Toward the beginning of the shot, the armature is relatively cool. As more current travels through the armature, the temperature begins to rise in places where the current density is highest. The temperature rise on the interface is countered by cooling from the cool lubricant being supplied. Only a small spot on the trailing edge of the armature is calculated to reach the melting temperature, however, this spot is so small that no melting is expected to actually occur. The lack of melting is consistent with experimental observations.

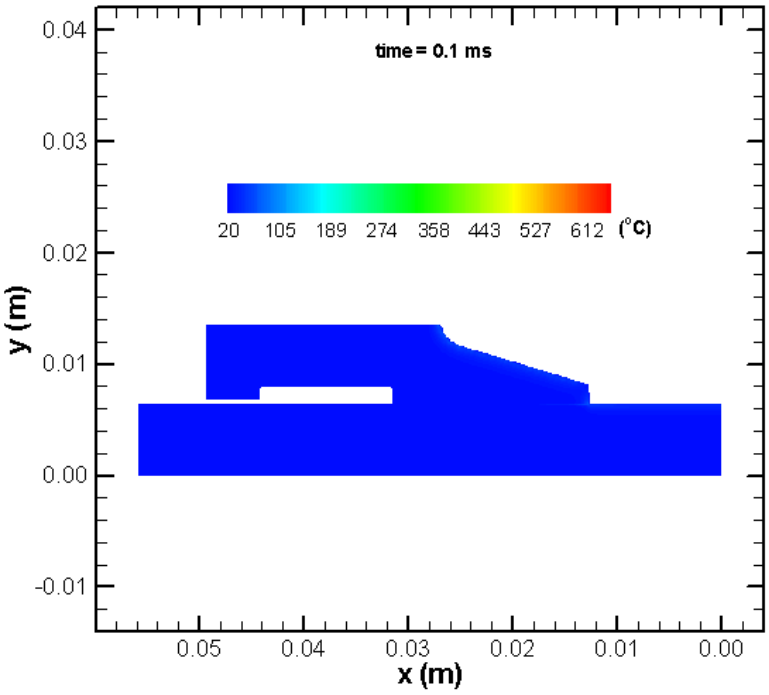

(a)

Figure 3.21: Temperature distribution at different times

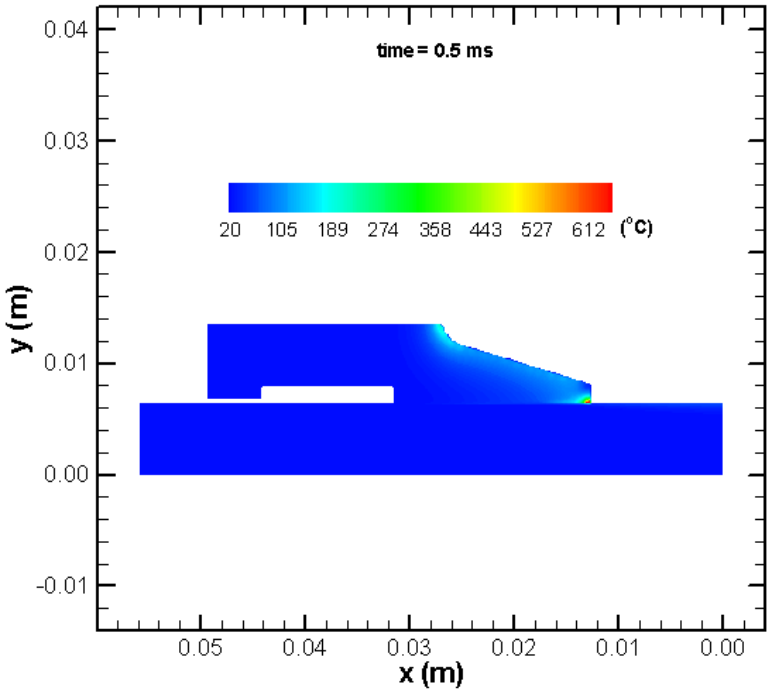

(b)

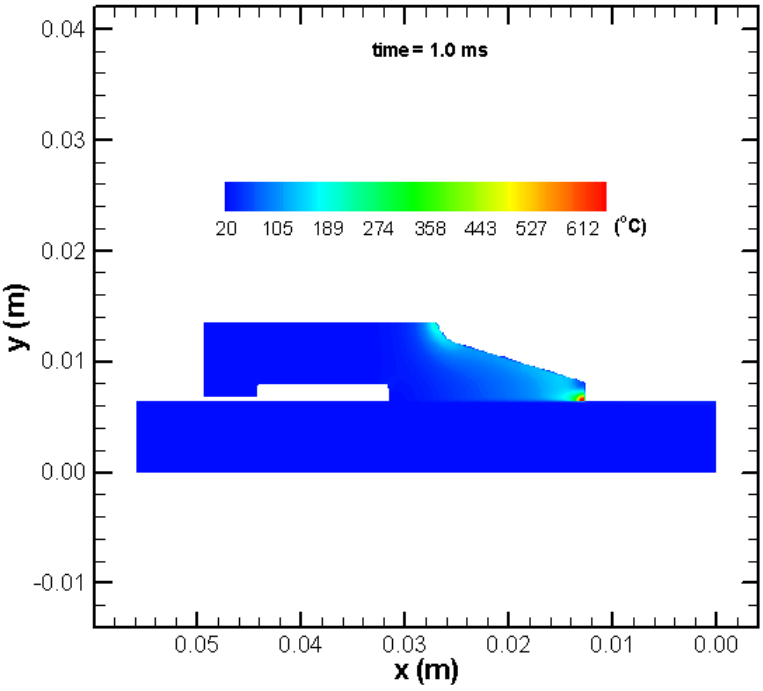

(c)

Figure 3.21 continued

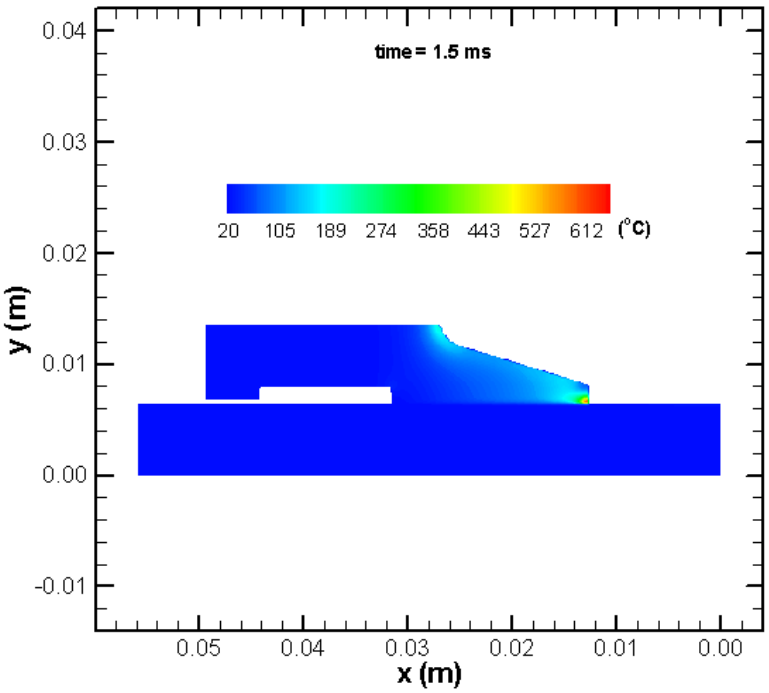

(d)

Figure 3.21 continued

A history of the net forces acting on the armature is shown in Figure 3.22. The electromagnetic force, $F_{emag,}$ is highly dependent on the current history as shown by Equation 3.28 which is an alternate method of calculating the electromagnetic force in the x-direction if the inductance gradient is known. By rearranging the equation it can be calculated that the inductance gradient for this armature is approximately 0.493 μH for every time during the shot. It is expected that the inductance gradient is nearly constant for all times during the launch because it is predominantly based on the armature geometry. The frictional and viscous forces, F_f and F_v respectively, are small enough that the total net force acting on the armature, F_{total}, is almost identical to the electromagnetic force. Additionally, the frictional force quickly falls to nearly zero as the lubricant pressure separates the armature from the rail. In the model, some error in the calculation

of the contact pressure was allowed because a fairly large error in the contact pressure causes only a small error in the armature deflection. The frictional force is directly related to the contact pressure; therefore errors in contact pressure also have little effect on the net force acting on the armature.

$$F_{emag} = L' \frac{I^2}{2} \tag{3.28}$$

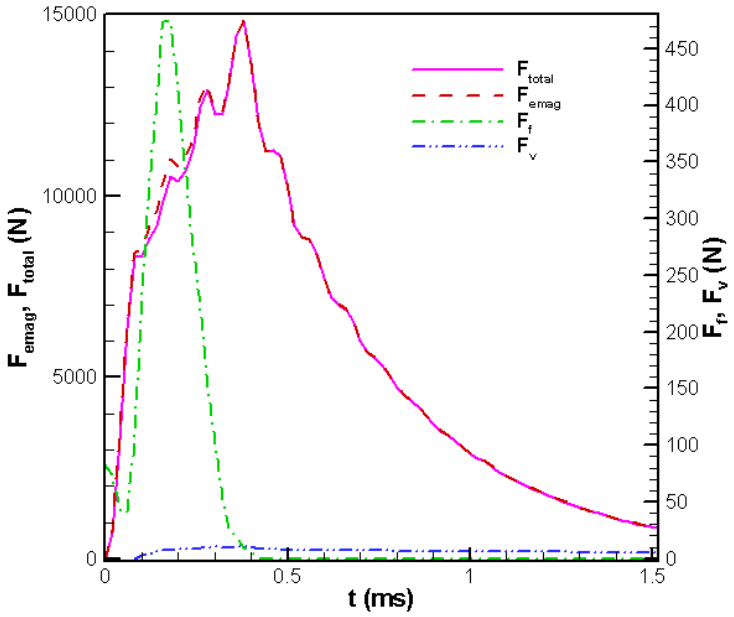

Figure 3.22: *x* direction armature force history

The net force on the armature causes it to accelerate along the rails. The shape of the acceleration profile in Figure 3.23 is very similar to that of the net force on the armature. Only a small deviation in shape is caused by the decrease in accelerated mass as the lubricant is released through the injection system.

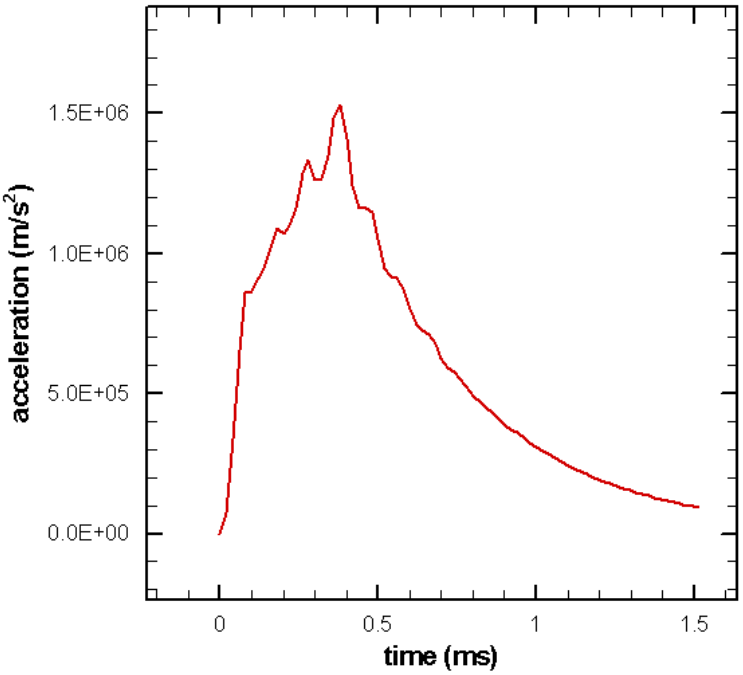

Figure 3.23: Armature acceleration history

Figure 3.24 shows the velocity history of the armature during a shot. At the very beginning of a shot, the frictional force keeps the armature stationary. As the current increases, the armature quickly breaks free allowing the lubricant to be injected. The velocity reached by the armature as it exits the launcher is around 900 m/s.

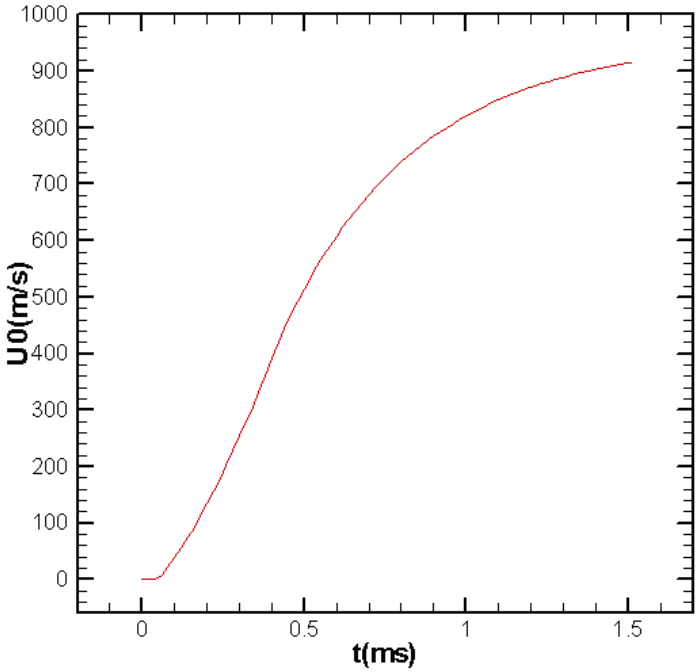

Figure 3.24: Armature velocity history

A comparison between the calculated and experimentally observed position history of the armature is presented in Figure 3.25. The experimental data is gathered through sensors which detect when the armature passes by. The experimental results are in good agreement with the calculated armature position history. Because the electromagnetic force is the dominant cause of the armature acceleration, the agreement between the experimental and numerically found armature position shows that the calculated electromagnetic body forces closely approximate the actual physics when using the two dimensional simplified model.

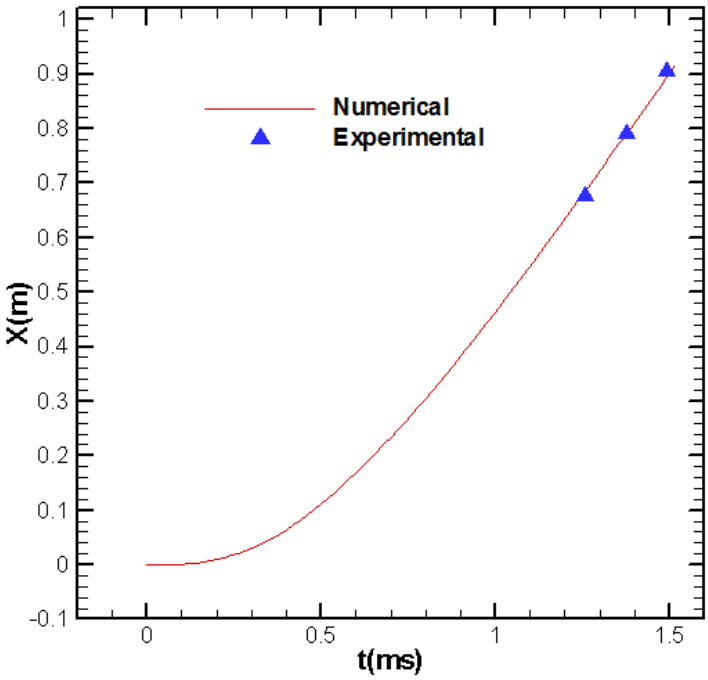

Figure 3.25: Comparison of predicted armature location history with experimental measurements

A history of the amount of lubricant left inside the reservoir is shown in Figure 3.26. The reservoir begins with a charge of 0.9 g which is delivered to the pocket as the armature accelerates. At the end of the shot, there is only a small amount of lubricant left in the reservoir. However, even if the reservoir were to empty out there may still be lubricant inside the pocket. Figure 3.27 illustrates the lubricant consumption history of one pocket. Q_{out} is the amount of lubricant delivered to the pocket, Q_l and Q_r are the amounts leaked from the leading edge and the trailing edge of the pocket respectively, and Q_{net} is the amount of lubricant inside the pocket. Because the pocket never fills up, no lubricant leaks from the leading edge. As the armature picks up speed the amount of fluid inside the pocket increases because there is a lot of lubricant coming from the reservoir. As the armature reaches high velocities, the interface gap height increases and

more lubricant is leaked through the trailing edge of the pocket causing the amount of lubricant inside the pocket to decrease. The pocket is almost entirely emptied by the end of the shot. If both the amount of lubricant left in the reservoir and the pocket reached zero, the shot would most likely transition due to starvation of the interface.

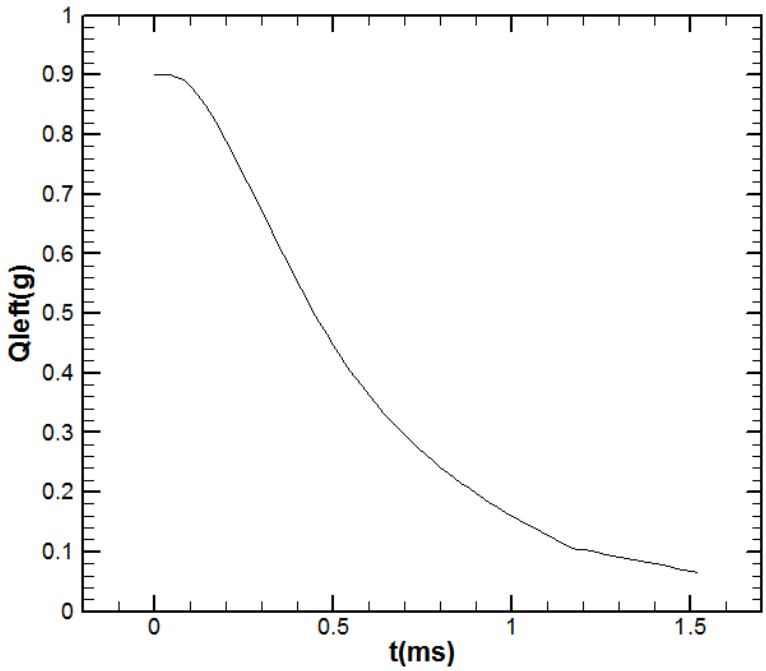

Figure 3.26: History of the amount of lubricant left inside the reservoir.

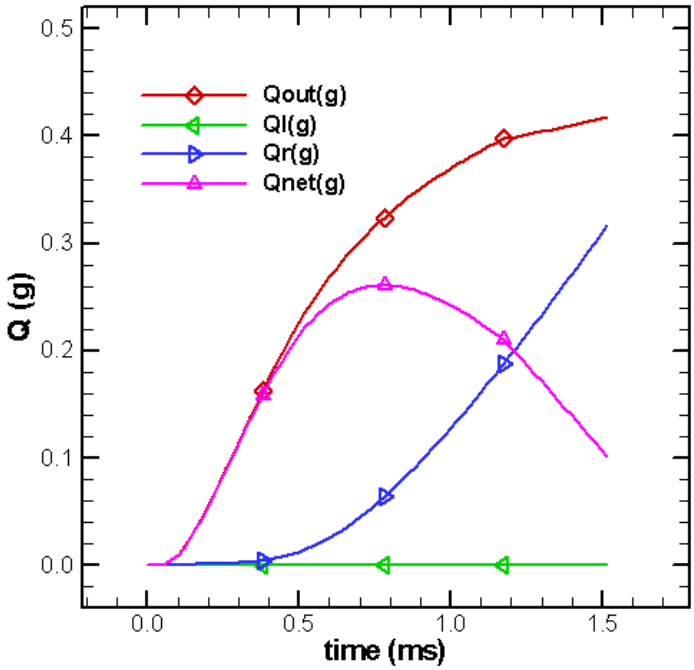

Figure 3.27: Mass flow amount history

The minimum gap height history for the shot is shown in Figure 3.28. Initially, the minimum gap height increases as lubricant separates the armature from the rail. However, as the current increases, a component of the electromagnetic force acts to push the armature and rail together. As the armature gains speed and eventually the electromagnetic force decreases, the minimum gap height becomes relatively large in this case.

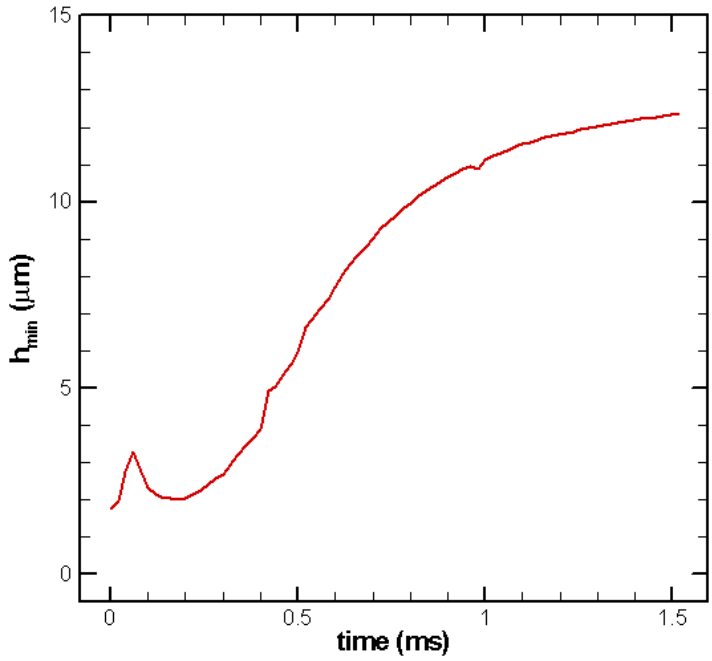

Figure 3.28: Minimum film thickness history

Figure 3.29 shows the lubricant pressures at different times. The magnetic pressure is only significant near the trailing edge of the interface. This is because both the current and magnetic flux densities also concentrate near the trailing edge of the interface and have negligible values near the leading edge. The fluid pressure is highest toward the center of the interface as would be expected from a hydrodynamic bearing. In this case the fluid pressure remains high enough that cavitation does not occur in the lubricant. The total pressure is the sum of the magnetic and fluid pressures and is constrained by the boundary conditions.

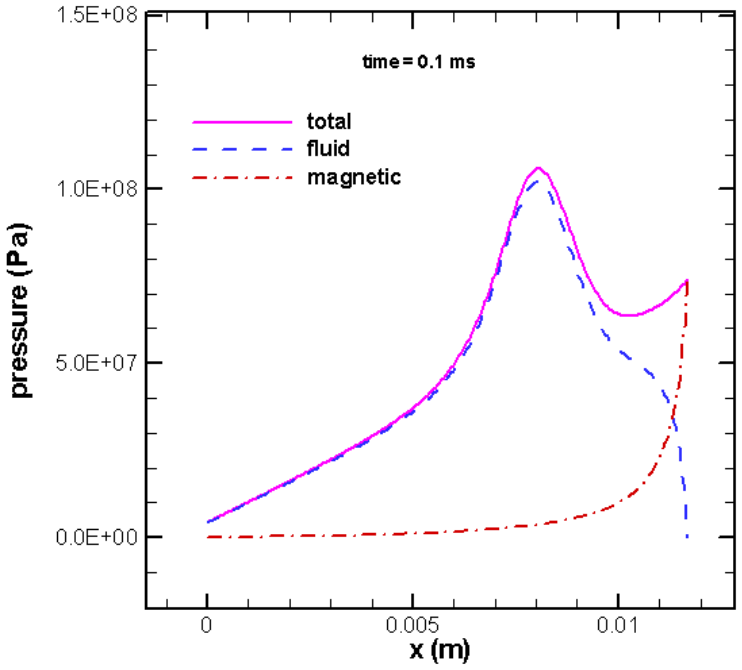

(a)

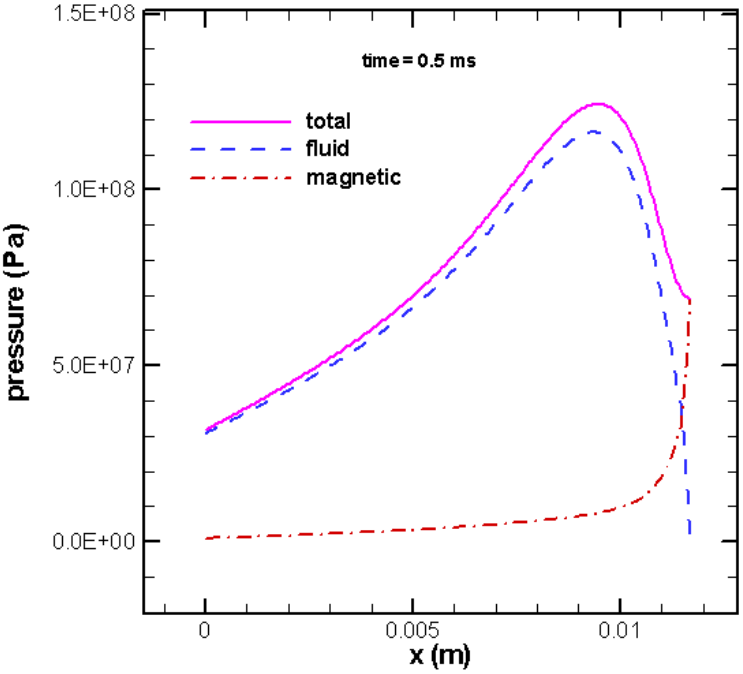

(b)

Figure 3.29: Pressures in the fluid at different times

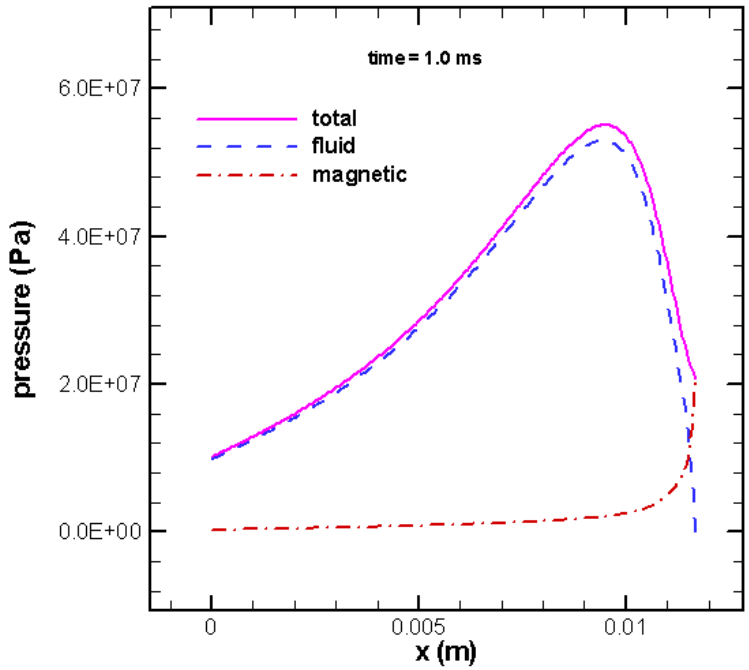

(c)

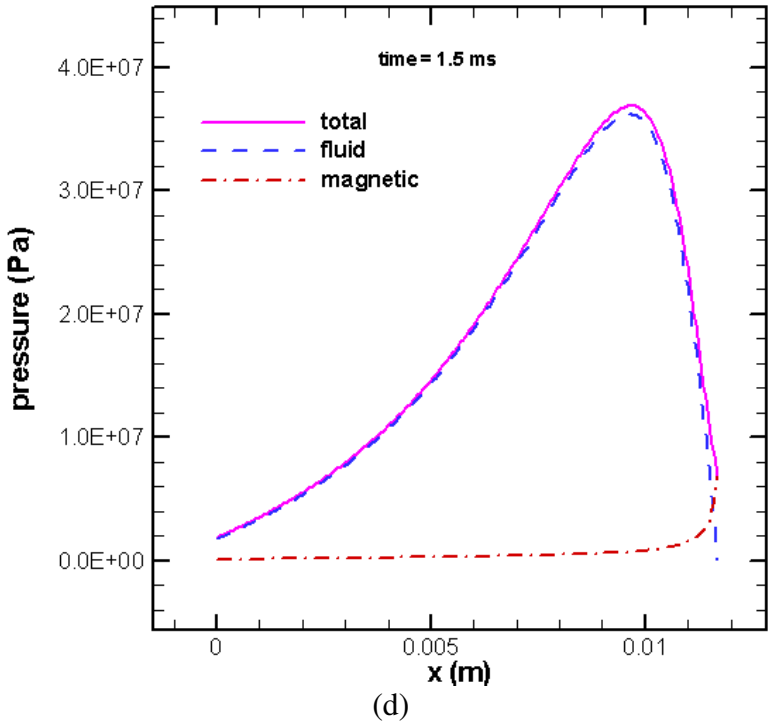

(d)

Figure 3.29 continued

The distributed forces acting on the armature in the transverse direction are presented in Figure 3.30. In the figure, the positive forces push the armature away from the rail, while the negative forces pull it closer. The contact pressure has an effect only at the beginning of the shot while the fluid total pressure and magnetic distributed force act against one another for the entire shot. The resultant distributed load on the armature is negative toward the front of the armature but positive toward the trailing edges.

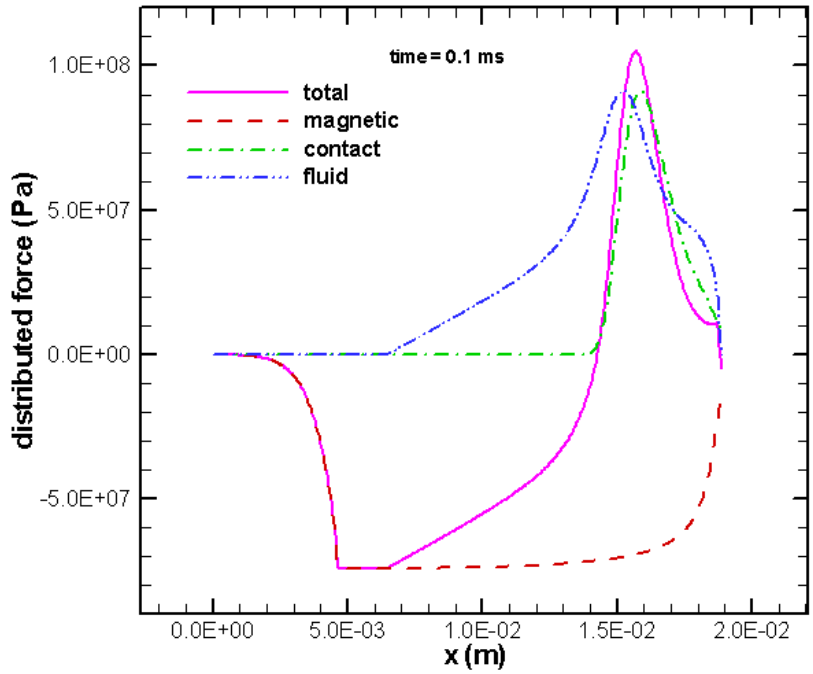

(a)

Figure 3.30: Distributed forces on the armature leg at different times

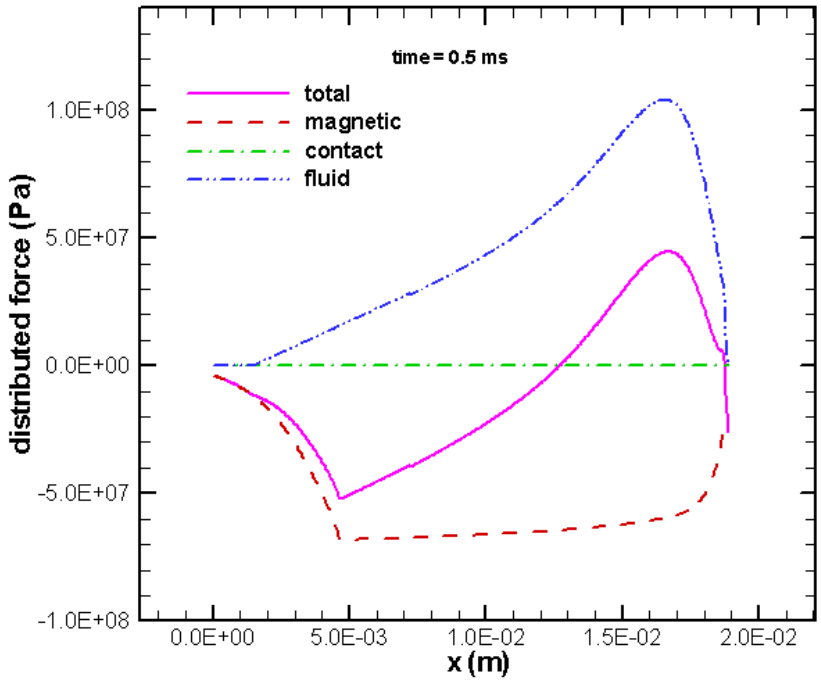

(b)

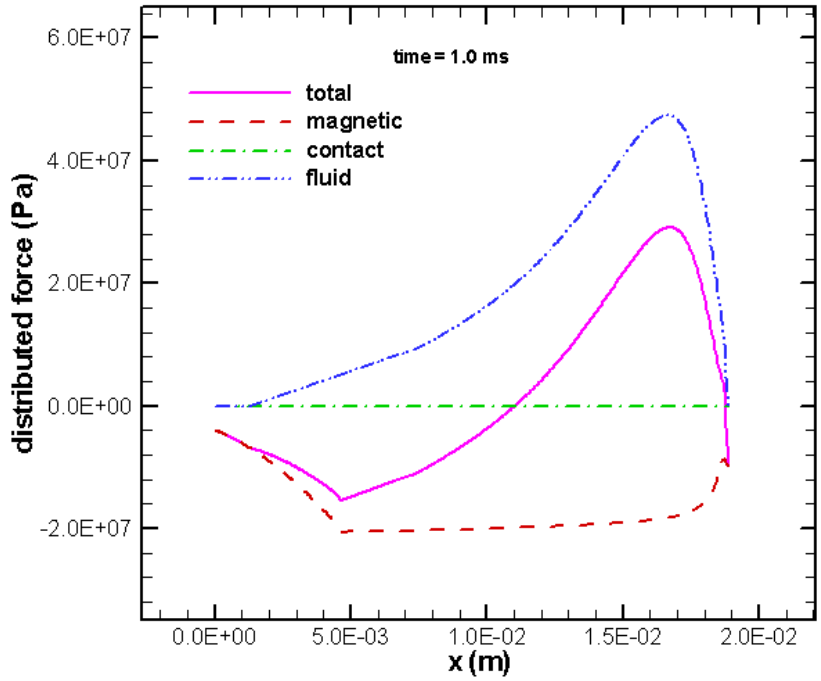

(c)

Figure 3.30 continued

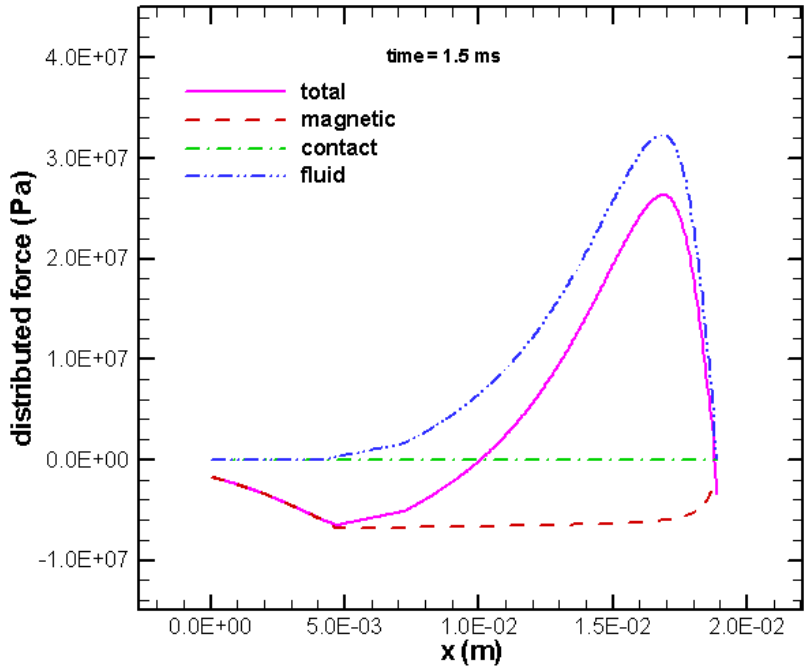

(d)

Figure 3.30 continued

The interface gap profile is illustrated in Figure 3.31. At the beginning of the shot the armature is deformed by contact pressure only. As current is applied, the electromagnetic forces deform the armature farther into the rail as shown. Then, as the armature gains velocity, the hydrodynamic pressure increases the overall gap height until the end of the shot.

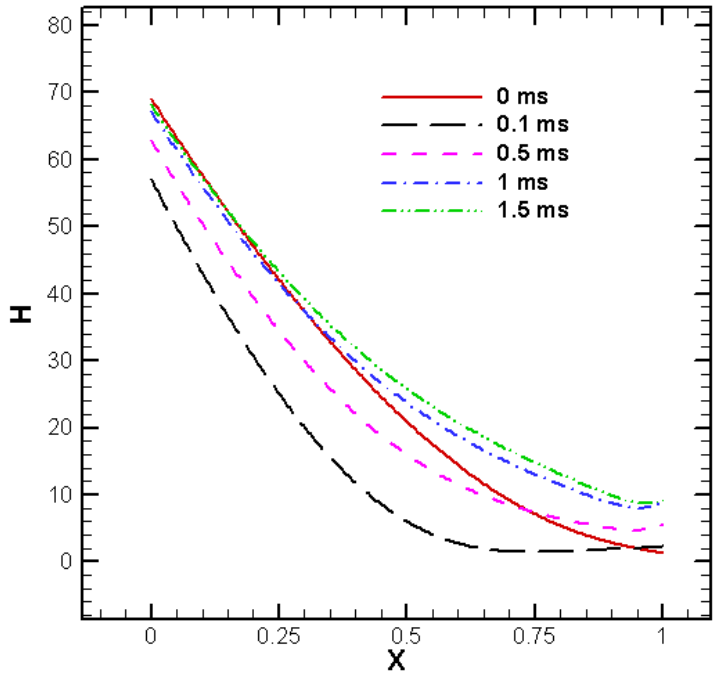

Figure 3.31: Nondimensional interface gap profiles at different times

Figure 3.32 presents the lubricant flow patterns in the armature-rail interface. The upper boundary of the region is consistent with the gap profiles shown above. It can be seen that as the gap height rises toward the end of the shot, more lubricant leaks out of the trailing edge. At the leading edge some of the lubricant is recycled back into the pocket for later use. The flow is constrained by the no-slip boundary conditions using an armature fixed coordinate system.

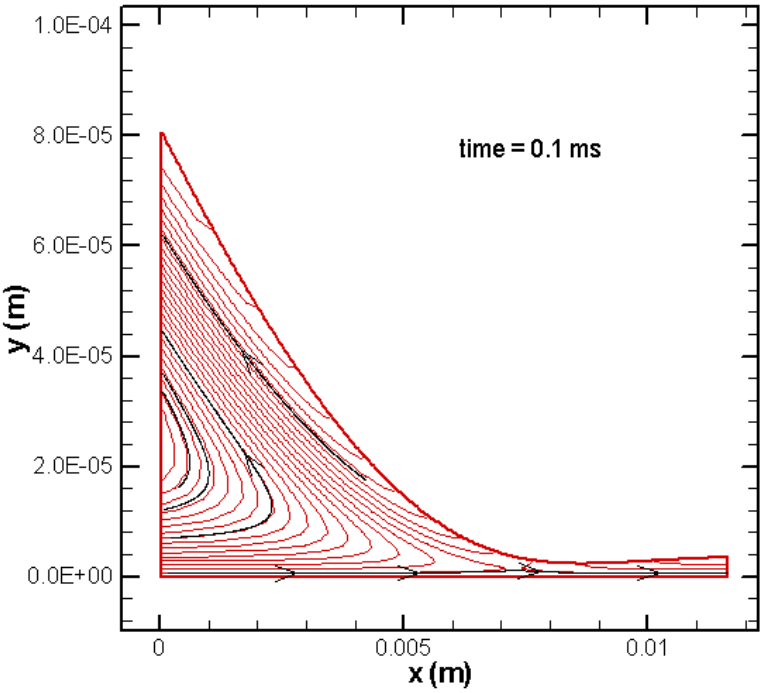

(a)

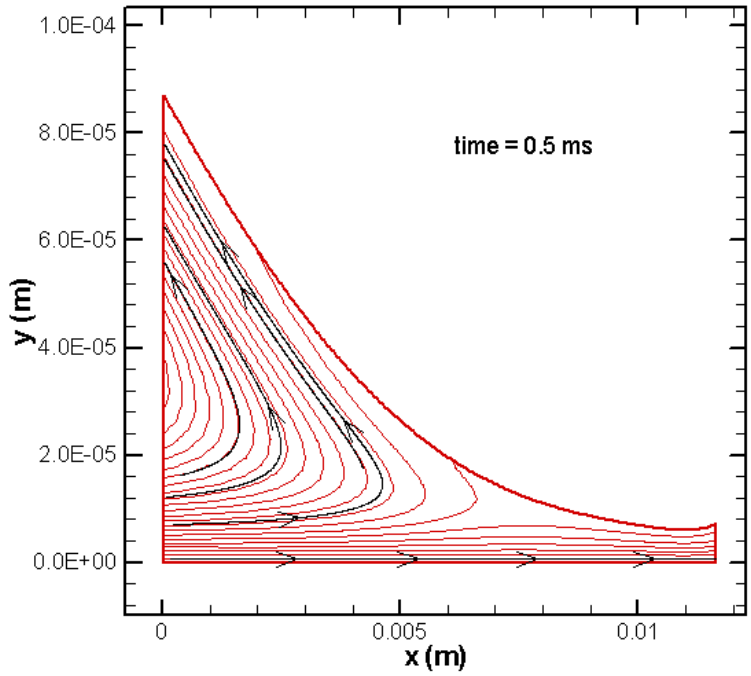

(b)

Figure 3.32: Fluid flow patterns at different times

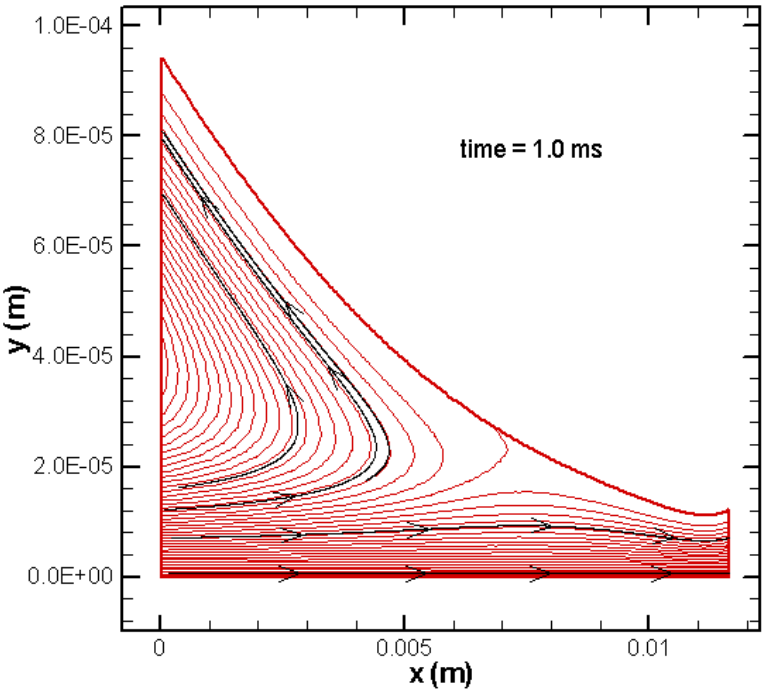

(c)

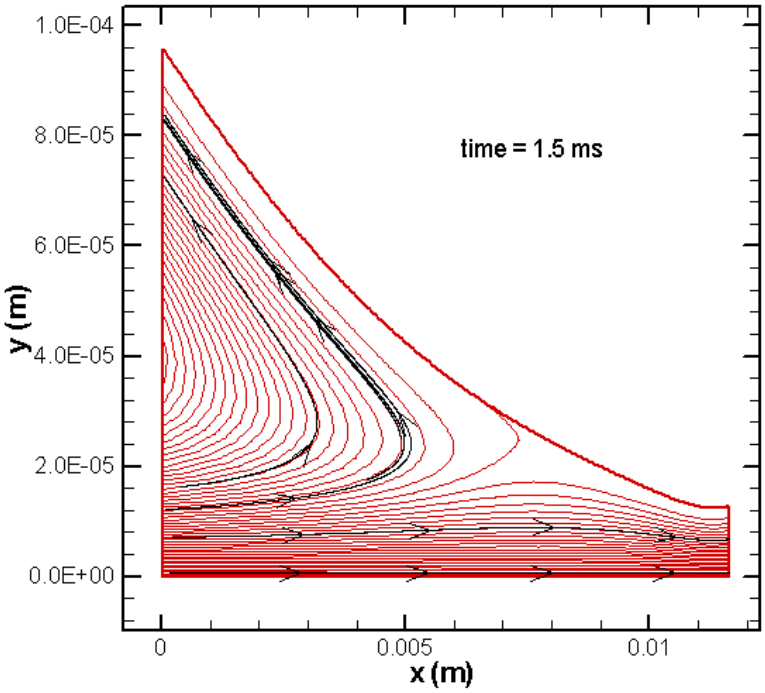

(d)

Figure 3.32 continued

The base case armature shot on the Georgia Institute of Technology launcher was optimized so there was just enough lubricant inside of the reservoir to prevent a transition. The results predict that the shot should not transition. Both the reservoir and the pocket are close to empty at the end of the shot meaning that a shot with less lubricant is likely to transition. The minimum gap height history also shows that the gap heights are sufficient to avoid a transition due to extensive wear or surface damage.

3.2 NRL Shot 223

The NRL launcher is developed by the Naval Research Laboratories. The launcher is similar to the base case launcher, but much larger. The rails are seven meters long and spaced 1.800 in apart. The armature also has the same general shape as the base case but is larger. A sketch of the armature used for shot 223 is shown in Figure 3.33. The armature is 4.929 in long, about three and a half times as long as the base case armature. The interface leading edge width is 1.796 in and the trailing edge nominal width is 1.846 in causing an interference fit as in the base case. The lubricant injection system is somewhat different from the base case however. There are two pockets and four reservoirs. The pockets are relatively shorter and deeper than the base case. Each pocket is fed by two long slender reservoirs with a separate injection conduit for each. The reservoir bottom is set between the pockets allowing the injection conduits to be oriented perpendicular to the armature-rail interface. Even though the armature is larger than the base case, the injection conduits are the same diameter of 0.039 in and only slightly longer. The cartridges have an inner diameter of 0.293 in and a length of 1.6 in.

Each cartridge is sealed with a Mylar sheet which ruptures when the armature accelerates. The initial charge of gallium lubricant inside each cartridge is 9.4 g. The total mass of the armature and four empty cartridges is 402.2 g.

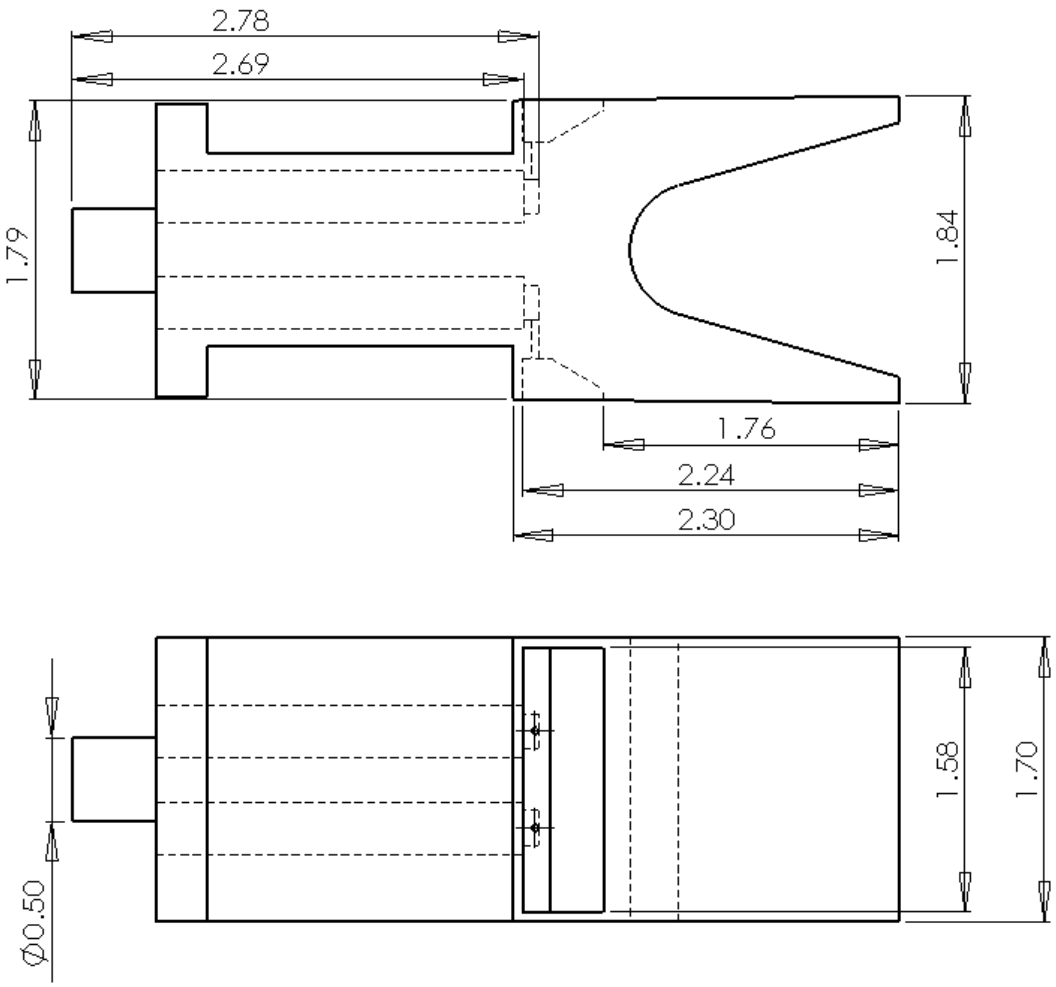

Figure 3.33: Sketch of the NRL shot 223 armature, dimensions are in inches

3.2.1 Electromagnetic Field Modeling

The electromagnetic field is calculated in the same way as was done for the base case. The same equations will apply, however, the two dimensional simplified region

will now be a projection of the NRL launcher and armature used in shot 223. The magnetic fields the armature is subject to are three dimensional in nature. However, to simplify the problem it was shown that only one component of the magnetic field was dominant. The two dimensional simplifying assumptions must be validated for this larger armature to ensure the model can still be used. The armature is modeled in COMSOL as was done for the base case and compared to the steady state results from the model. Figure 3.34 shows agreement between the magnetic flux distributions inside the armature. The boundary conditions on the outside of the rail used for the model are slightly different than the three dimensional COMSOL simulation so a correction factor will be needed as in the base case.

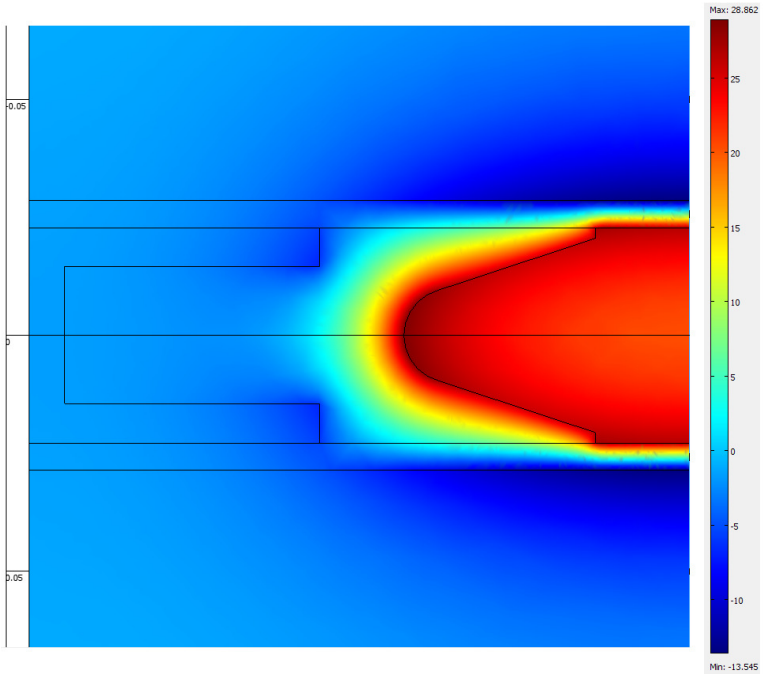

(a)

Figure 3.34: Comparison of magnetic flux distributions calculated by (a) COMSOL and (b) finite difference method, units in T

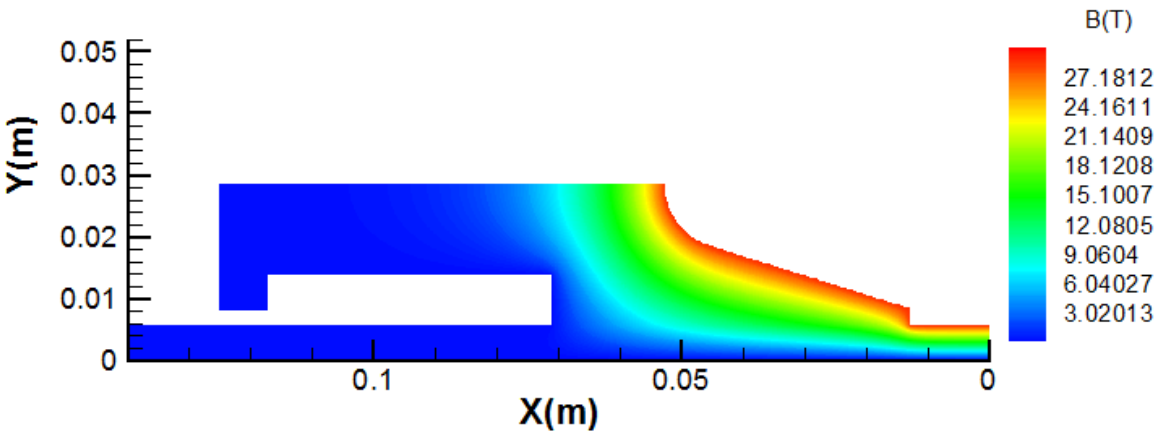

(b)

Figure 3.34 continued

The electric current distributions for the steady state case are presented in Figure 3.35. The two and three dimensional models reach similar results for the distributions and current paths shown by the arrows. Figure 3.36 checks the components of the magnetic flux in the two recessive directions. As it can be seen, the magnetic field is dominant in only one direction. Therefore, the two dimensional simplified model can be used for the electromagnetic field.

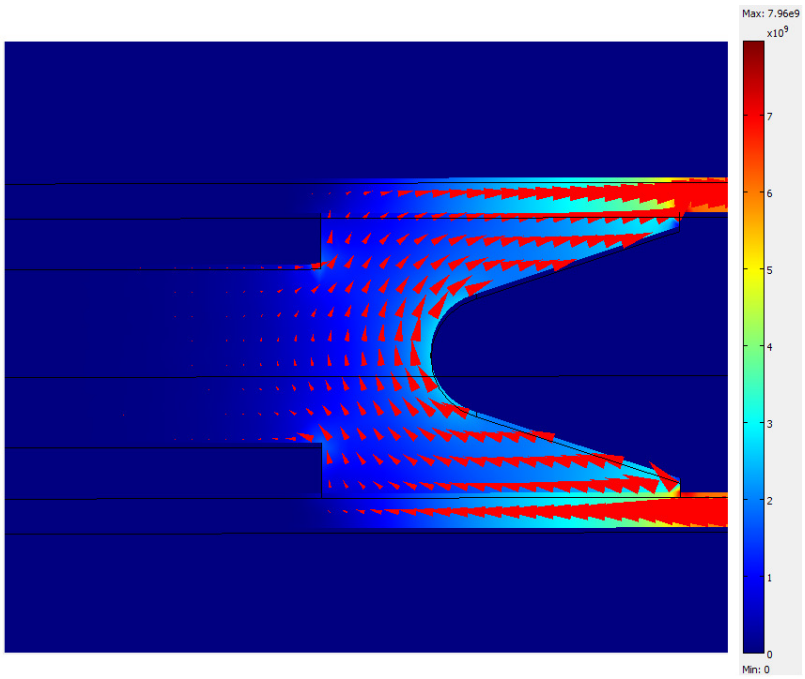

(a)

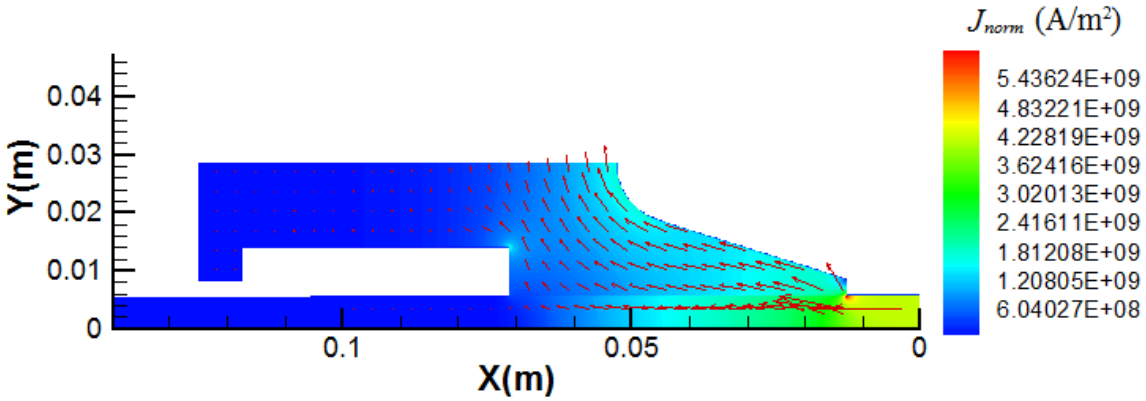

(b)

Figure 3.35: Comparison of current distributions calculated by (a) COMSOL and (b) finite difference method, units in A/m^2

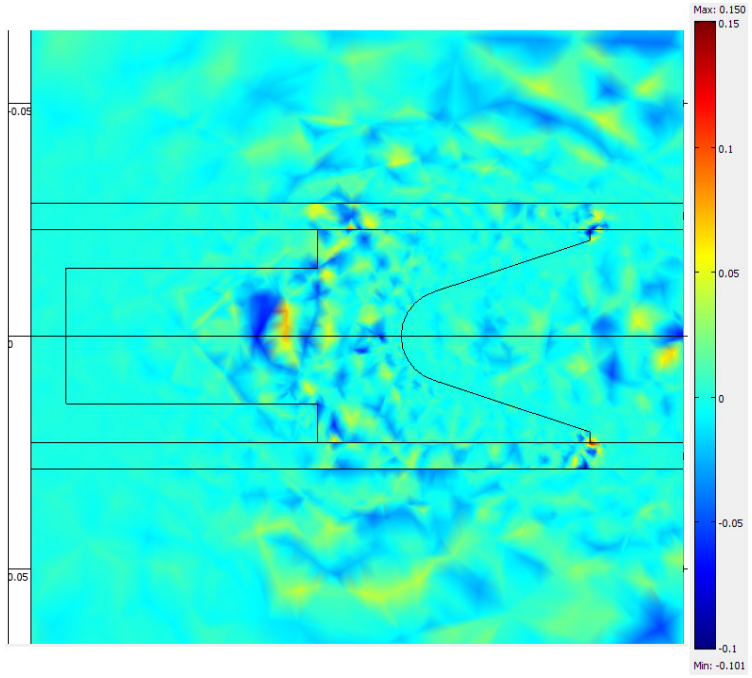

(a)

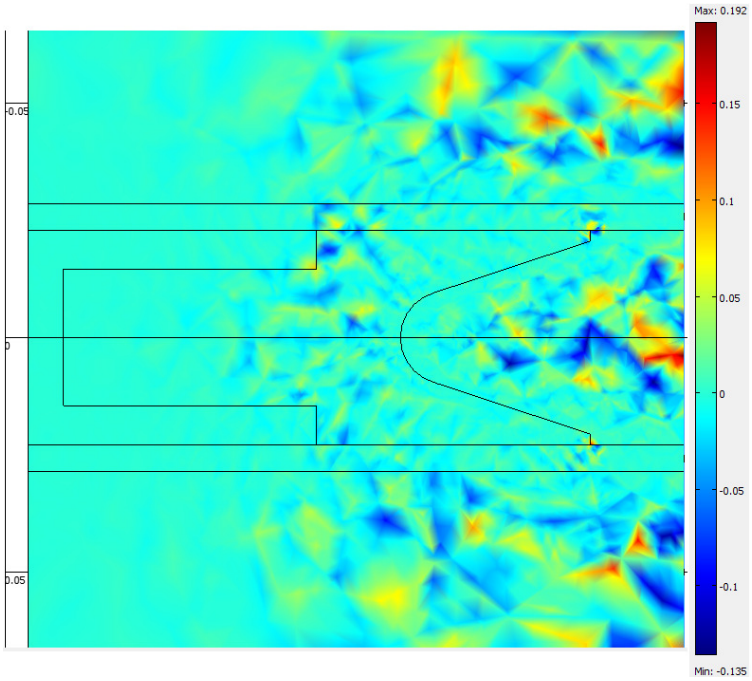

(b)

Figure 3.36: Magnetic flux density in the direction (a) parallel to the rails (b) transverse to the rails, units in T

3.2.2 Thermal Field Modeling

The thermal field for the NRL shot 223 armature is calculated in the same way as the thermal field for the base case was calculated. The same boundary conditions and assumptions will be applied to the new larger region. An ANSYS model is created to verify the finite difference temperature field using PLANE 13. Figure 3.37 compares the two methods of calculation with a high temperature boundary condition of 600 °C. The two methods yield almost identical results.

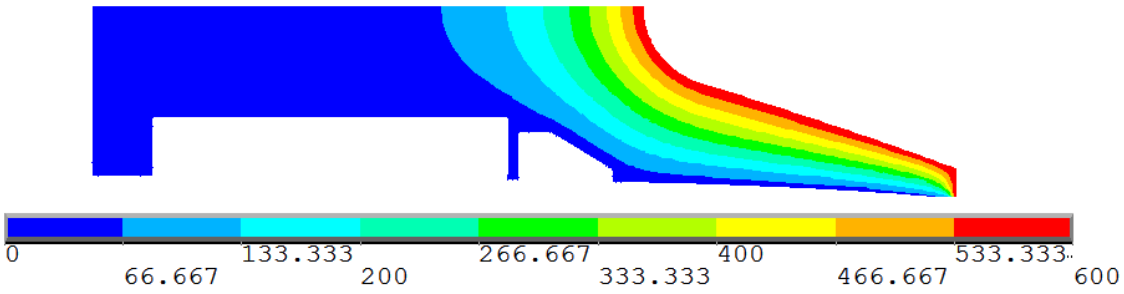

(a)

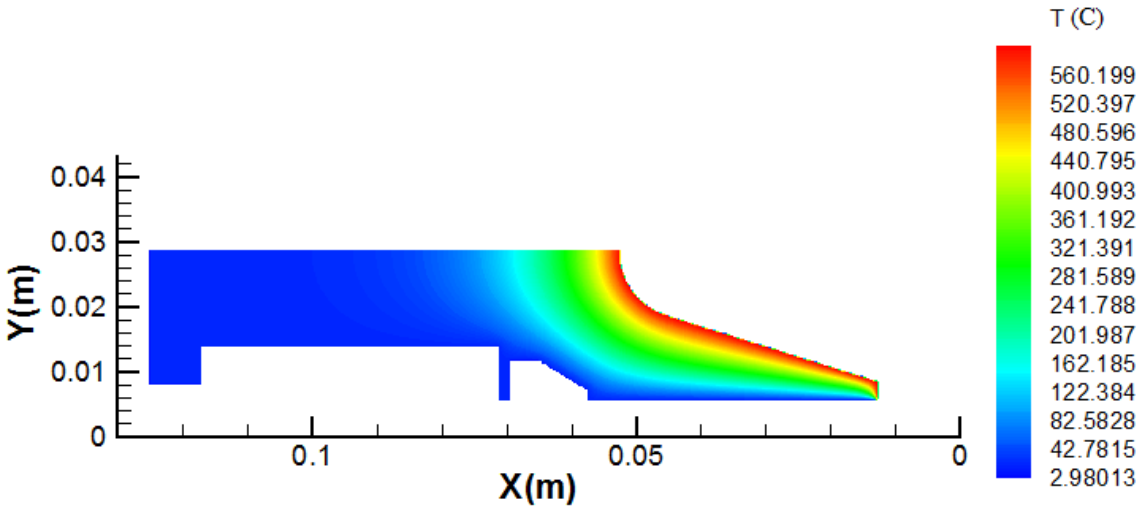

(b)

Figure 3.37: Temperature field validation calculated by (a) ANSYS and (b) finite difference method, units in C

3.2.3 Armature Deflection Modeling

The armature used for NRL shot 223 is similar in shape to the base case armature, but it is about 3-4 times as large. Therefore, it will be much stronger and capable of withstanding higher forces. The equivalent cantilever beam cross sectional properties used to calculate the deflection due to forces and pressures on the armature must be determined. The armature is modeled in ANSYS using PLANE 183 as done for the base case and loaded with forces of 500 N, 1000 N, 2000 N, and 4,000 N. The cross sectional area of the equivalent cantilever beam is adjusted until it agrees with the ANSYS model. Figure 3.38 displays the results obtained using the ANSYS model and the equivalent cantilever beam.

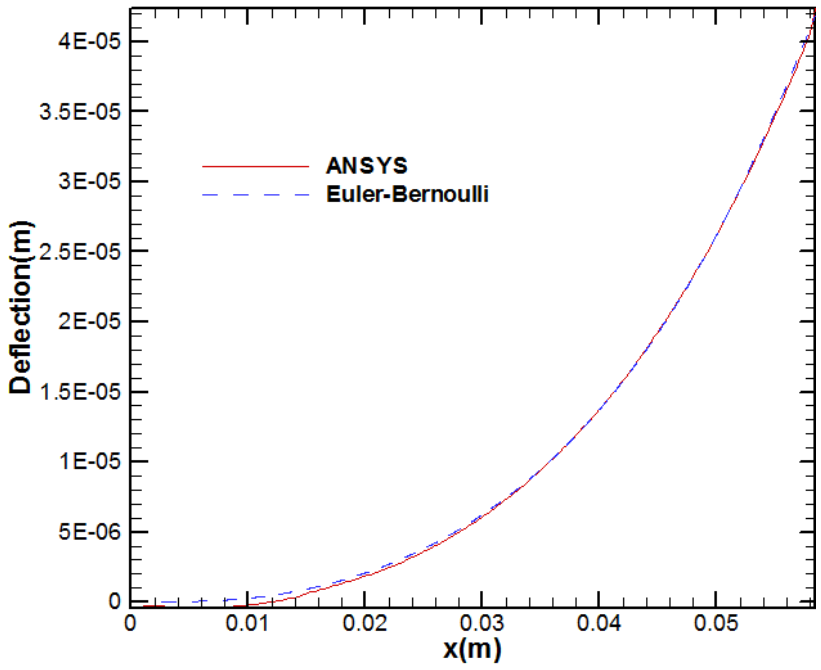

(a)

Figure 3.38: Comparison of armature wing deflection between ANSYS and Euler-Bernoulli models with a shear force of (a) 500 N, (b) 1000 N, (c) 2000 N, and (d) 4000 N

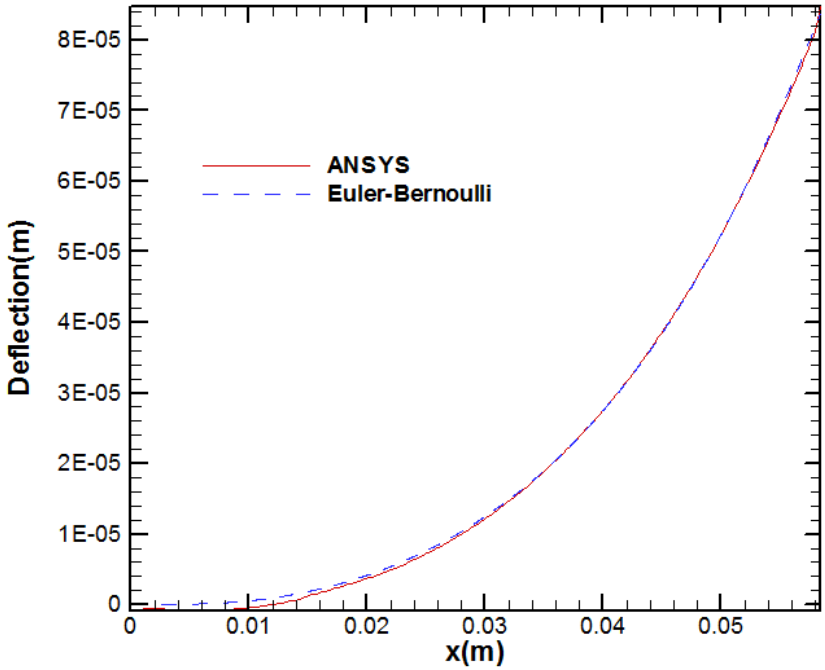

(b)

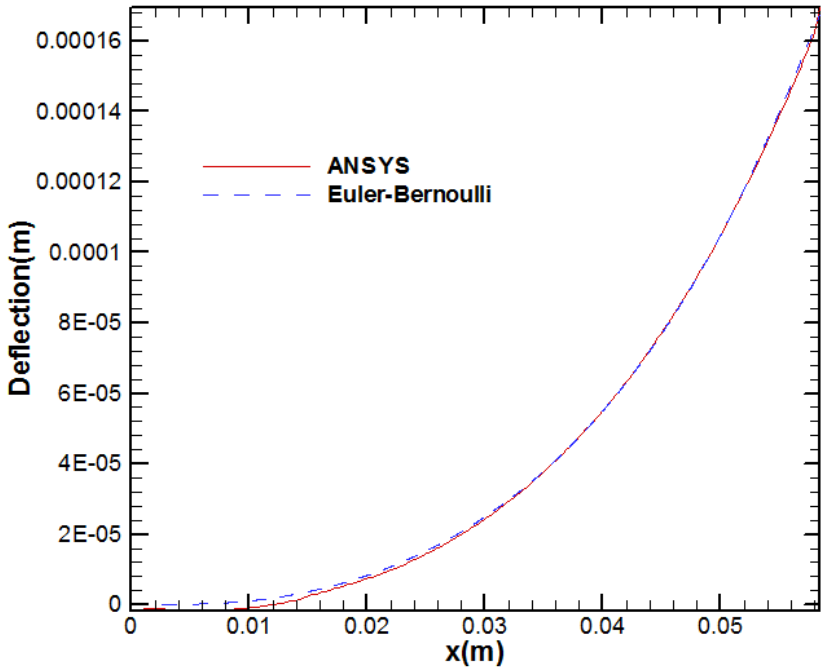

(c)

Figure 3.38 continued

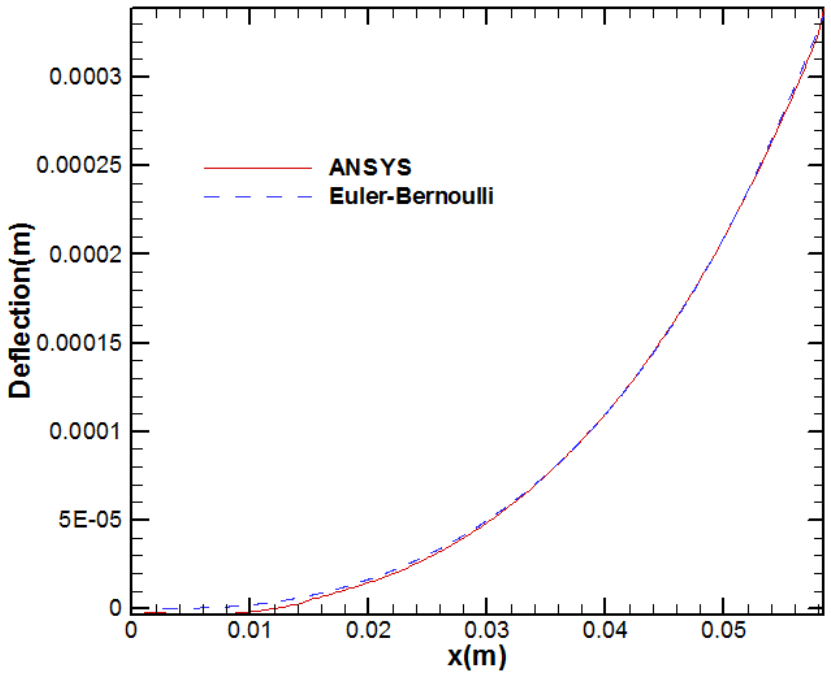

(d)

Figure 3.38 continued

The contact pressure and more importantly the deflection due to the contact pressure calculated with the equivalent cantilever beam must also be validated. ANSYS is used with PLANE 183, setting up the contacting surfaces with TARGE169 and CONTA 172 as was done for the base case. Both models are analyzed for interferences of 0.726 mm and 1.016 mm. The results of the contact pressure calculation in Figure 3.39 show some variation. The Greenwood-Williamson model predicts higher peak contact pressures and a smaller contact area. The results are within the same order of magnitude. Additionally, the deflection caused by the contact pressure is illustrated in Figure 3.40. Even with the variation in contact pressure, the deflection caused by contact is very similar between the two models.

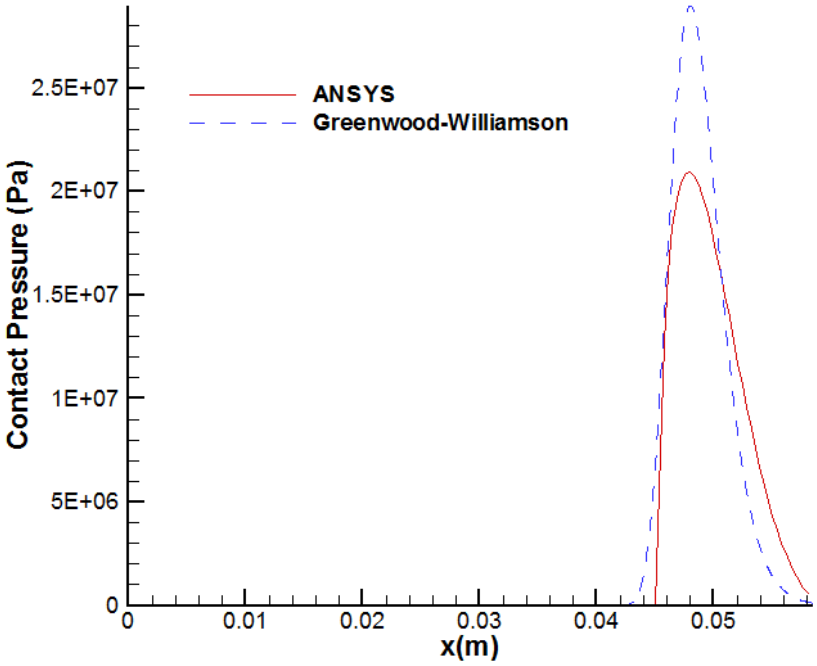

(a)

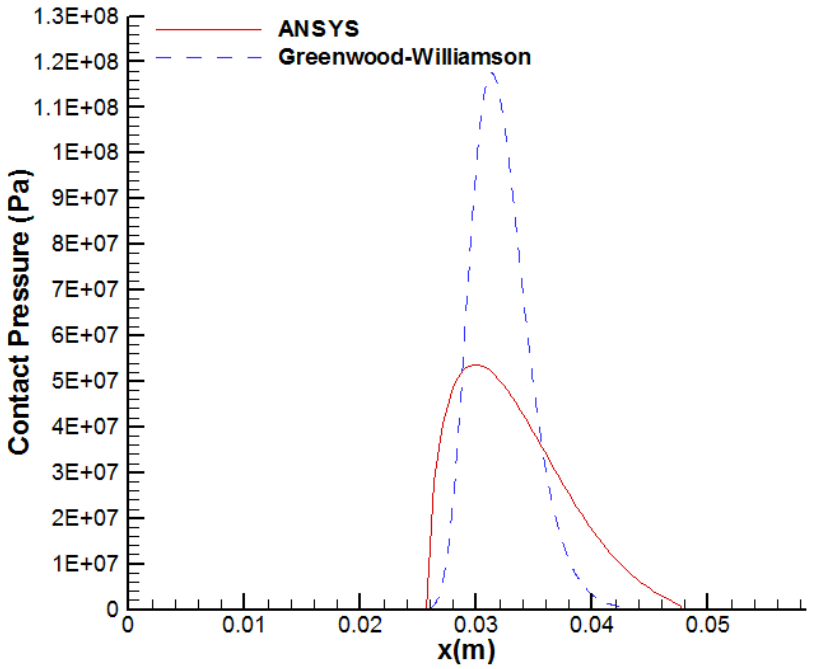

(b)

Figure 3.39: ANSYS and Greenwood-Williamson model contact pressure for an interference of (a) 0.762 mm and (b) 1.016 mm

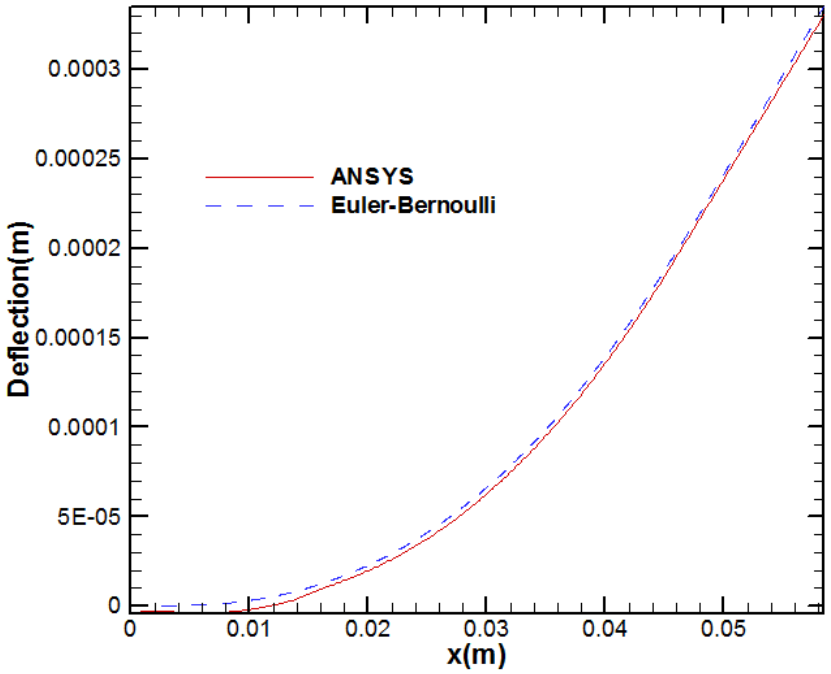

(a)

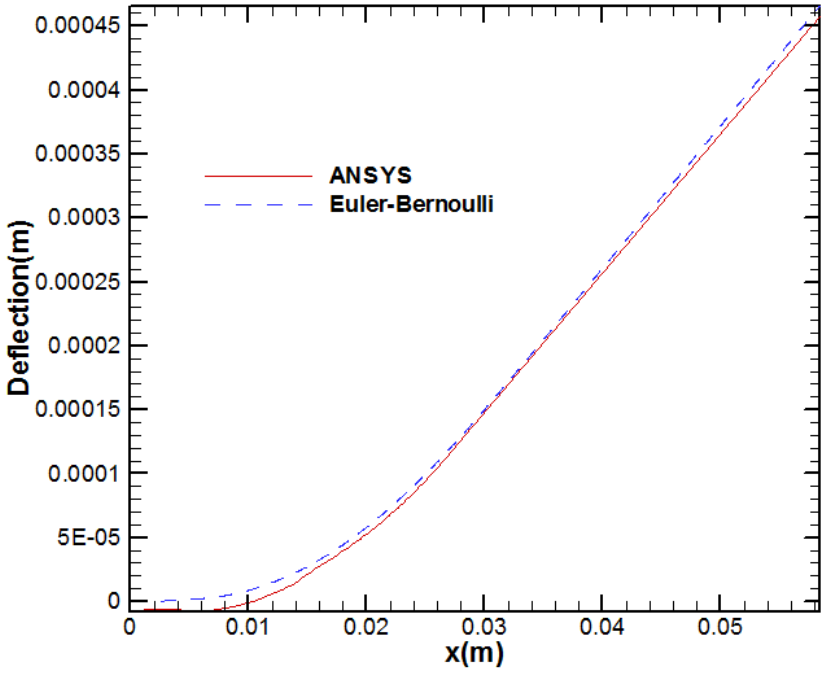

(b)

Figure 3.40: ANSYS and Euler-Bernoulli contact deformation for an interference of (a) 0.762 mm and (b) 1.016 mm

The equivalent cantilever beam used to calculate the deformation due to thermal loading must also have new cross sectional properties assigned to simulate the NRL shot 223 armature. The thermal models will be used to calculate the thermal field and the thermal deflection on the armature at the interface. As was done for the base case, the cross sectional area will be adjusted until the ANSYS and Euler-Bernoulli models agree. Because the NRL shot 223 armature is of a more robust design, a shear force of 300 N is used instead of the 200 N used in the base case to test the superposition of the two equivalent cantilever beams. The results of the two methods are shown in Figure 3.41 when setting the temperature boundary conditions in the same way as was done to develop the equivalent thermal beam for the base case.

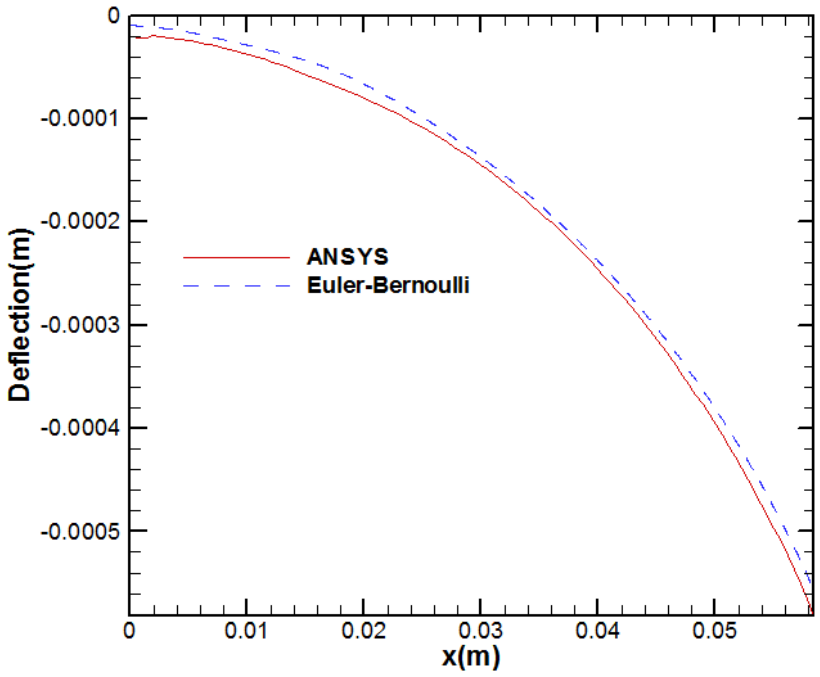

(a)

Figure 3.41: Comparison of armature wing deflection between ANSYS and Euler-Bernoulli models for high boundary temperatures of (a) 200 °C, (b) 300 °C, (c) 400 °C, and (d) 600 °C

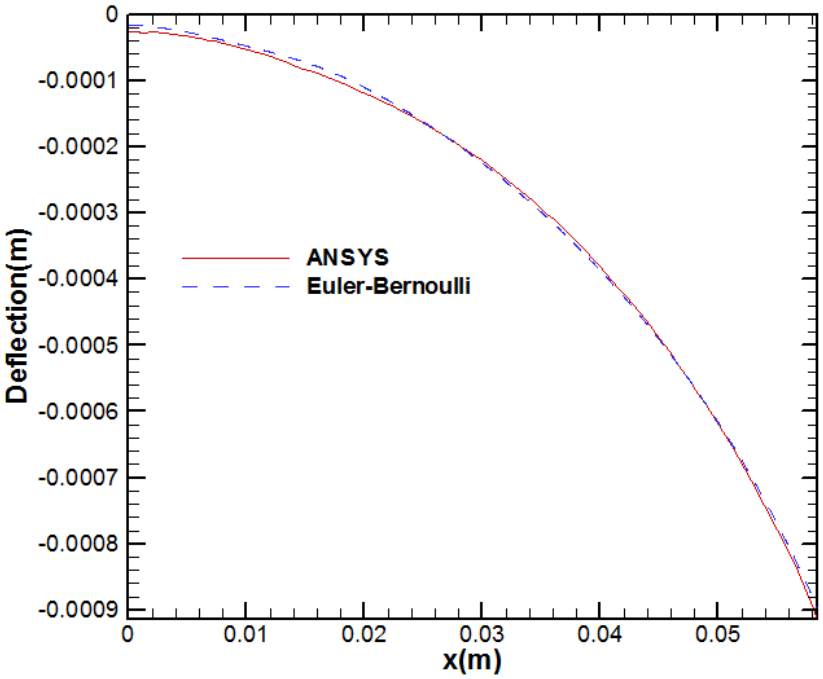

(b)

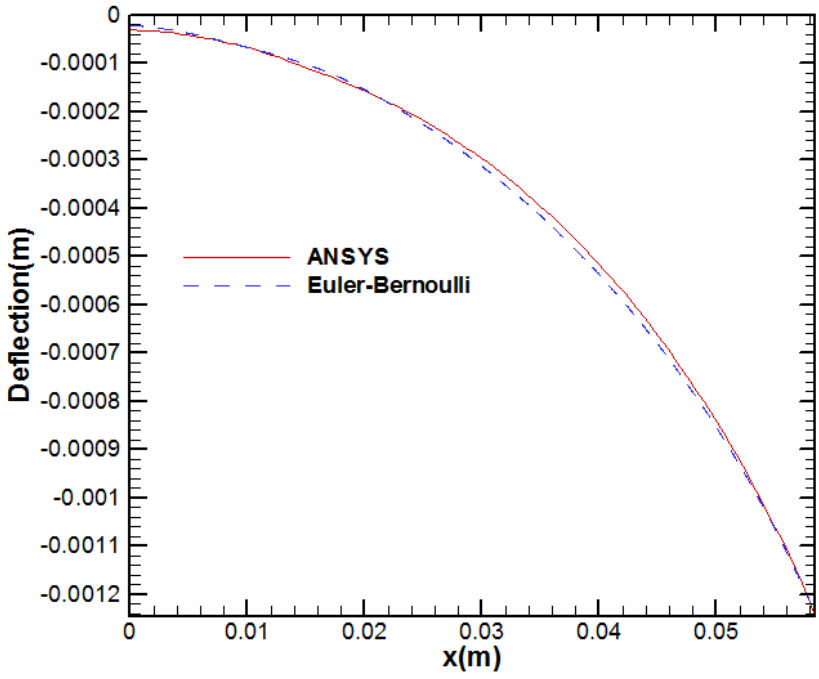

(c)

Figure 3.41 continued

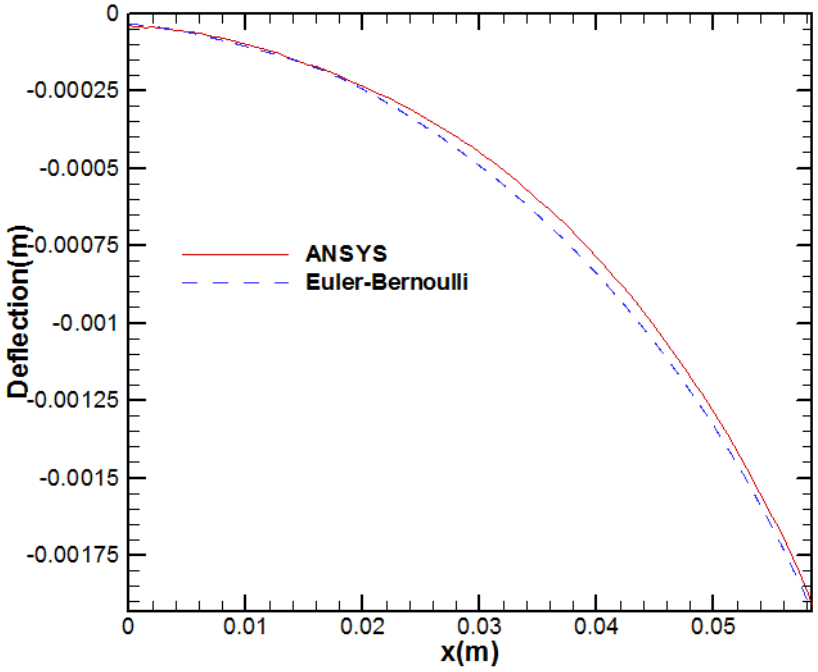

(d)

Figure 3.41 continued

3.2.4 Lubricant Modeling

The lubricant injection system has a different arrangement than the base case armature. There are two reservoirs per pocket, each with its own injection conduit. Using symmetry, the flow through one of the injection conduits will be evaluated and doubled. Again, the Bernoulli equation with head loss and a time dependent term is used. Figure 3.42 diagrams the injection system and calculational nodes. The pressure at each node can be found in the same way they were found for the base case. Equation 3.29 is the quadratic equation which can be solved to yield the mass flow rate of lubricant into one pocket. Here, the friction factor, f, from the Moody diagram is 0.03 and the head loss factor, k_e, is about 1.5.

Figure 3.42: Schematic of the NRL shot 223 injection system and node points (not to scale)

$$\left(\frac{f \frac{L_p}{2R_p} + K_e + 1}{2\rho\pi^2 R_p^4} \right) \dot{Q}^2 + \frac{L_p}{\pi R_p^2 dt} \dot{Q} - \left(\frac{L_p \dot{Q}_{pre}}{\pi R_p^2 dt} + P_1 - P_2 \right) = 0 \tag{3.29}$$

It was found analytically and backed by experimental observations that the pocket drains out before the reservoir is emptied for this shot. When this happens the reservoir is still supplying lubricant to the interface, but the gap height eventually falls into the solid-solid contact range due to lubricant leakage from the gap. To model this occurrence, it is assumed that the lubricant fills the gap from the trailing edge to some point between the leading and trailing edges. That is to say there is a single interface between the lubricated and the non-lubricated sections, shown in Figure 3.43. The pressure inside the lubricated region of the interface is calculated as in the base case. Any lubricant squeezed back into the empty region by the collapse of the gap is neglected. The location of this interface is found by using a mass flow rate balance at an assumed location of the interface. The mass flow rate going into the interface must be equal to the mass flow rate calculated by integrating the fluid density times, *u*, the velocity component parallel to the rail, calculated as done for the base case, from the

bottom to the top of the gap. If the mass flow rate into the interface is more than what is going out, the interface is moved toward the empty region. If the opposite is true, the interface moves toward the full region (see Figure 3.43 below). This process is iterated until the approximate interface position is found.

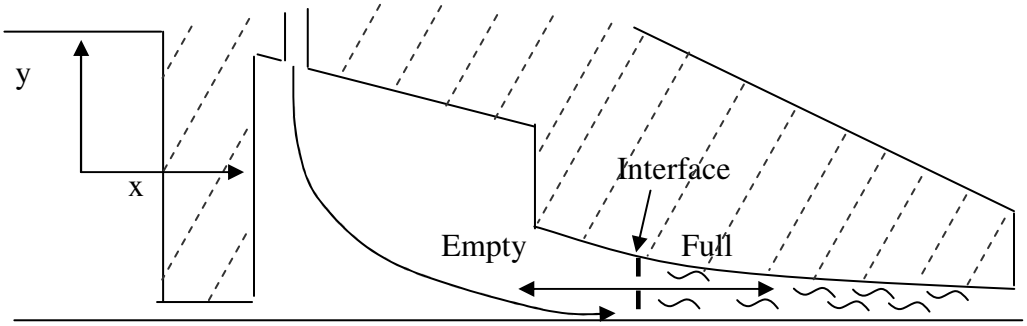

Figure 3.43: Interface configuration after the pocket is emptied (not to scale)

3.2.5 Results and Discussions

The Magneto-Elastothermohydrodynamic model used for the base case has been modified to simulate NRL shot 223. Physical parameters are calculated at every time step. NRL shot 223 showed a transition toward the end of the shot, however, x-ray photographs of the armature leaving the launcher shows that the reservoirs are mostly full of lubricant at the end of the shot. Figure 3.44 shows the muzzle voltage history recorded during the shot. In the figure the shot begins at about 0.5 ms. At approximately 3.5 ms after the beginning of the shot, a noticeable amount of muzzle voltage is seen. However, the voltage is fairly low. A transition is usually marked when the muzzle voltage exceeds 100 V. Therefore, it officially transitions at about 4.5 ms into the shot even though there may be some light current arcing or other phenomena before this occurs. Even after the

transition, the muzzle voltage remains relatively low until the current path is broken at the end of the shot, about 6 ms after the beginning. Because the model does not incorporate the wear or surface damage which occurs after the shot transitions, this model is not valid after a transition and any numerical result beyond the transition point must be used with extreme caution or discarded.

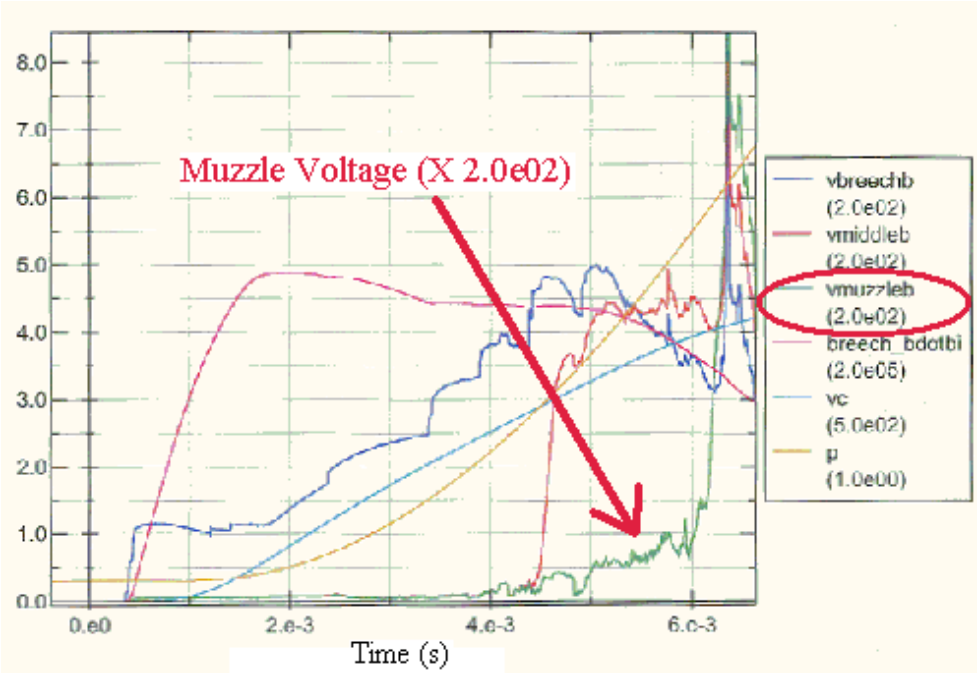

Figure 3.44: Experimental muzzle voltage

The current shown in Figure 3.45 is calculated from the experimentally recorded current history. The current rises quickly at the beginning of the shot. At about 1.8 ms, a maximum current of about 1 MA is achieved. The current undergoes a slight, gradual decrease before leveling off, then decreasing again as the shot ends. Even at the end of

the shot, the current is still about 650 kA. In addition to having overall higher values, this current profile is more level than the one used for the base case.

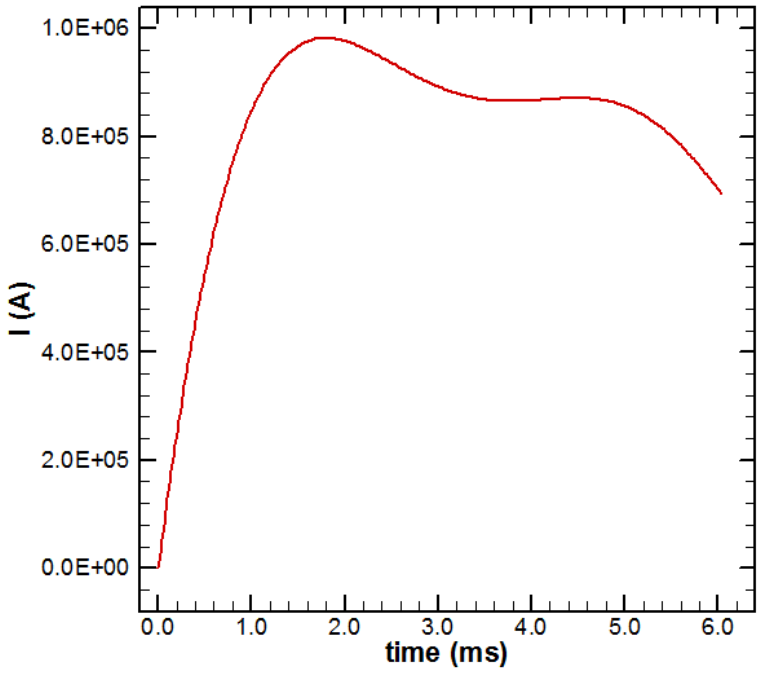

Figure 3.45: Electric current history

The computed magnetic flux resulting from passing an electric current through the rails and armature is shown in Figure 3.46 for different times. Using symmetry, only half the region is calculated and shown below. The magnetic flux is distributed in a way that it is most dense where the armature meets the air on the trailing edges. Because the current quickly rises, the magnetic flux is already close to the peak values only 1.0 ms into the shot. At 1.8 ms the magnetic flux reaches its highest values, then declines slightly toward the end of the shot.

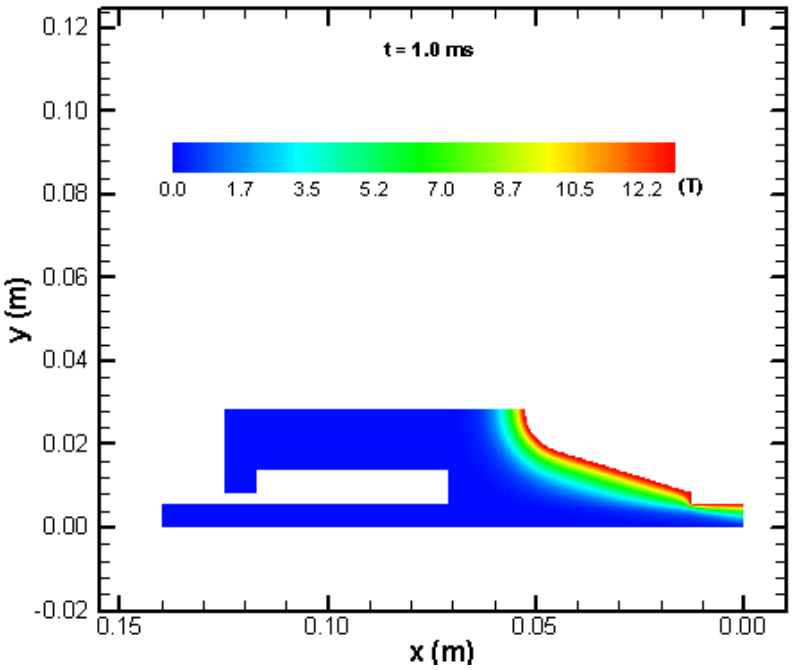

(a)

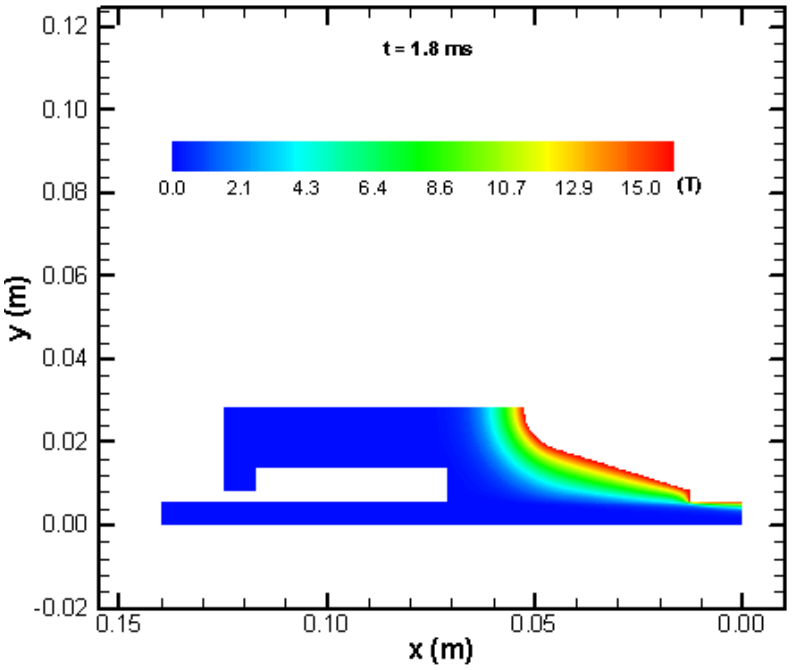

(b)

Figure 3.46: Magnetic flux density distribution at different times

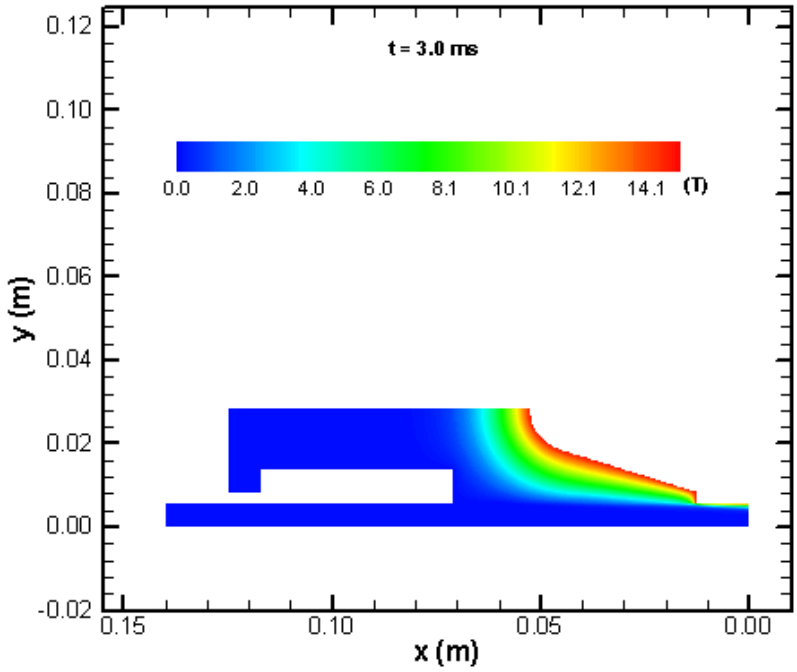

(c)

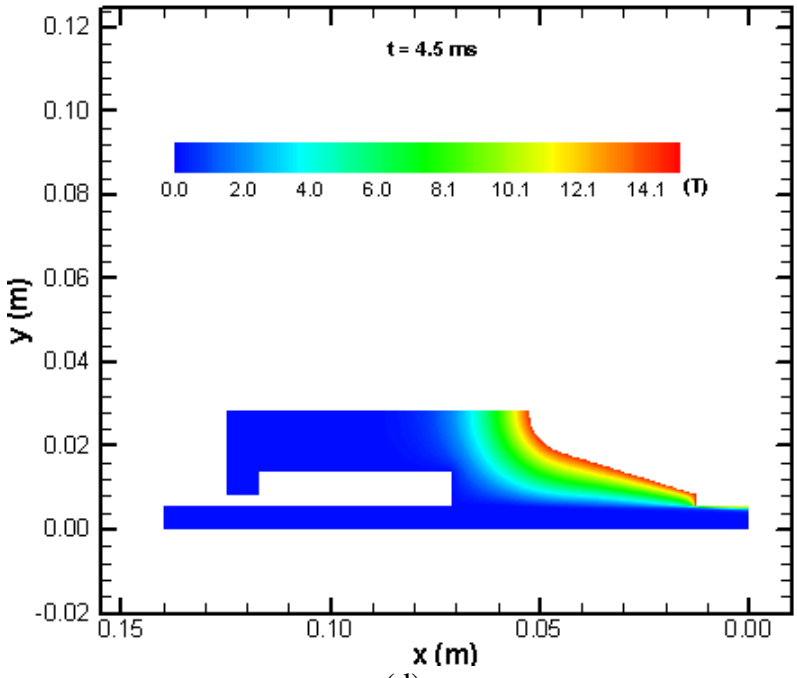

(d)

Figure 3.46 continued

The electric current distribution for NRL shot 223 is illustrated in Figure 3.47. The electric current density is concentrated in the same positions as the magnetic flux density. Towards the beginning of the shot, the electric current density is spread out fairly evenly along the trailing edges. As the armature velocity increases, the velocity skin effect pulls the electric current density toward the trailing edges of the interface.

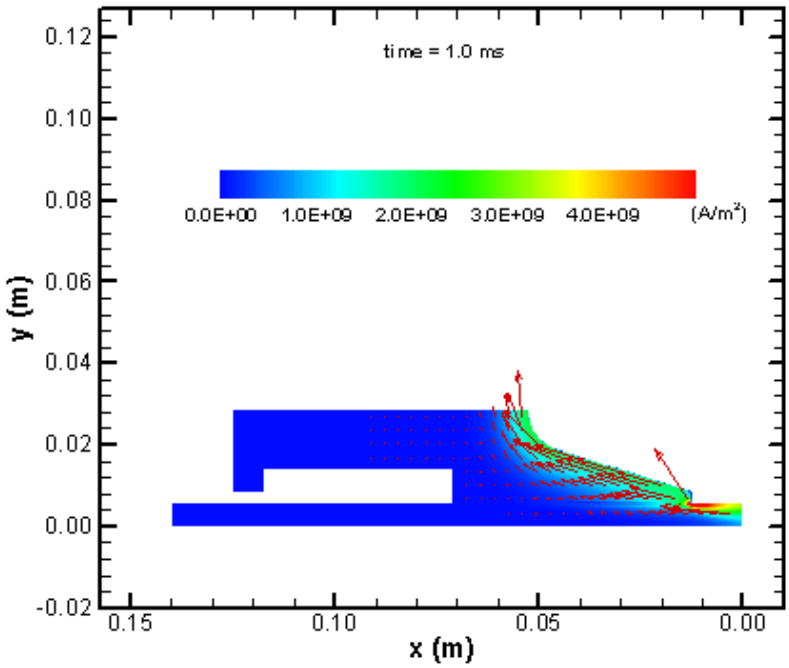

(a)

Figure 3.47: Electric current distribution at different times

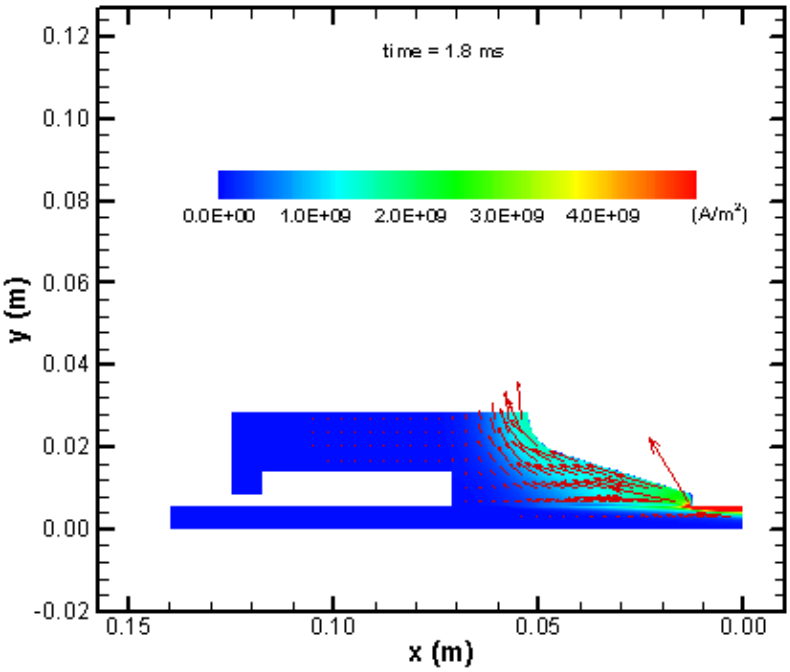

(b)

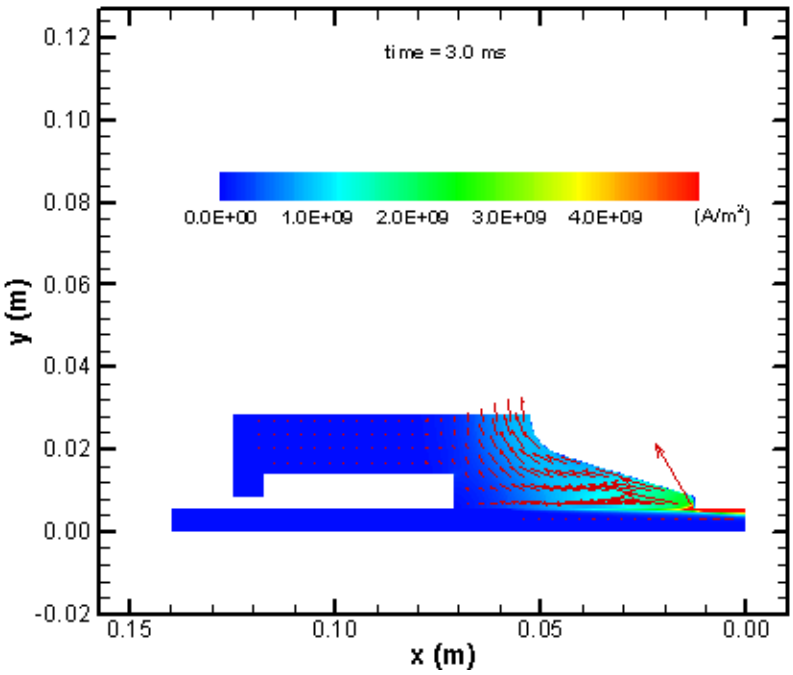

(c)

Figure 3.47 continued

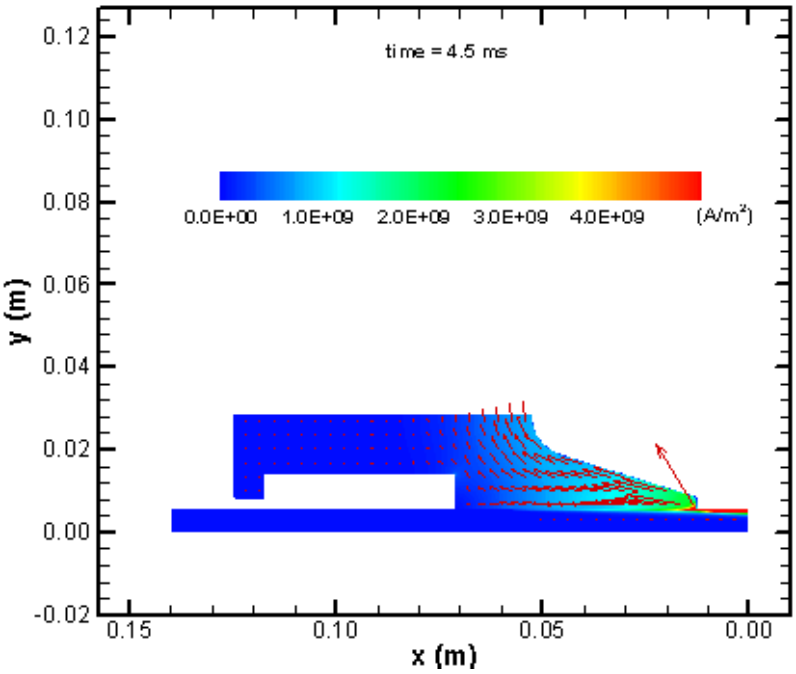

(d)

Figure 3.47 continued

Figure 3.48 presents the body forces calculated due to electromagnetic interactions. The forces are concentrated in the same locations as both the current density and the magnetic flux density. Because the current history is fairly smooth over the times shown, the magnitude of the forces is also smooth. For this armature, as in the base case, there is a component of the magnetic force which acts to separate the armature trailing edges. In general, the force density is smaller for the NRL shot 223 armature than was found in the base case; however, the volume of the armature is much larger so the net force will be larger.

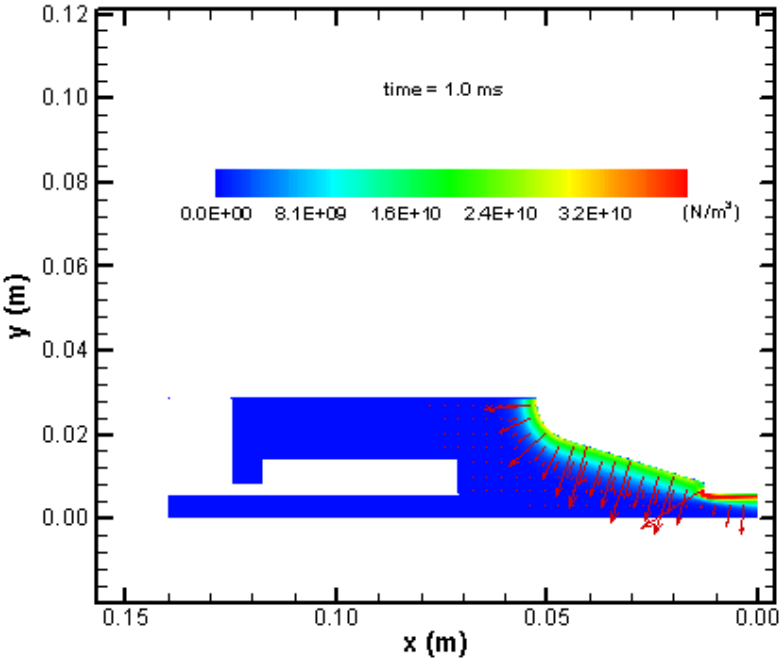

(a)

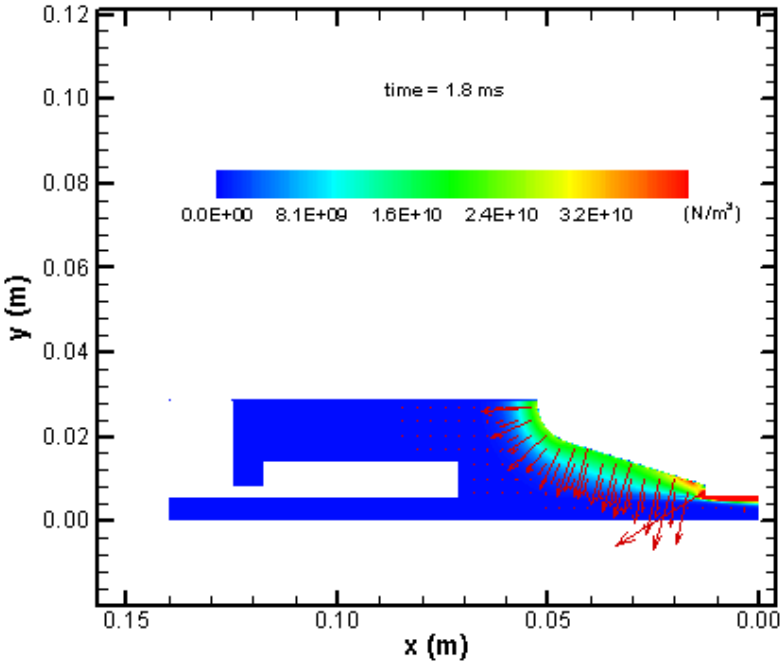

(b)

Figure 3.48: Magnetic body force distribution at different times

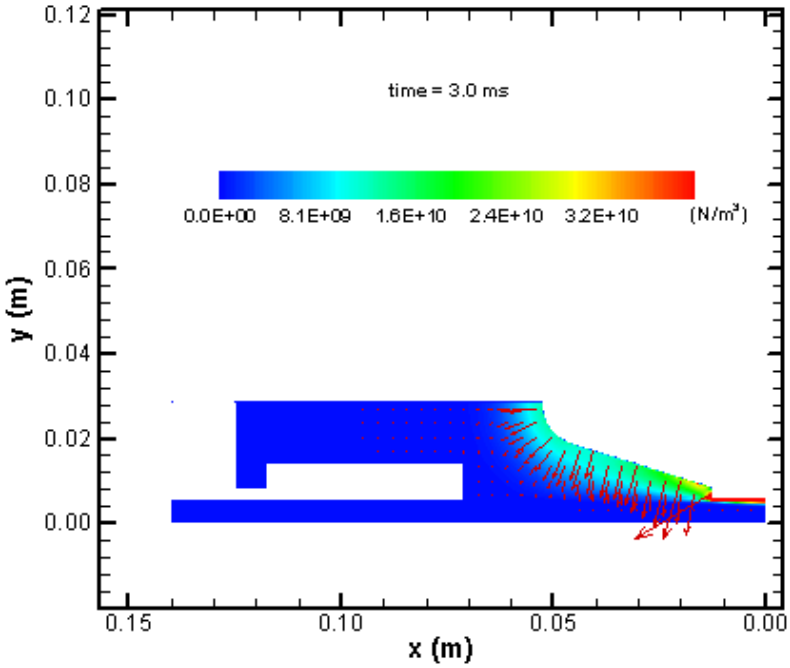

(c)

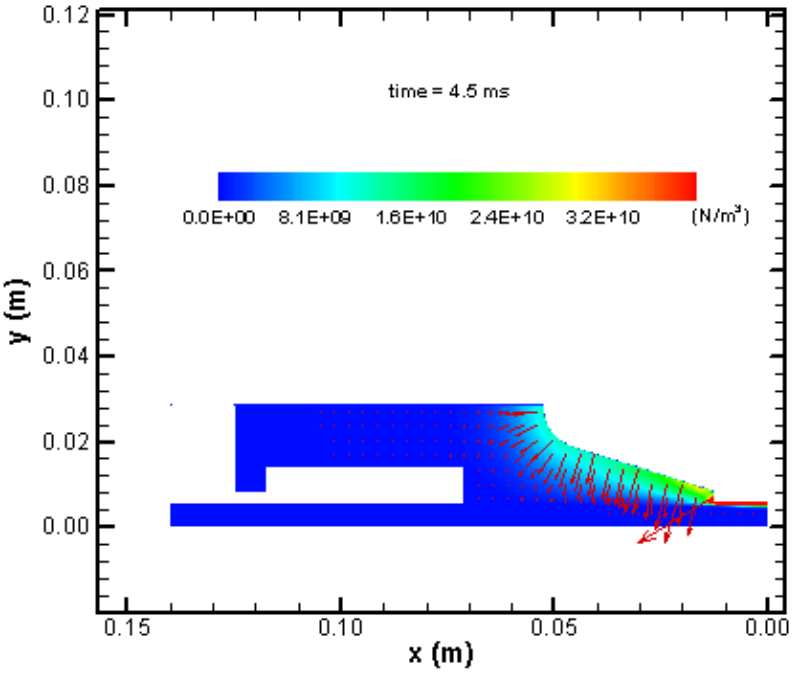

(d)

Figure 3.48 continued

The temperature profile is displayed in Figure 3.49 at different times. Toward the beginning of the shot, the armature-rail interface generates a considerable amount of heat. Even at 1.8 ms the temperatures at the interface are greater than anywhere else in the armature. As the shot advances, the currents become concentrated at the trailing edge of the interface and the resulting joule heating increases the temperature in the trailing end of the armature. Only a small region on the armature is predicted to reach the melting temperature using the model. The region is small enough to assume melting will not occur.

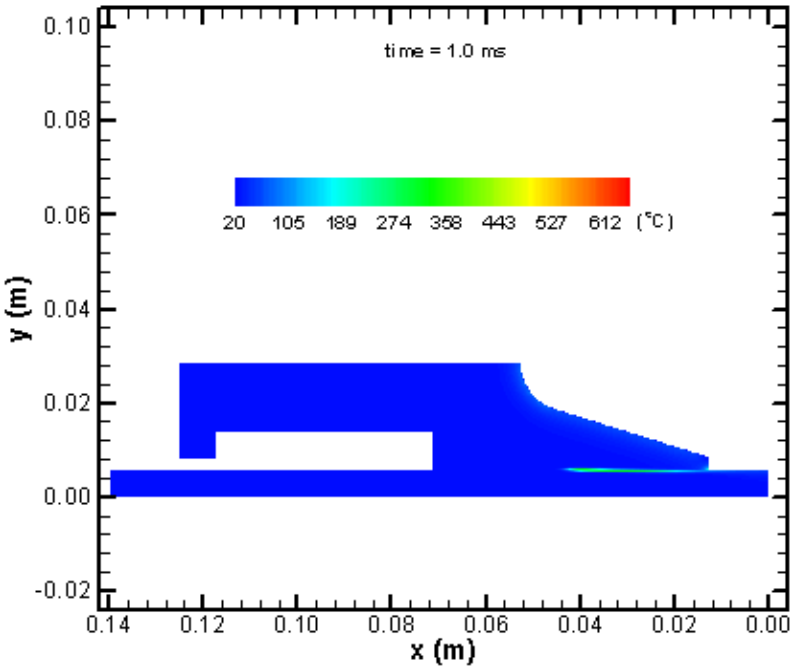

(a)

Figure 3.49: Temperature distribution at different times

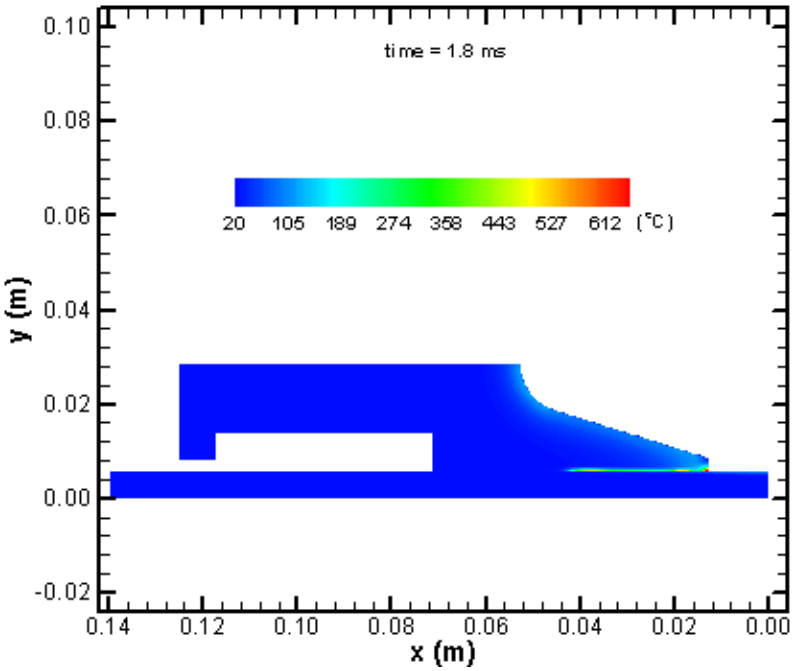

(b)

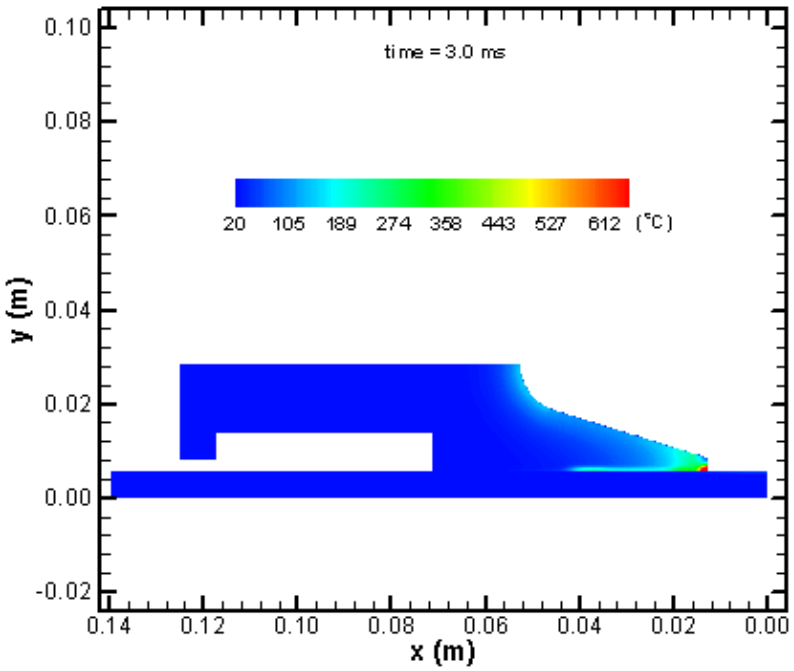

(c)

Figure 3.49 continued

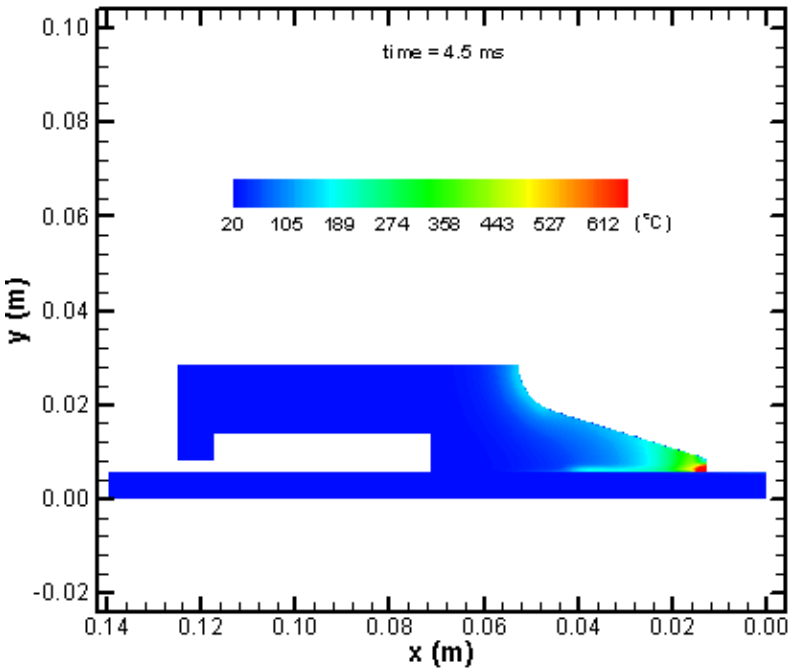

(d)

Figure 3.49 continued

The net forces acting on the armature are shown in Figure 3.22. The electromagnetic force, $F_{emag,}$ is approximately proportional to the square of the current profile with a maximum of over 200 kN at about 1.8 ms. The frictional and viscous forces, F_f and F_v respectively, are small enough that the total net force acting on the armature, F_{total} is almost identical to the electromagnetic force over most of the shot. However, at the beginning of the shot the frictional force is sufficient to create some variation between the total force and the electromagnetic force. The results shown beyond the transition point, about 4.5-5.0 ms, can not be accurately used.

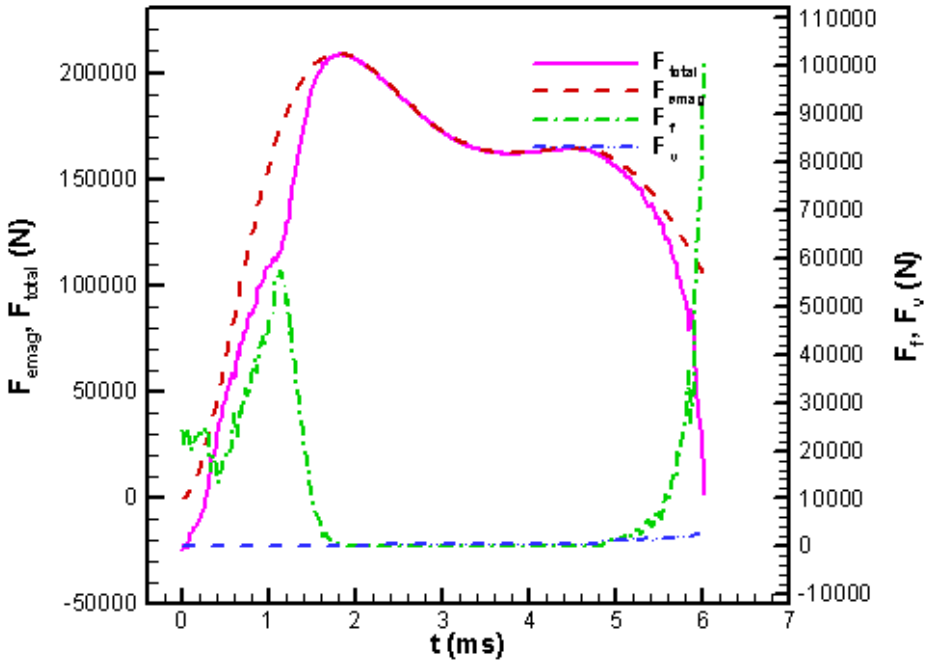

Figure 3.50: *x* direction armature force history

The net force on the armature causes it to accelerate along the rails. The acceleration history for the armature is shown in Figure 3.51. The armature is briefly held in place by the frictional force at the beginning of the shot. Then it reaches a maximum acceleration of almost 500,000 m/s^2 at 1.8 ms. The armature acceleration drops off slightly after the maximum until the transition.

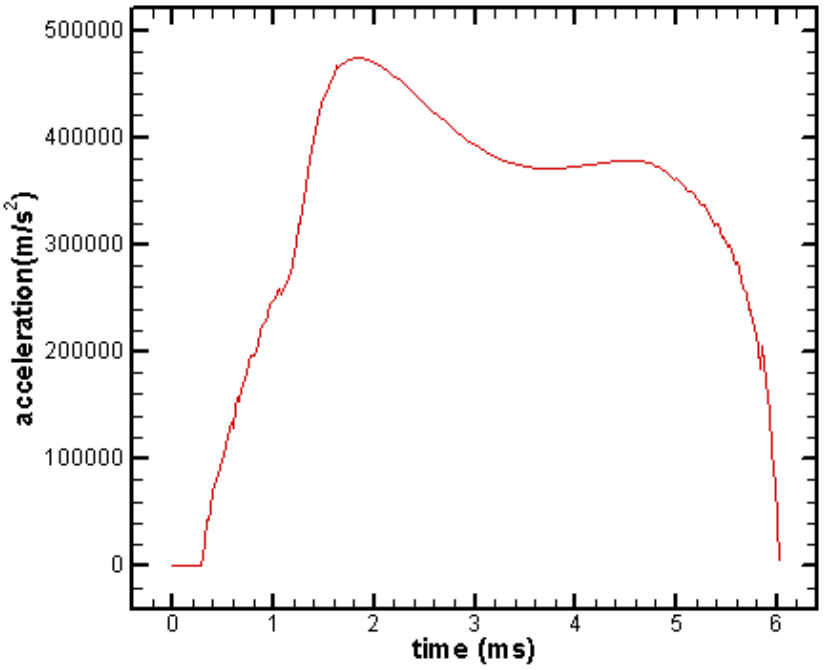

Figure 3.51: Armature acceleration history

The velocity profile predicted with the numerical model is compared to the experimentally observed armature velocity in Figure 3.52. The numerical results agree fairly well with the experimental velocity. The velocity profile has a fairly smooth increase, which is a direct result of the smooth acceleration profile. The velocity reached when the shot transitions is about 1600 m/s, however, the muzzle velocity in the experiment was about 2100 m/s. Figure 3.53 compares the numerical prediction of the armature position with the experimental results. The position of the transition is about 3.2 m from the starting position.

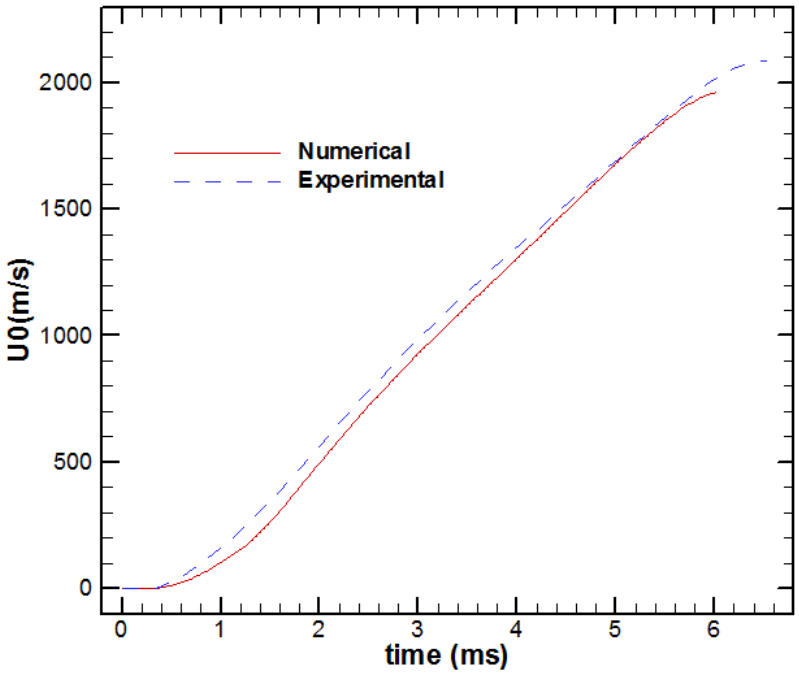

Figure 3.52: Comparison of predicted armature velocity history with experimental measurements

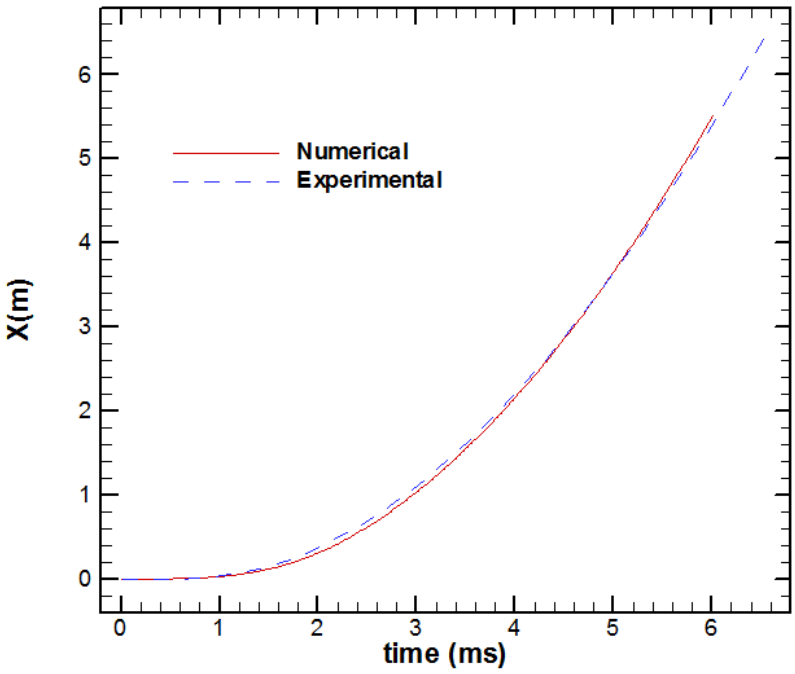

Figure 3.53: Comparison of predicted armature location history with experimental measurements

A history of the amount of lubricant left inside each of the four reservoirs, Q_{left} is shown in Figure 3.54. Each reservoir begins with a charge of 9.4 g which is delivered to the pocket as the armature accelerates. At the end of the shot, each reservoir is still about 75 percent full. An x-ray taken as the armature exited the launcher validates that the reservoirs are about 75 percent full at the end of a shot. Figure 3.55 illustrates the lubricant consumption history of one pocket. Q_{out} is the amount of lubricant delivered to the pocket from the two injection conduits, Q_l and Q_r are the amounts leaked from the leading edge and the trailing edge of the pocket respectively, and Q_{net} is the amount of lubricant inside the pocket. Because the pocket never fills up, no lubricant leaks from the leading edge. As the armature velocity increases the amount of fluid inside the pocket increases because there is a lot of lubricant coming from the reservoir. As the armature reaches high velocities, the fluid pressure increases the gap height and more lubricant is leaked through the trailing edge of the pocket causing the amount of lubricant inside the pocket to decrease. The pocket entirely empties out at about 4.7 ms, however, there is still lubricant being supplied to the interface from the reservoir.

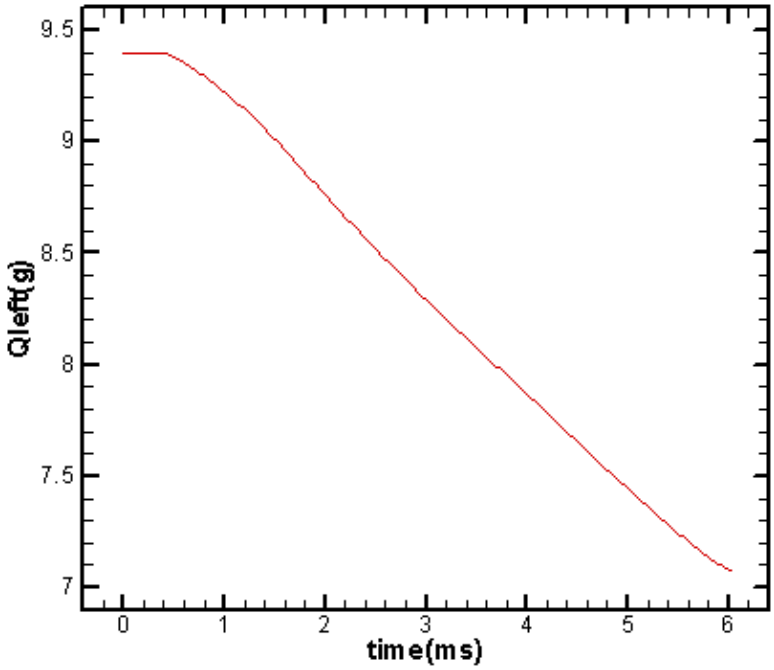

Figure 3.54: History of the amount of lubricant left inside each reservoir.

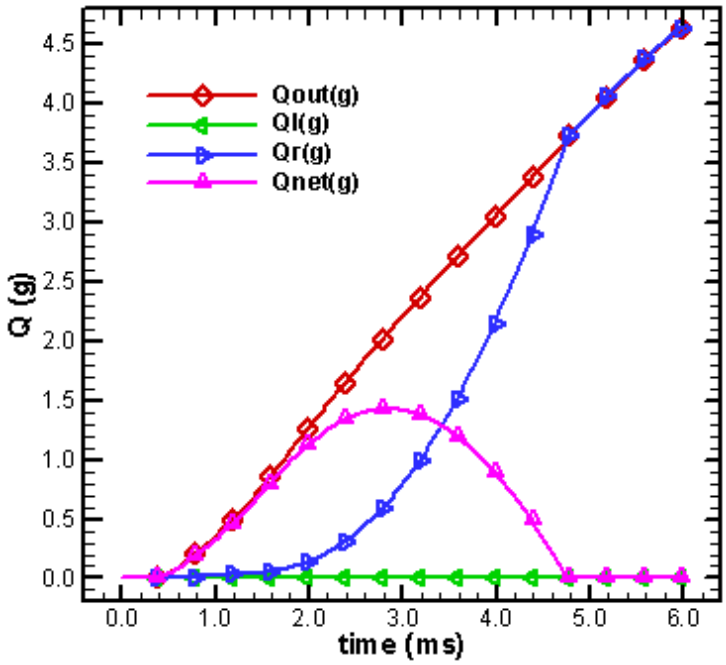

Figure 3.55: Mass flow amount history

The minimum gap height history for the shot is shown in Figure 3.56. For NRL shot 223 the magnetic force initially is successful in decreasing the gap height. As the armature picks up speed the fluid pressure increases the height of the interface gap. When the lubricant inside the pocket runs out, the interface begins to empty out and the gap begins to collapse. Initially, there is a large decrease in gap height at 4.7 ms, then because there is so little lubricant coming out of the reservoir the gap height decreases farther as the interface empties. The result is a gap height that is about the same size as the surface roughness combined with extremely high velocities leading to excessive wear and surface damage which can cause a transition. Additionally, a partially lubricated interface can also cause transitions due to current arcing in the empty regions. Therefore, the model predicts a possible transition about at 4.7 ms or later. This falls close to the experimental time at transition of 4.5 ms.

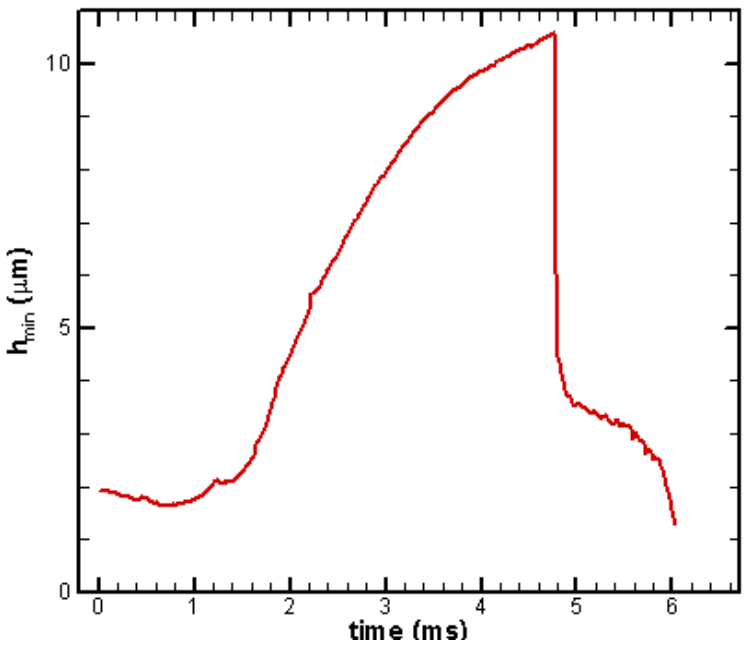

Figure 3.56: Minimum film thickness history

The lubricant pressures at different times are illustrated in Figure 3.57. The magnetic pressure is only significant at the trailing edge of the interface, where the current and magnetic flux densities are concentrated. At 1.0 ms there is a small amount of cavitation in the lubricant at a position of 0.024 m from the trailing end of the pocket. This cavitation is so light that it is not likely to cause transition. As the armature velocity increases, the fluid pressure increases and eliminates the cavitation. At 4.8 ms the pocket is empty and the armature-rail interface is beginning to empty out. Because there is no lubricant in the empty region, there can be no lubricant pressure.

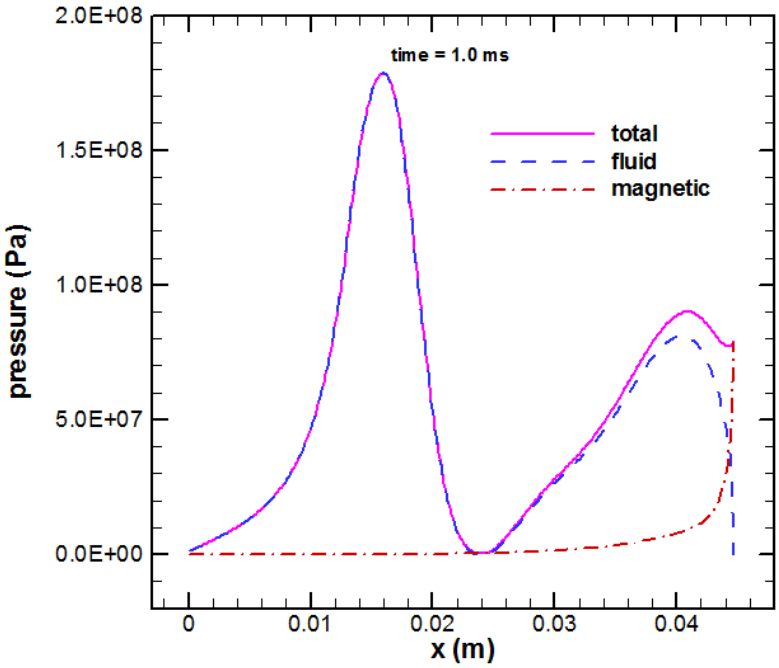

(a)

Figure 3.57: Pressures in the fluid at different times

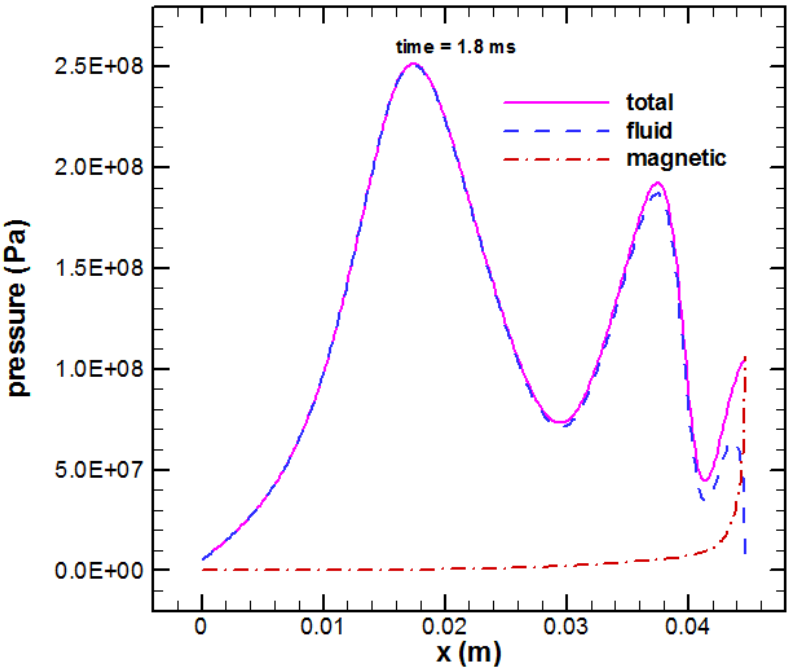

(b)

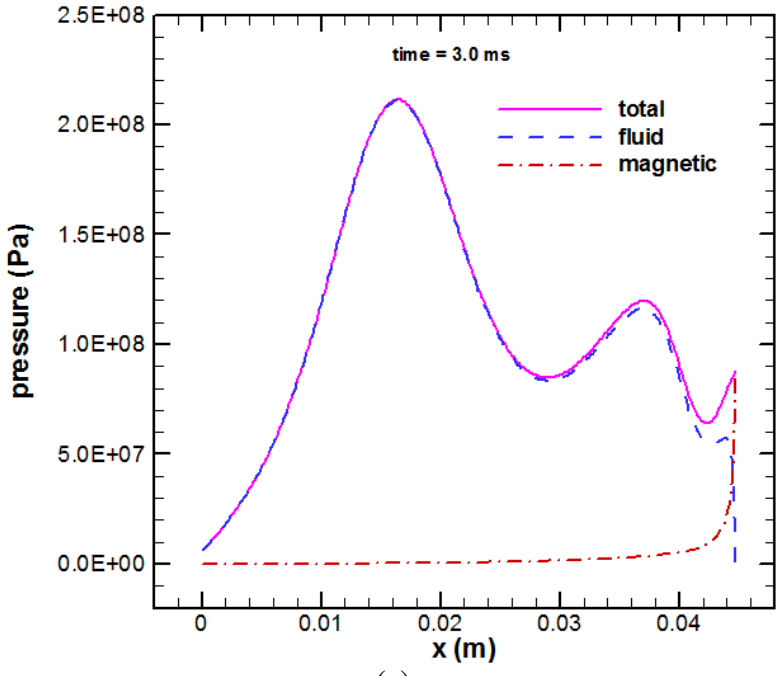

(c)

Figure 3.57 continued

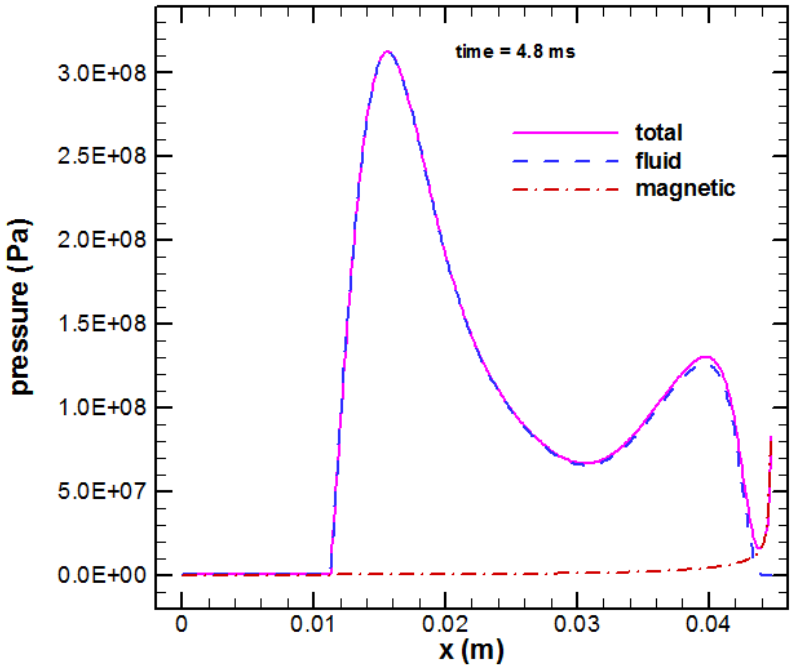

(d)

Figure 3.57 continued

The distributed forces acting on the armature in the transverse direction are displayed in Figure 3.58. The positive forces push the armature away from the rail, while the negative forces pull it closer. The magnetic forces tend to pull the armature into the rail due to the direction of the magnetic body force in the armature. The contact force is high initially, but as the armature speeds up the armature is lifted out of contact by the larger fluid distributed force. The total distributed force that acts on the armature is the sum of the magnetic, contact, and fluid forces.

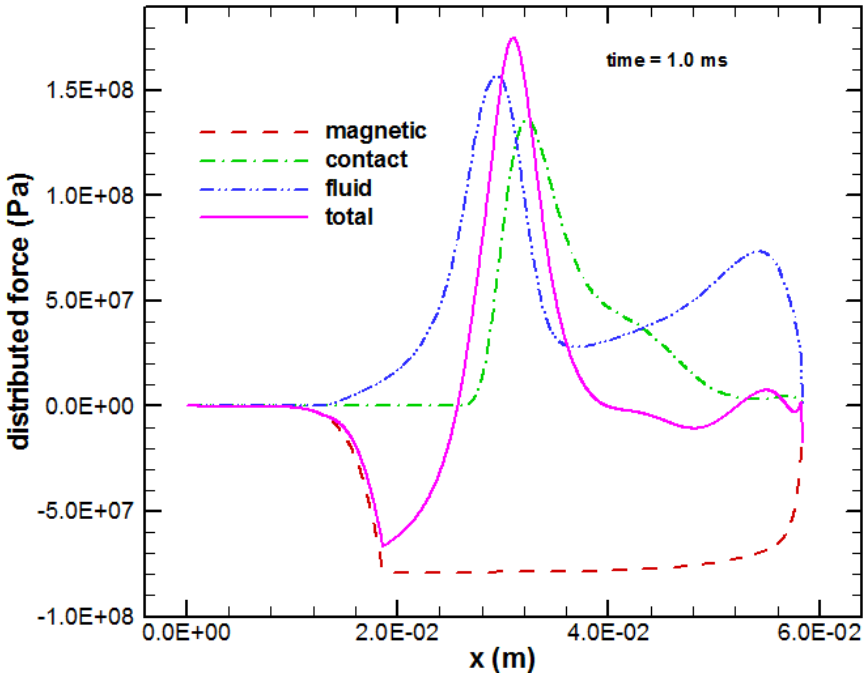

(a)

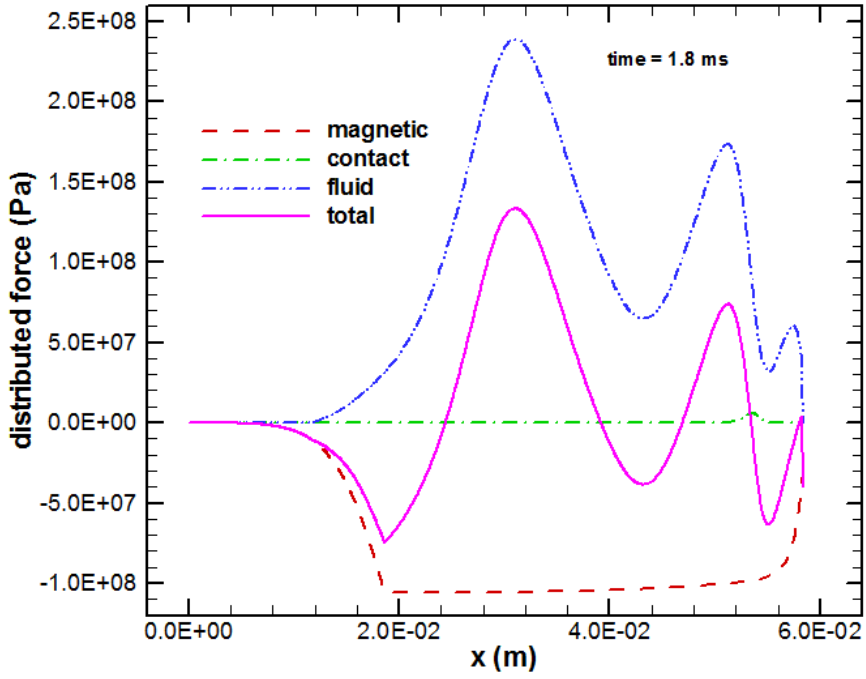

(b)

Figure 3.58: Distributed forces on the armature leg at different times

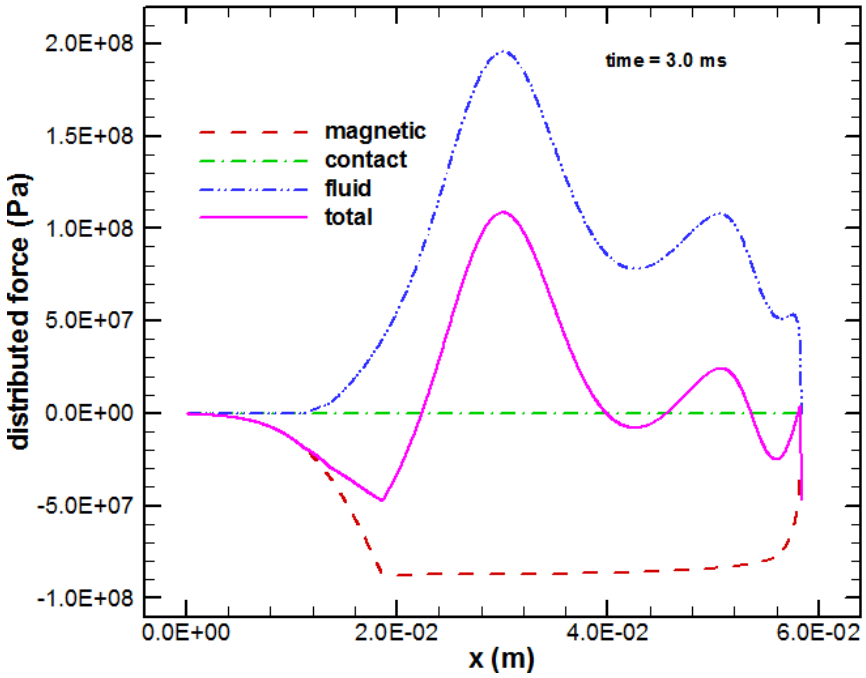

(c)

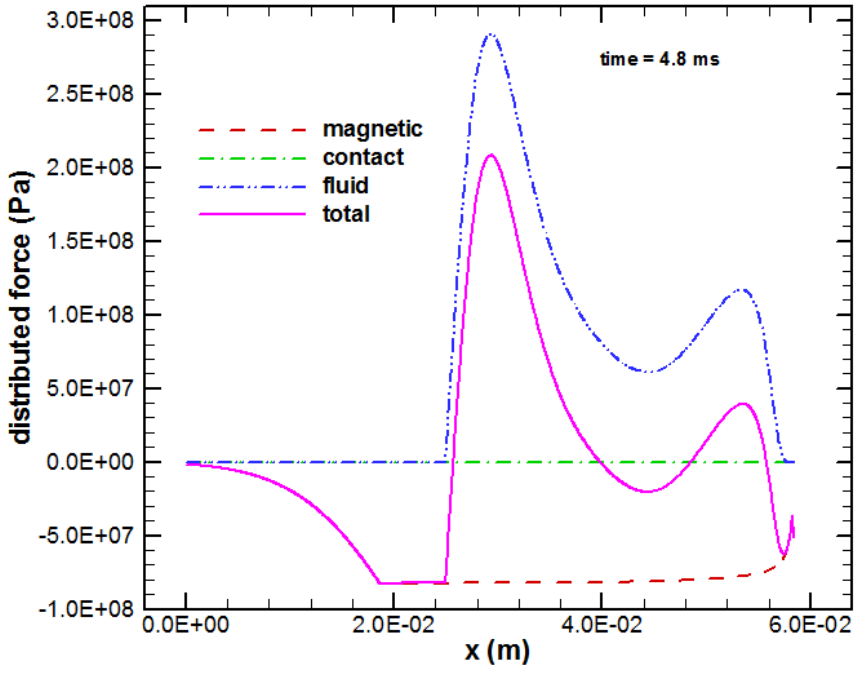

(d)

Figure 3.58 continued

Figure 3.59 shows the nondimensional interface gap. Initially, the contact pressure alone deforms the gap. As the current increases and the shot proceeds the armature is deformed by the forces acting on it resulting in the gap profiles shown. At 3.0 ms the gap is fairly high due to the large fluid pressures. However, at 4.8 ms when the gap begins to empty, there is less area being pushed on by the fluid and the gap height falls.

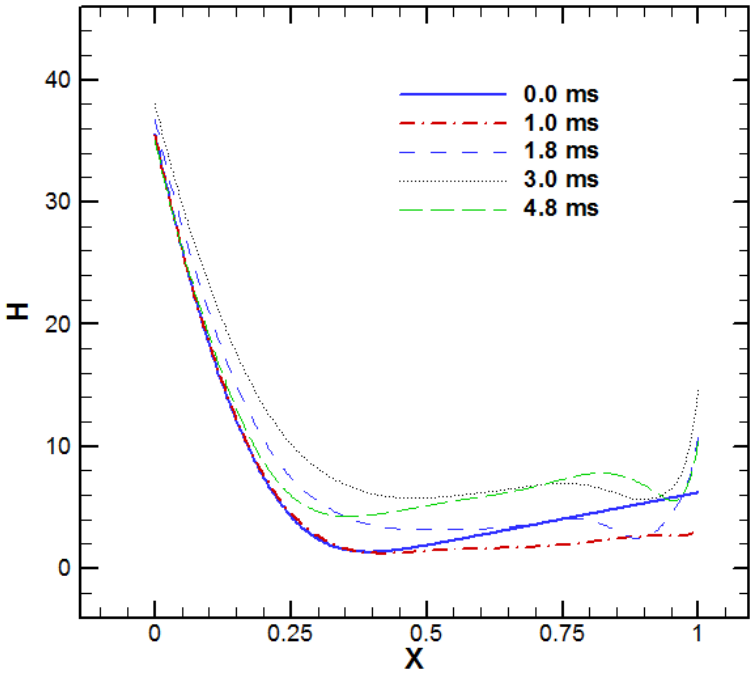

Figure 3.59: Nondimensional interface gap profiles at different times

The lubricant flow patterns in the armature-rail interface for different times are presented in Figure 3.60. The upper boundary of the region is the dimensional form of the gap profiles shown above. As the gap height rises, more lubricant flows out of the trailing edge. After the pocket empties out the interface begins to empty out. At 4.8 ms

it is seen that there is no lubricant flow in the empty portion of the interface. In actuality, there is lubricant flow from the reservoir, however it is mixed with air and difficult to predict. The model accounts for the lubricant being supplied to the interface but does not calculate the flow patterns until it reaches the full portion.

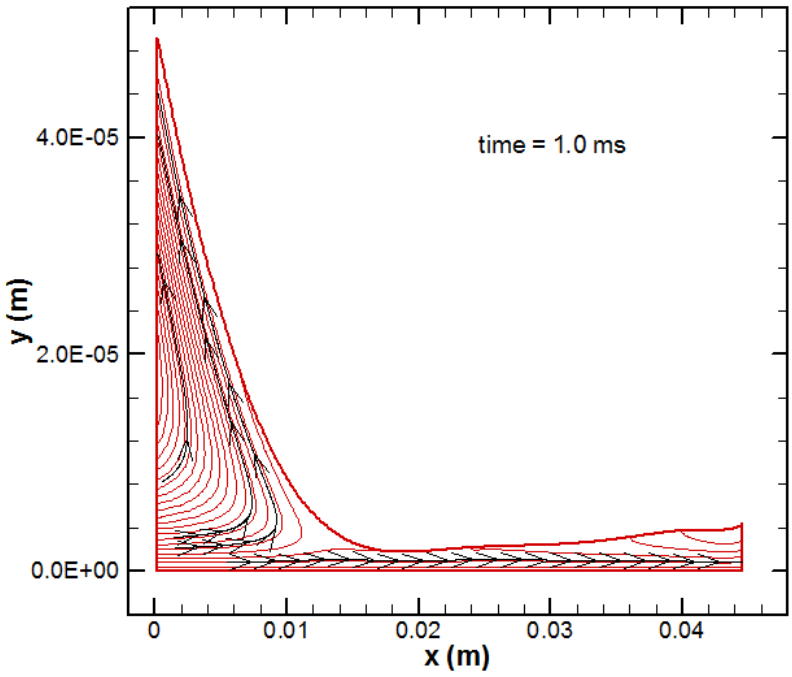

(a)

Figure 3.60: Fluid flow patterns at different times

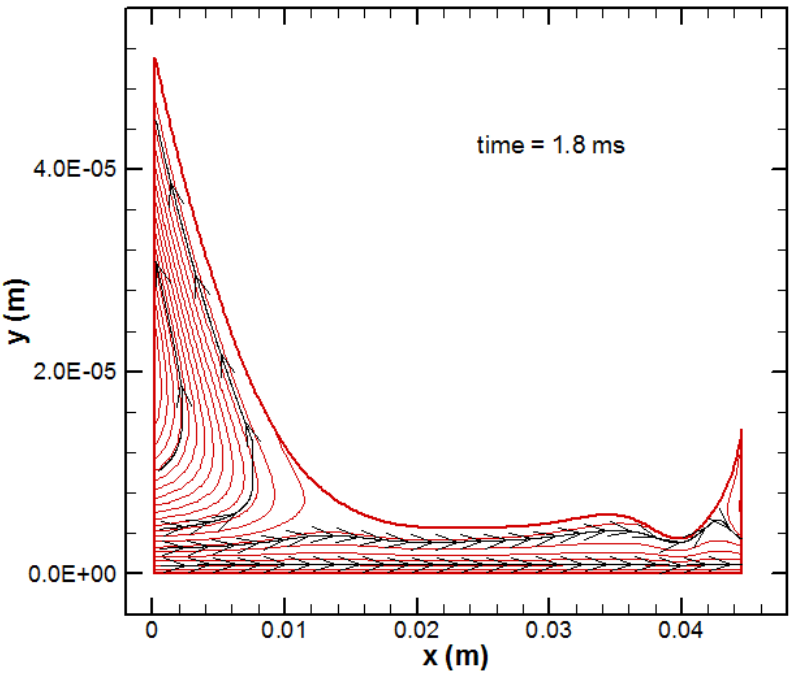

(b)

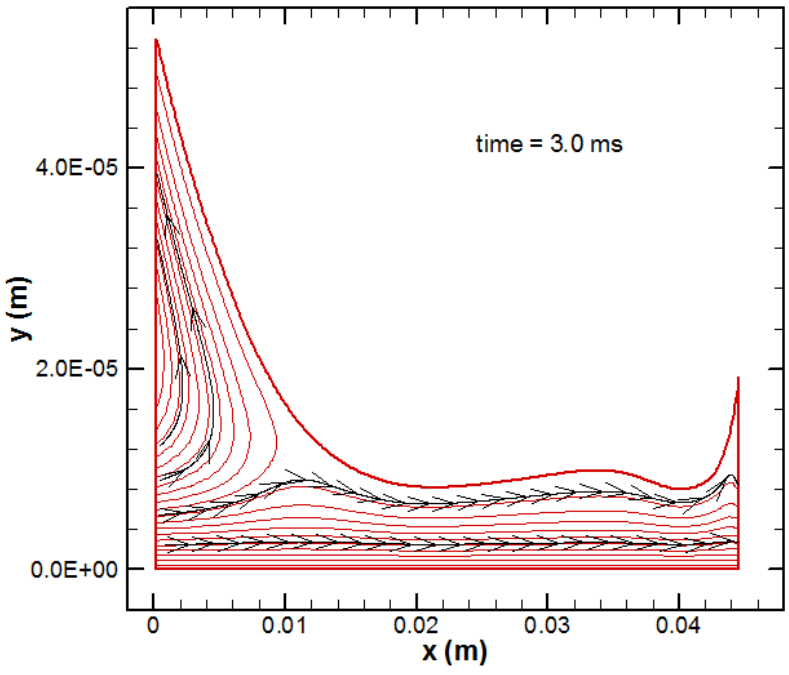

(c)

Figure 3.60 continued

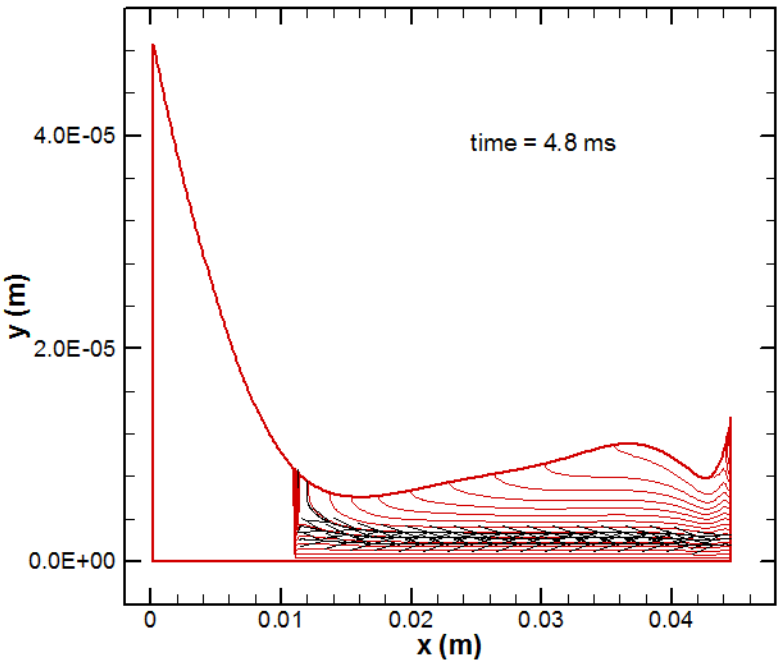

(d)

Figure 3.60 continued

The experimental data collected during NRL shot 223 showed gently increasing muzzle voltage from 3.5 ms to the end of the shot. The muzzle voltage remained under the 100 V which denotes a transition until 4.5 ms. An x-ray of the armature taken as it exited the launcher showed that the reservoirs were still 75 percent full. The simulation results are consistent, since they indicate each reservoir to be about 75 percent full at the end of the shot. The analysis shows that there is too much restriction in the injection conduit to keep lubricant in the pocket towards the end of the shot resulting in a partial dry-out of the interface at about 4.7 ms. The interface gap falls suddenly when it begins to dry out, then slowly recedes as the interface dry-out proceeds. The emptying of the interface most likely accounts for the slowly increasing muzzle voltage observed in the experiment from 3.5 ms to 4.5 ms as the electric current jumps over the empty gap and

the minimum gap heights fall into the solid-solid contact range placing the error in the time of the simulated transition somewhere between 0.2 ms and 1.2 ms. However, it also could mark the actual transition at 4.5 ms and the gradual buildup of muzzle voltage could be a result of an experimental anomaly, meaning the error in the transition prediction is closer to 0.2 ms.

3.3 NRL Shot 406

The armature used for NRL shot 406 is very similar to the armature used for shot 223. The only difference between the two armatures is the injection system. A sketch of the NRL shot 406 armature is shown in Figure 3.61. The injection system for shot 406 uses one reservoir to feed the two pockets using two conduits per pocket. The injection conduits have a diameter of 0.103 in and are perpendicular to the rail in one plane but slanted in a perpendicular plane such that they both meet at the axis of the reservoir. The pockets are almost the same size as those used for shot 223. The cartridge is 2.25 in long with an inner diameter of 0.54 in. The initial charge of gallium lubricant inside the cartridge is 50.4 g. The total mass of the armature and the empty cartridge is 369.58 g. Due to the similarities with the armature used for NRL shot 223 the electromagnetic field, thermal field, and armature deflection modeling is no different for NRL shot 406. Even the same equivalent cantilever beams can be used to calculate the deflection for both armatures. The launcher used for NRL shot 406 uses 7.0 m long rails spaced 1.8 inches apart creating the same interference fit as in shot 223.

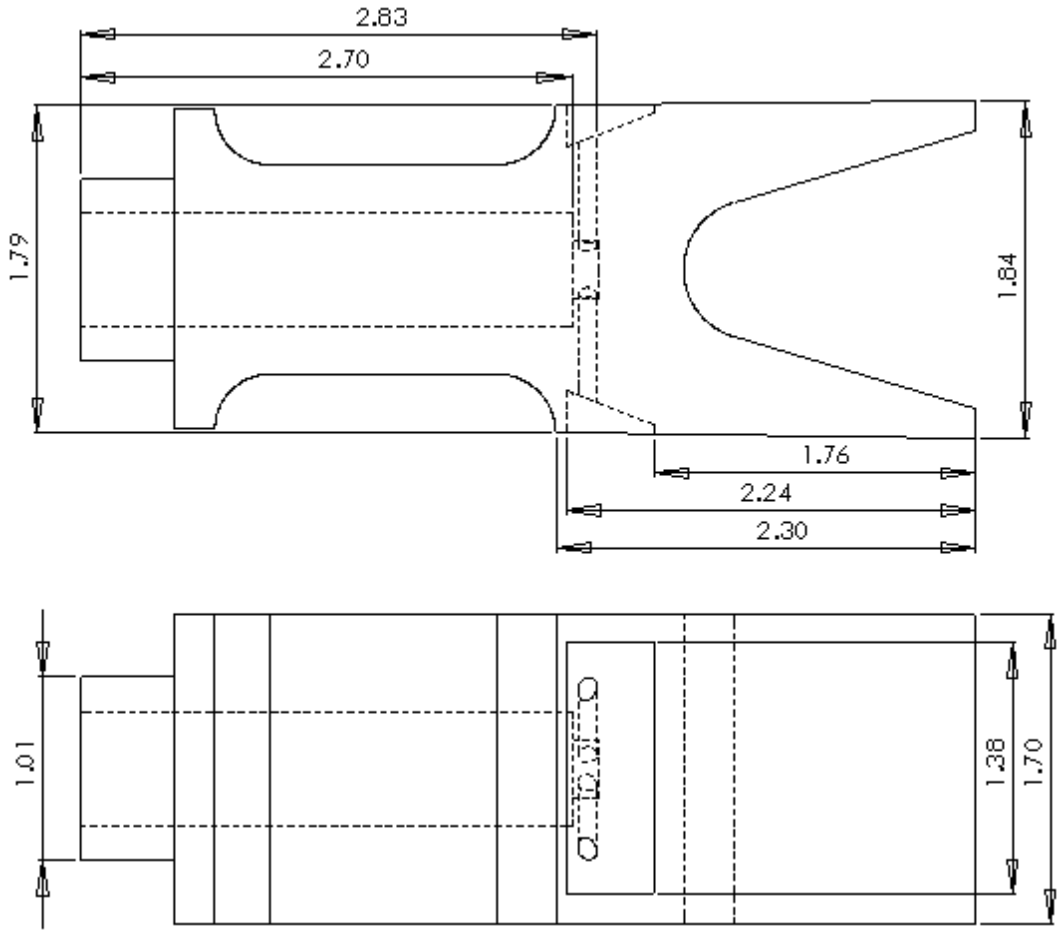

Figure 3.61: Sketch of the NRL shot 406 armature, dimensions are in inches

3.3.1 Lubricant Modeling

The lubricant injection system for NRL shot 406 has a configuration which is different than the previous two armatures. It has only one reservoir like the base case, but has four injection conduits like NRL shot 223. The armature-rail interface is modeled using the same equations and methods as were used for shot 223. However, to calculate the amount of flow going into the pocket from the injection conduits the equation must be derived for the new configuration. Using symmetry, the entire injection system is analyzed by modeling the flow through one conduit. The system is broken into

calculational nodes as shown in Figure 3.62. There is a four outlet tee in the injection system combined with a sharp reduction in diameter as the lubricant flows from conduit D to conduit A. The four outlet tee adds head loss to the system and is approximated by adding the equivalent amount of length normalized by the diameter of a standard tee. Equations 3.30 and 3.31 calculate the pressure at nodes 2 and 3 in terms of the average flow velocity through conduits D and A. Here, the friction factors, f_D and f_A, for conduits D and A are about .017 and .022 respectively and the head loss factors, k_{eD} and k_{eA}, are about 0.4 and 1.48 respectively. Additionally, the equivalent length over diameter added by the tee, k_{tee}, is 30. Four times the amount of lubricant is flowing through conduit D as is flowing through conduit A, therefore, to express flow velocity in terms of flow rate through conduit A, the mass flow rate terms in Equations 3.32 and 3.33 differ by a factor of four. Equations 3.30-3.33 are combined to form Equation 3.34 which can be solved for the mass flow rate of lubricant through conduit A. The pressure at the bottom of the reservoir and at the outlet of conduit A are calculated in the same manner as they were for shot 223.

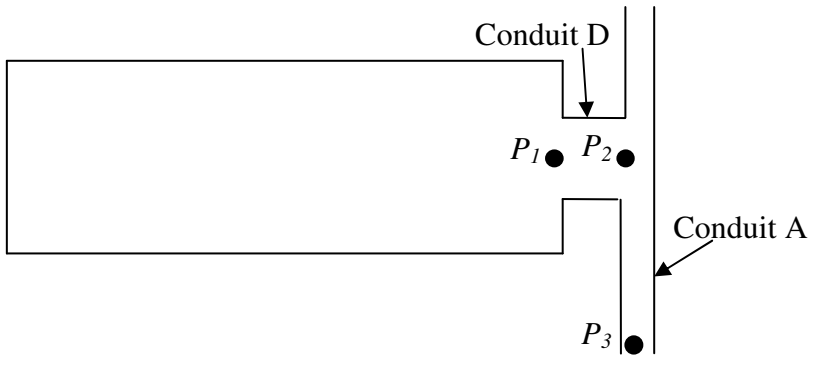

Figure 3.62: Schematic of the NRL shot 406 injection system and node points (not to scale)

$$P_2 = P_1 - \rho\left[\left(f_D\frac{L_D}{2R_D} + k_{eD}\right)\frac{V_D^2}{2} + L_D\frac{\partial V_D}{\partial t}\right] + \rho a L_D - \rho\frac{V_D^2}{2} \tag{3.30}$$

$$P_3 = P_2 - \rho\left\{\left[f_A\left(k_{tee} + \frac{L_A}{2R_A}\right) + k_{eA}\right]\frac{V_A^2}{2} + L_A\frac{\partial V_A}{\partial t}\right\} + \rho\frac{V_D^2}{2} - \rho\frac{V_A^2}{2} \tag{3.31}$$

$$V_D = 4\frac{\dot{Q}}{\rho\pi R_D^2} \tag{3.32}$$

$$V_A = \frac{\dot{Q}}{\rho\pi R_A^2} \tag{3.33}$$

$$\begin{aligned}&\left\{\frac{8}{\rho\pi^2 R_D^4}\left[f_D\frac{L_D}{2R_D} + k_{eD}\right] + \frac{1}{2\rho\pi^2 R_A^4}\left[f_A\left(k_{tee} + \frac{L_A}{2R_A}\right) + k_{eA} + 1\right]\right\}\dot{Q}^2 \\ &+\left(\frac{4L_D}{\pi R_D^2 dt} + \frac{L_A}{\pi R_A^2 dt}\right)\dot{Q} - \left(\left(\frac{4L_D\dot{Q}_{pre}}{\pi R_D^2 dt} + \frac{L_A\dot{Q}_{pre}}{\pi R_A^2 dt}\right) + P_1 - P_3 + \rho a L_D\right) = 0\end{aligned} \tag{3.34}$$

The 7.0 m long rails used in the launcher for shot 406 are manufactured in two pieces and joined with a lap joint. It has been found through experimental data that a transition occurs at the joint. It has also been observed that there is lubricant leaking from the joint when the shot is complete. The joint occurs 2.8 m from the beginning of the rails and leaves a gap of 0.019 in across the width of the rail as shown in Figure 3.63.

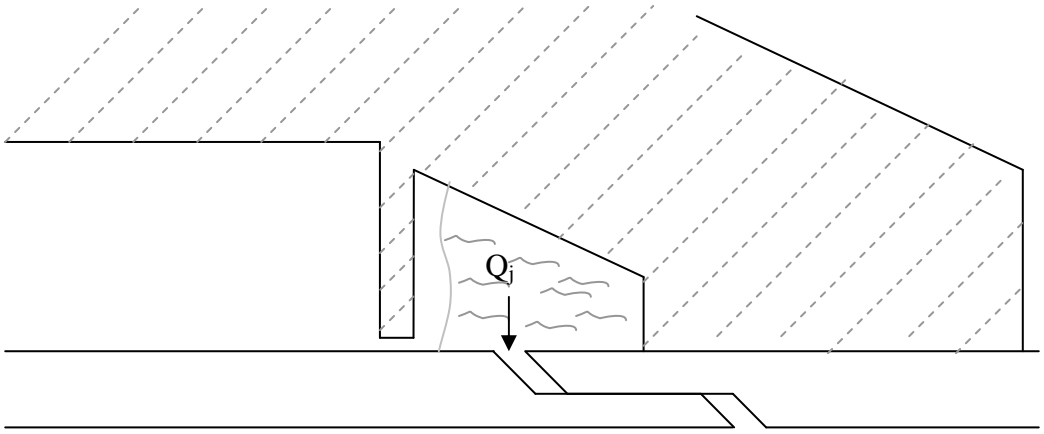

Figure 3.63: Schematic of the armature passing over the joint (not to scale)

To account for the lubricant lost through the joint, it is modeled as an orifice. For this rough approximation, only the lubricant leaked through the joint while the pocket passes over the gap is considered. Analyzing the lubricant leaked while the joint is passing over the rest of the interface would require a re-derivation of the Reynolds Equation to include the leakage term. However, it is assumed that due to the small gap height at the trailing edge of the pocket and the short duration of time that the joint will take to reach the trailing edge, the majority of the lubricant leaked through the joint is leaked from the pocket directly. The equation for the mass of lubricant which flows through an orifice is Equation 3.35. In the simulation when the armature reaches the joint, the pressure difference over the modeled orifice is averaged from the leading edge to the trailing edge of the pocket with the pressure on the outside of the orifice being atmospheric. The average pressure difference is then used as the quantity P_1- P_2. The orifice flow factor, k_o, is assumed to be 0.62. The area of the orifice, A_t, is calculated by multiplying the 0.019 in gap by the width of the pocket into the page. The duration the joint is within the filled portion of the pocket is found by dividing the pocket length by

the armature velocity. The resulting mass of lubricant is subtracted from the net mass of lubricant inside of the pocket.

$$Q_j = k_o A_T t \sqrt{\rho(P_1 - P_2)} \tag{3.35}$$

3.3.2 Results and Discussions

The same model that was used to analyze NRL shot 223 is used for NRL shot 406 with the modifications made to the lubrication system and the addition of a model for the joint, where the two parts of the rail meet. The muzzle voltage for the shot is shown in Figure 3.64. The shot transitions at about 3.3 ms, which corresponds to the time at which the armature reaches the joint. The shot ends at about 4.7 ms which is marked by the large spike in muzzle voltage as the armature leaves the launcher and breaks the current path between the rails.

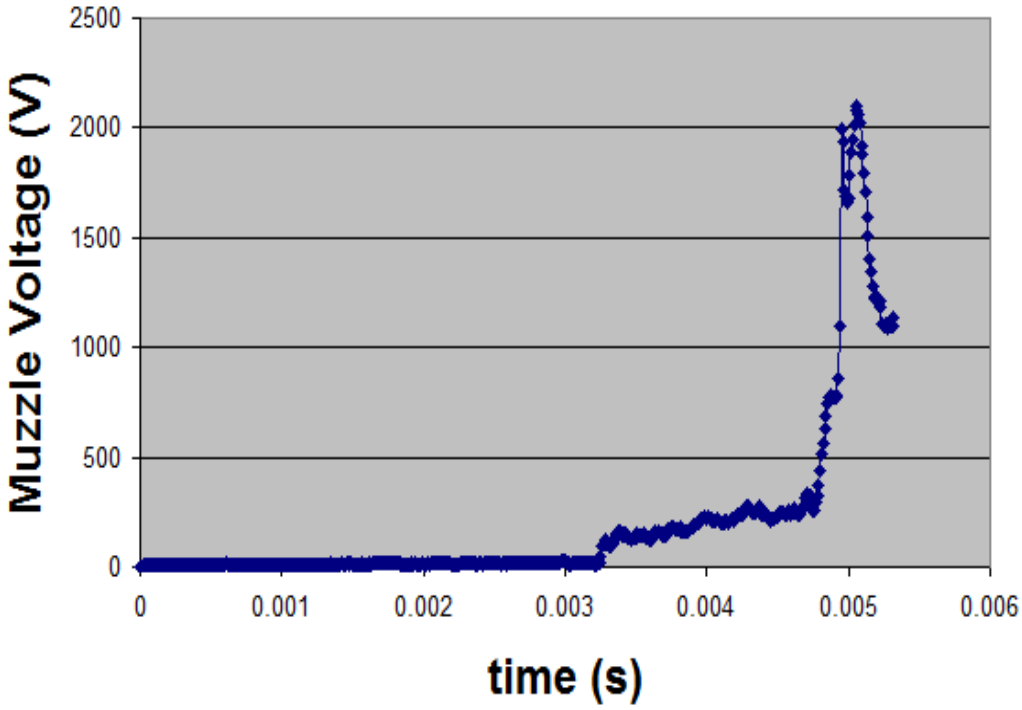

Figure 3.64: Experimental muzzle voltage

The electric current history for this shot is presented in Figure 3.65. The shape of the current history is nearly parabolic. However it is skewed toward the beginning of the shot. The capacitors are fired closer together in this shot as it only lasts 4.7 ms compared to shot 223 which lasted 6.0 ms. The current reaches a maximum of almost 1.4 MA at about 1.5 ms into the shot. This is slightly higher and sooner than the maximum for shot 223. By the end of the shot the current is still about 640 kA at 4.7 ms.

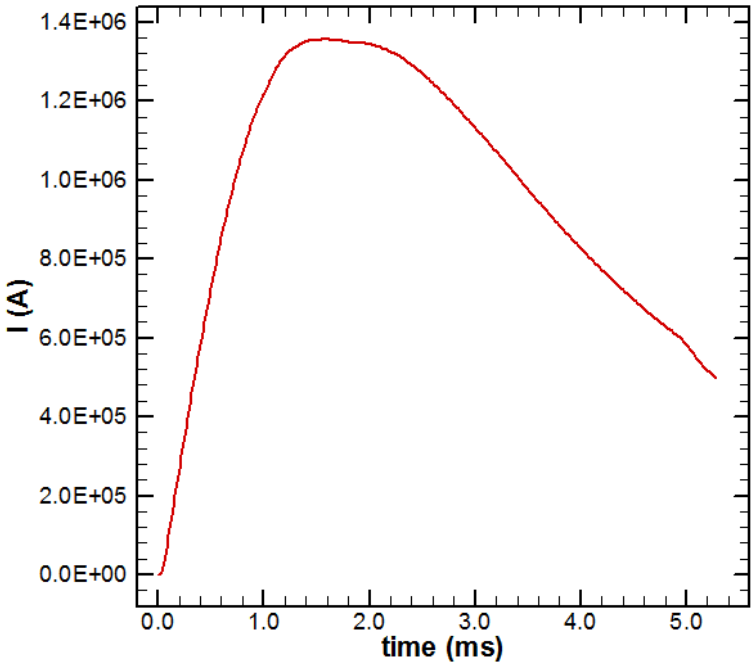

Figure 3.65: Electric current history

The magnetic flux density calculated is highly dependent on the current being passed though the railgun. Figure 3.66 shows the magnetic flux densities calculated at various times. Towards the beginning of the shot, the current rises so rapidly that even at 0.5 ms the magnetic flux densities have already reached values of about 9.0 T. The peak values of magnetic flux of 18.0 T occur at 1.5 ms coinciding with the peak current. The magnetic flux density declines slowly after the maximum is reached and is still above one half the peak values near the end of the shot.

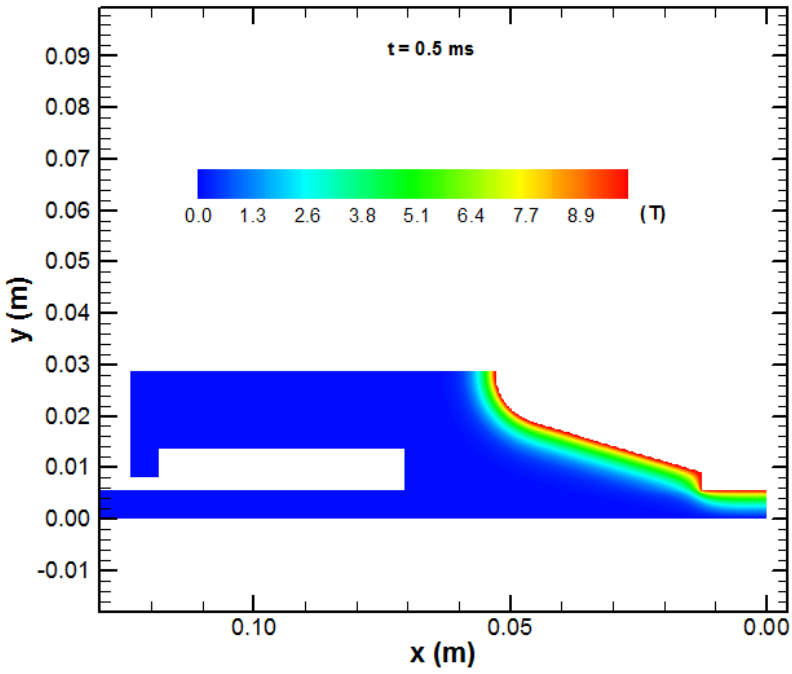

(a)

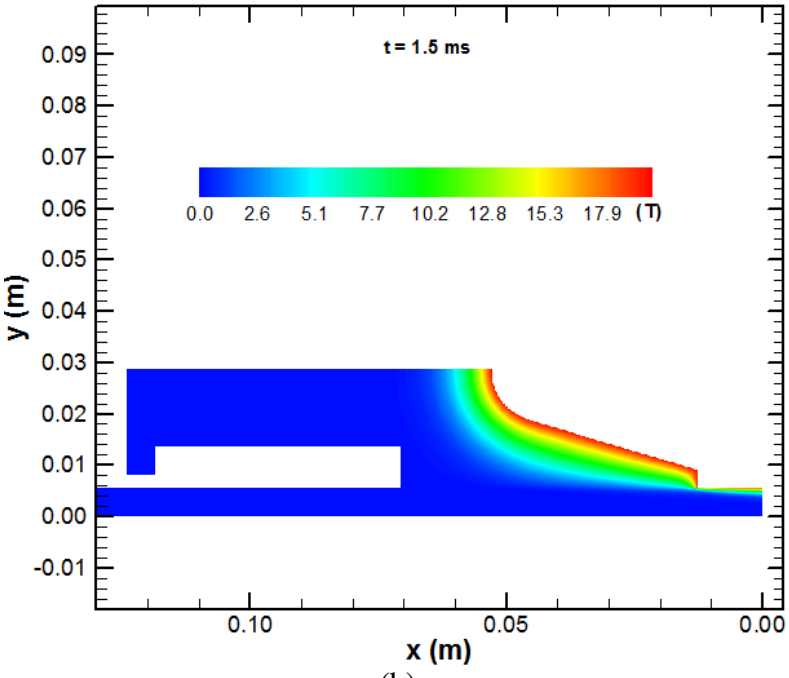

(b)

Figure 3.66: Magnetic flux density distribution at different times

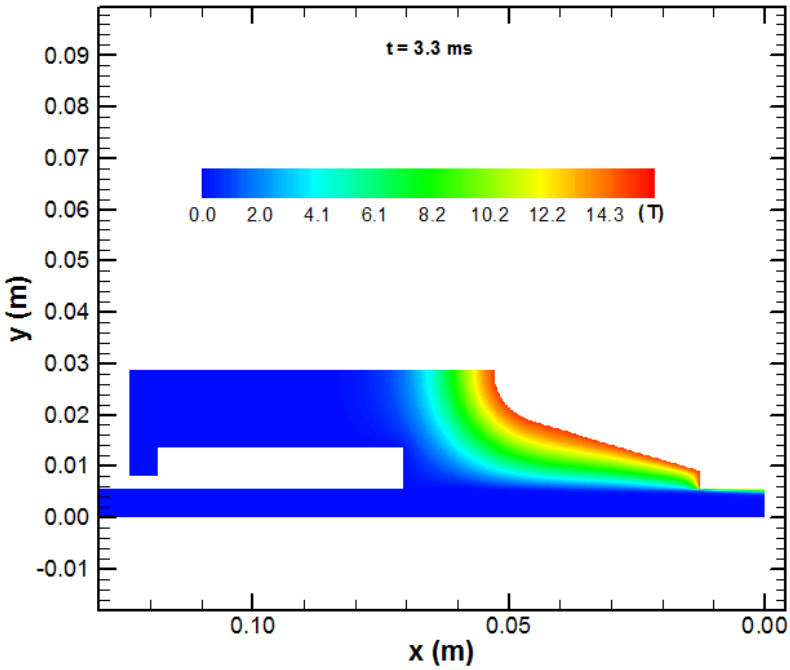

(c)

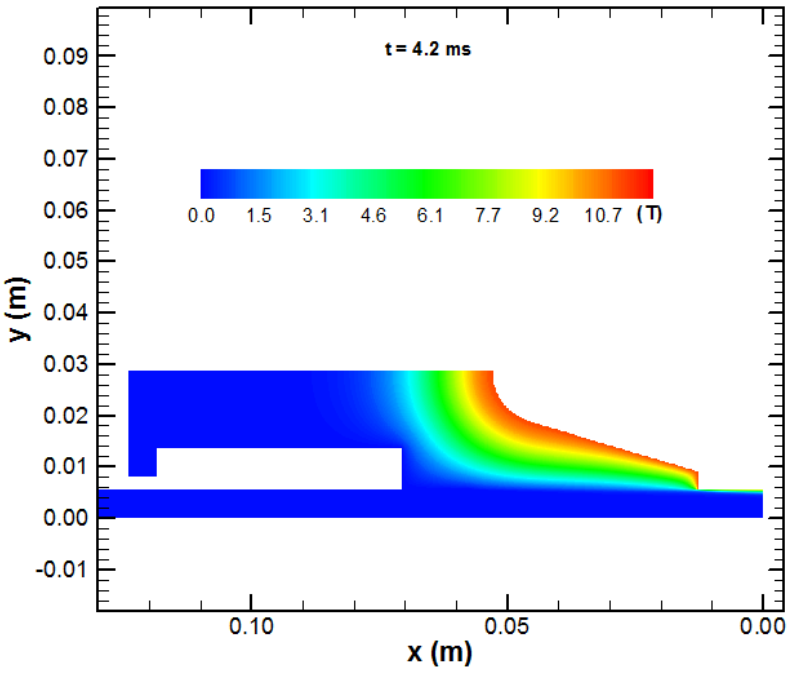

(d)

Figure 3.66 continued

Figure 3.67 illustrates the electric current densities inside the armature. The electric current is concentrated on the trailing edges of the armature along the boundary between the armature and the air. After the maximum current is reached, the velocity skin effect pulls the current density toward the trailing edge of the interface. By the end of the shot, the current density is almost entirely concentrated at the trailing edge of the interface.

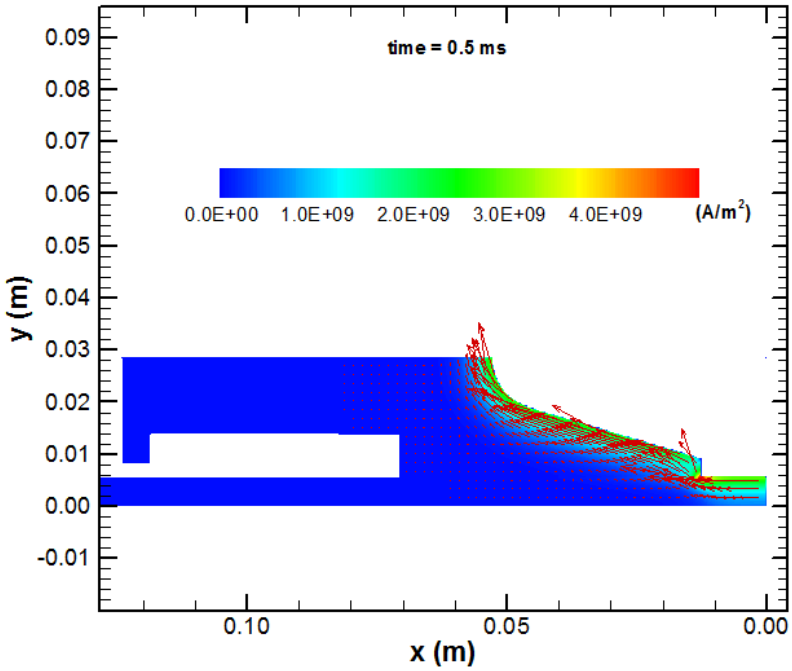

(a)

Figure 3.67: Electric current distribution at different times

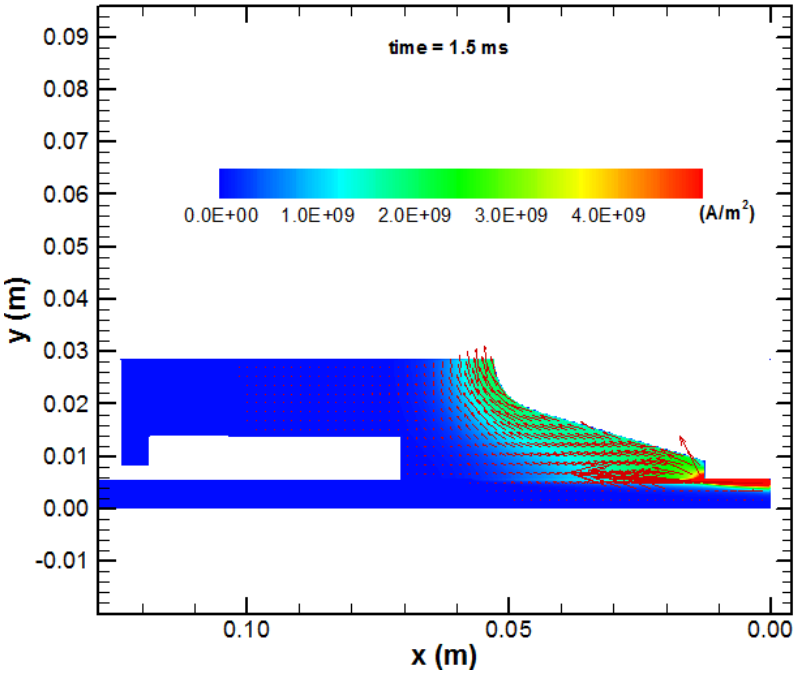

(b)

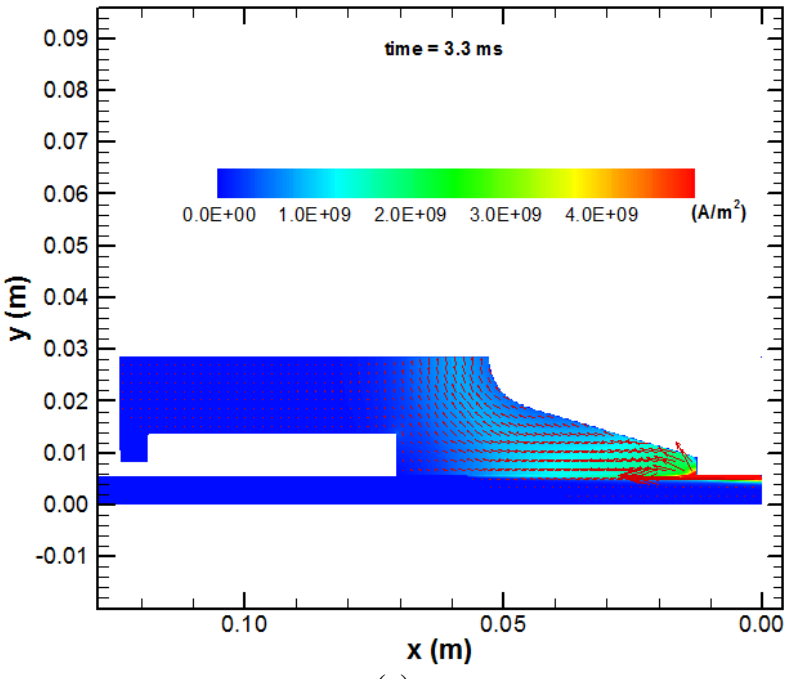

(c)

Figure 3.67 continued

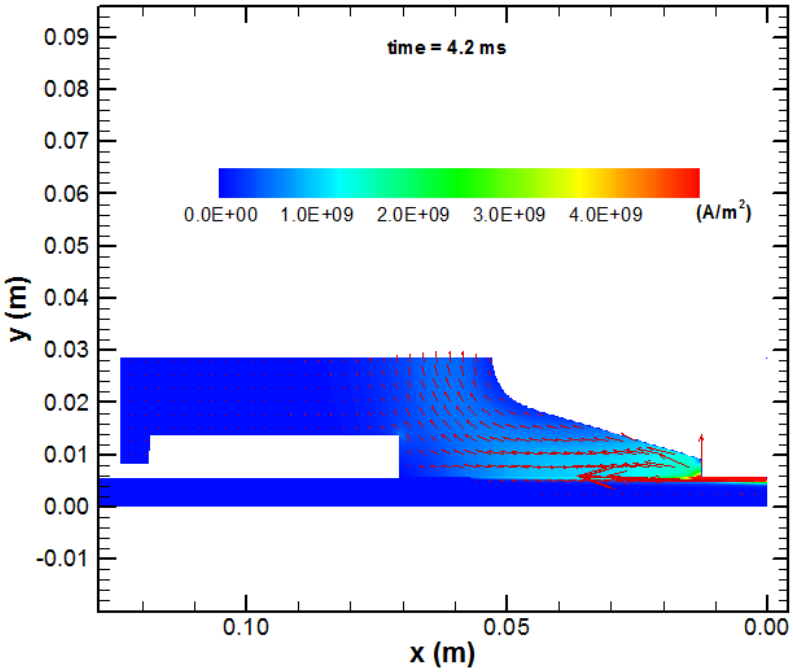

(d)

Figure 3.67 continued

The body forces on the armature are displayed in Figure 3.68. The forces are most concentrated in areas where the magnetic flux density and electric current density are highest. The body forces act to both accelerate the armature along the rails and to pull the armature into the rails indicated by the directional arrows. The magnetic body forces tend to increase quickly and gradually decrease as the shot comes to an end. However, they remain fairly high as the armature reaches the muzzle. The magnitudes of the forces for shot 406 are generally higher than were seen in shot 223 which is due to the higher electric current.

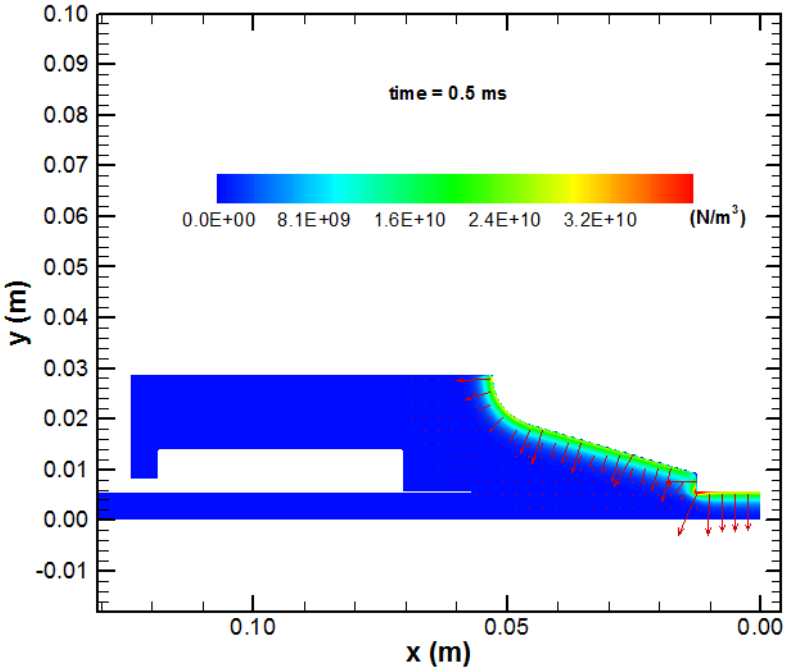

(a)

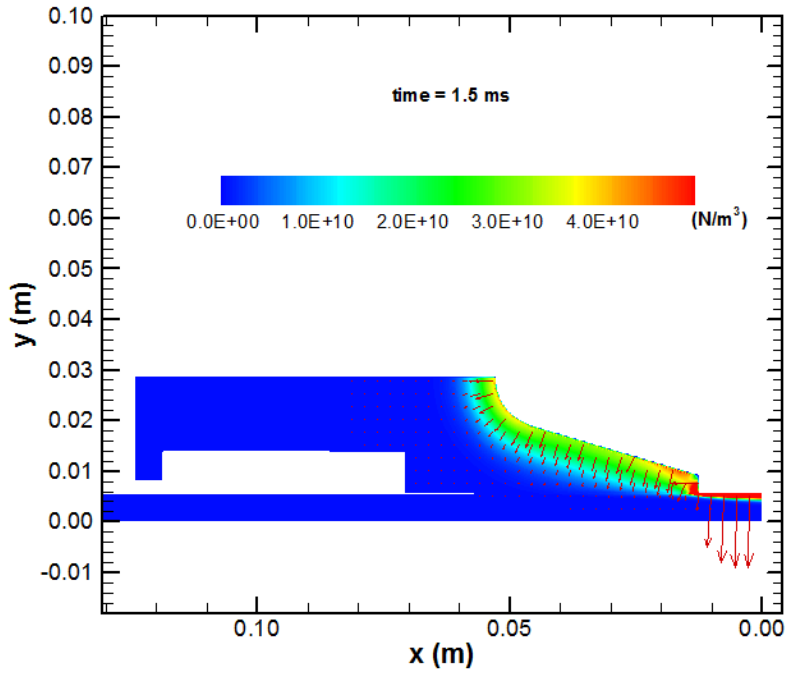

(b)

Figure 3.68: Magnetic body force distribution at different times

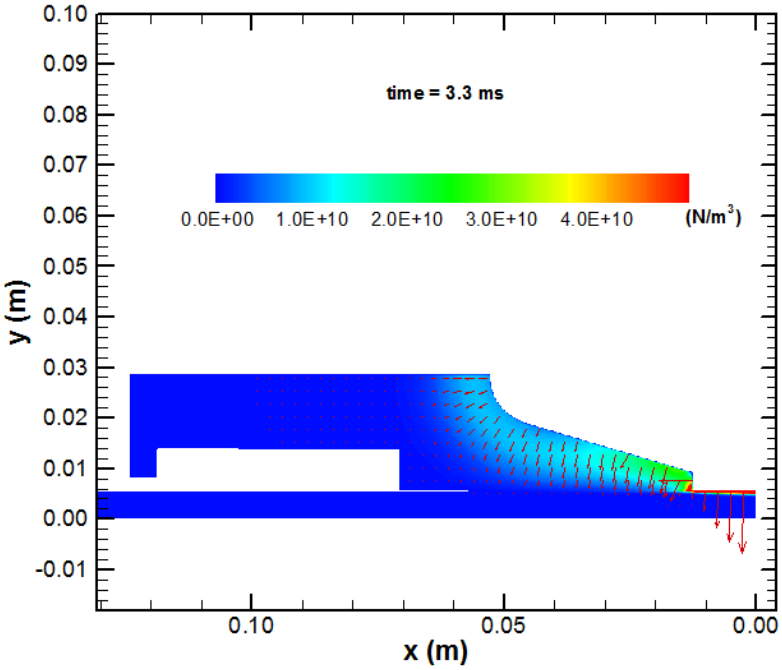

(c)

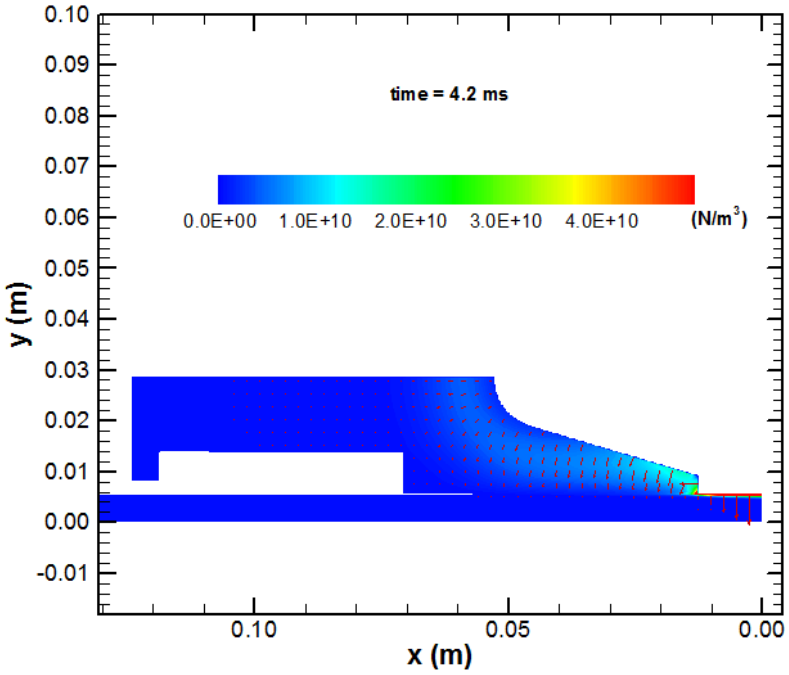

(d)

Figure 3.68 continued

The temperature field is calculated and illustrated in Figure 3.69 for various times into the shot. As was seen with shot 223, the armature-rail interface generates a considerable amount at the beginning of the shot. However, a hot spot develops at the trailing edge of the armature where the highest current densities exist. The temperature in this spot reaches the melting temperature, but the region is small enough that melting is not probable. The other warm region is on the radius in the center of the armature shown by the arrows in Figure 3.69d. This area also has large current densities leading to higher joule heating rates.

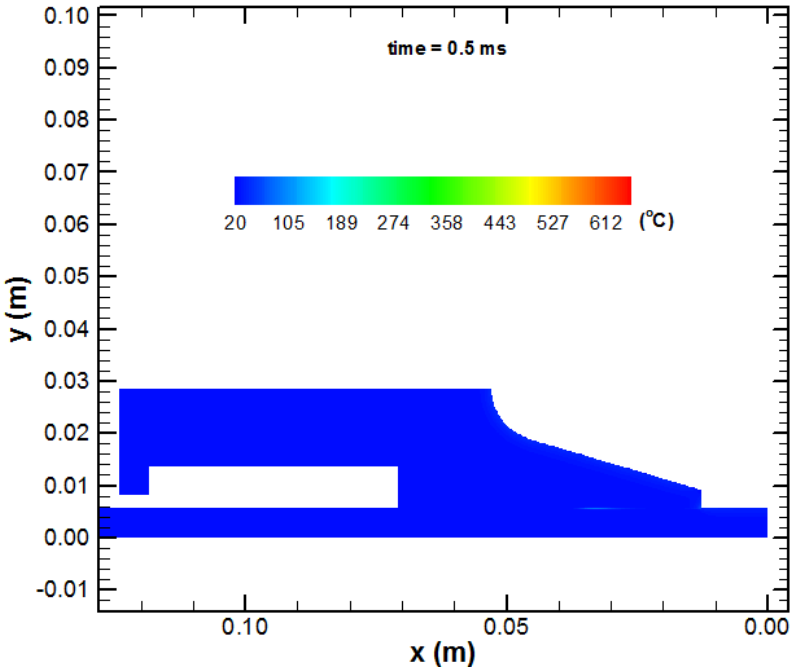

(a)

Figure 3.69: Temperature distribution at different times

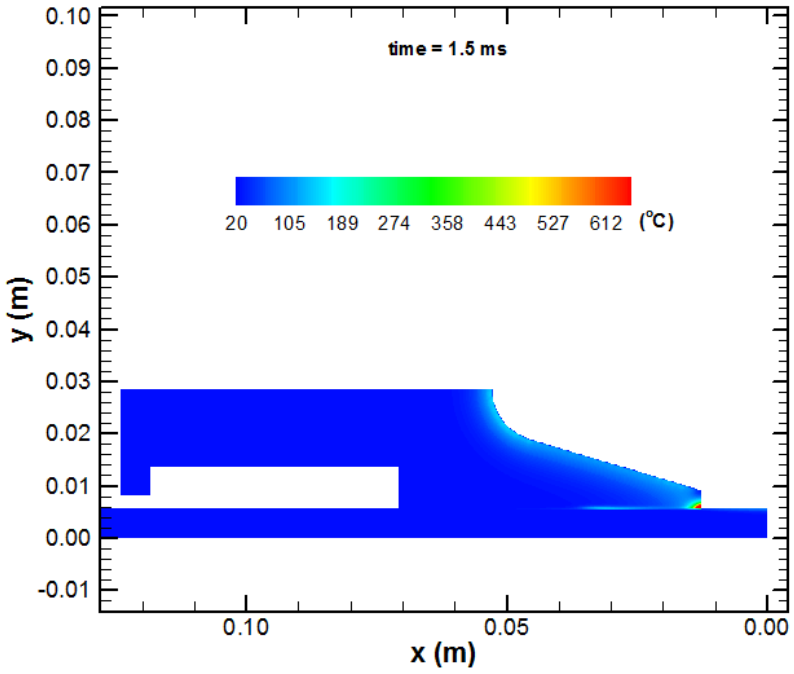

(b)

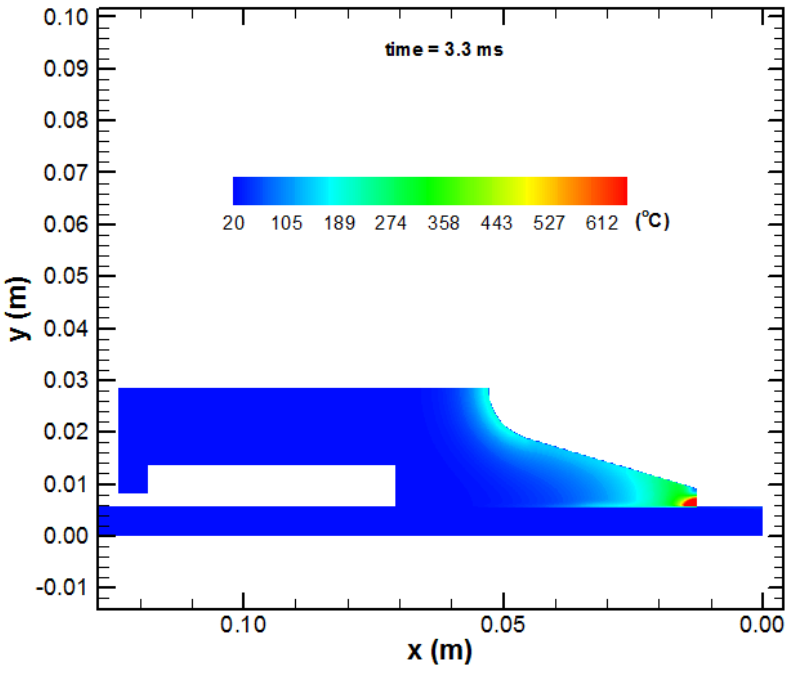

(c)

Figure 3.69 continued

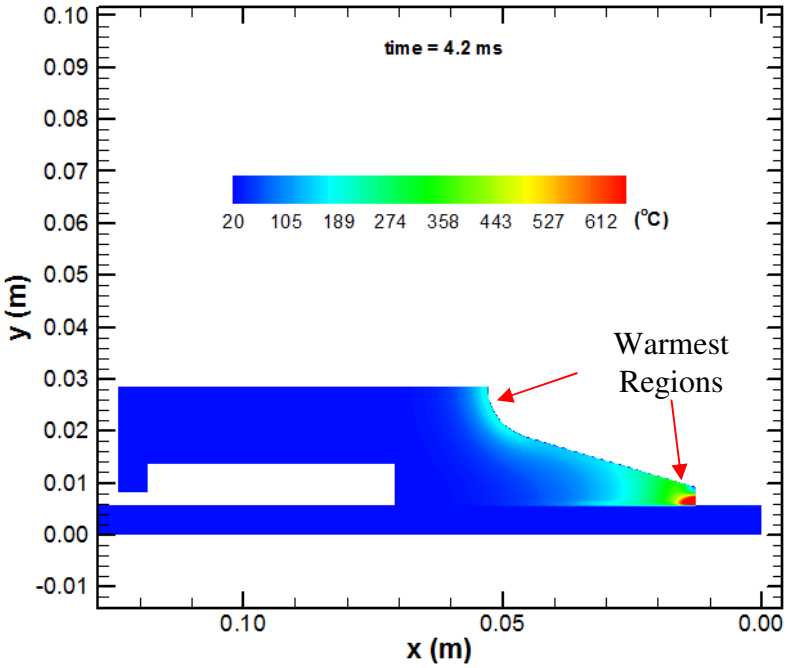

(d)

Figure 3.69 continued

Figure 3.70 shows the net forces acting on the armature in the x direction. Similarly to shot 223, the electromagnetic force, $F_{emag,}$ is almost proportional to the square of the current profile. The maximum net force in the x direction is higher than in shot 223, at over 300 kN occurring at about 1.5 ms. The frictional and viscous forces, F_f and F_v respectively, are very small for this shot. The total net force acting on the armature, F_{total} is nearly identical to the electromagnetic force due to the small effect of friction and viscous forces.

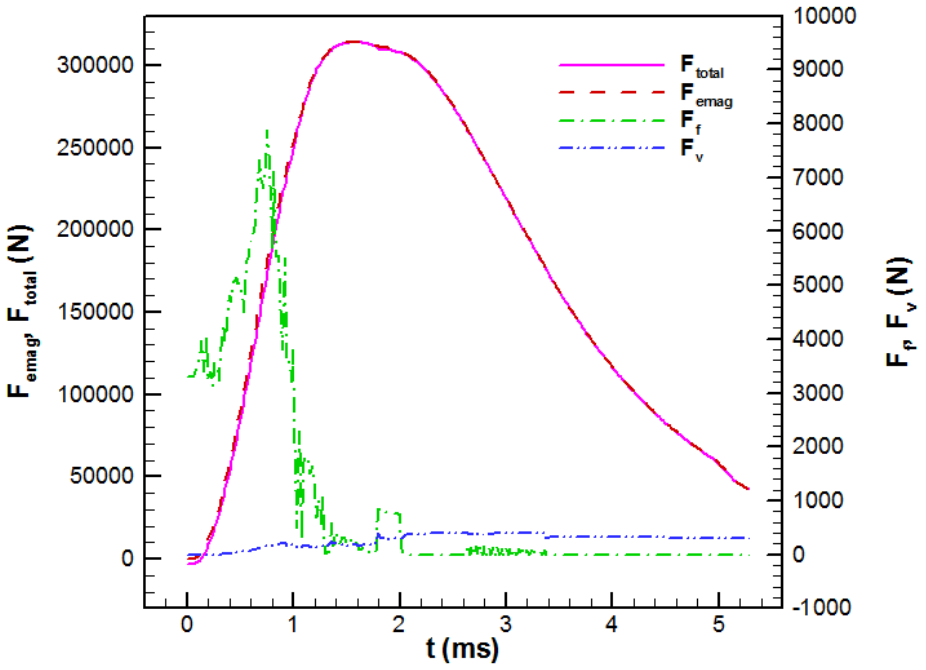

Figure 3.70: *x* direction armature force history

The acceleration of the armature is calculated from the net force in the x direction and the accelerated mass of the armature and any lubricant remaining inside. The acceleration history found is shown in Figure 3.71. The general shape of the profile is parabolic and similar to the shape of the current profile. The acceleration quickly increases to reach a maximum of 750,000 m/s^2 at about 1.5 ms. It then smoothly declines but remains positive as the shot completes.

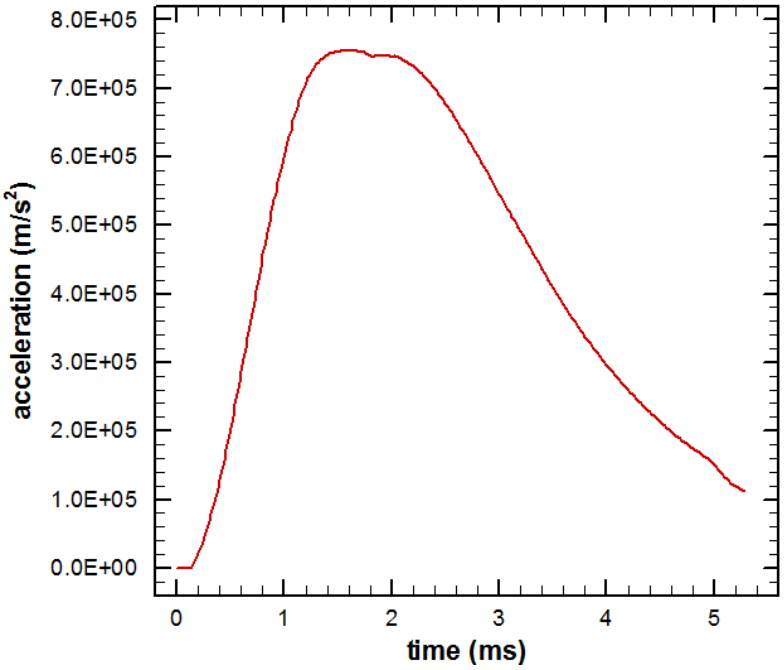

Figure 3.71: Armature acceleration history

The calculated velocity is compared to the armature velocity experimentally observed in shot 406 in Figure 3.72. The numerical results agree very well with the experiment until the experimental transition point at 3.3 ms. After the transition, the model is not valid due to wear, surface damage, and current arcing, however, the numerically predicted velocity is only slightly higher than the experimental velocity after the transition. The armature exits the muzzle of the launcher at a speed of about 2200 m/s at a time of about 4.7 ms. The velocity when the transition occurs is about 1650 m/s. The predicted armature position is very close to the experimentally observed position as presented in Figure 3.73. At the initiation of the shot the armature is located 0.4 m into the launcher, so when it reaches a position of 6.6 m it has reached the muzzle. The transition occurs at a time of 3.3 ms, or when the armature is about 2.4 m from its starting point.

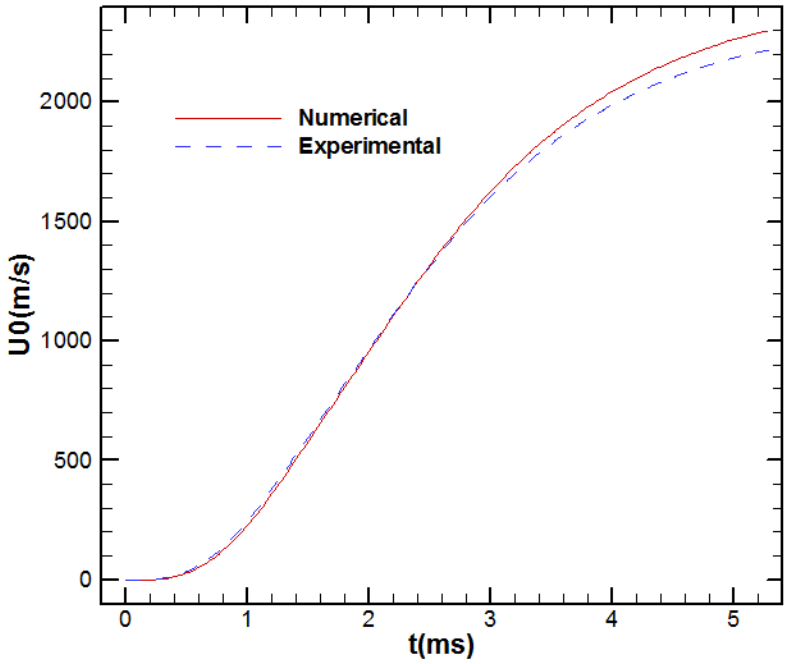

Figure 3.72: Comparison of predicted armature velocity history with experimental measurements

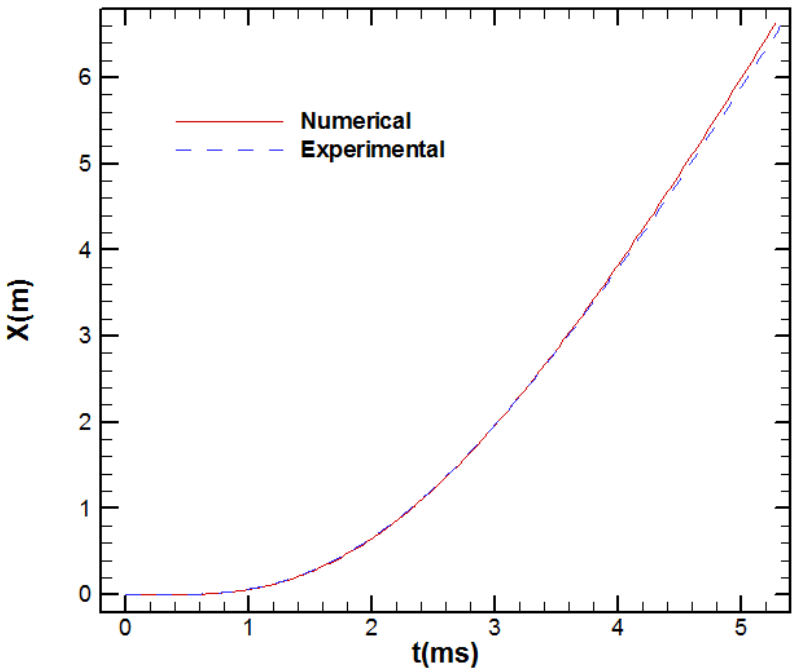

Figure 3.73: Comparison of predicted armature location history with experimental measurements

A history of the amount of lubricant left inside the reservoir, Q_{left} is displayed in Figure 3.74. The reservoir begins with a charge of 50.4 g which is delivered to the pocket as the armature accelerates. At the end of the shot, there is still about 6.0 g of lubricant left in the reservoir. Figure 3.75 illustrates the lubricant consumption history of one pocket. Q_{out} is the amount of lubricant delivered to the pocket, Q_l and Q_r are the amounts leaked from the leading edge and the trailing edge of the pocket respectively, Q_{net} is the amount of lubricant inside the pocket, and Q_j is the amount of lubricant leaked from the joint. The lubricant leaked from the rear of the interface is small compared to the amount supplied from the reservoir at the beginning of the shot. Therefore, the pocket fills at a time of about 1.8 ms and lubricant begins to leak from the leading edge of the pocket. At a time of 3.3 ms the pocket travels over the joint in the rail and looses 0.026 g of lubricant. The lubricant lost from the joint is small enough to be neglected. Around the same time that the armature reaches the joint, the pocket begins to empty. By the end of the shot, there is still about 3.5 g of lubricant inside the pocket. The actual shot transitions when the armature reaches the gap; however, as the figures below show, the transition is not due to a lack of lubrication supplied to the interface.

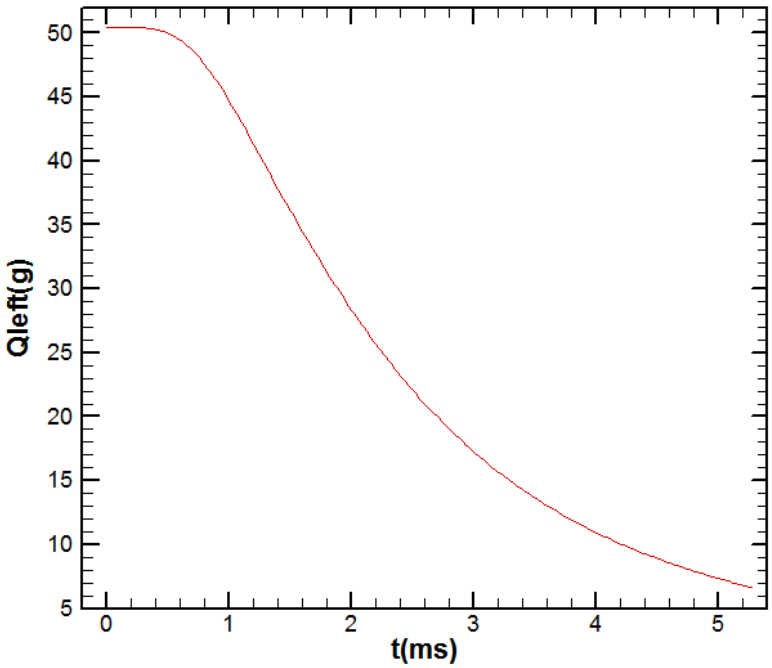

Figure 3.74: History of the amount of lubricant left inside the reservoir.

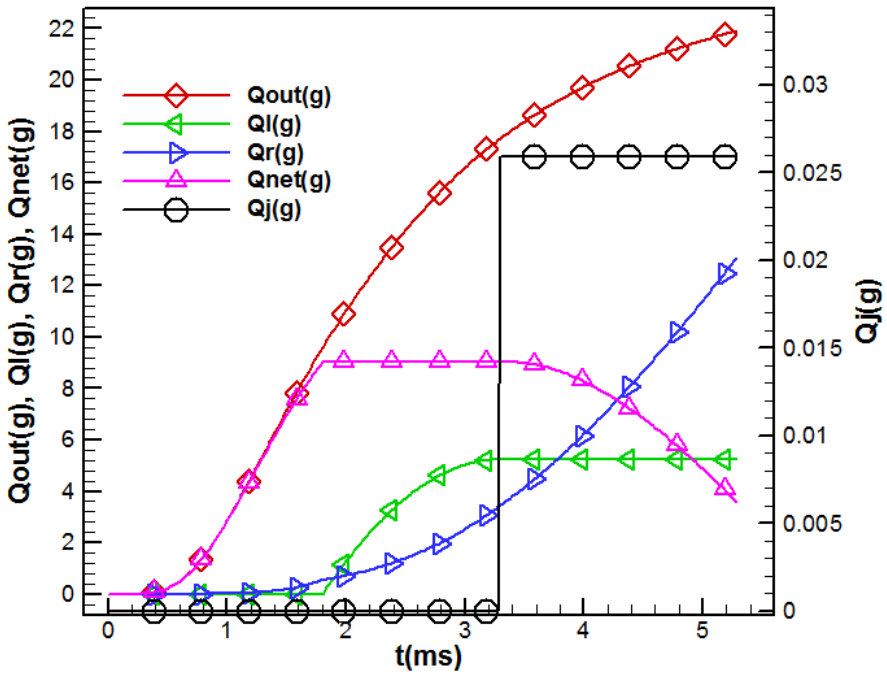

Figure 3.75: Mass flow amount history

The minimum gap height history for the shot is presented in Figure 3.76. The minimum gap height is fairly level at the beginning of the shot. It increases as the armature speeds up. There is a decrease in the minimum gap height predicted when the pocket fills. However, as the armature accelerates, the minimum gap height increases for the rest of the shot. There is no major change to the minimum gap height as the armature passes over the joint at 3.3 ms. By the end of the shot, the minimum gap height reaches about 21 μm.

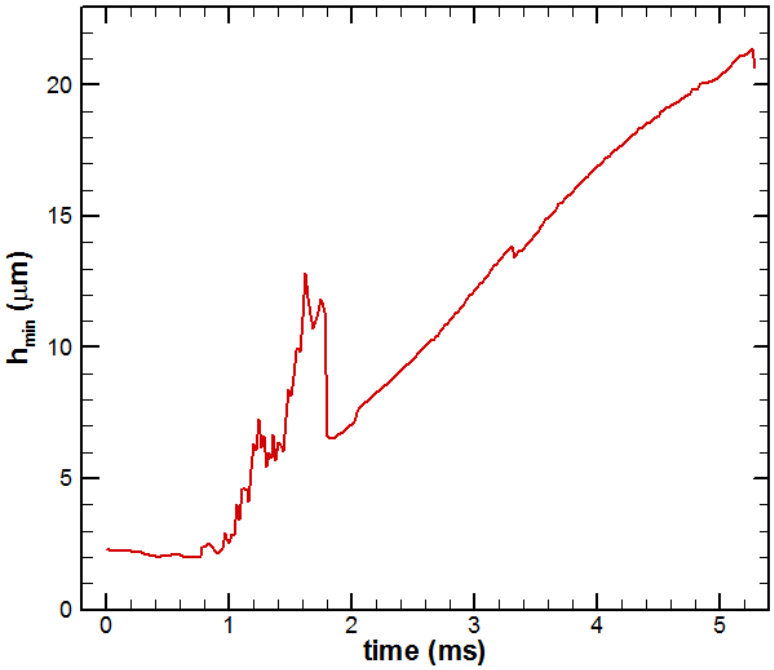

Figure 3.76: Minimum film thickness history

Figure 3.77 displays the lubricant pressures at different times. The magnetic component of the total pressure is only significant at the trailing edge of the interface, where the current and magnetic flux densities are concentrated. The pressure at the

trailing edge of the pocket is sufficient to prevent cavitation even at the beginning of the shot. It can be seen that the boundary condition at the beginning of the interface increases from 0.5 ms to 1.5 ms as the pocket is filling up, then decreases from 3.3 ms to 4.2 ms as the pocket empties.

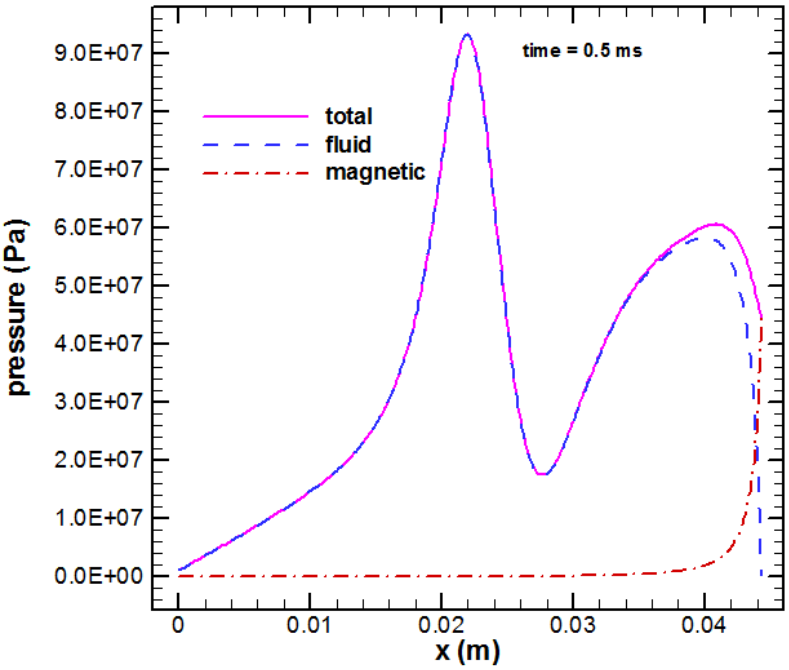

(a)

Figure 3.77: Pressures in the fluid at different times

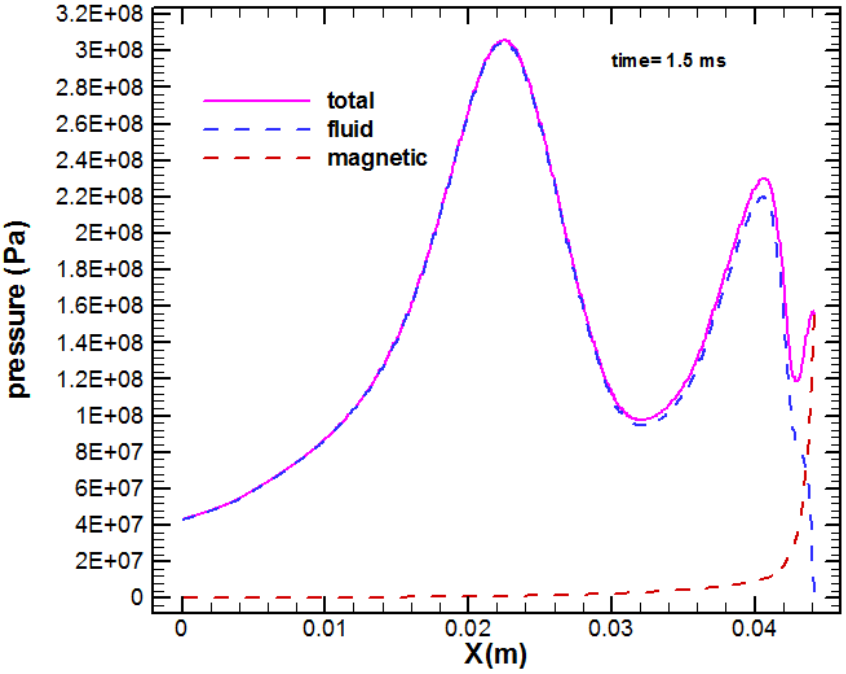

(b)

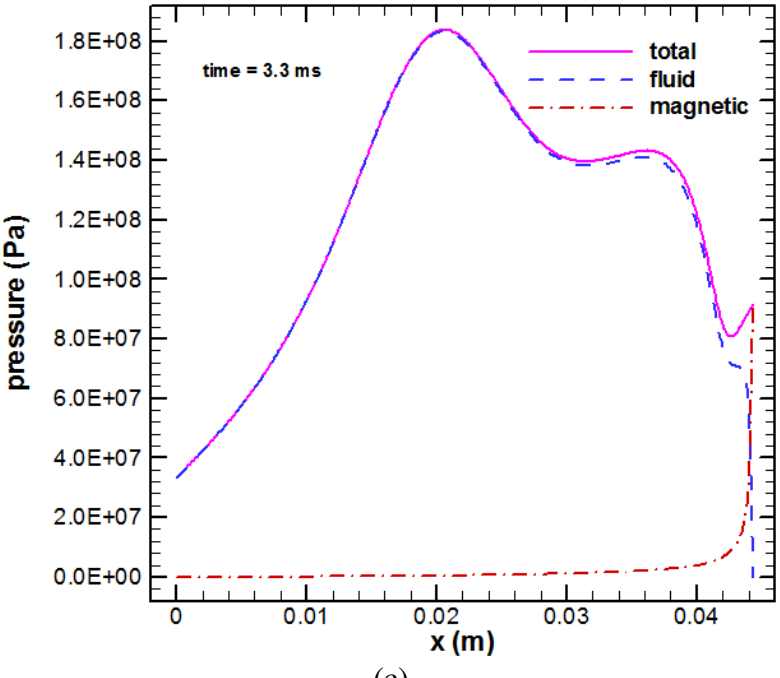

(c)

Figure 3.77 continued

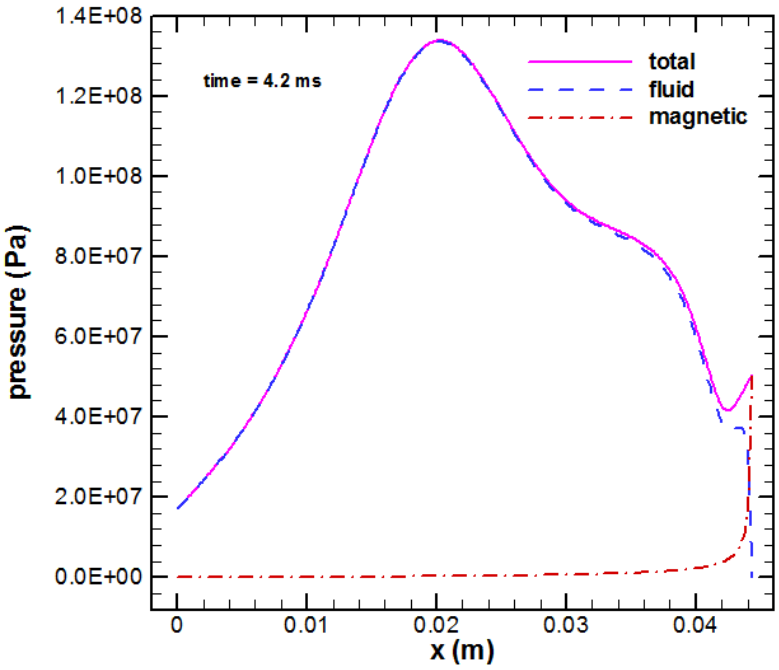

(d)

Figure 3.77 continued

The distributed forces acting on the armature in the transverse direction are displayed in Figure 3.78. The positive forces push the armature away from the rail, while the negative forces pull it closer. The magnetic forces tend to pull the armature into the rail due to the direction of the magnetic body force in the armature. The contact force is high only at the beginning of the shot. As the armature speeds up it is lifted out of contact by the large fluid distributed force. The total distributed force that acts on the armature is the sum of the magnetic, contact, and fluid forces.

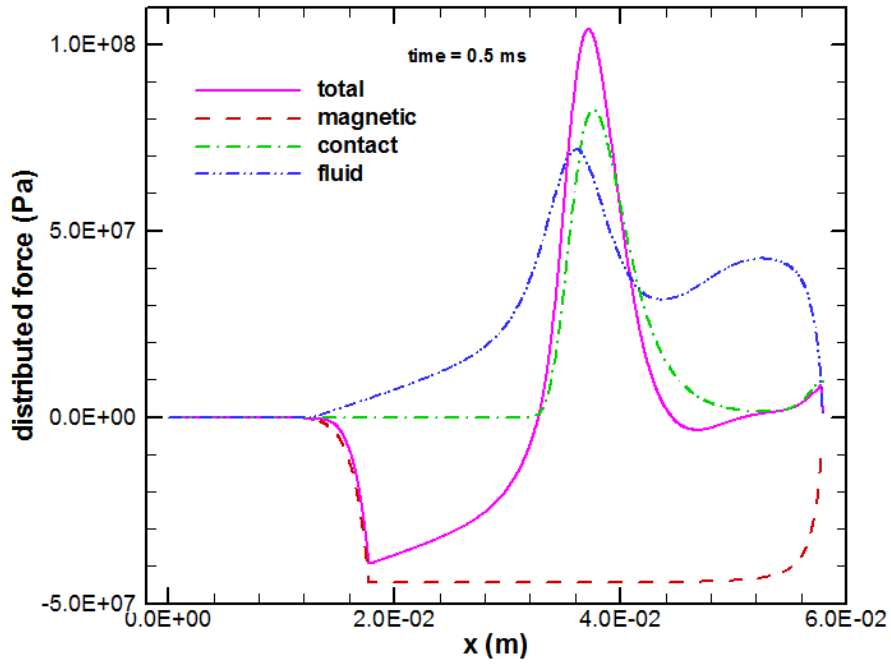

(a)

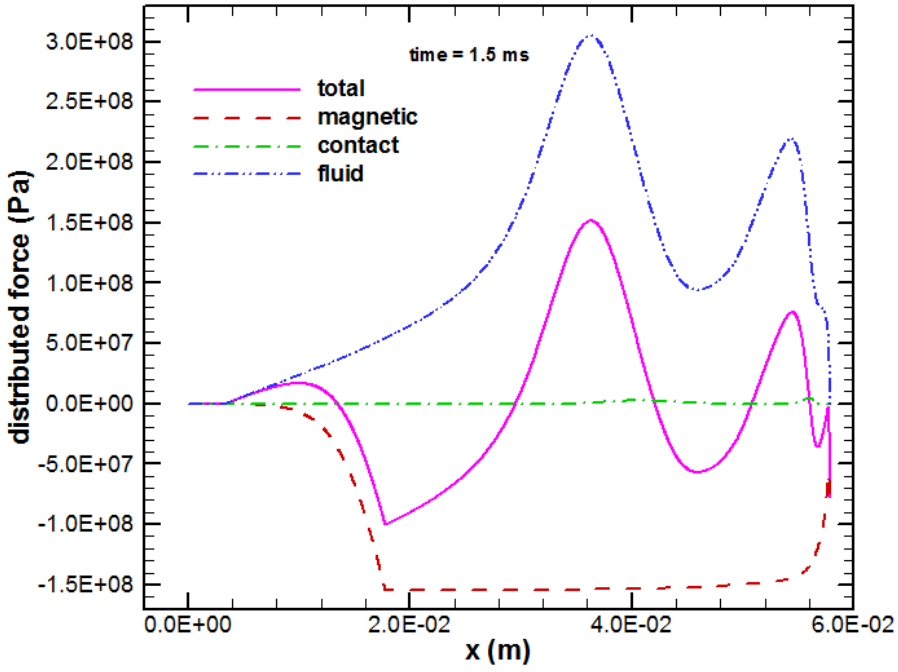

(b)

Figure 3.78: Distributed forces on the armature leg at different times

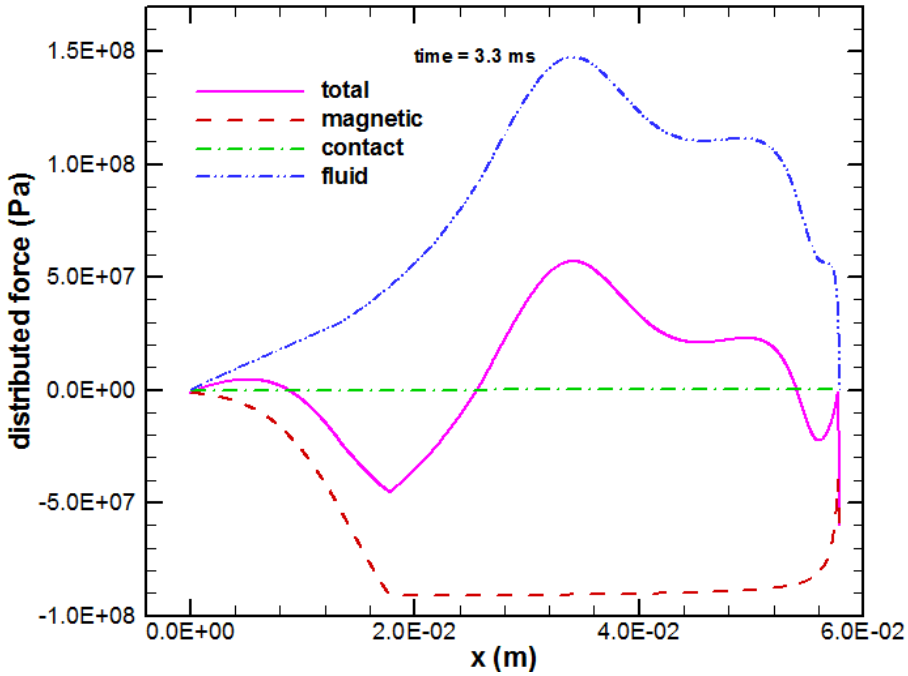

(c)

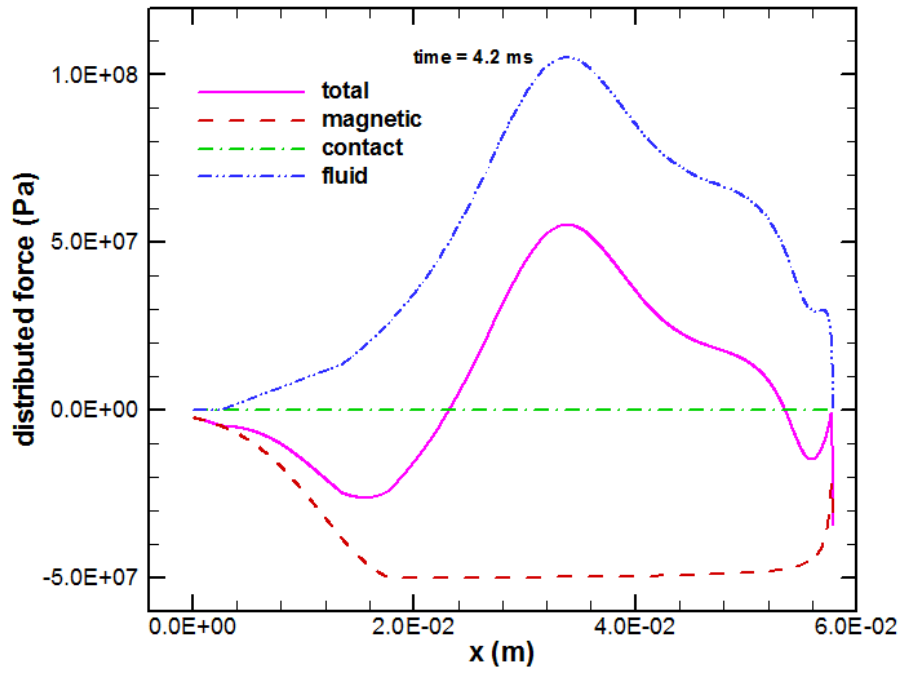

(d)

Figure 3.78 continued

Figure 3.79 illustrates the nondimensional interface gap at various different times. Initially, the contact pressure alone deforms the gap. As the current is applied the armature is deformed by magnetic, thermal, and fluid forces. The gap profile is smooth toward the beginning of the shot. As the shot proceeds the gap height increases in general due to the larger hydrodynamic forces caused by the armature velocity as well as decreasing electromagnetic forces after the maximum current is reached at about 1.5 ms. The gap profiles for NRL shot 406 do not present a geometry which would cause a transition.

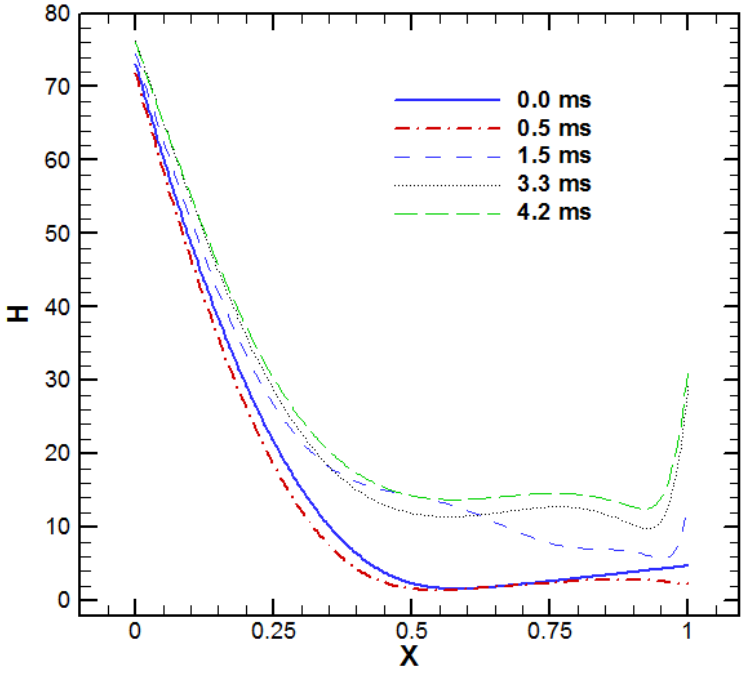

Figure 3.79: Nondimensional interface gap profiles at different times

The lubricant flow patterns in the armature-rail interface for different times are displayed in Figure 3.80. The region is bounded by the rail on the bottom and the armature on the top. The no-slip boundary conditions applied to the armature drag lubricant along the rail. Initially the gap is very small from about 0.02 m to the trailing edge. As the gap height increases, more lubricant is carried towards the trailing edge and leaks from the gap. There is no interface dry-out predicted for this shot.

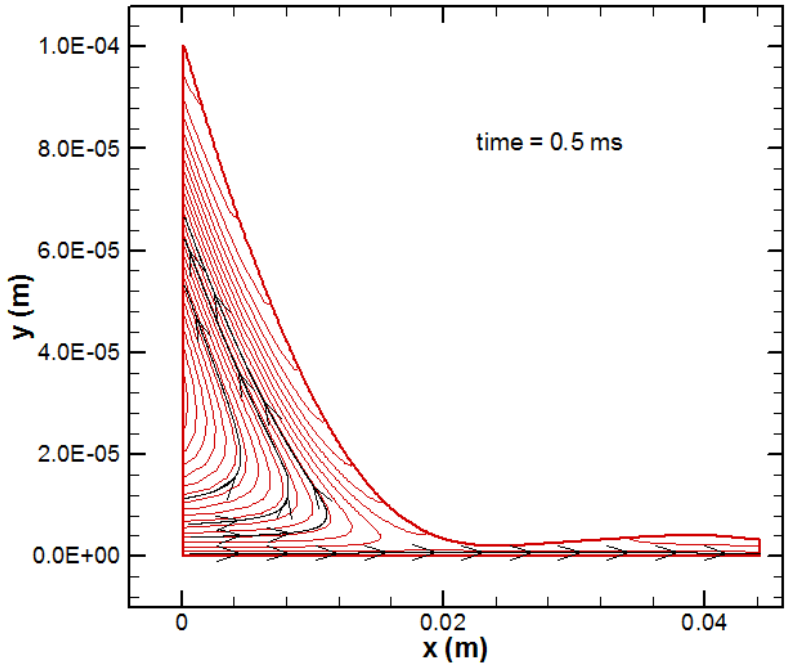

(a)

Figure 3.80: Fluid flow patterns at different times

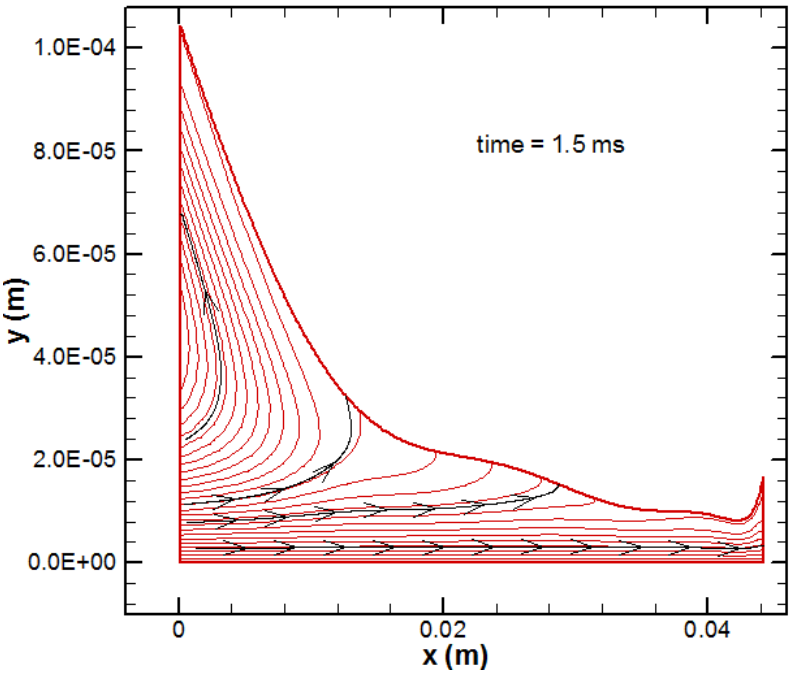

(b)

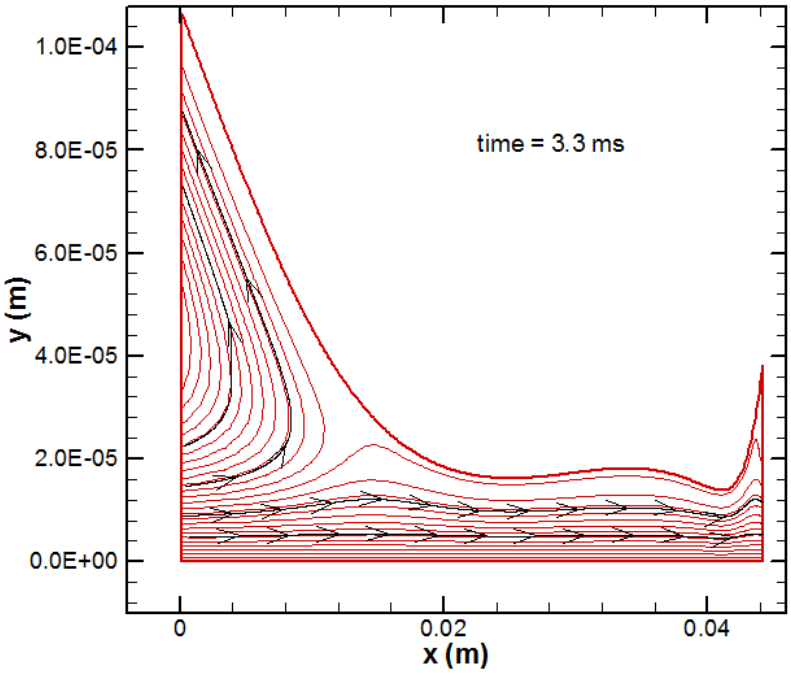

(c)

Figure 3.80 continued

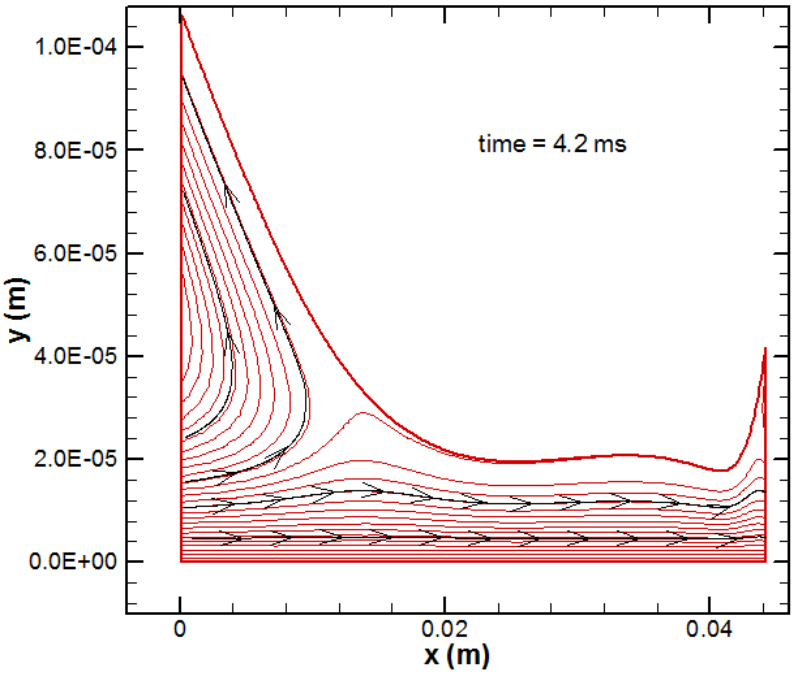

(d)

Figure 3.80 continued

The armature used for NRL shot 406 is nearly identical to the armature used for NRL shot 223 in terms of the exterior dimensions. The major difference between the two is the lubricant injection system. NRL shot 406 has only one reservoir feeding the two pockets where shot 223 has four. Also, the rails used for shot 406 are longer and manufactured in two pieces creating a gap when assembled. The muzzle voltage for this shot indicated a transition when the armature passed over the joint. The joint is modeled as an orifice and the amount of lubricant calculated to leak out of the gap is accounted for to determine if a lack of lubricant is the cause of the transition. The results show that both the pocket and reservoir have lubricant inside at the end of the shot. Only an insignificant amount of lubricant is predicted to leak from the joint. The gap heights toward the end of the shot are sufficient to prevent surface wear. It is shown that the

transition is not a result of a lack of lubricant supplied to the interface. The transition must be caused by some factors not considered in this analysis such as deformation of the joint into the armature or current arcing as the current path jumps from one piece of the rail to the other.

3.4 IAP Shot 7

Another armature and launcher has been designed by IAP. The launcher used for IAP shot 7 is a 1.0 MJ design with 4.0 m long rails. The armature has the same general shape as the previous ones, but only about half the size of the armature used for NRL shot 223. The armature used for shot 7, shown in Figure 3.81, is 2.988 in long, with a maximum lubrication length of 1.688 in. The nominal width at the trailing edge of the interface is 1.008 in. With a rail spacing of 0.984, an interference fit is created from the beginning of the shot. The lubricant injection system has one reservoir which feeds two pockets. The injection conduit consists of a conduit parallel with the reservoir which branches off at a tee into two smaller conduits perpendicular to the reservoir before reaching the pockets. The cartridge has an inner diameter of 0.293 in, the same as NRL shot 223 but a shorter length of 1.766 in. The cartridges are initially filled with 7.8 g of lubricant and sealed with a thin Mylar sheet. The armature and empty cartridge have a combined mass of 39.3 g.

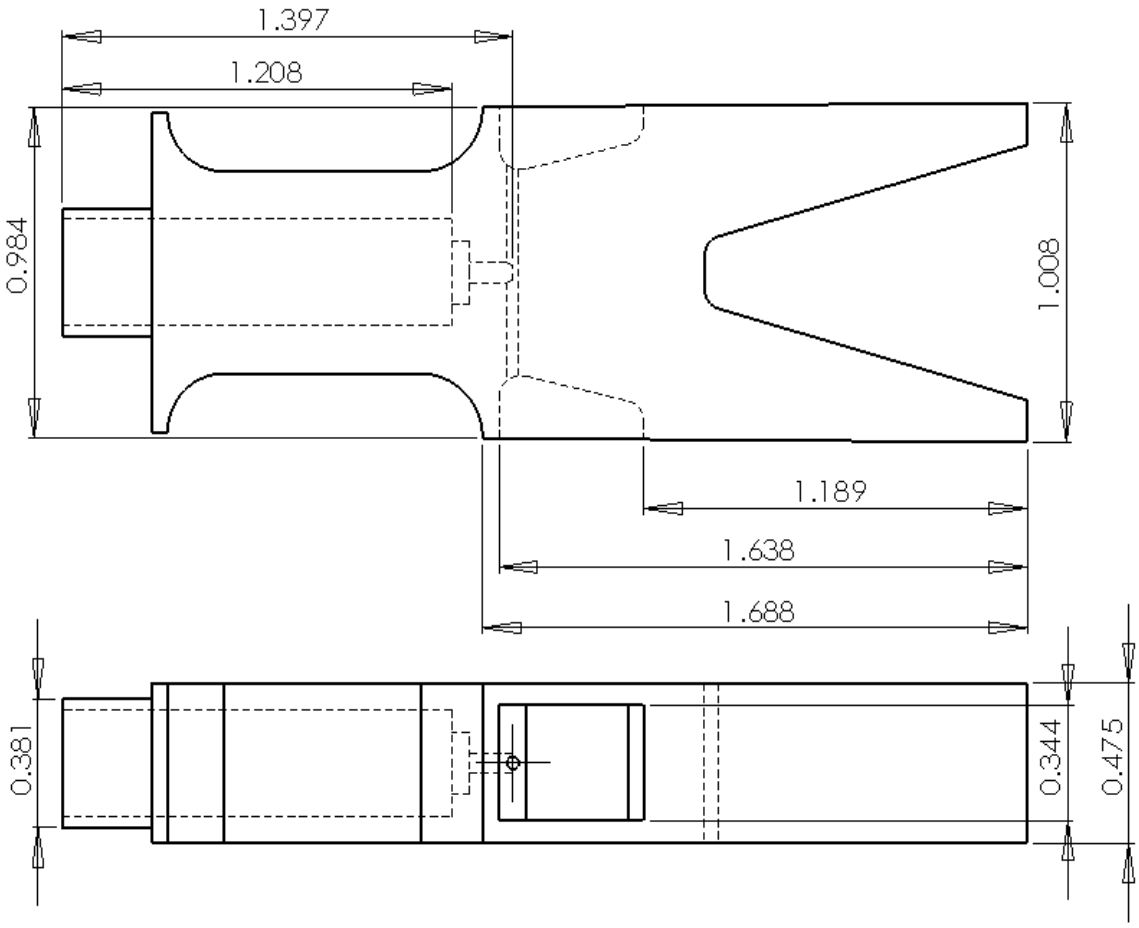

Figure 3.81: Sketch of the IAP shot 7 armature, dimensions are in inches

3.4.1 Electromagnetic Field Modeling

The simplified two dimensional model for IAP shot 7 uses the projected armature and rail areas as was done for the previous models to calculate the electromagnetic field. Because this armature is so similar to those previously mentioned, the same equations and boundary conditions are applied. To validate the two dimensional approximation, a COMSOL steady state simulation is compared to the finite difference solution to a steady state case. Figure 3.82 displays the results of both calculations. As in the previous cases,

the boundary condition on the outside of the rails is slightly different between the two methods. However, the magnetic flux distribution inside the armature is very similar.

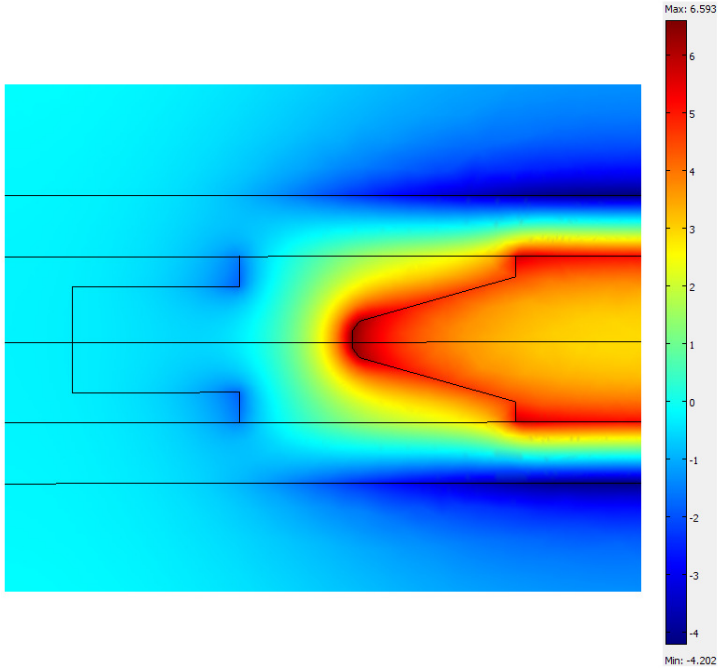

(a)

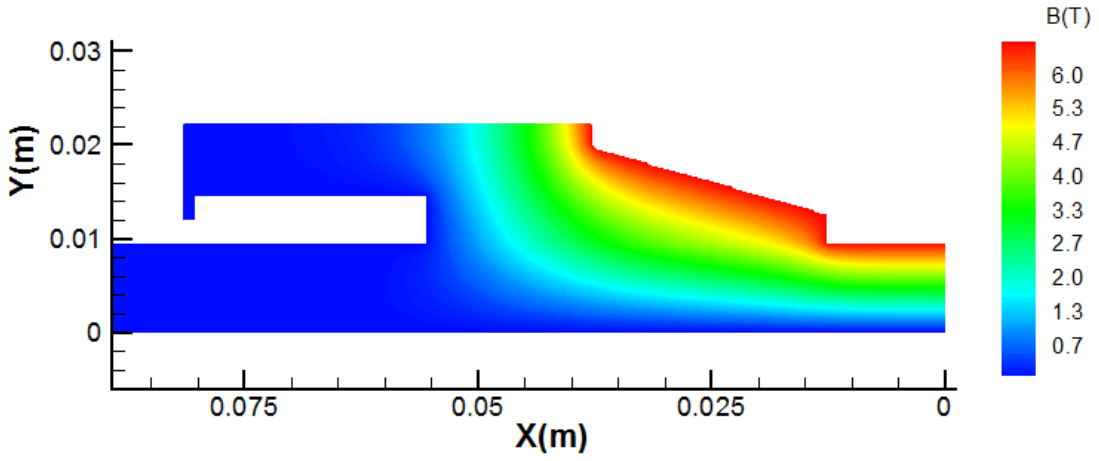

(b)

Figure 3.82: Comparison of magnetic flux distributions calculated by (a) COMSOL and (b) finite difference method, units in T

Figure 3.83 illustrates the similar current distributions achieved by both methods. For the steady state case, the electric current concentrates on the curved radius in the middle of the armature as well as on the trailing edge of the interface. The distribution and current direction agrees fairly well between the two methods. The magnetic flux density components which were neglected in the finite difference solution are show in Figure 3.84. The magnitudes are sufficiently low to support the simplification of only considering the effect of the dominant component.

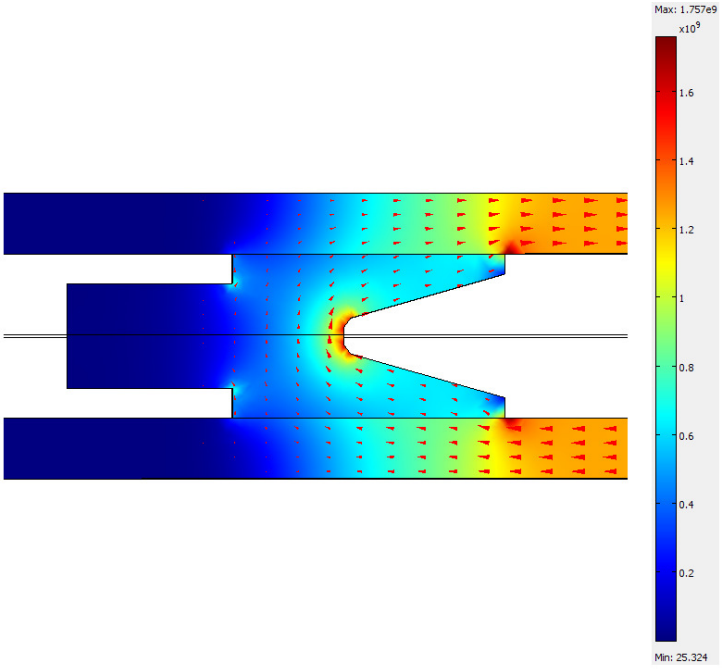

(a)

Figure 3.83: Comparison of current distributions calculated by (a) COMSOL and (b) finite difference method, units in A/m^2

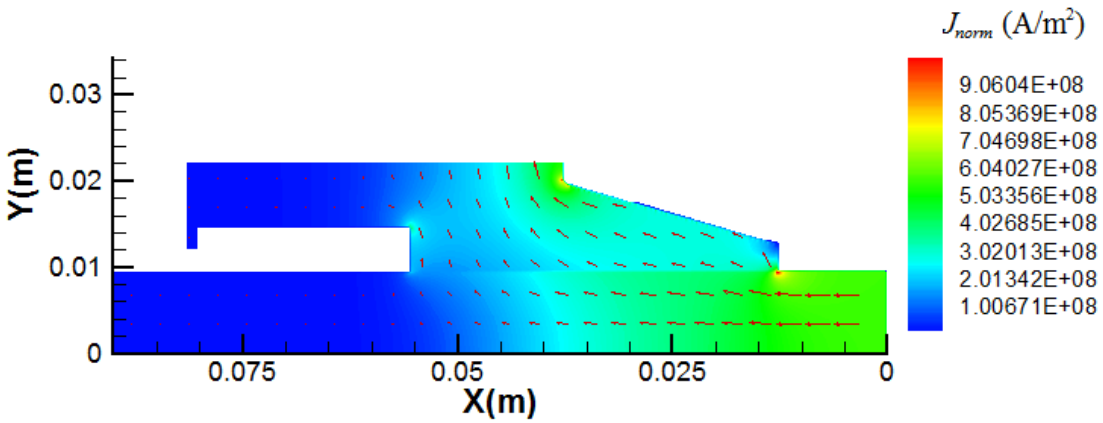

(b)

Figure 3.83 continued

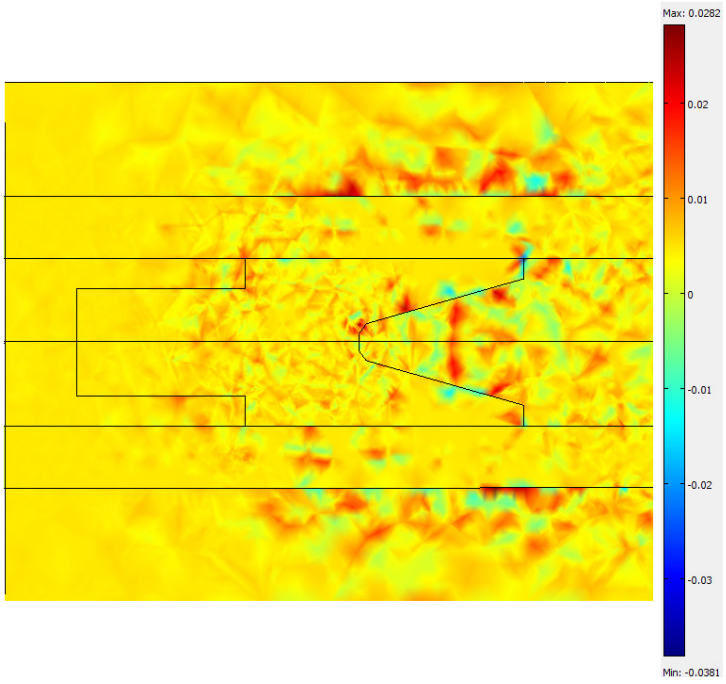

(a)

Figure 3.84: Magnetic flux density in the direction (a) parallel to the rails (b) transverse to the rails, units in T

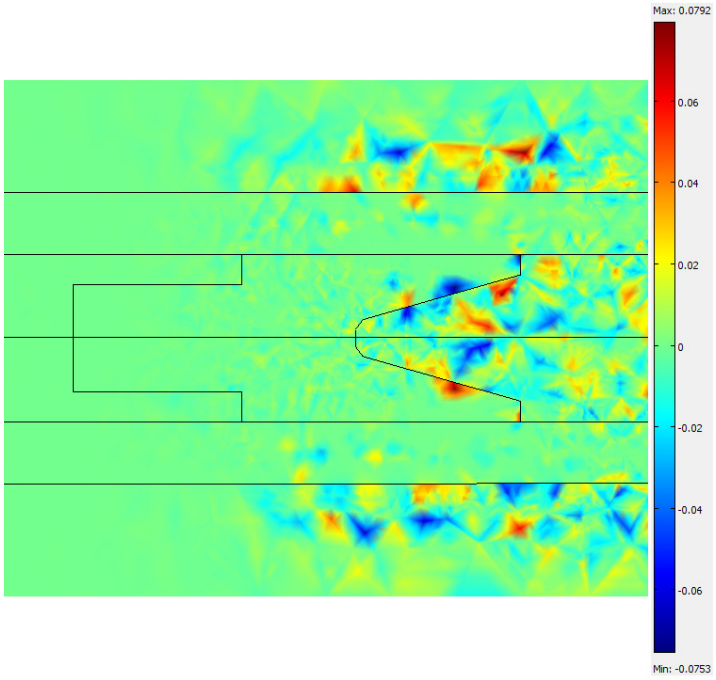

(b)

Figure 3.84 continued

3.4.2 Thermal Field Modeling

Calculation of the thermal field is done in the same way for IAP shot 7 as the previous thermal fields were calculated. The armature cross section is modeled using symmetry. The thermal field calculation is verified by using an ANSYS model with the same boundary conditions as the previous armatures. Figure 3.85 shows that the ANSYS model and the finite difference models agree.

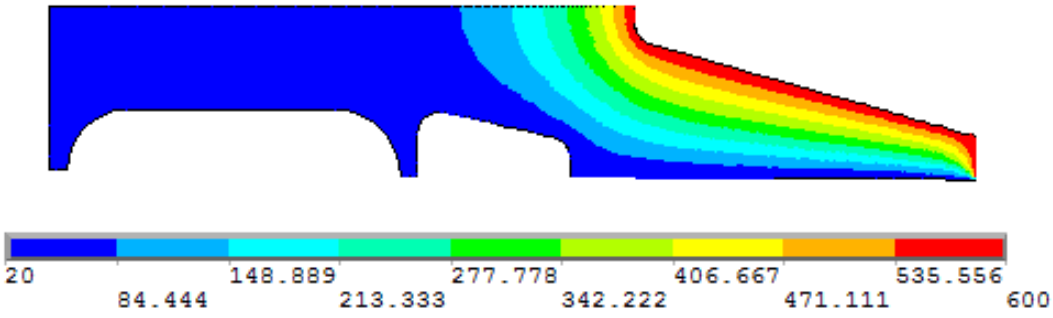

(a)

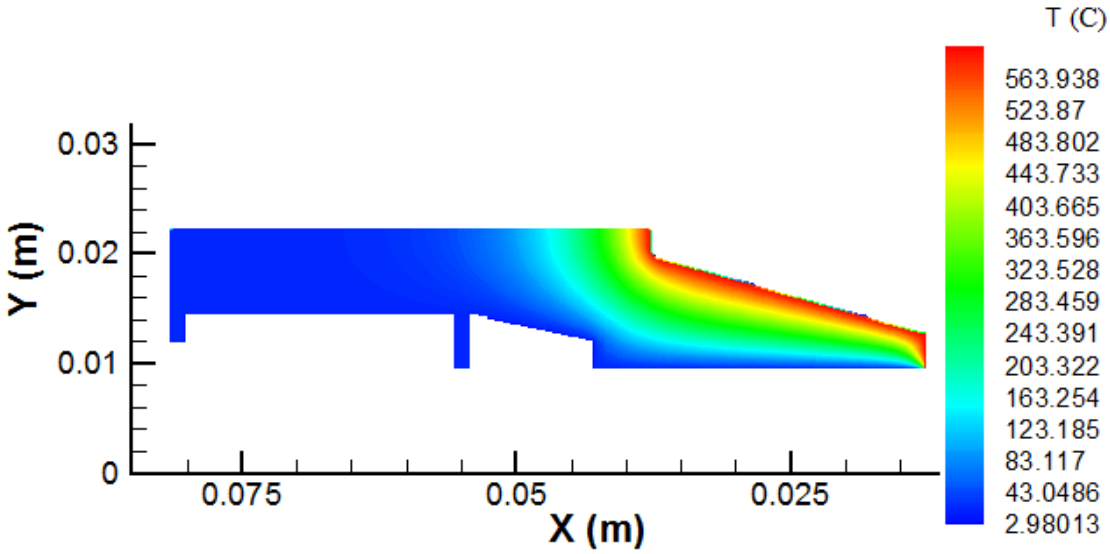

(b)

Figure 3.85: Temperature field validation calculated by (a) ANSYS and (b) finite difference method, units in C

3.4.3 Armature Deflection Modeling

The equivalent cantilever beam cross section used to calculate the armature deflection due to non-thermal effects is found with the same method as was used for the previous armatures. The armature used for IAP shot 7 is also larger than the base case, therefore it will also be capable of supporting higher loads. The forces used to validate the deflection are 500 N, 1000 N, 2000 N, and 4000 N. Figure 3.86 shows that the equivalent cantilever beam deflection is in agreement with the ANSYS results. It is

important to note that from an x position of approximately 0.0012 m to 0.0127 m the deflection is inside the pocket and will not be used, therefore, error in this region is acceptable.

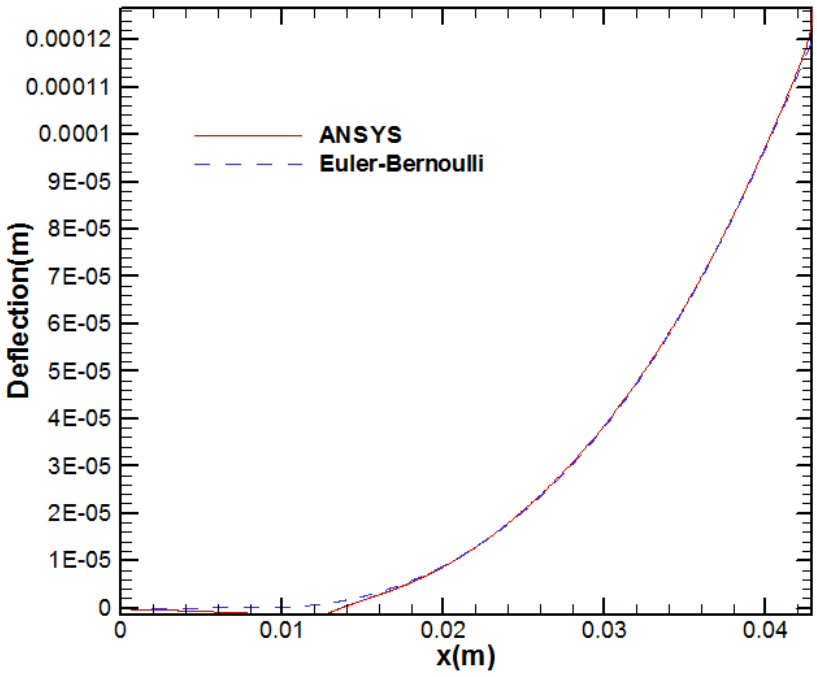

(a)

Figure 3.86: Comparison of armature wing deflection between ANSYS and Euler-Bernoulli models with a shear force of (a) 500 N, (b) 1000 N, (c) 2000 N, and (d) 4000 N

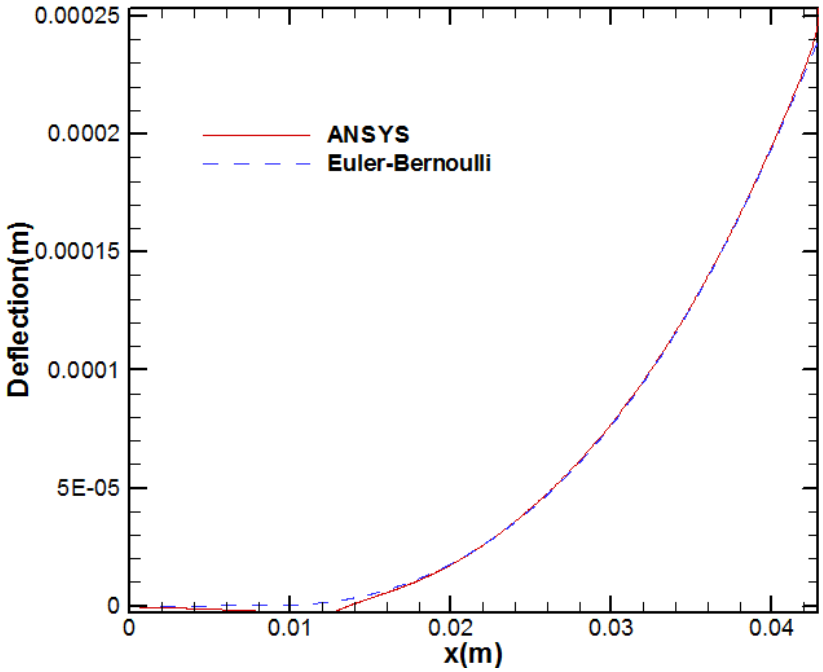

(b)

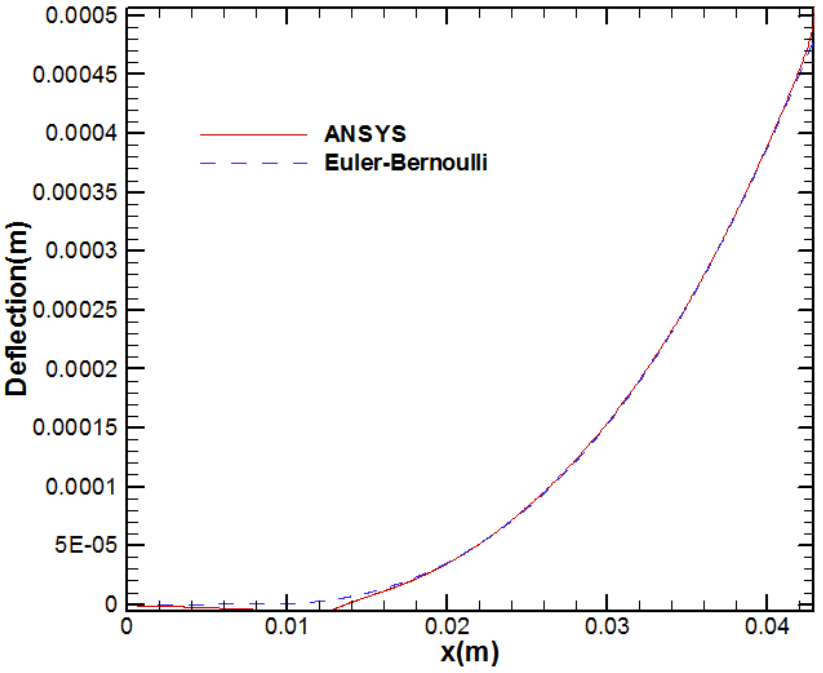

(c)

Figure 3.86 continued

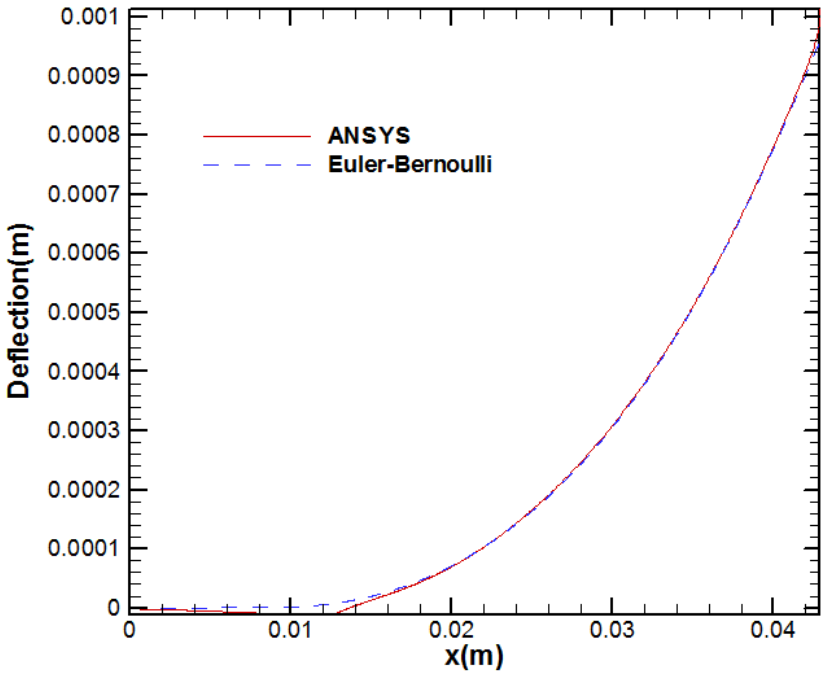

(d)

Figure 3.86 continued

Using the equivalent cantilever beam, the calculation of the contact pressure and the resulting deformation must also be validated. The validation is done as it was for the previous armatures, by comparing an ANSYS simulation with a prescribed interference between the rail and armature to the finite difference solution using the equivalent cantilever beam with the Greenwood-Williamson contact model with the same interferences. Figure 3.87 shows that there is some variation between the two simulations using interferences of 0.8636 mm and 0.9144 mm. However, the contact pressures are on the same order of magnitude and as previously explained, this variation will not greatly affect the results of the study. The more important quantity to consider is the deflection caused by contact shown in Figure 3.88. There is only a small variation between the two methods in calculating the deflection caused by contact.

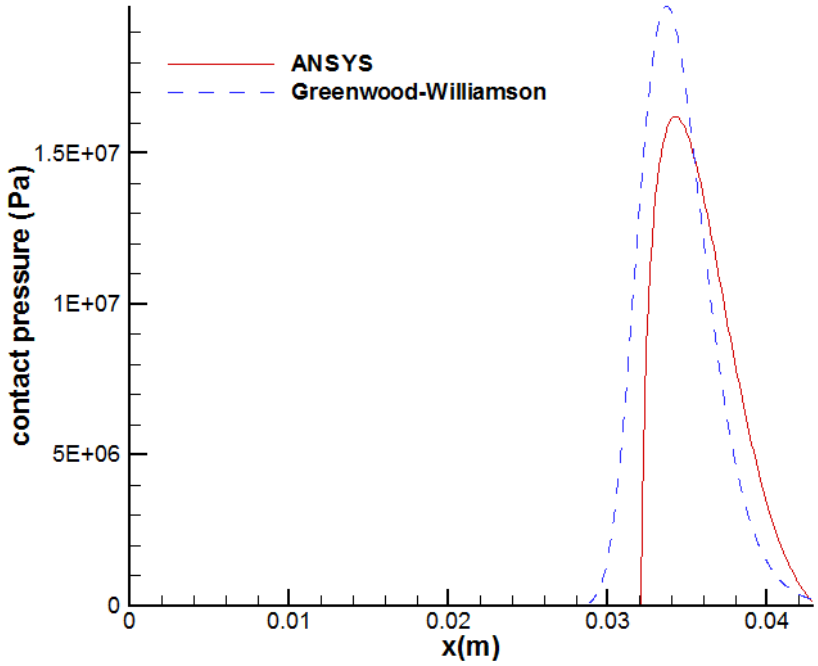

(a)

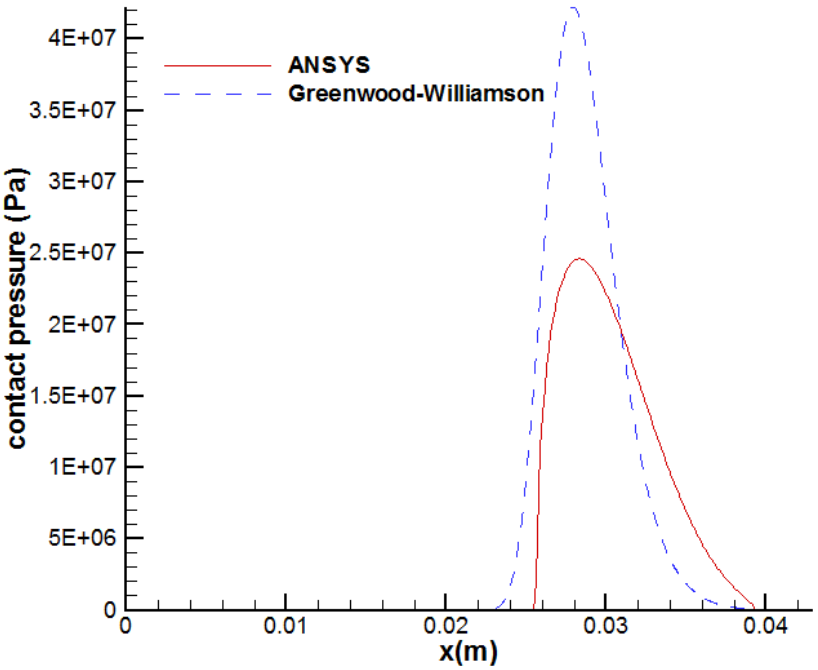

(b)

Figure 3.87: ANSYS and Greenwood-Williamson model contact pressure for an interference of (a) 0.8636 mm and (b) 0.9144 mm

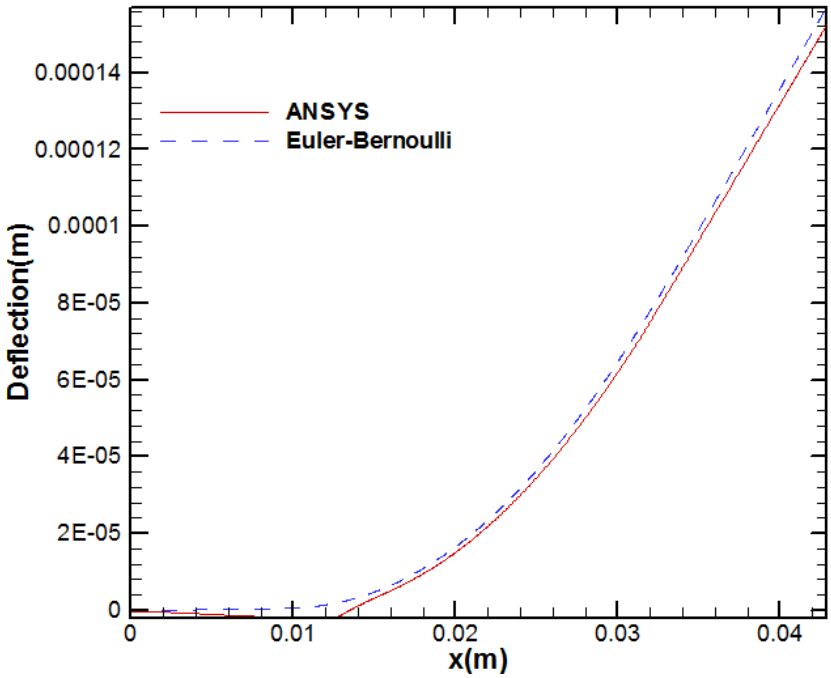

(a)

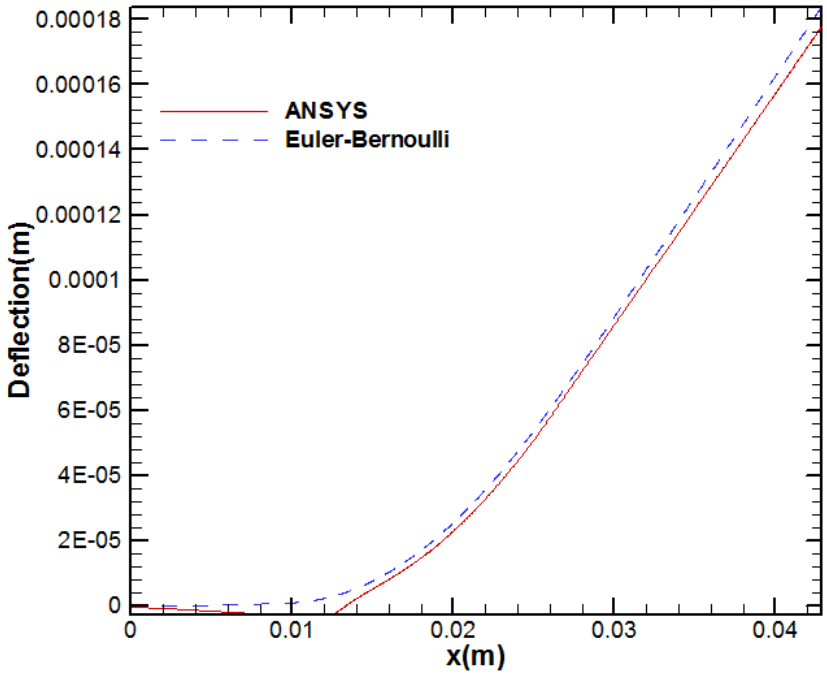

(b)

Figure 3.88: ANSYS and Euler-Bernoulli contact deformation for an interference of (a) 0.8636 mm and (b) 0.9144 mm

The thermal loads applied must also be analyzed using a different equivalent cantilever beam. The equivalent thermal beam is found in the same way as it was found for NRL shot 223. Therefore, due to the stiffer armature, a shear force of 300 N is applied to the trailing end of the armature. Figure 3.89 shows that the ANSYS simulation agrees very closely with the thermal beam approximation with high temperature boundaries of 200 °C, 300 °C, 400 °C, and 600 °C. The deflection from an x position of about 0.0012 m to 0.0127 m coincides with the pocket region and will not be used in simulation.

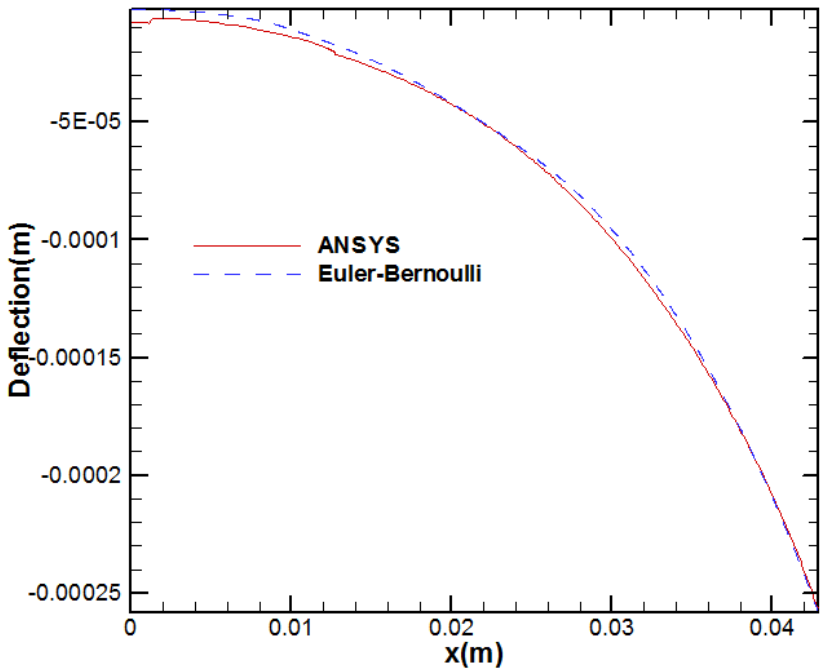

(a)

Figure 3.89: Comparison of armature wing deflection between ANSYS and Euler-Bernoulli models for high boundary temperatures of (a) 200 °C, (b) 300 °C, (c) 400 °C, and (d) 600 °C

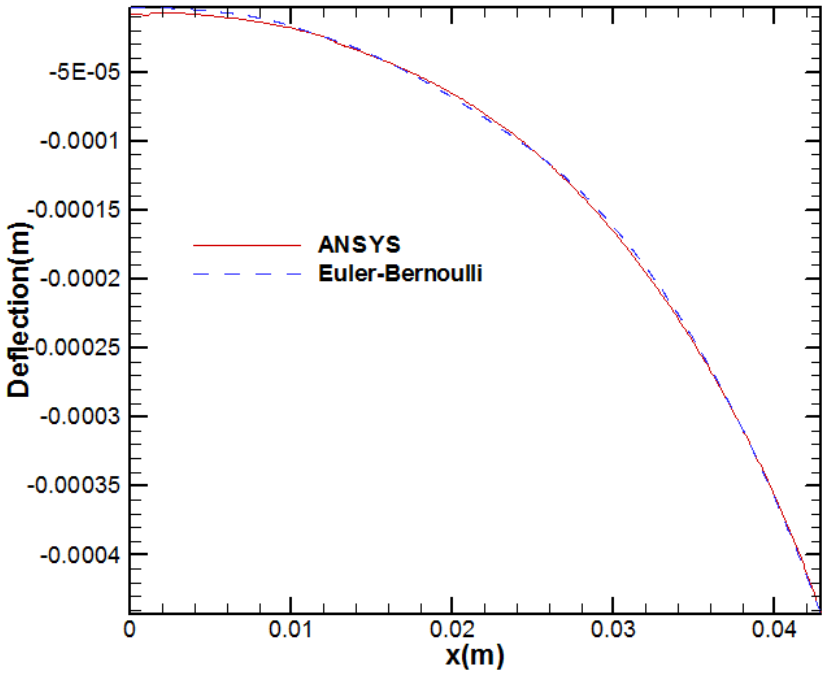

(b)

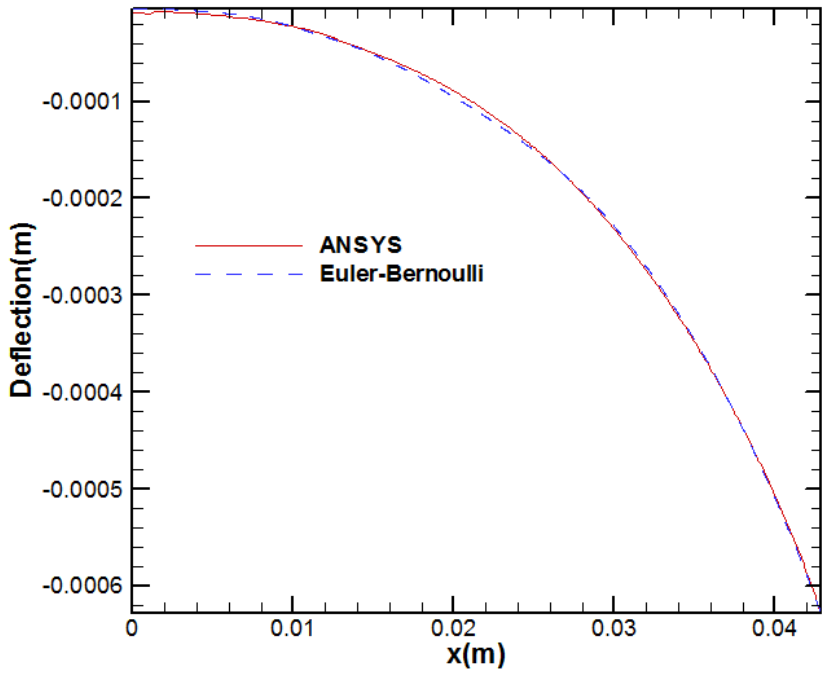

(c)

Figure 3.89 continued

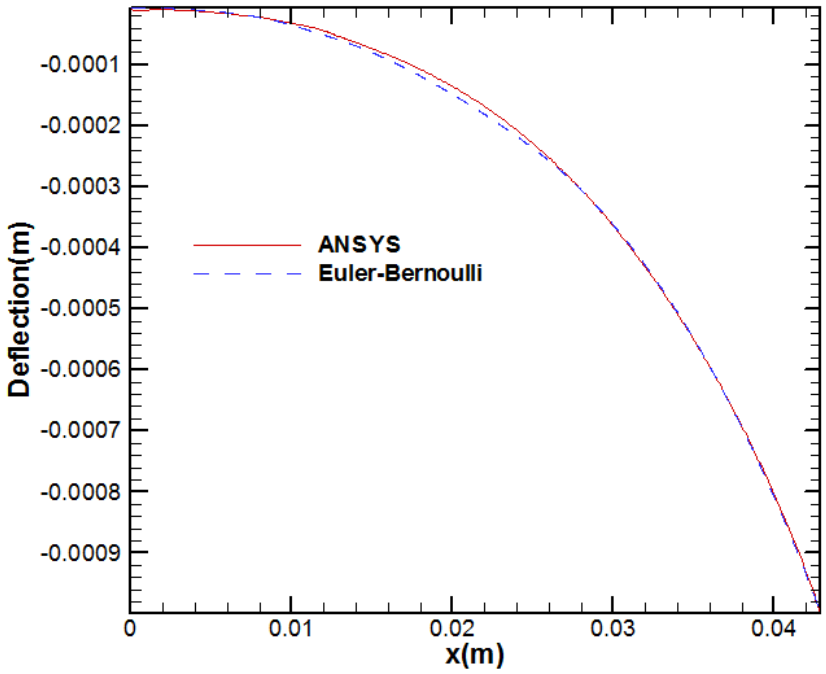

(d)

Figure 3.89 continued

3.4.4 Lubricant Modeling

The armature used for IAP shot 7 has a lubricant injection system which is different from that of the previous armatures. There is one reservoir which feeds both pockets like the base case injection system. However, the lubricant goes from the reservoir into a conduit parallel to the rails, then branches in a tee to each pocket. However, the two conduits running out of the tee are smaller than the one going in so the modeling will add the head loss from the tee with the head loss from a sharp edged contraction. The system is broken up into calculational nodes as shown in Figure 3.90, conduit D is between nodes 1 and 2 while conduit A is between nodes 2 and 3. Equations 3.36 and 3.37 find the pressures at nodes 2 and 3. Equations 3.36-3.39 are combined and the derivatives are discretized to yield Equation 3.40, a quadratic equation which can be

solved for the mass flow rate of lubricant into one pocket. Here, the friction factors, f_D and f_A, for conduits D and A are .024 and .027 respectively and the head loss factors, k_{eD} and k_{eA}, are about 0.5 and 1.3 respectively. Additionally, the equivalent length over diameter added by the tee, k_{tee}, is 30.

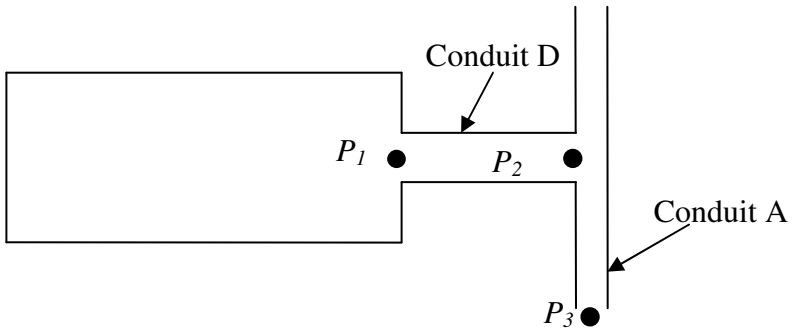

Figure 3.90: Schematic of the IAP shot 7 injection system and node points (not to scale)

$$P_2 = P_1 - \rho\left[\left(f_D\frac{L_D}{2R_D}+k_{eD}\right)\frac{V_D^2}{2}+L_D\frac{\partial V_D}{\partial t}\right]+\rho a L_D-\rho\frac{V_D^2}{2} \tag{3.36}$$

$$P_3 = P_2 - \rho\left\{\left[f_A\left(k_{tee}+\frac{L_A}{2R_A}\right)+k_{eA}\right]\frac{V_A^2}{2}+L_A\frac{\partial V_A}{\partial t}\right\}+\rho\frac{V_D^2}{2}-\rho\frac{V_A^2}{2} \tag{3.37}$$

$$V_D = 2\frac{\dot{Q}}{\rho\pi R_D^2} \tag{3.38}$$

$$V_A = \frac{\dot{Q}}{\rho\pi R_A^2} \tag{3.39}$$

$$\begin{aligned}&\left\{\frac{2}{\rho\pi^2 R_D^4}\left[f_D\frac{L_D}{2R_D}+k_{eD}\right]+\frac{1}{2\rho\pi^2 R_A^4}\left[f_A\left(k_{tee}+\frac{L_A}{2R_A}\right)+k_{eA}+1\right]\right\}\dot{Q}^2\\&+\left(\frac{2L_D}{\pi R_D^2 dt}+\frac{L_A}{\pi R_A^2 dt}\right)\dot{Q}-\left(\left(\frac{2L_D\dot{Q}_{pre}}{\pi R_D^2 dt}+\frac{L_A\dot{Q}_{pre}}{\pi R_A^2 dt}\right)+P_1-P_3+\rho a L_D\right)=0\end{aligned} \tag{3.40}$$

The pressures at nodes 1 and 3 are calculated in the same way as they were calculated while analyzing NRL shot 223. The model uses the same Reynolds Equation and calculational method for the lubricant inside the interface as the previous armatures. Additionally, the model is able to calculate dry-out of the armature-rail interface if the pocket empties out but the reservoir does not, as was done in the model of NRL shot 223.

3.4.5 Results and Discussions

Few changes were made to the Magneto-Elastothermohydrodynamic model used for NRL shot 223 to analyze IAP shot 7. The major differences are the modeling of the new lubrication system, the different equivalent cantilever beams, and using the new projected region. The muzzle voltage history displayed in Figure 3.91 shows that the shot does not transition before the armature exits the launcher at about 4.7 ms. However, at about 4.15 ms into the shot, there is some noticeable muzzle voltage which remains under 50 V or half of the voltage which would describe a transition. This phenomenon can be referred to as a slight or weak transition and was present in the muzzle voltage of NRL shot 223 just before the end of the shot from about 3.5 ms to 4.5 ms. This feature could be a result of something as insignificant as dust falling on the rail, or it could be caused by the emptying of the pocket and the beginning of a transition.

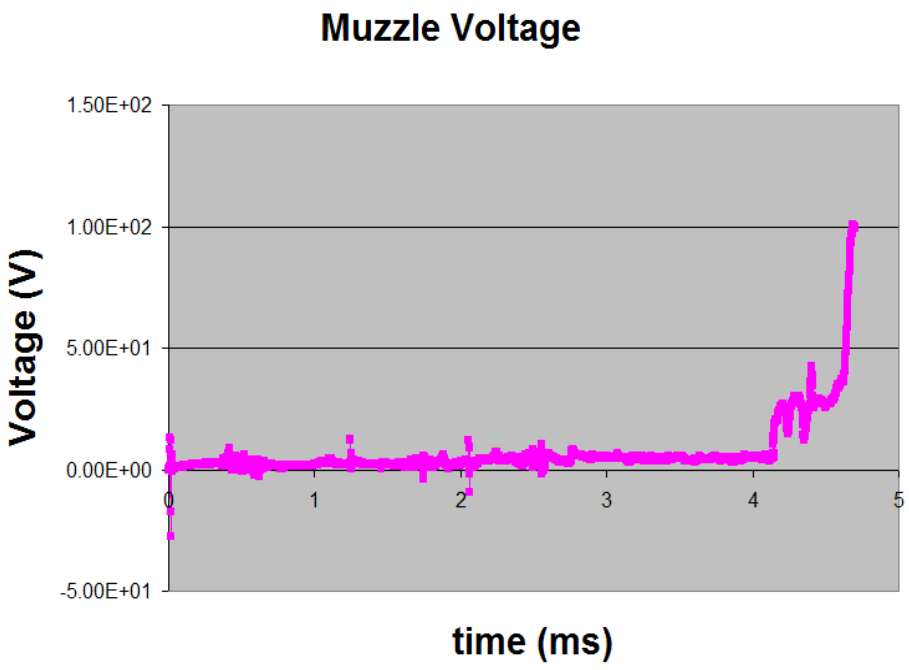

Figure 3.91: Experimental muzzle voltage

The current history for IAP shot 7 is presented in Figure 3.92. It is similar in shape to the current histories of the previous armatures. It quickly rises at the beginning of the shot, levels off toward the middle and gently recedes as the shot ends. The maximum current is about 285 kA reached approximately 1.65 ms, however there is a three-humped pattern in which each hump reaches a local maximum close to 285 kA. The three humps are most likely caused by the delayed discharging of three capacitor banks, each discharged after the current supplied from the previous one begins to fall. The current at the end of the shot is about 130 kA.

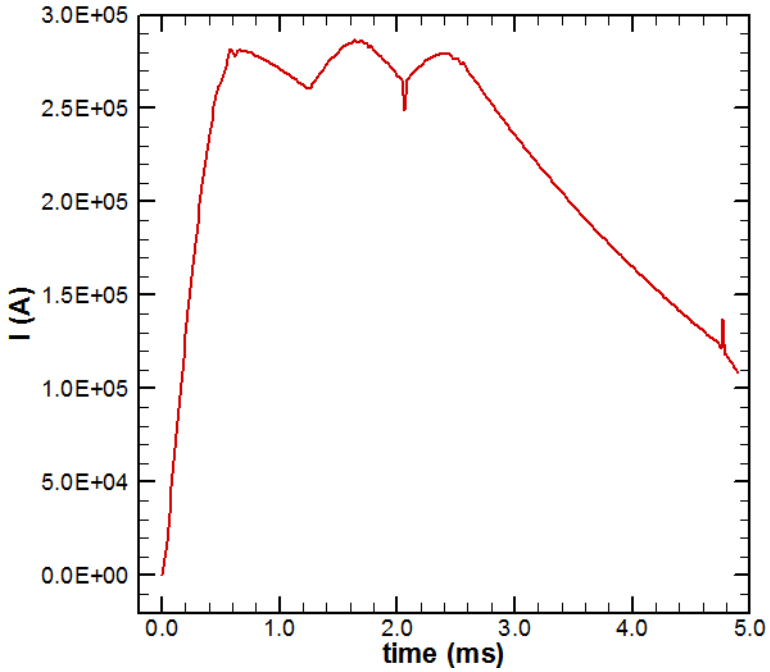

Figure 3.92: Electric current history

Figure 3.93 presents the computed magnetic flux density in the rail an armature at various times from the beginning of the shot. The magnetic flux concentrates on the trailing edges of the armature as was seen with the previous simulations. The magnetic flux increases quickly such that it is close to its highest values at 0.5 ms. At 1.66 ms the magnetic flux is at approximately the highest values. By 3.0 ms the magnetic flux has already began to decline in value and by 4.5 ms it is about half of its peak strength.

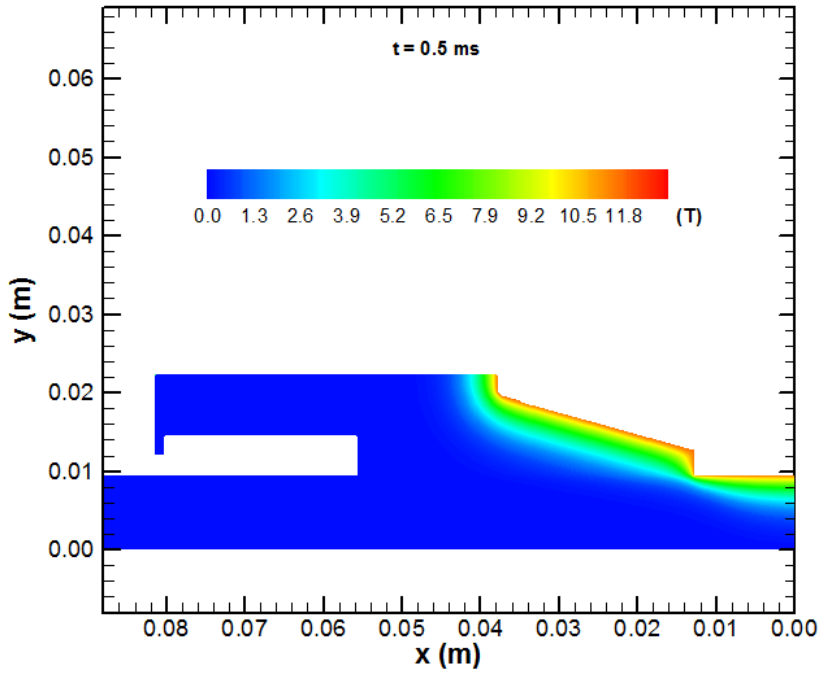

(a)

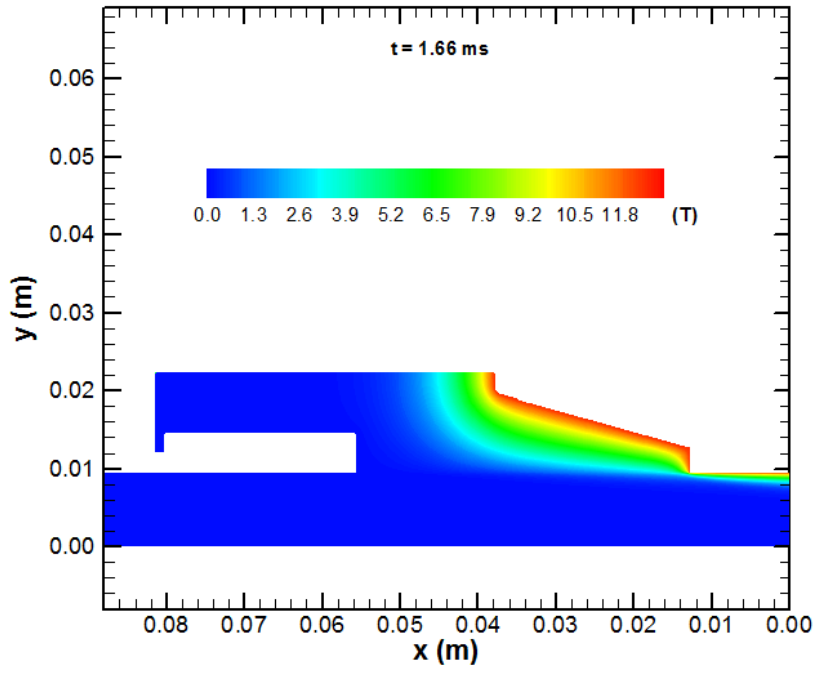

(b)

Figure 3.93: Magnetic flux density distribution at different times

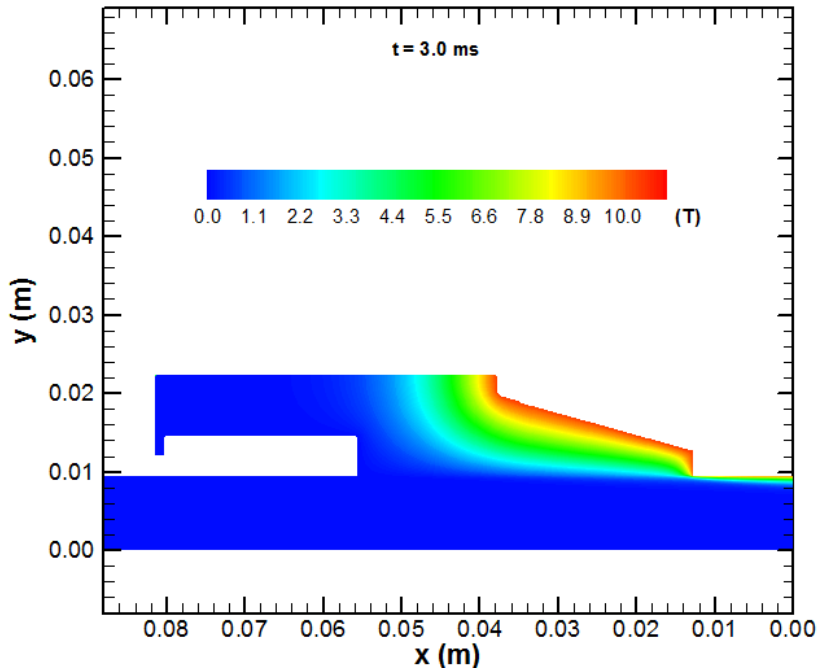

(c)

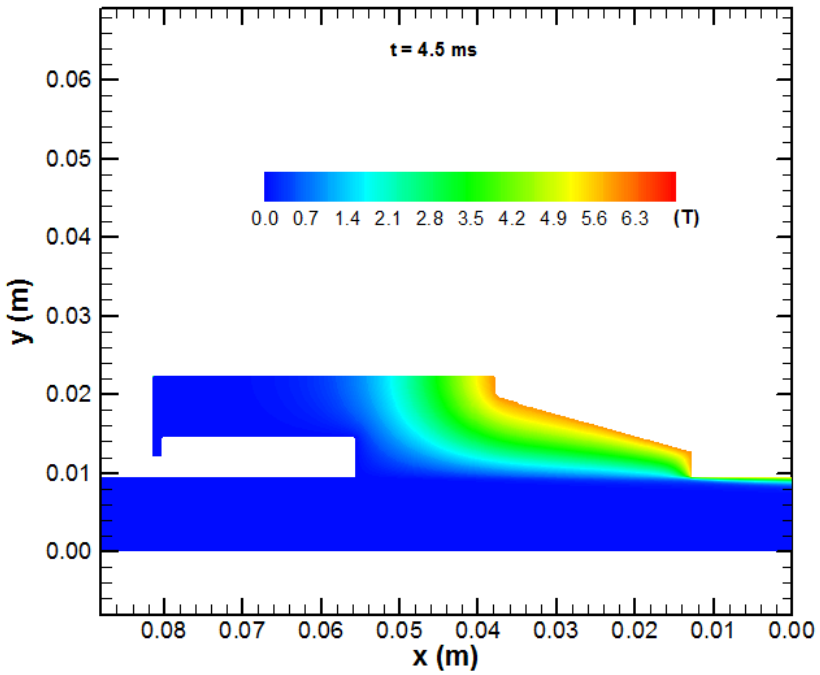

(d)

Figure 3.93 continued

The electric current distribution at various times for IAP shot 7 is illustrated in Figure 3.94. The electric current density is concentrated on the trailing edges of the armature initially. As the armature speeds up, the velocity skin effect pulls the current density toward the trailing edge of the interface. By the end of the shot, the current density is pulled away from the center of the armature and very concentrated at the trailing edge of the interface.

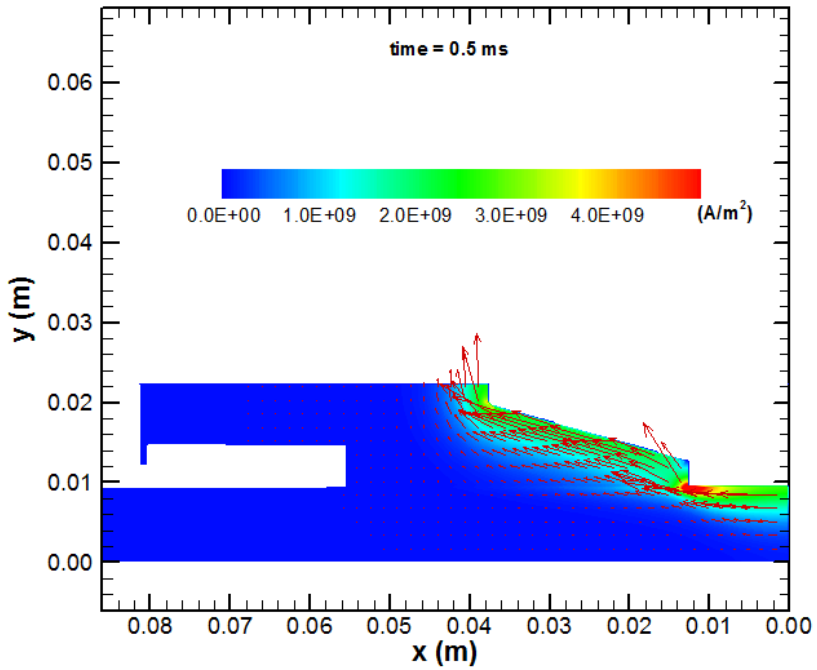

(a)

Figure 3.94: Electric current distribution at different times

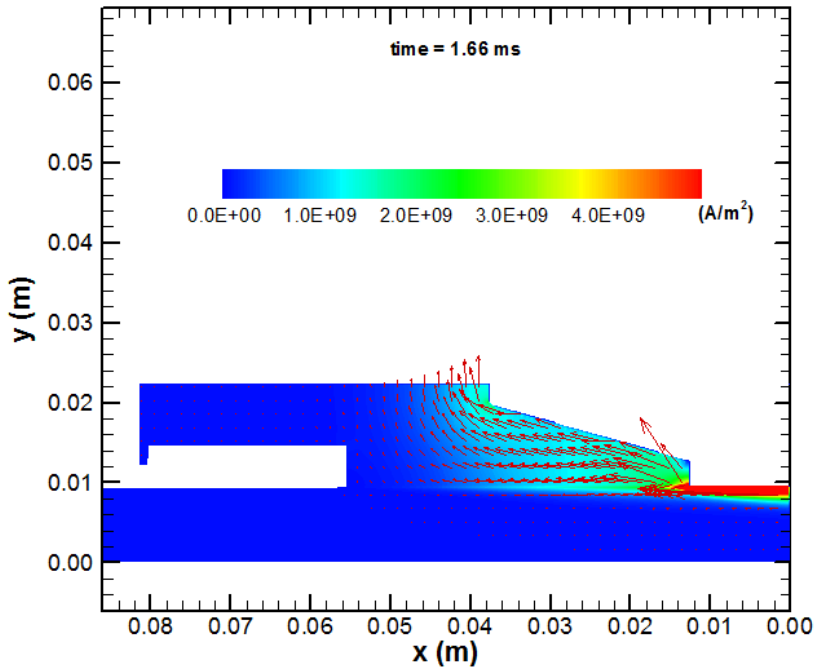

(b)

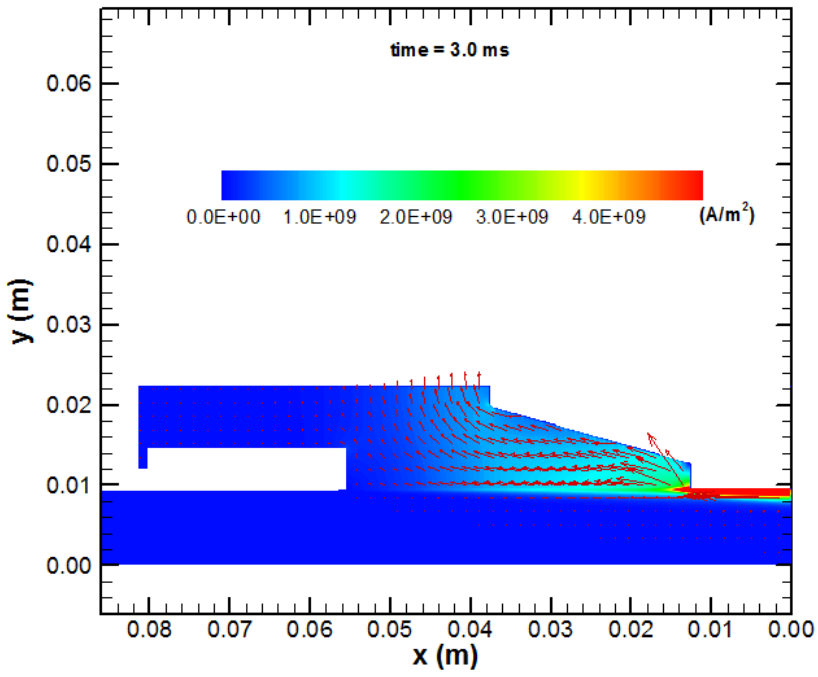

(c)

Figure 3.94 continued

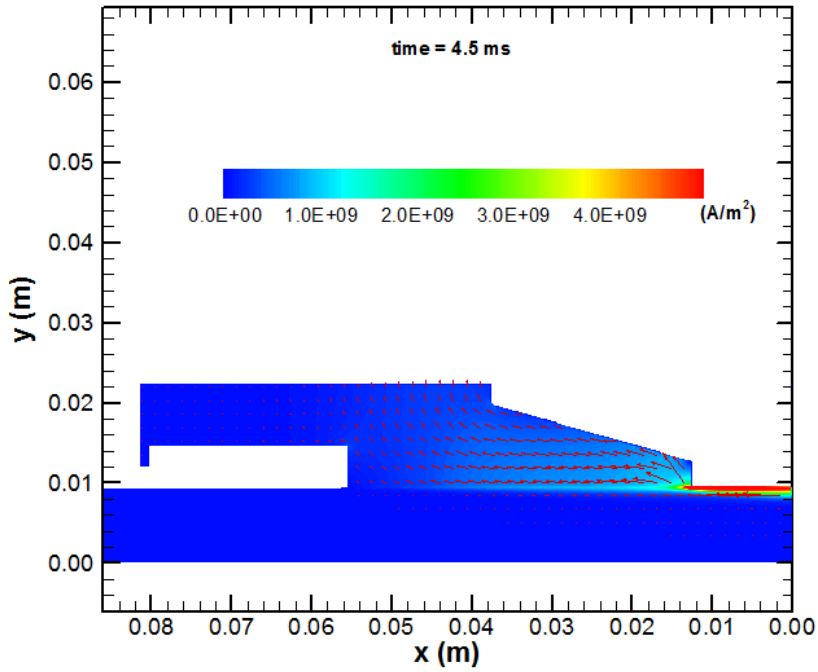

(d)

Figure 3.94 continued

Figure 3.95 shows the body forces due to electromagnetic interactions. One component of the forces pushes the armature along the rail while the other pushes it into the rail. The electromagnetic forces are concentrated in the same locations as the magnetic flux and current densities due to their physical relationship. Even though this armature is smaller than the one used for NRL shot 223 the magnitude of the force densities are about the same. However, when integrated, the smaller volume leads to a generally smaller net magnetic force pushing the armature along the rails. Towards the end of the shot, the forces on the armature significantly decrease due to the falling current and magnetic flux.

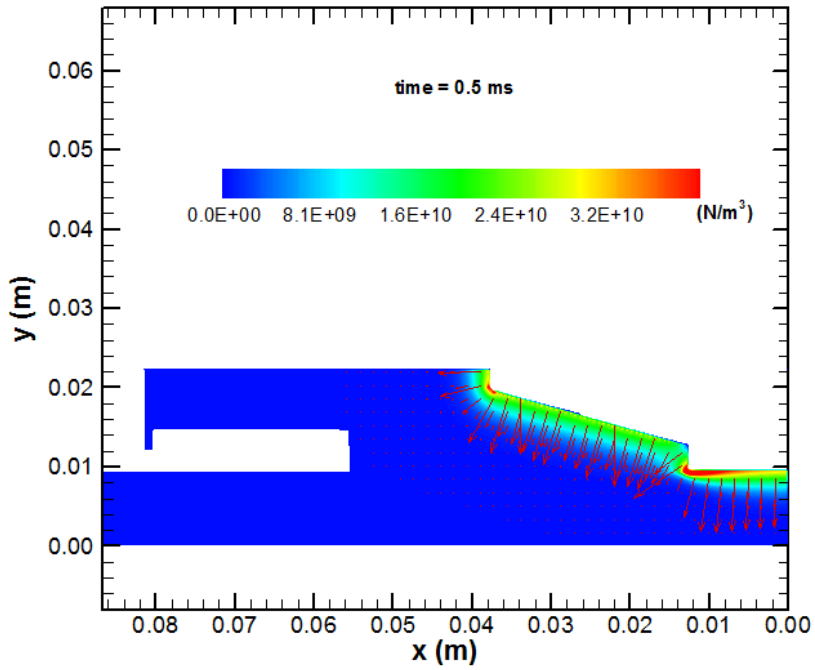

(a)

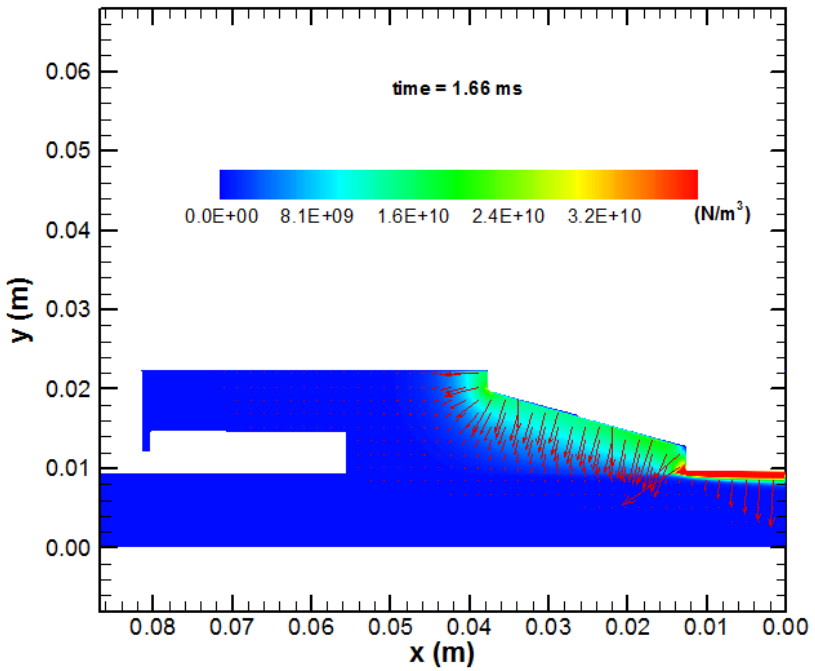

(b)

Figure 3.95: Magnetic body force distribution at different times

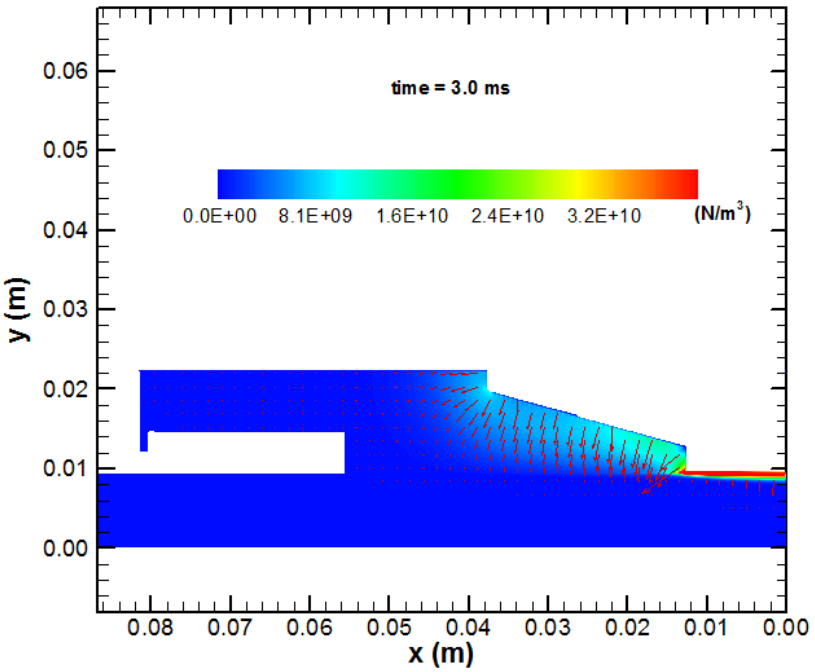

(c)

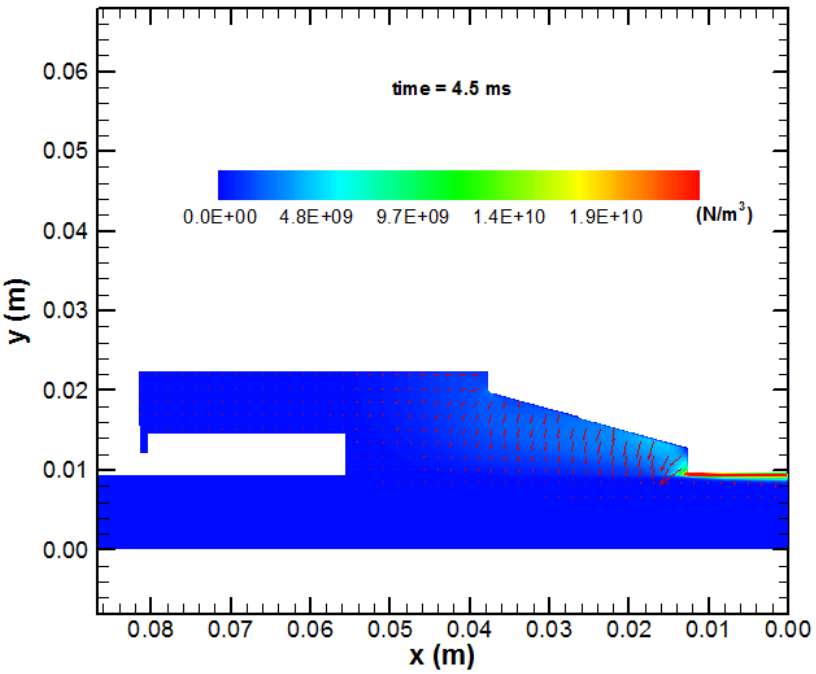

(d)

Figure 3.95 continued

The temperature profile is displayed in Figure 3.96 at various times. At 0.5 ms the armature-rail interface and the trailing edge of the center of the armature begin to heat up. As the shot progresses, lubricant both cools the interface and eliminates solid-solid contact so only the trailing edge of the interface and the center of the armature are noticeable warmer than the rest of the armature. Toward the end of the shot the two areas with substantially higher temperatures are at the center of the armature and the trailing edge of the interface as shown by the arrows in Figure 3.96d. It is predicted that a small portion of the armature will reach the melting temperature; however, this region is small enough to assume melting does not occur.

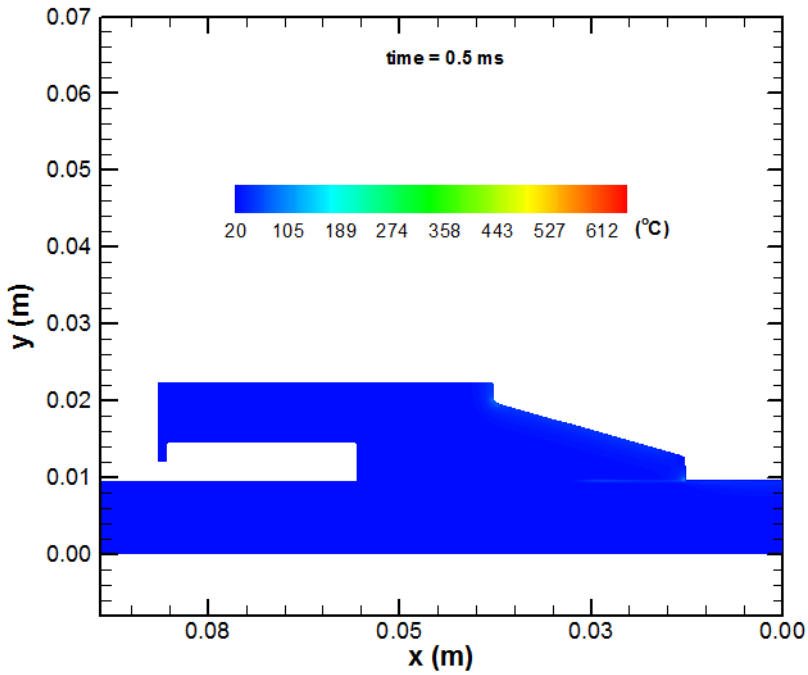

(a)

Figure 3.96: Temperature distribution at different times

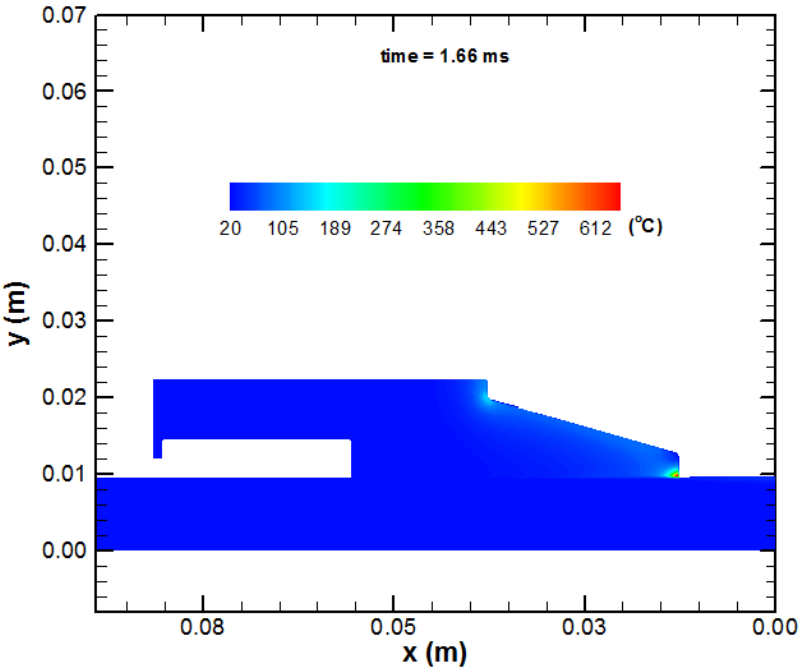

(b)

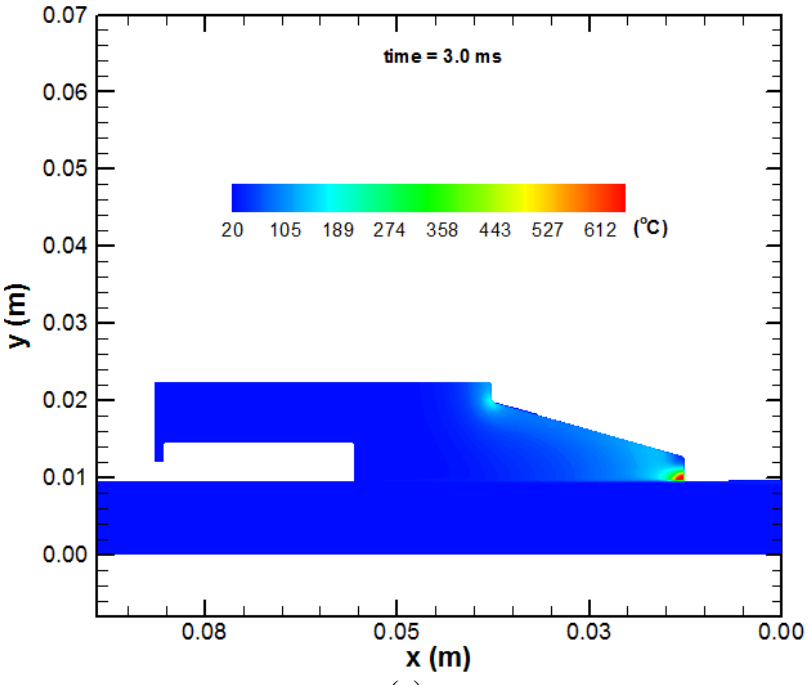

(c)

Figure 3.96 continued

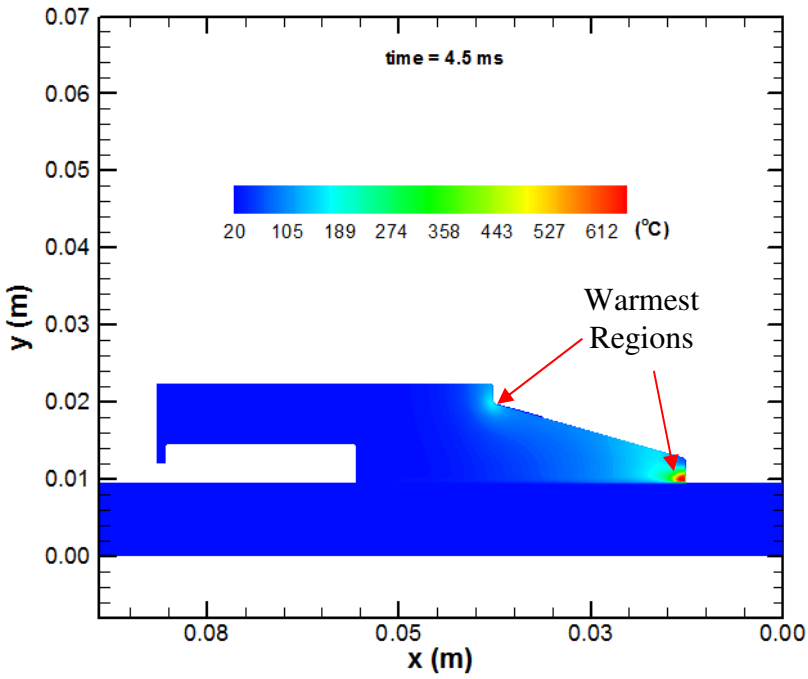

(d)

Figure 3.96 continued

Figure 3.97 shows the net forces acting on the armature in the direction of the rails. The electromagnetic force, $F_{emag,}$ is proportional to the square of the current profile and reaches a maximum of approximately 19 kN at about 1.66 ms. The frictional and viscous forces, F_f and F_v respectively, are small enough that the total net force acting on the armature, F_{total} is almost identical to the electromagnetic force over the entire shot. Moreover, the frictional force is almost zero for most of the shot, having a very small magnitude at the beginning only.

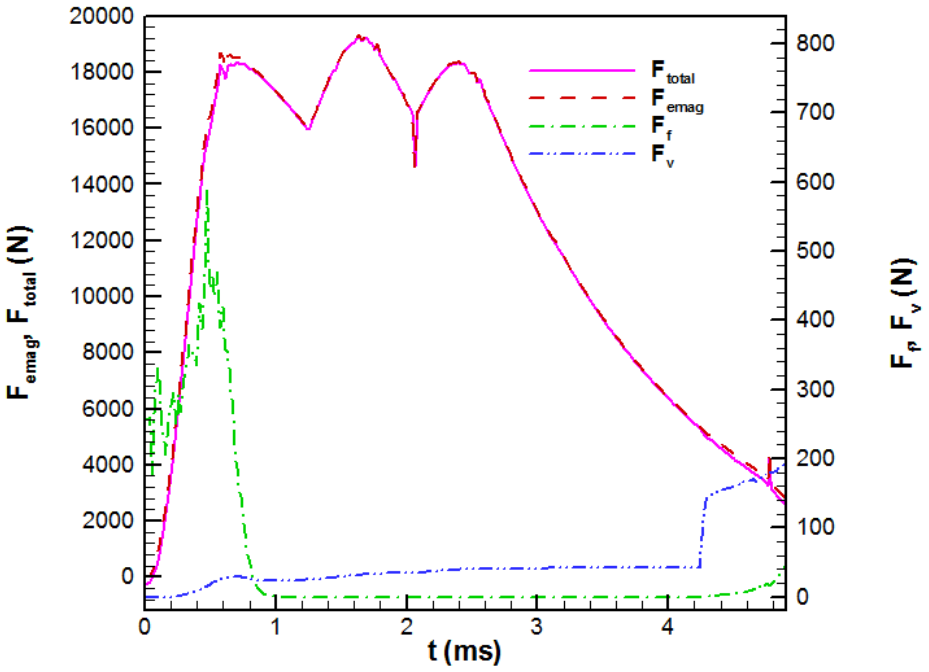

Figure 3.97: *x* direction armature force history

The armature acceleration history is almost a direct result of the total force from the previous figure. The slight variation between the shape of the acceleration curve and the total force curve is due to the change in mass as the lubricant is leaked. Therefore, the armature acceleration history in Figure 3.98 is shaped like both the current profile and the net magnetic force in the *x* direction. The maximum acceleration obtained during the shot is about 410 km/s^2 at a time of 1.66 ms.

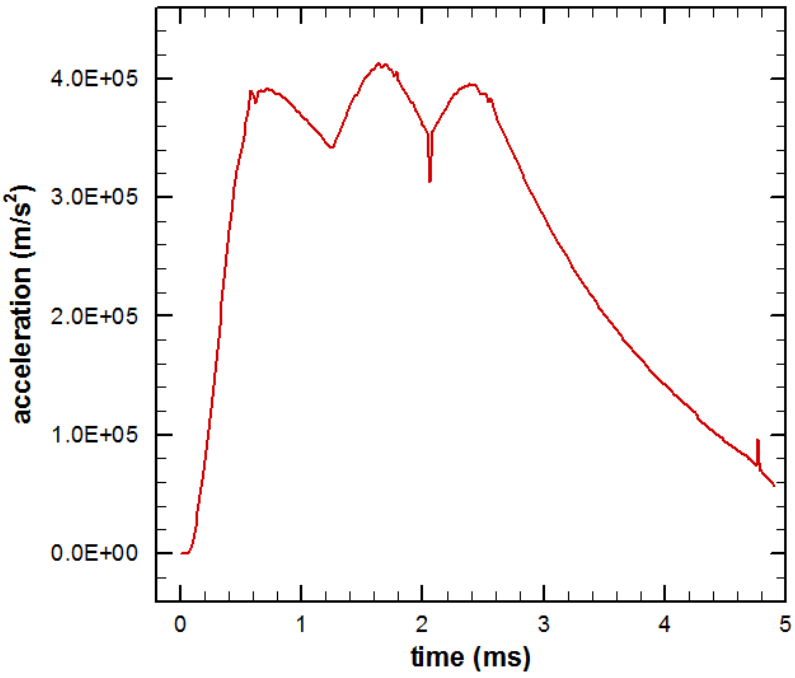

Figure 3.98: Armature acceleration history

The velocity profile predicted with the numerical model is very close to the experimentally observed armature velocity shown in Figure 3.99. The velocity increases fairly smoothly, then begins to level off as the shot reaches the end. The muzzle velocity of the armature is almost 1300 m/s. The armature position history predicted is also compared to the experimental data in Figure 3.100. The predicted position is almost identical to the position history recorded during the shot. The armature exits the muzzle when it gets to a position of about 3.6 m at about 4.7 ms.

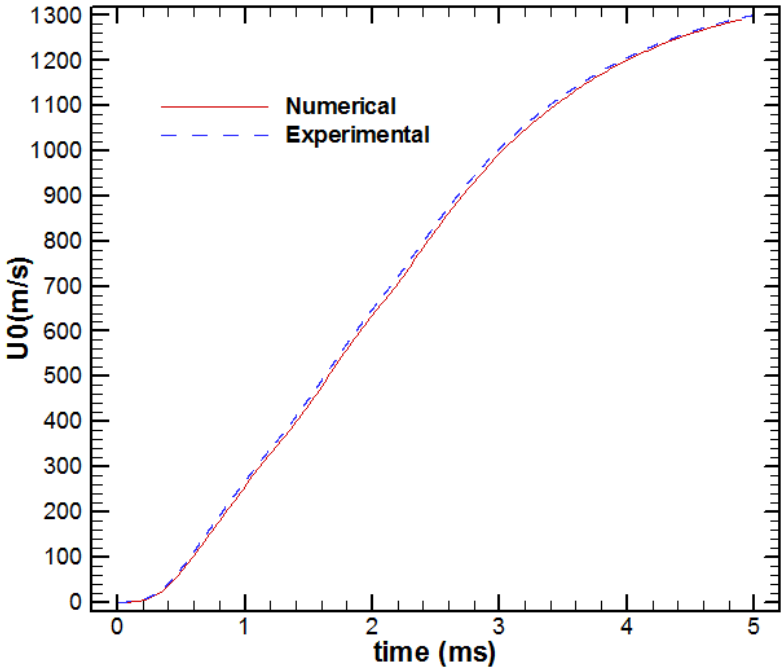

Figure 3.99: Comparison of predicted armature velocity history with experimental measurements

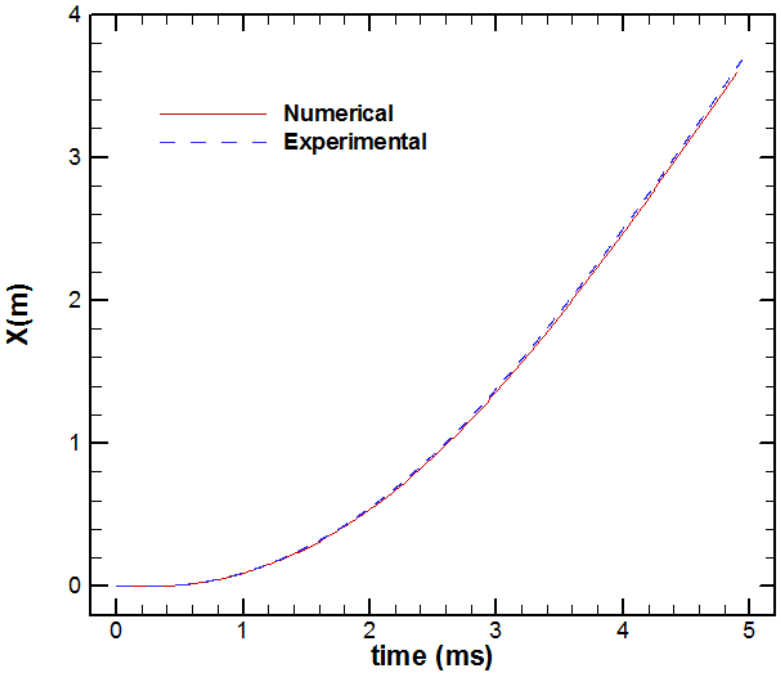

Figure 3.100: Comparison of predicted armature location history with experimental measurements

A history of the amount of lubricant left inside the reservoir, Q_{left} is shown in Figure 3.101. The reservoir begins with a charge of 7.8 g which is delivered to the pockets through the conduits as the armature accelerates. At the end of the shot, a little more than half the initial charge remains in the reservoir. The lubricant consumption history of one pocket is illustrated in Figure 3.102. Q_{out} is the amount of lubricant delivered to the pocket, Q_l and Q_r are the amounts leaked from the leading edge and the trailing edge of the pocket respectively, and Q_{net} is the amount of lubricant inside the pocket. Because the pocket never fills up, no lubricant leaks from the leading edge. The pocket partially fills until about 2.5 ms, and then begins to empty as the interface calls for more lubricant. At about 4.2 ms the pocket empties out completely, however lubricant from the reservoir is still being supplied to the interface.

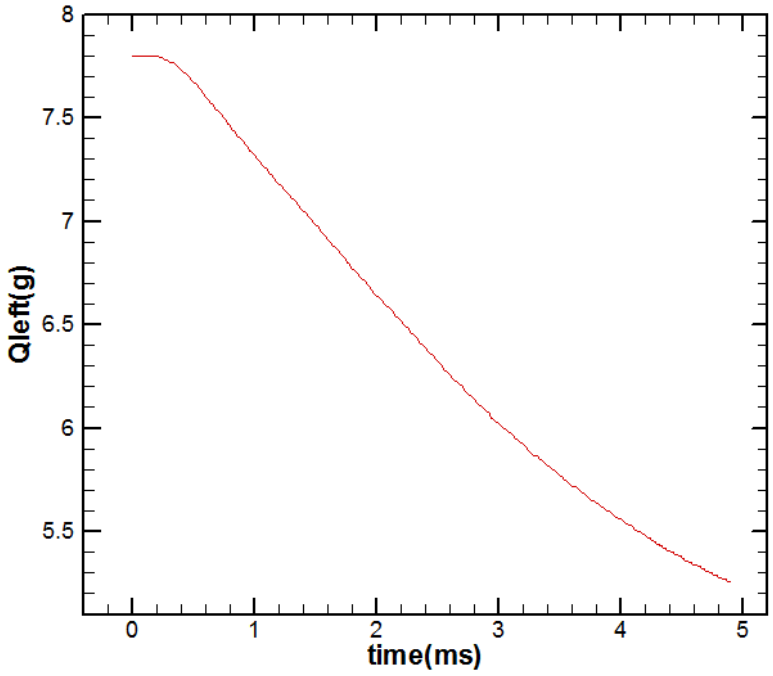

Figure 3.101: History of the amount of lubricant left inside each reservoir.

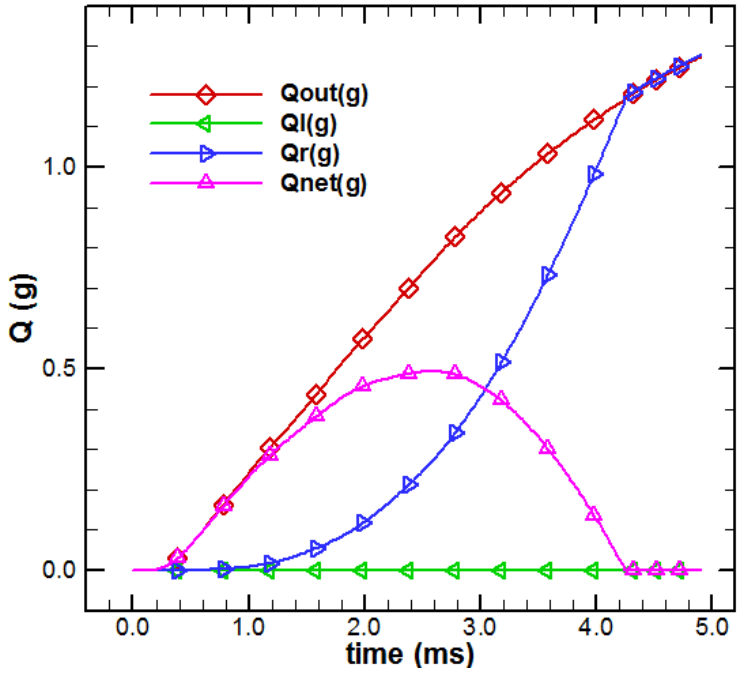

Figure 3.102: Mass flow amount history

The minimum gap height history for the shot is shown in Figure 3.103. The magnetic forces pulling the armature into the rail are well balanced with the fluid pressure at the beginning of the shot, keeping a fairly high gap height. As the armature picks up speed the fluid pressure increases the height of the interface gap. When the lubricant inside the pocket runs out, the interface begins to empty out and the gap begins to collapse. Initially, there is a large decrease in gap height at 4.2 ms, then the gap height almost stabilizes to the point where there is a sufficient supply of lubricant from the reservoir to maintain a large enough gap to prevent surface wear. As the shot ends, the interface is still full enough to maintain a minimum gap height of about 3.5 μm. This could explain why the shot has only a weak transition.

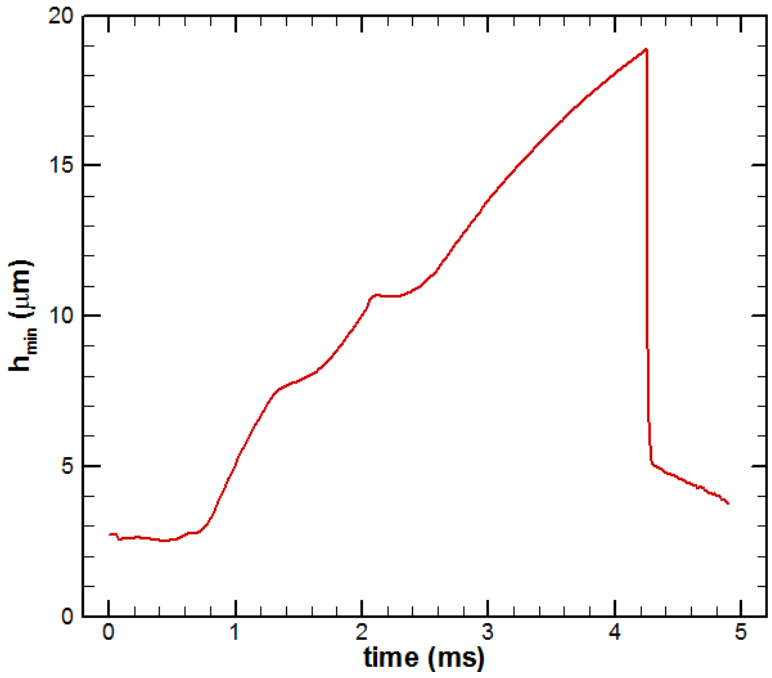

Figure 3.103: Minimum film thickness history

The lubricant pressures at different times are displayed in Figure 3.104. The magnetic pressure is low over most of the interface and only significant at the trailing edge of the interface. There is no cavitation predicted inside the interface. The fluid pressure goes from having a two-peaked shape to almost a parabolic shape, then back to a two-peaked shape at the end of the shot. At a time of 4.5 ms the armature-rail interface is beginning to empty. This can be seen because there is no fluid pressure in the empty region.

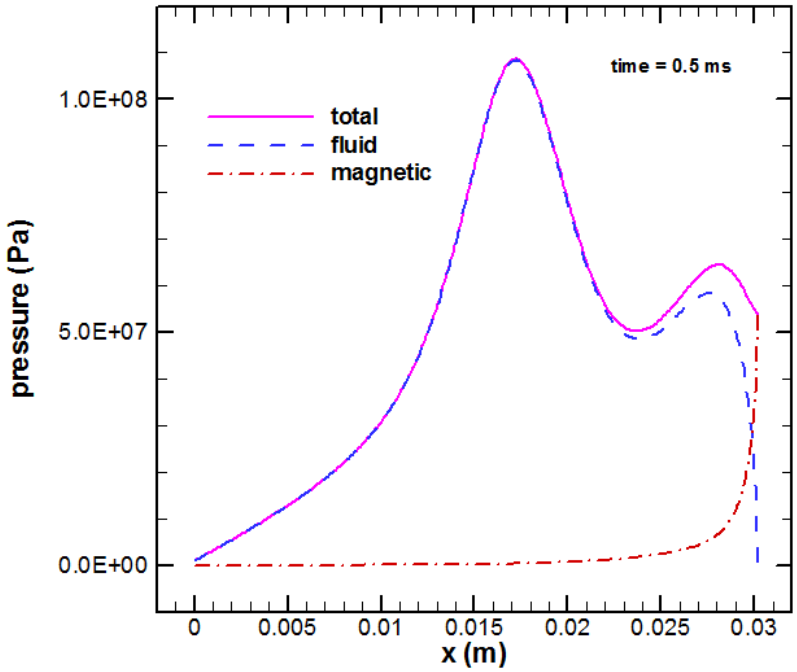

(a)

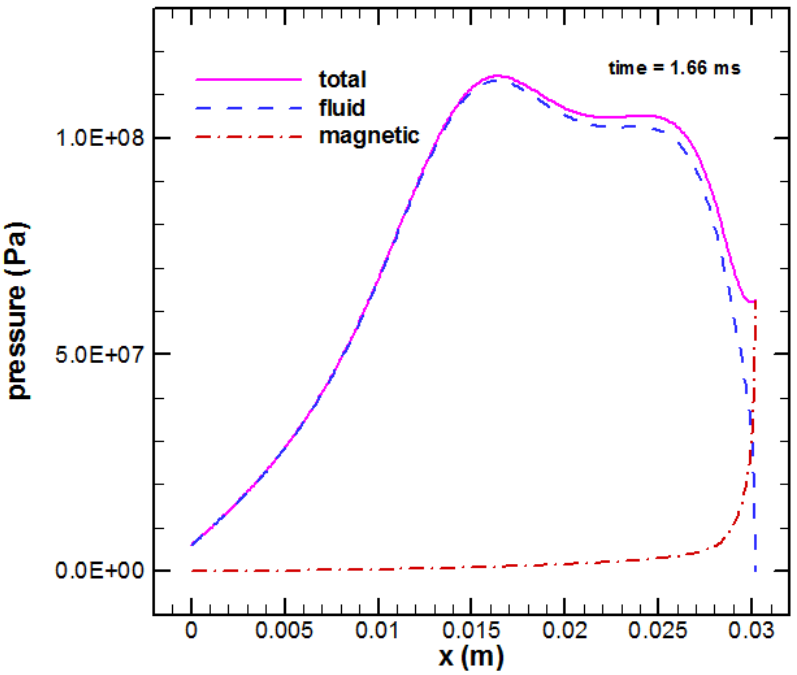

(b)

Figure 3.104: Pressures in the fluid at different times

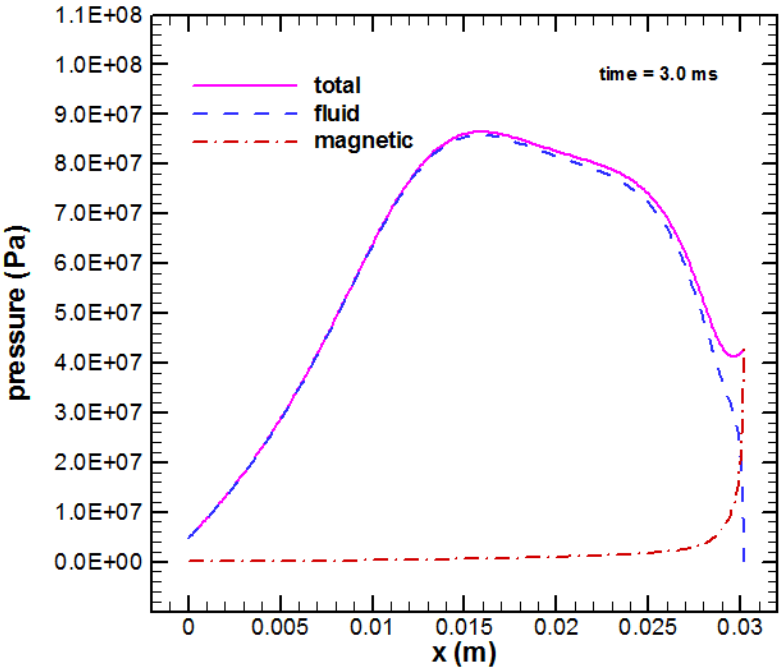

(c)

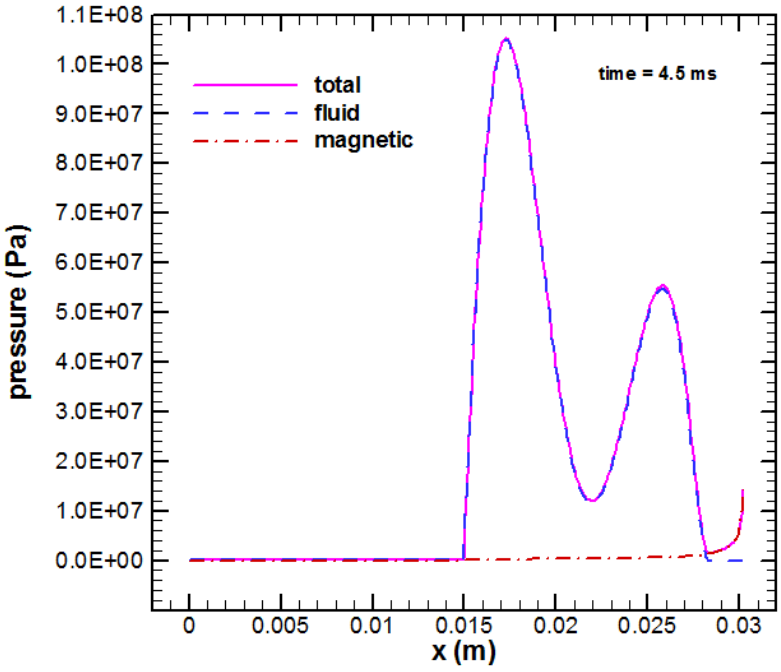

(d)

Figure 3.104 continued

Figure 3.105 shows the distributed forces acting on the armature in the transverse direction. The positive forces push the armature away from the rail, while the negative forces pull it closer. The magnetic force is similar in shape for all of the times but has different magnitudes. The contact force is fairly small by 0.5 ms and almost nonexistent over most of the shot. The fluid pressure is as shown in the previous figure. The total distributed force is the sum of the three other forces.

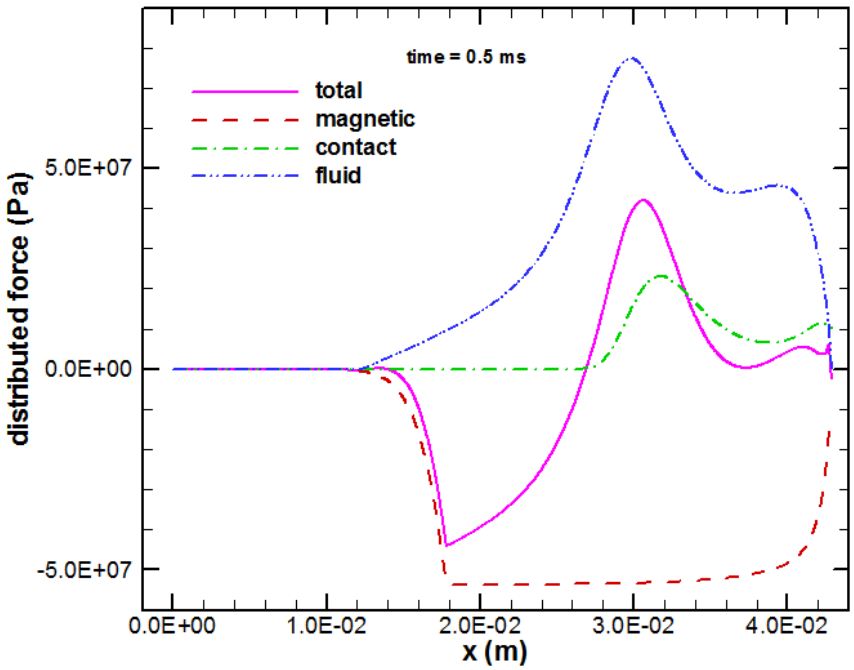

(a)

Figure 3.105: Distributed forces on the armature leg at different times

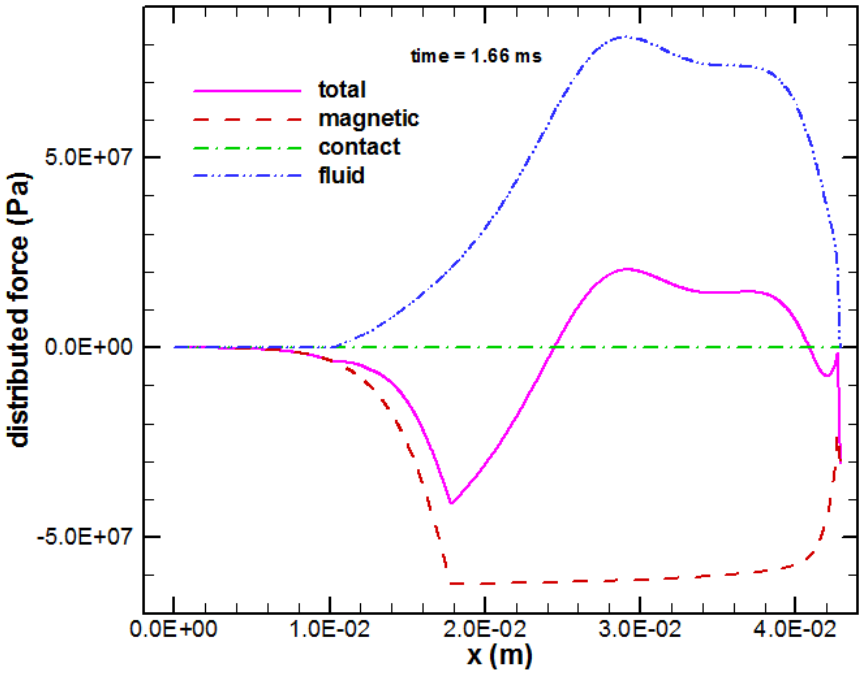

(b)

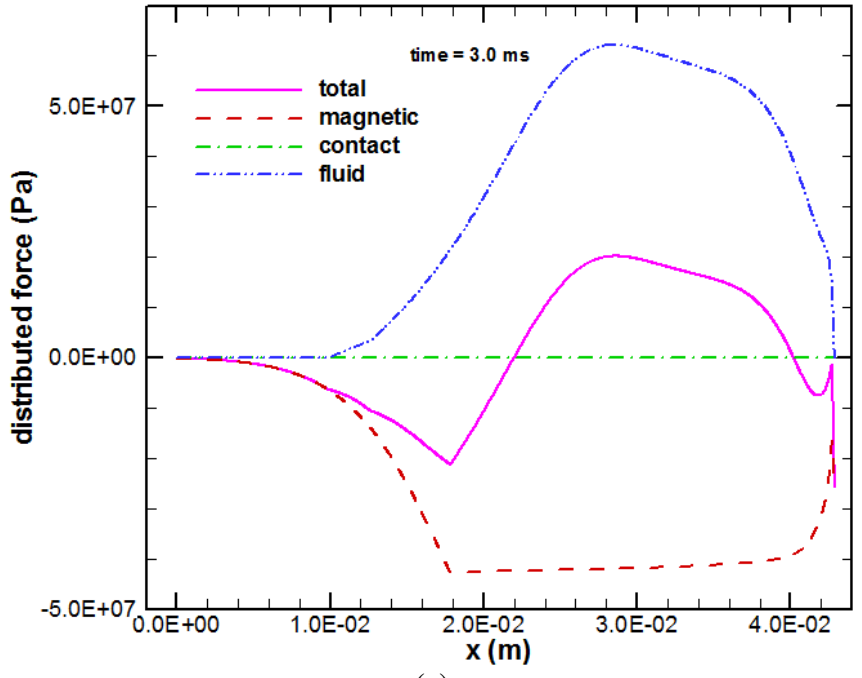

(c)

Figure 3.105 continued

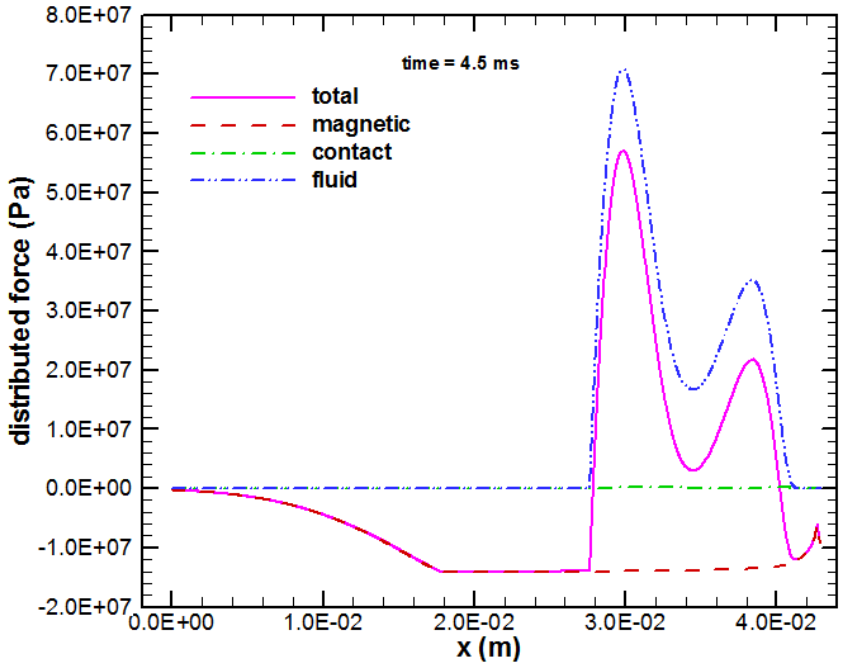

(d)

Figure 3.105 continued

Figure 3.106 presents the nondimensional interface gap profile at different times. At a time of 0.0 ms, the contact pressure alone deforms the gap. As the shot proceeds the armature is deformed by the forces acting on it resulting in the gap profiles shown. Because the pressure in the lubricant is well balanced with the magnetic forces exerted, at a time of 0.5 ms the gap is approximately the same as it was when the shot started. The gap height rises as the armature speeds up. When the interface begins to empty out the gap begins to collapse but is still generally higher than its initial position as the shot nears the end at 4.5 ms.

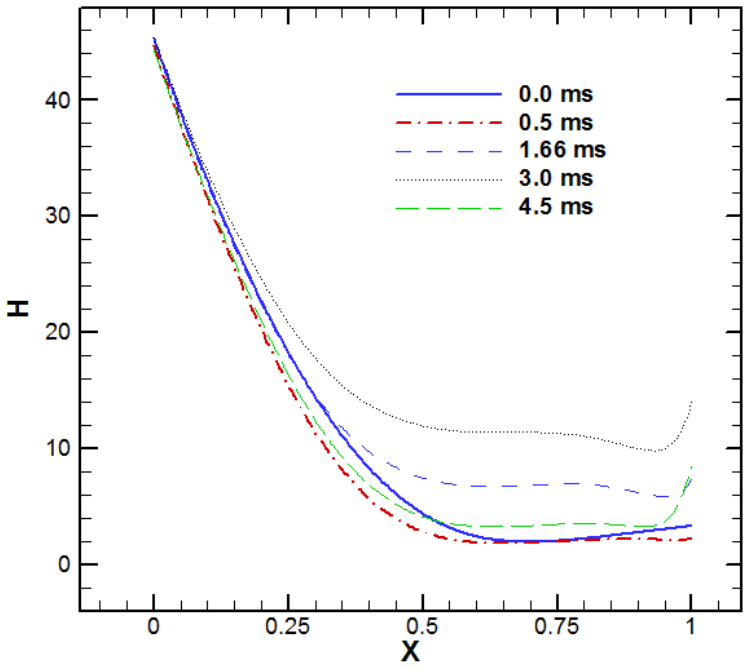

Figure 3.106: Nondimensional interface gap profiles at different times

The lubricant flow patterns in the armature-rail interface at different times are presented in Figure 3.107. Toward the beginning of the shot, the gap geometry drags a lot of lubricant along. As the armature speeds up and the gap height increases, more lubricant flows out of the trailing edge. After the pocket empties out the interface begins to empty out and the gap falls. At 4.5 ms it is seen that there is no lubricant flow in the empty portion of the interface. In this case there is still lubricant being supplied to the interface by the reservoir at the end of the shot as was seen with NRL shot 223.

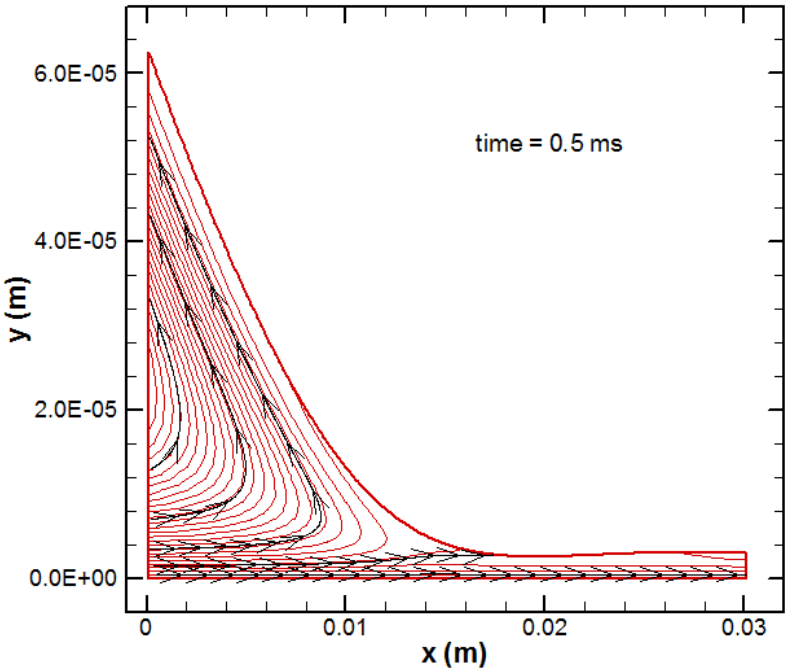

(a)

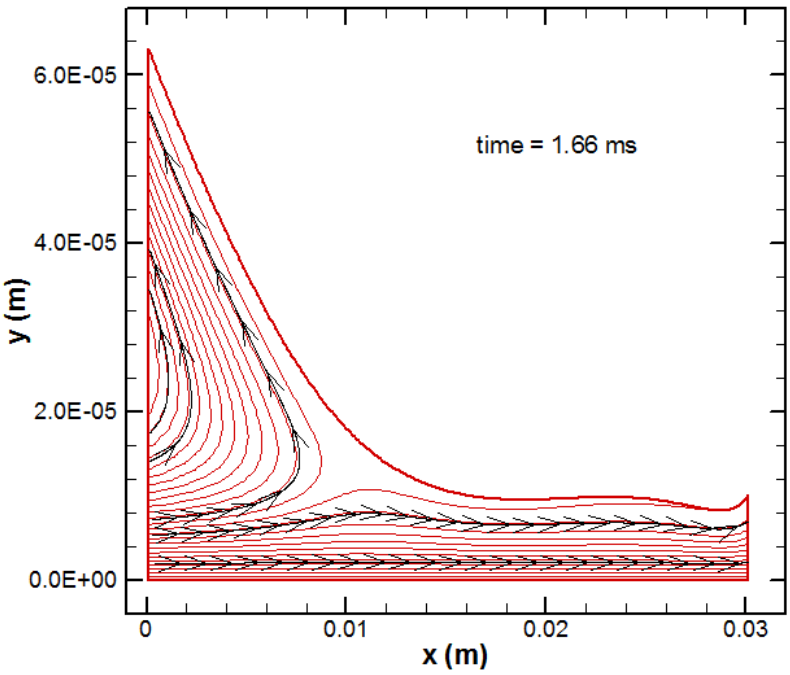

(b)

Figure 3.107: Fluid flow patterns at different times

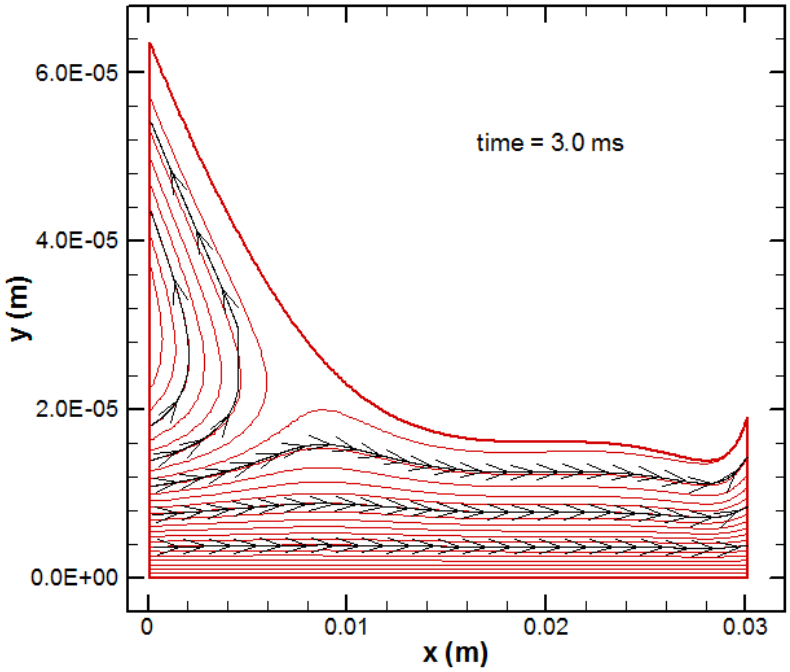

(c)

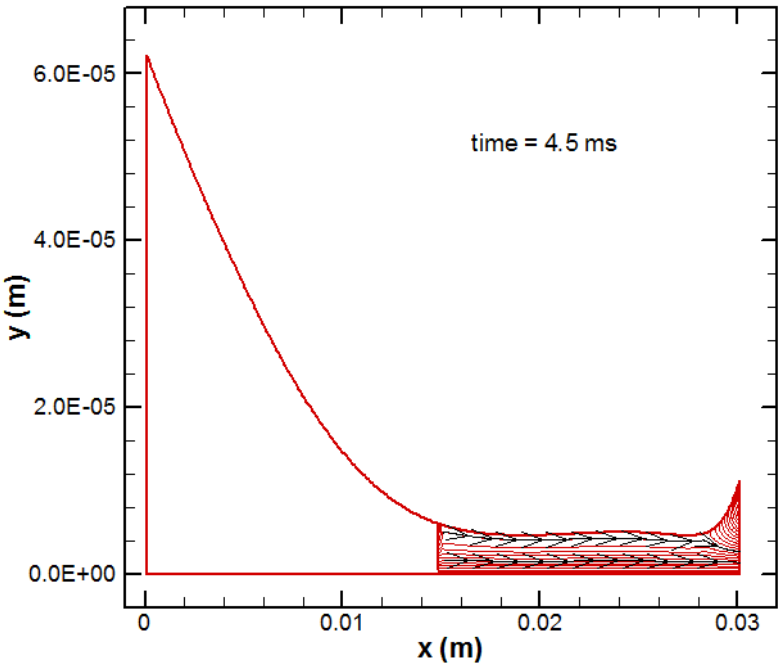

(d)

Figure 3.107 continued

The experimental muzzle voltage for IAP shot 7 showed some similarities with that of NRL shot 223 in that some voltage began building up at 4.15 ms, however, it remained under 50 V until the end of the shot. The armature used for IAP shot 7 was analyzed with the same model used for NRL shot 223 by updating the projected area used for the electromagnetic and thermal fields, finding new equivalent cantilever beams to calculate the armature deflection, and re-modeling the injection system. The results show similar circumstances. The reservoir is predicted to contain over 50 percent of the initial load at the end of the shot, and the pocket is determined to empty out around 4.2 ms causing the interface to begin drying out. Also the gap height is predicted to sharply decrease when the pocket emptied out and then decrease more gradually as the shot ends. The predicted interface dry-out coincides very well with the slight increase in muzzle voltage as was found when analyzing NRL shot 223.

3.5 GTL-2-4C

The GTL-2-4C armature was launched on the launcher designed by the University of Texas at Austin's Institute for Advanced Technology (IAT). All of the previous launchers have been rectangular bore launchers, meaning the armature is launched through a rectangular channel made by the rails. The launcher used for the GTL-2-4C armature is a round bore launcher with a rail length of 4.0 m. The bore diameter of the launcher is 2.126 in. A cross section of the rails is shown in Figure 3.109.

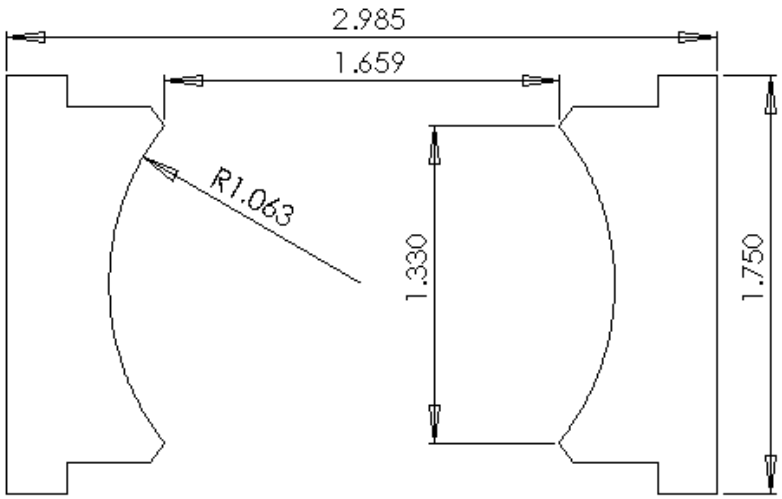

Figure 3.108: Sketch of the IAT GTL-2-4C rails, dimensions are in inches

To fit inside the rails the armature has a cylindrical shape as opposed to the extruded planar shapes of the armatures previously discussed. The armature is almost three inches long with a maximum diameter of 2.153 in at the trailing edge creating an interference fit. The armature has a slit which divides the trailing edges into four pads which contact the rails. The maximum lubricated length for this armature is 2.180 in. There are four pockets, each with its own conduit and reservoir to deliver the lubricant. Each cartridge is initially filled with a charge of 6.7 g of lubricant. The armature and empty cartridges have a combined mass of 390.04 g. Due to the cylindrical shape of the armature and launcher, special consideration will have to be taken to simulate the shot. The previous simulations used symmetry to analyze a half armature model, this simulation will use symmetry to analyze a quarter armature model.

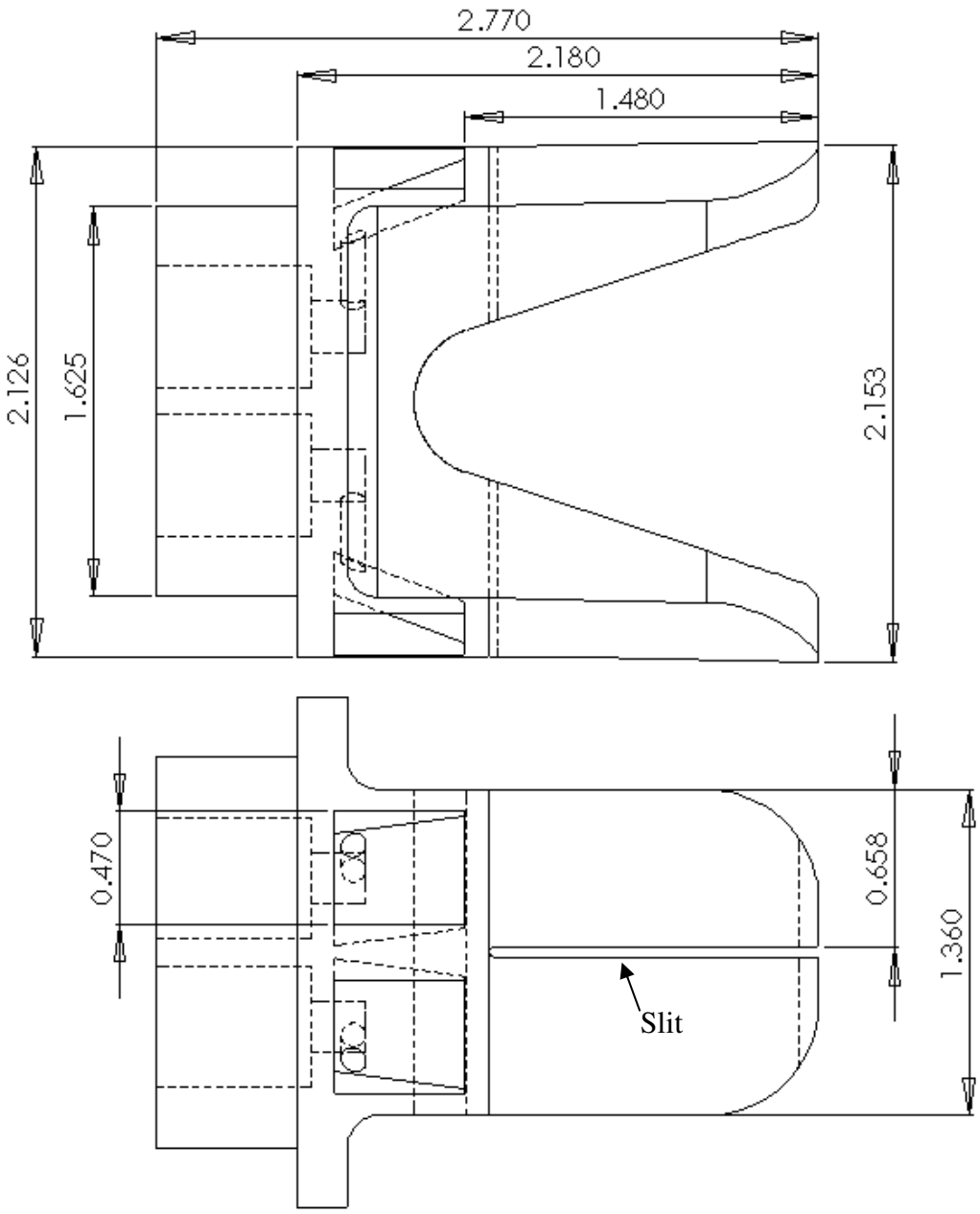

Figure 3.109: Sketch of the IAT GTL-2-4C armature, dimensions are in inches

3.5.1 Electromagnetic Field Modeling

The model previously used to analyze the electromagnetic field assumes that the electromagnetic forces acting on the armature act in only the x and y directions. In order to use the same model on the GTL-2-4C armature, COMSOL is used to show that the

electromagnetic forces act dominantly in the x and y directions. A 3D steady state model of the armature and rails is created as it was for the previous armatures. It is shown in Figure 3.110 that inside the armature the electromagnetic forces are dominant in the x and y directions shown on the left. On the right, one can see that the force arrows inside the armature have only a small component in the horizontal or z direction.

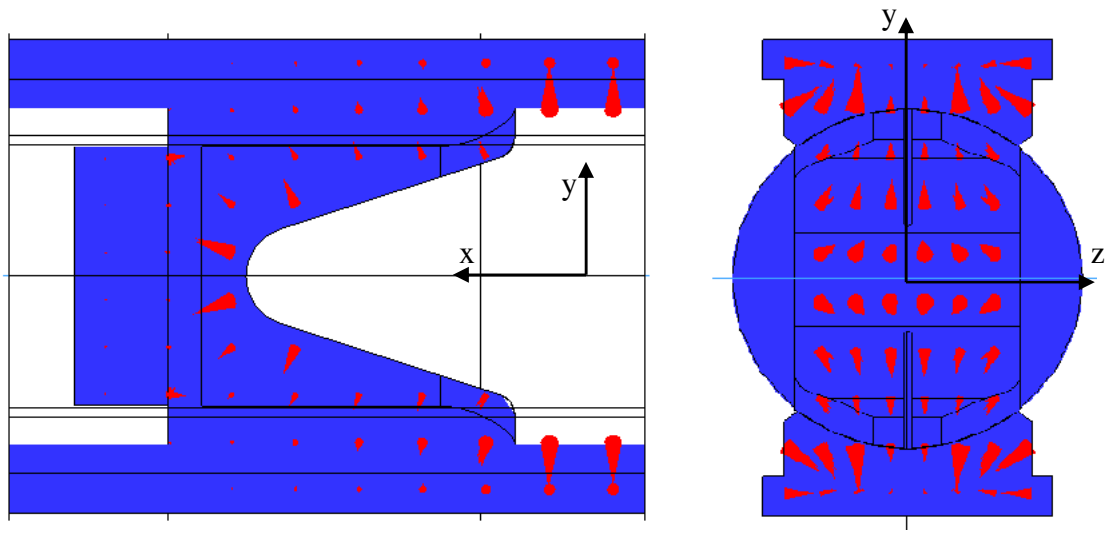

Figure 3.110: 3D COMSOL steady state electromagnetic forces

Validations must also be done to ensure that the magnetic field can accurately be simplified to one dimension. Figure 3.111 displays the results of the (a) the COMSOL calculation of the magnetic flux density and (b) the finite difference calculation of magnetic flux density using the 2D projected area in the direction into the page. The two methods agree fairly well. There is a difference in the magnetic flux density calculated on the outsides of the rails so a correction factor will again be needed.

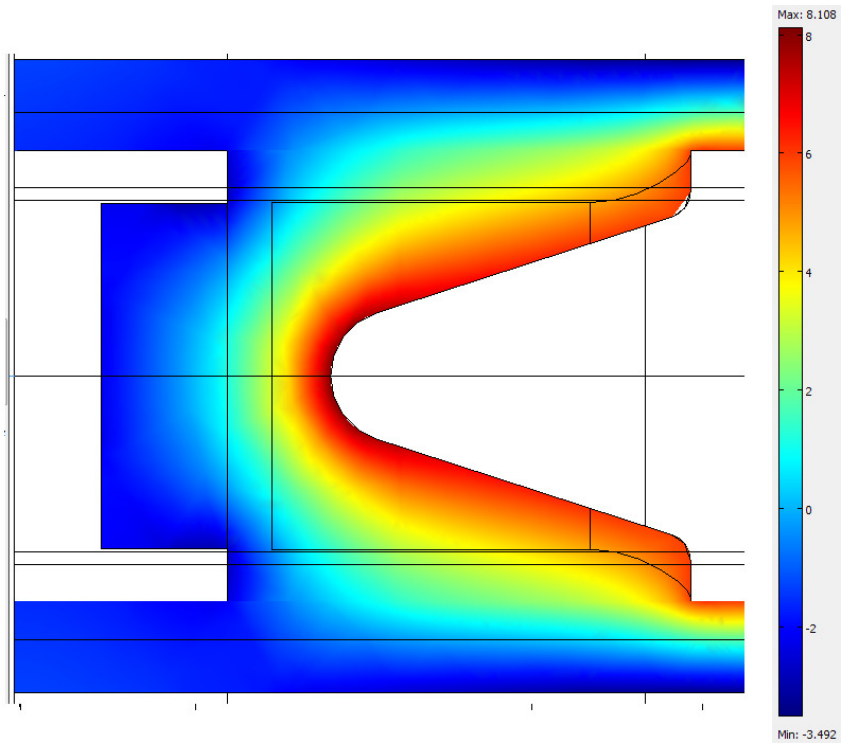

(a)

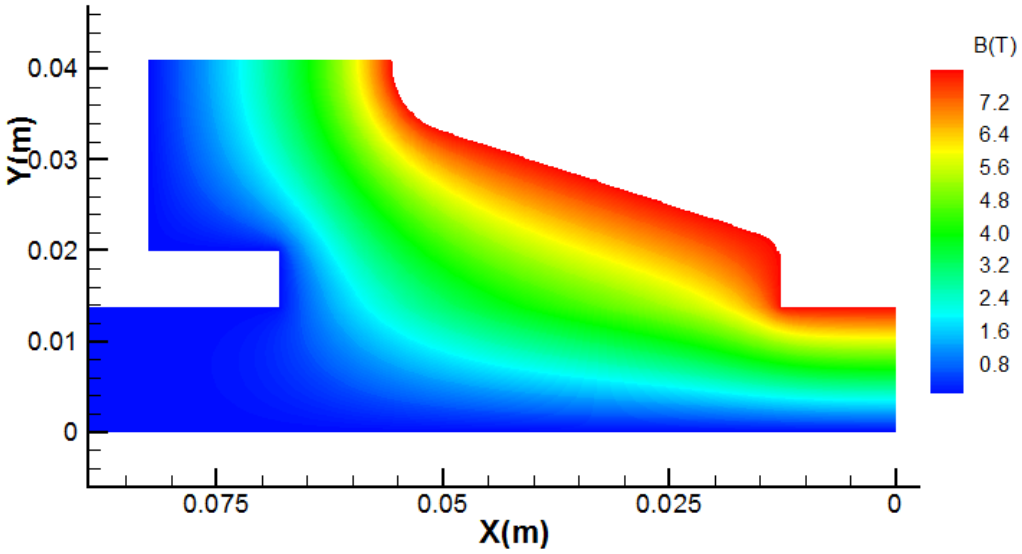

(b)

Figure 3.111: Comparison of magnetic flux distributions calculated by (a) COMSOL and (b) finite difference method, units in T

The electric current will also be dominant in the x and y directions if the force is dominant in the x and y directions and the magnetic flux is dominant in the z direction. Figure 3.112 illustrates the similar current distributions achieved by both methods. For a steady state case, the electric current is fairly evenly distributed with concentrations at the trailing edges of the interface, the central radius on the rear of the armature, and at the sharp corner inside the leading edge of the interface. The basic assumption that the magnetic flux is dominant in the direction into the page is validated in Figure 3.113. The magnetic flux densities are negligibly small in the other two directions.

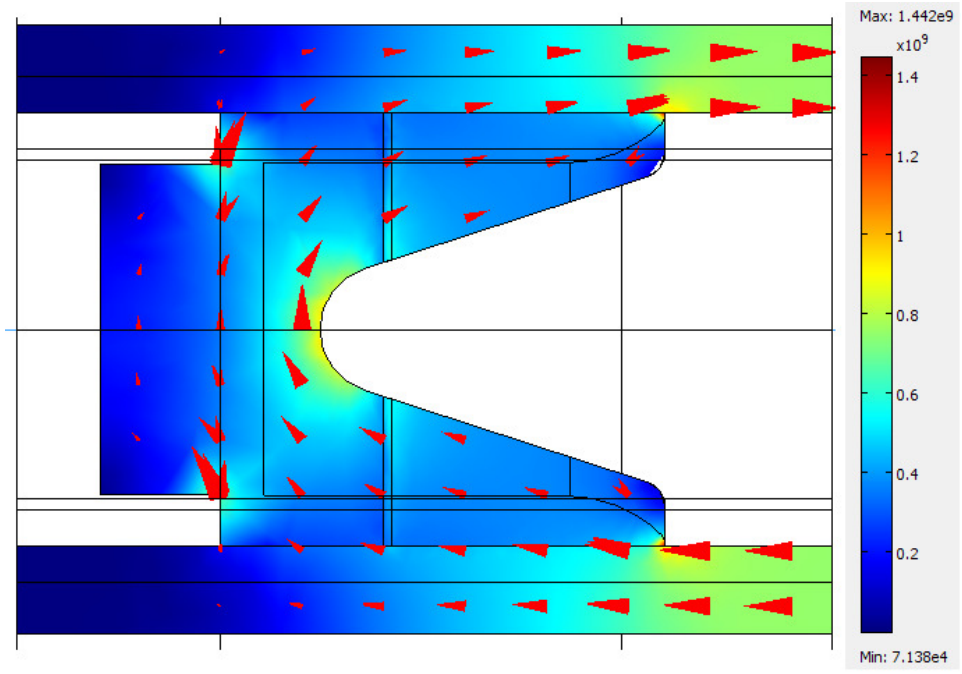

(a)

Figure 3.112: Comparison of current distributions calculated by (a) COMSOL and (b) finite difference method, units in A/m^2

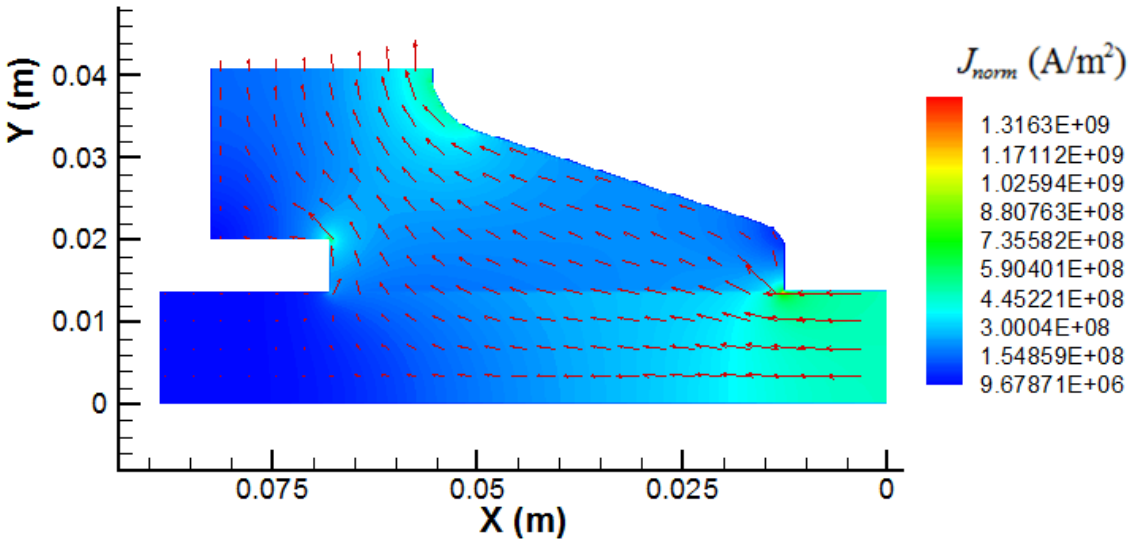

(b)

Figure 3.112 continued

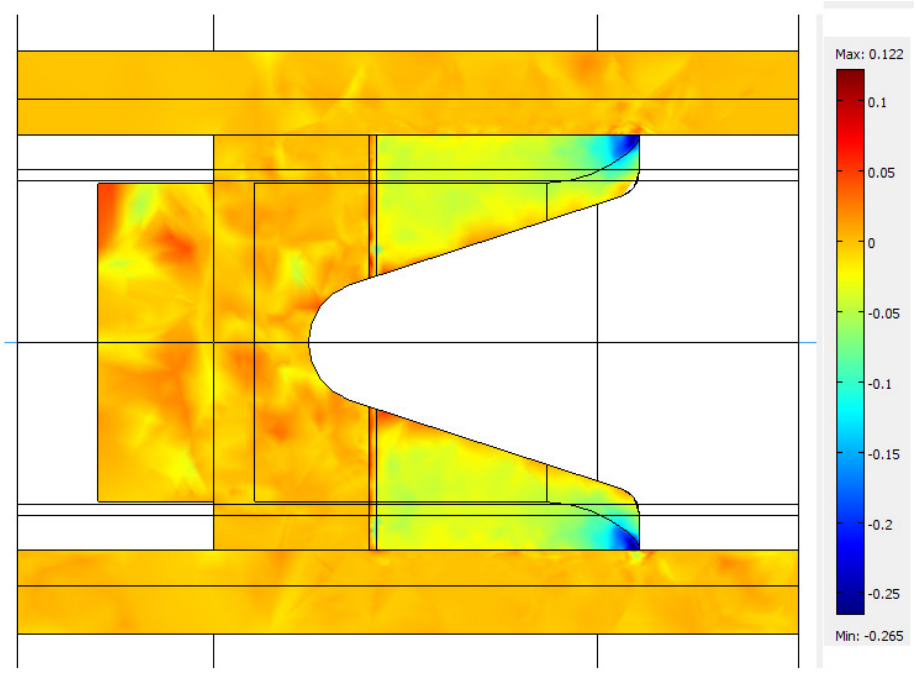

(a)

Figure 3.113: Magnetic flux density in the direction (a) parallel to the rails (b) transverse to the rails, units in T

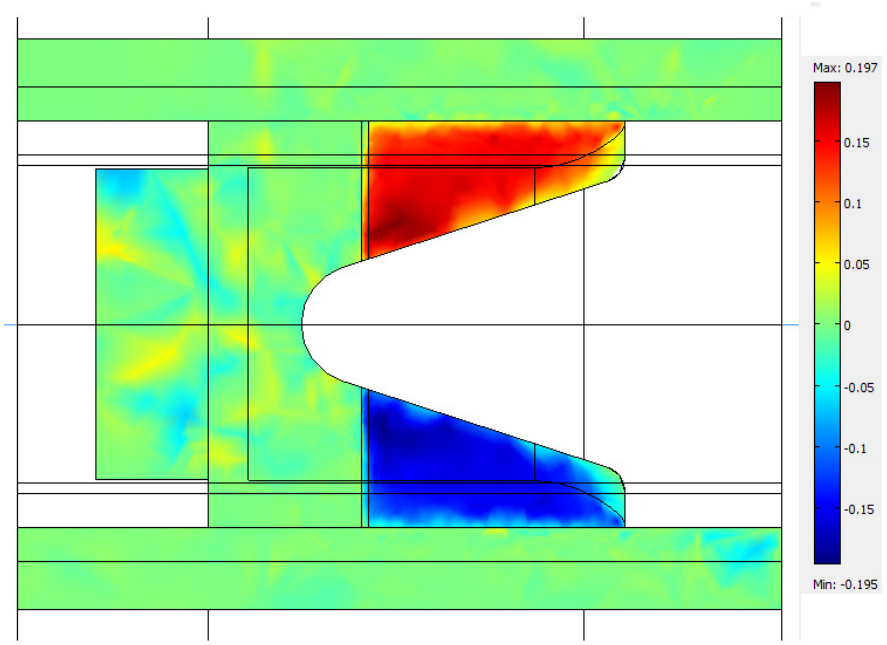

(b)

Figure 3.113 continued

3.5.2 Thermal Field Modeling

To calculate the thermal field on this armature a 3D COMSOL General Heat Transfer (htgh) model is used and compared to the 2D finite difference model using the area of a slice along one side of the slit through the rear of the armature. Using symmetry only half of the armature is modeled. In the model, the radii on the trailing edges of the armature are neglected for modeling simplicity. To mimic the operating conditions, the surfaces which face the rail are constrained to the low temperature of 20 °C shown in light blue in the top of Figure 3.114. Surfaces which are most likely to have high current densities and, thus, a large amount of joule heating shown in dark blue at the bottom of Figure 3.114 are given a high temperature. All other boundaries are adiabatic. The results of the 3D COMSOL simulation agree very well with the simplified 2D finite difference calculation as illustrated in Figure 3.115.

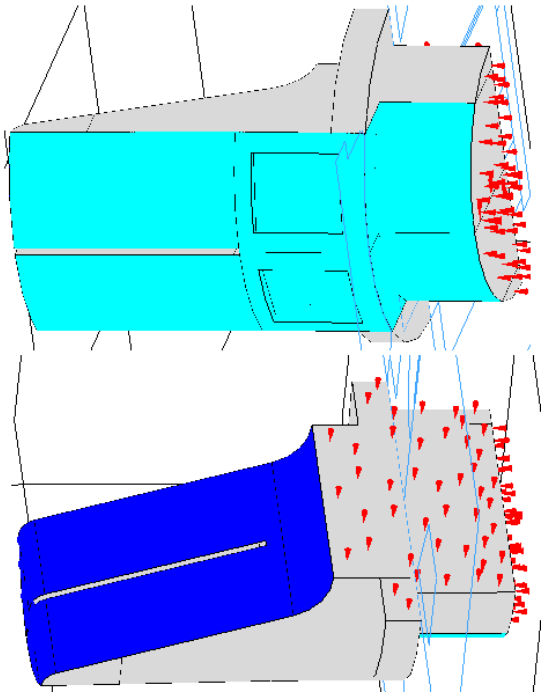

Figure 3.114: COMSOL model, light blue is a low temperature boundary, dark blue is a high temperature boundary, and grey or tan is an adiabatic boundary

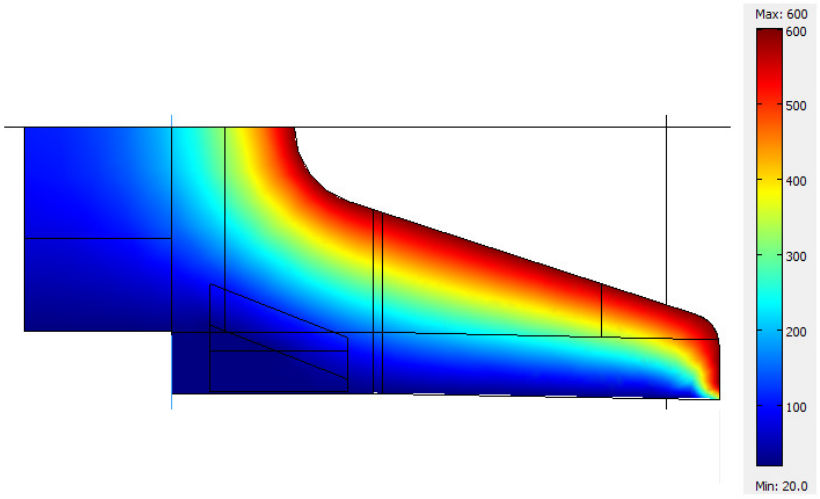

(a)

Figure 3.115: Temperature field validation calculated by (a) COMSOL and (b) finite difference method, units in C

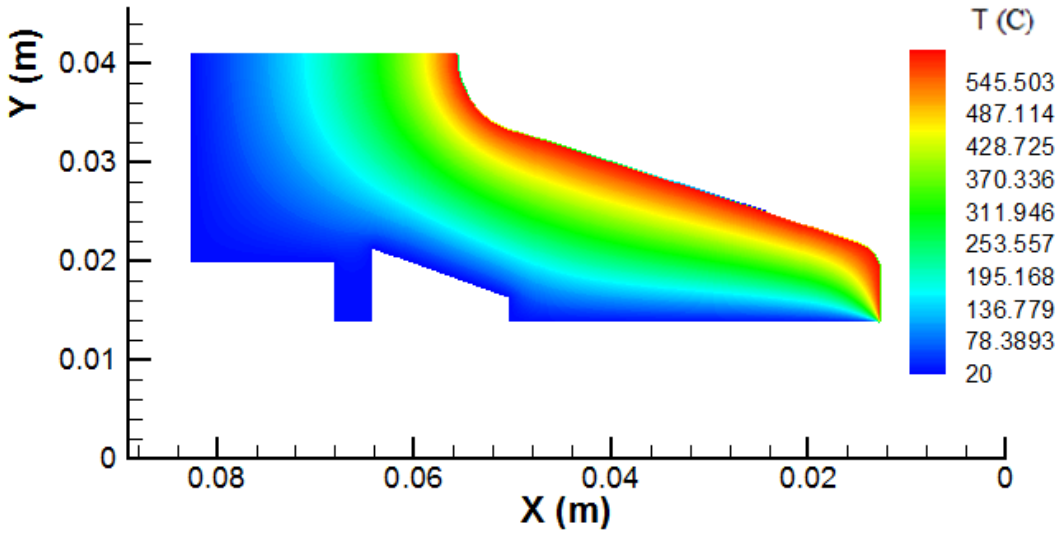

(b)

Figure 3.115 continued

3.5.3 Armature Deflection Modeling

It was previously shown that the electromagnetic forces in the armature are dominant in the x and y directions. The lubricant pressure will deform the armature in the radial direction. However, the radius of the armature will be much larger than the lubricant gap height allowing for the curvature of the armature to be neglected when calculating the lubricant pressure. Therefore, to model the armature deflection due to non-thermal forces, a 3D COMSOL Structural Mechanics Module is used applying radial forces at the trailing edge of the armature. The armature is constrained at the leading edge to have no motion in the direction of the rail. Again, the radii on the trailing edges are neglected for modeling simplicity. The radial deflection at the slit between the armature pads is compared to the vertical deflection of an equivalent Euler-Bernoulli cantilever beam. The cantilever support will be set at the leading edge of the armature-rail interface. The cross sectional properties of the equivalent beam will be adjusted until

the deflections match. The cases displayed in Figure 3.116 have distributed loads of 500 N, 1000 N, 2000 N, and 4000 N applied radially to the trailing edge of each of the four pads on the COMSOL model and vertically on the end of the equivalent cantilever beam in the Euler-Bernoulli model. The two methods are almost identical even inside the pocket region.

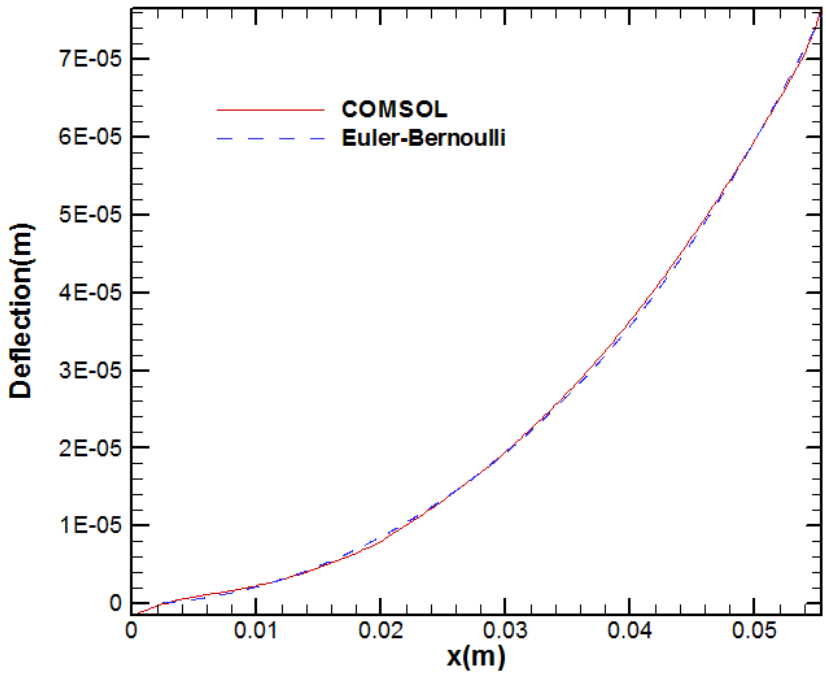

(a)

Figure 3.116: Comparison of armature wing deflection between COMSOL and Euler-Bernoulli models with a shear force of (a) 500 N, (b) 1000 N, (c) 2000 N, and (d) 4000 N

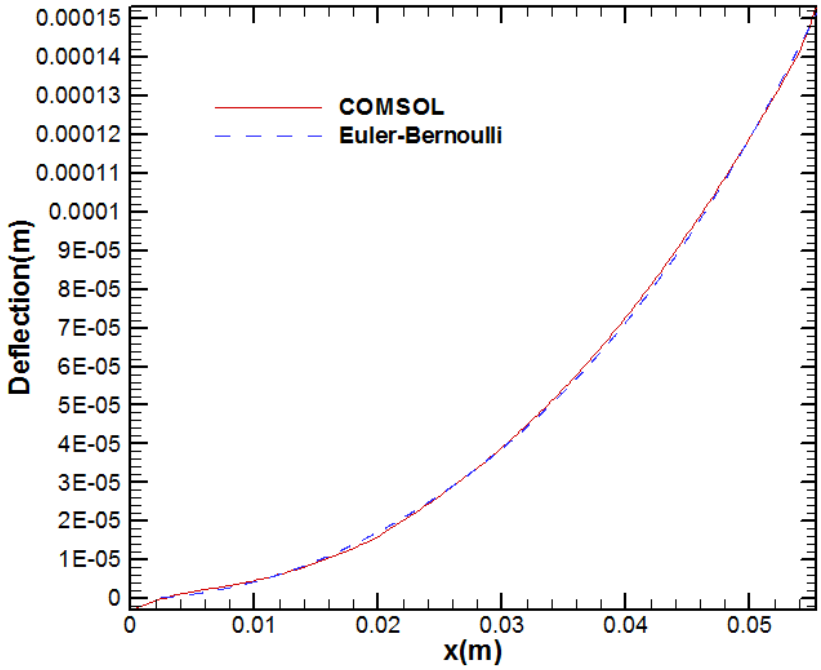

(b)

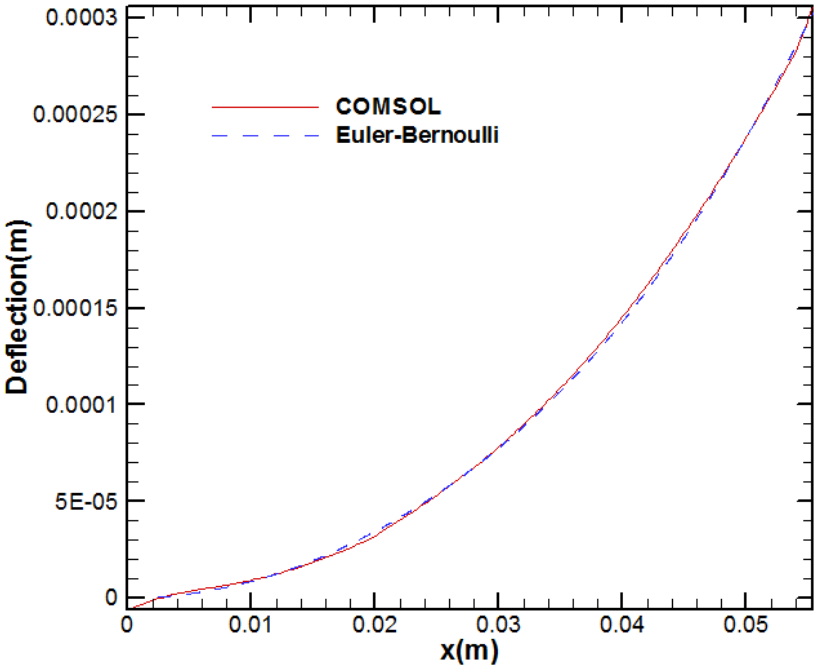

(c)

Figure 3.116 continued

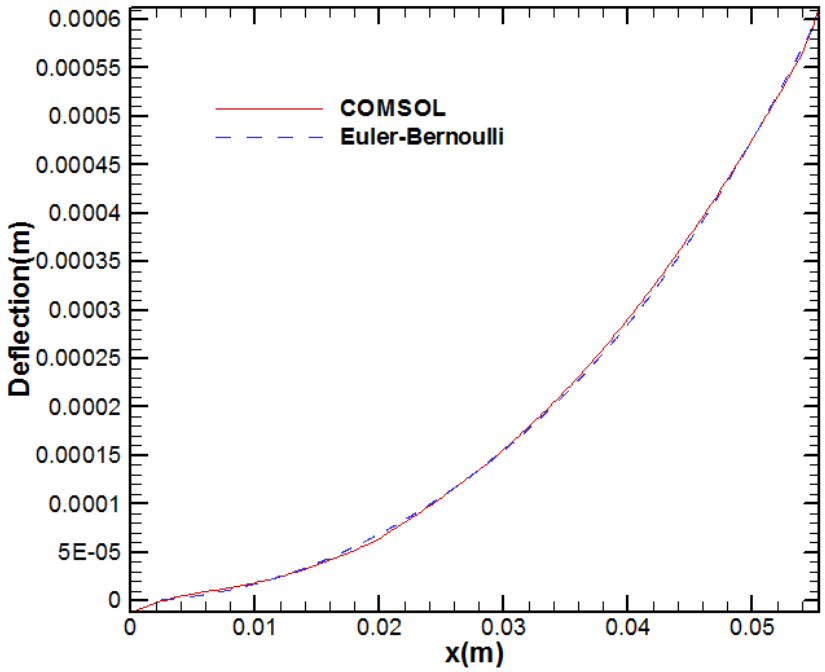

(d)

Figure 3.116 continued

The calculation of the contact pressure on the armature must also be validated. A fully three dimensional model could be used as it was for the deflection due to a shear forces and thermal effects, however, three dimensional ANSYS contact models require a large amount of computational time and resources. While analyzing the previous armatures, it was assumed that the contact pressure will have small or negligible effect on the shot. Therefore, only a rough estimate of the contact pressure is needed as long as the deflection due to contact agreed with the deflection found in the ANSYS model. The same assumptions are used to check the contact analysis on the GTL-2-4C armature. The armature is approximated with its projected area allowing a two dimensional contact analysis to be conducted in the same way as it has been done for the previous armatures. The results from the ANSYS model are compared to the method of using the Greenwood-

Williamson model along with the equivalent cantilever beam cross section previously determined. Figure 3.117 shows that there is quite a bit of variation in the contact pressure between the two simulations using interferences of 1.0312 mm and 1.1582 mm. However, the contact pressures are on the same order of magnitude and at approximately the same locations. The deflection caused by contact calculated with the two methods is compared in Figure 3.118. The models calculate approximately the same amount of deflection due to contact on the armature even with such variation in the contact pressure calculated.

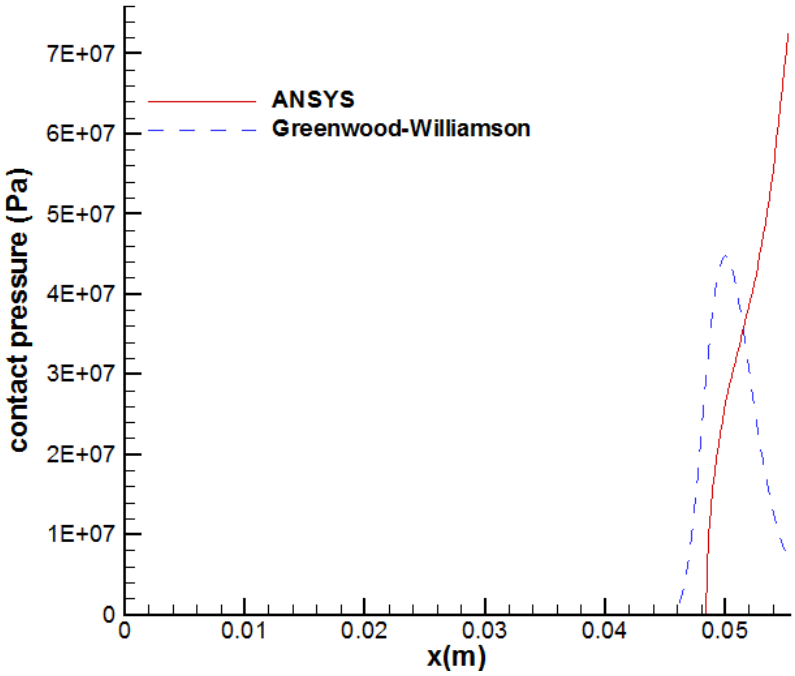

(a)

Figure 3.117: ANSYS and Greenwood-Williamson model contact pressure for an interference of (a) 1.0312 mm and (b) 1.1582 mm

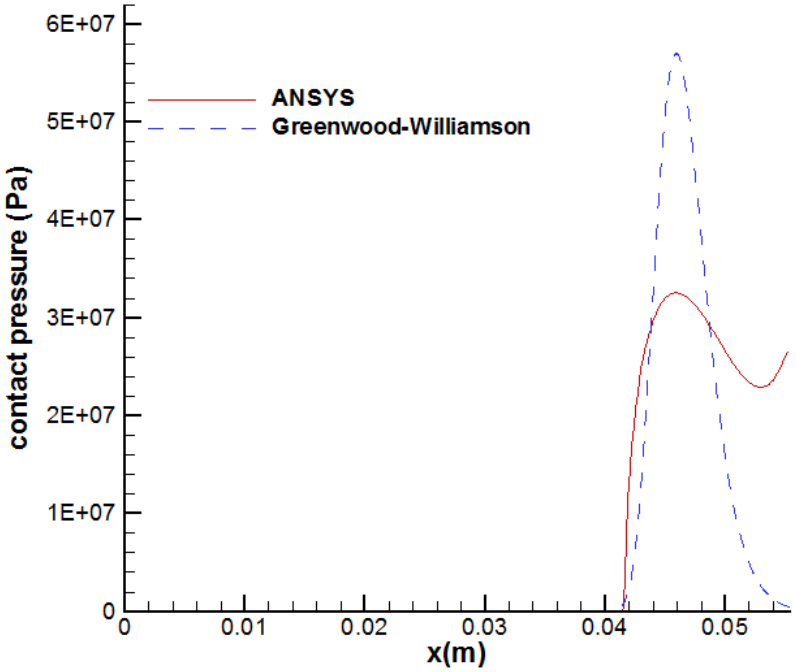

(b)

Figure 3.117 continued

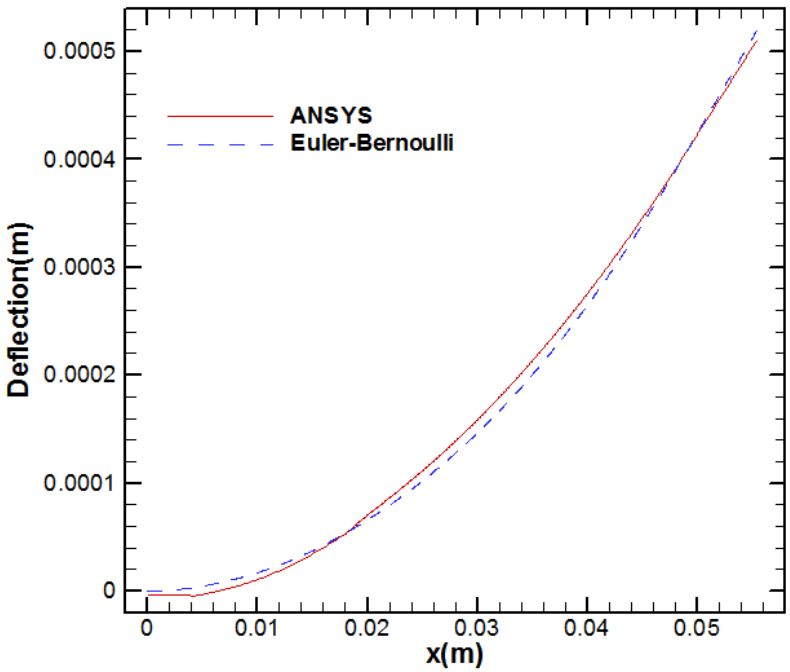

(a)

Figure 3.118: ANSYS and Euler-Bernoulli contact deformation for an interference of (a) 1.0312 mm and (b) 1.1582 mm

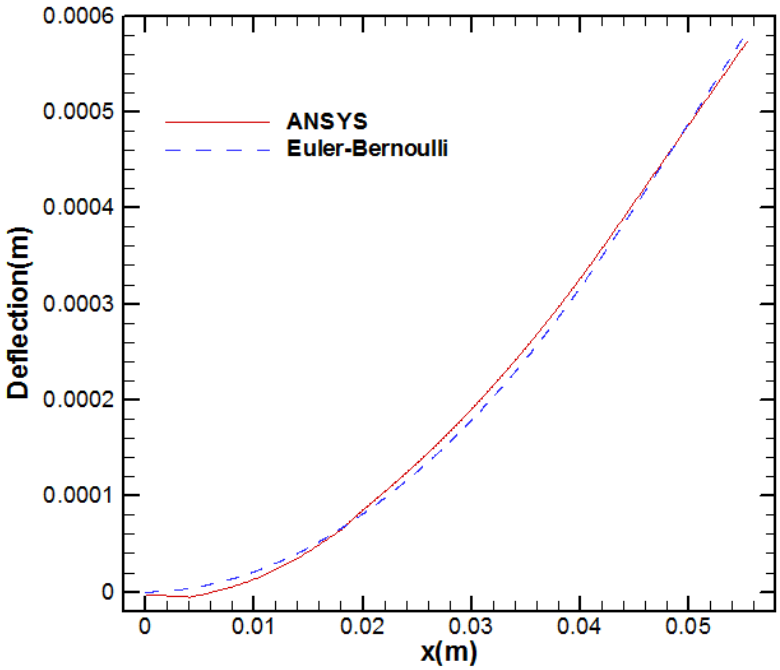

(b)

Figure 3.118 continued

The equivalent cantilever beam used to analyze the armature deflection due to thermal loads is found by calculating the thermal field and resulting deflection using the same COMSOL model used to validate the finite difference thermal field. The three dimensional COMSOL thermal model is coupled with the COMSOL model used to calculate the deflection due to a radial force on the trailing edge of the armature pad. A radial distributed force of 300 N is applied to the trailing edge of each armature pad and the high temperature boundary condition is varied. The radial deflection is taken from the bottom of the armature along the edge of the slit and compared to the Euler-Bernoulli model. The cross sectional properties of the thermal beam are adjusted until the two models agree as presented in Figure 3.119.

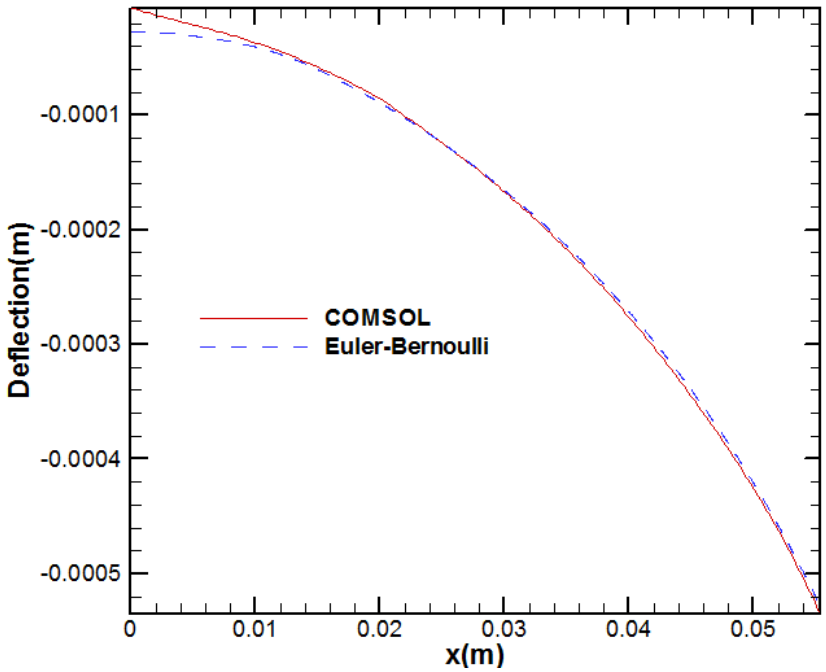

(a)

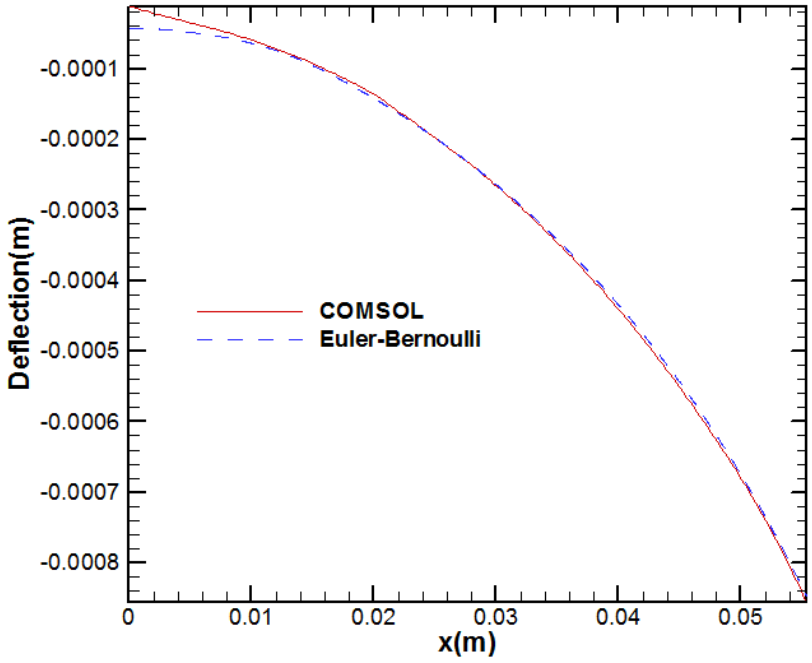

(b)

Figure 3.119: Comparison of armature wing deflection between COMSOL and Euler-Bernoulli models for high boundary temperatures of (a) 200 °C, (b) 300 °C, (c) 400 °C, and (d) 600 °C

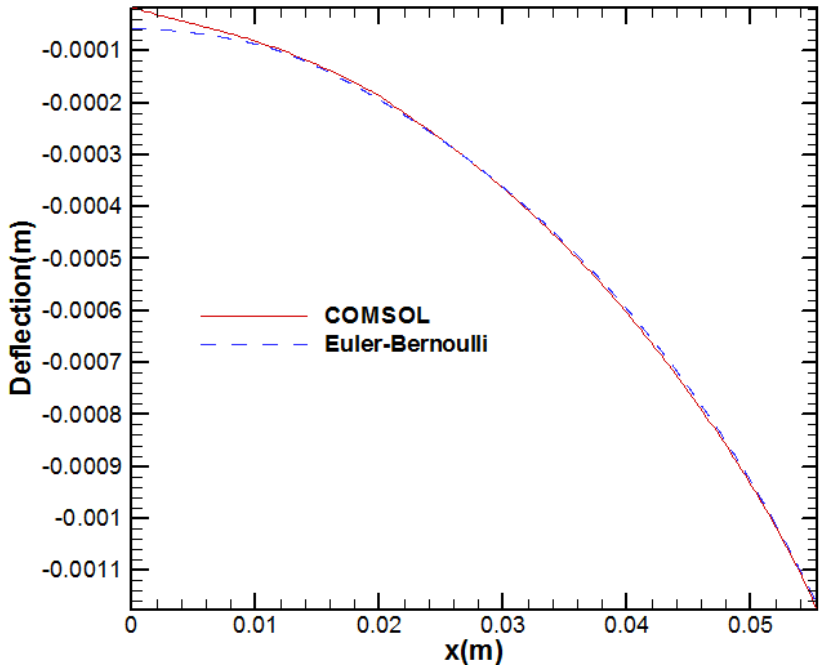

(c)

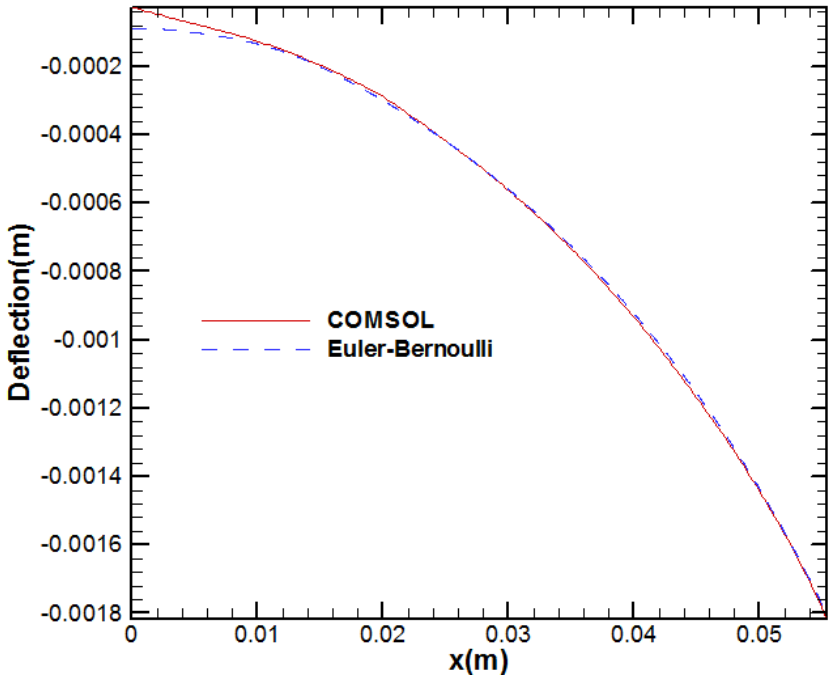

(d)

Figure 3.119 continued

3.5.4 Lubricant Modeling

Lubricant injection system for the IAT GTL-2-4C armature uses four reservoirs with separate injection conduits and pockets for each. Using symmetry, one of the four systems is analyzed. The injection system for one pocket is similar to the injection system used for IAP shot 7, except instead of a tee to split the flow to two pockets there is an elbow to divert it to one pocket. A schematic of the injection system is presented in Figure 3.120 with the calculational nodes identified. The conduit running out of the elbow is smaller in diameter than the conduit running into it causing further losses. Equations 3.41 and 3.42 calculate the pressure at nodes 2 and 3. When Equations 3.41-3.44 are combined, they yield the quadratic equation which can be solved for the mass flow rate of lubricant out of the reservoir, Equation 3.45. The pressures at nodes 1 and 3 are calculated as they have been for the previous models. Here, the friction factors, f_D and f_A, for conduits D and A are .017 and .022 respectively and the head loss factors, k_{eD} and k_{eA}, are about 0.5 and 1.2 respectively. Additionally, the equivalent length over diameter added by the elobw, k_{elbow}, is 30.

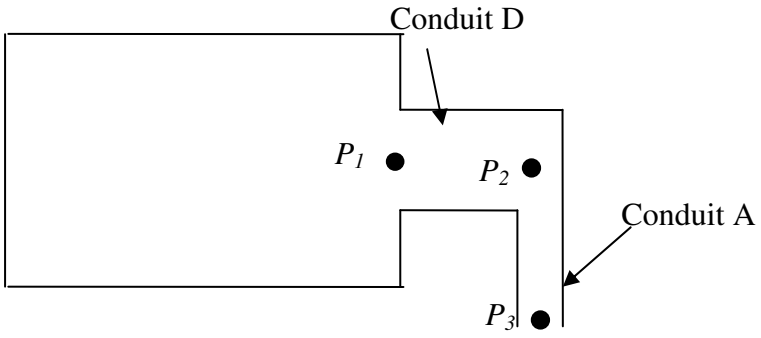

Figure 3.120: Schematic of the GTL-2-4C injection system and node points (not to scale)

$$P_2 = P_1 - \rho\left[\left(f_D\frac{L_D}{2R_D} + k_{eD}\right)\frac{V_D^2}{2} + L_D\frac{\partial V_D}{\partial t}\right] + \rho a L_D - \rho\frac{V_D^2}{2} \tag{3.41}$$

$$P_3 = P_2 - \rho\left\{\left[f_A\left(k_{elbow} + \frac{L_A}{2R_A}\right) + k_{eA}\right]\frac{V_A^2}{2} + L_A\frac{\partial V_A}{\partial t}\right\} + \rho\frac{V_D^2}{2} - \rho\frac{V_A^2}{2} \tag{3.42}$$

$$V_D = \frac{\dot{Q}}{\rho\pi R_D^2} \tag{3.43}$$

$$V_A = \frac{\dot{Q}}{\rho\pi R_A^2} \tag{3.44}$$

$$\begin{aligned}&\left\{\frac{1}{2\rho\pi^2 R_D^4}\left[f_D\frac{L_D}{2R_D} + k_{eD}\right] + \frac{1}{2\rho\pi^2 R_A^4}\left[f_A\left(k_{elbow} + \frac{L_A}{2R_A}\right) + k_{eA} + 1\right]\right\}\dot{Q}^2 \\ &+\left(\frac{L_D}{\pi R_D^2 dt} + \frac{L_A}{\pi R_A^2 dt}\right)\dot{Q} - \left(\left(\frac{L_D\dot{Q}_{pre}}{\pi R_D^2 dt} + \frac{L_A\dot{Q}_{pre}}{\pi R_A^2 dt}\right) + P_1 - P_3 + \rho a L_D\right) = 0\end{aligned} \tag{3.45}$$

The armature used for GTL-2-4C has a slit which splits the two armature-rail interfaces into four. As a result, the four pads are very narrow when compared to the length in the direction of motion. For the previous armatures, the long bearing assumption has been used to simplify the Reynolds Equation for the interface. This was done to reduce computational time and memory although it results in some error and neglects lubricant leakage from the side of the armature entirely. However, the four pads on GTL-2-4C are so narrow that there may be a large amount of lubricant leaking from the side of the armature. To account for this, the Reynolds Equation is derived for a two dimensional pressure field as Equation 3.46, or in nondimensional form Equation 3.47. This derivation of the Reynolds Equation assumes that the armature deforms in the z

direction only (towards or away from the rail) and neglects cavitation. Therefore, the gap height, local gap height, and flow factors are not functions of the y coordinate.

$$\frac{\partial}{\partial x}\left(\phi_x h^3 \frac{\partial P}{\partial x}\right)+\frac{\partial}{\partial y}\left(\phi_x h^3 \frac{\partial P}{\partial y}\right)=3\left(2\mu U+\rho a h_T^2\right)\frac{\partial h_T}{\partial x}+6\mu U\sigma\frac{\partial \phi_S}{\partial x}+12\mu\frac{\partial h_T}{\partial t} \tag{3.46}$$

$$\begin{aligned}&\frac{\partial}{\partial \bar{x}}\left(\phi_x \bar{h}^3 \frac{\partial \Phi}{\partial \bar{x}}\right)+\frac{4L^2}{Width^2}\frac{\partial}{\partial \bar{y}}\left(\phi_x \bar{h}^3 \frac{\partial \Phi}{\partial \bar{y}}\right)\\&=6\beta\frac{U}{U_{ref}}\frac{\partial \bar{h}_T}{\partial \bar{x}}+6\beta\bar{\sigma}\frac{U}{U_{ref}}\frac{\partial \phi_S}{\partial \bar{x}}+\Omega\bar{\rho}\frac{\partial \bar{h}_T^3}{\partial \bar{x}}+12\beta\lambda\frac{\partial \bar{h}_T}{\partial \bar{t}}\end{aligned} \tag{3.47}$$

Where: $\Omega=\frac{\rho_c a L}{P_{ref}-P_c}$, $\beta=\frac{\mu U_{ref} L}{h_0^2\left(P_{ref}-P_c\right)}$, $\lambda=\frac{L}{U_{ref} t_0}$, $\bar{x}=\frac{x}{L}$, $\bar{y}=\frac{2y}{Width}$, $\bar{\sigma}=\frac{\sigma}{h_0}$, and $\bar{h}=\frac{h}{h_0}$ are nondimensional variables.

The Reynolds Equation is solved numerically with the finite difference method. The region is a two dimensional region broken into node points. South to north refers to the y direction, while west to east refers to the x direction. Subscript S, N, W, E, and P refer to the quantity at the corresponding node while subscript s, n, w, and e refer to the quantity at the corresponding boundary of node P as shown in Figure 3.121. First the equation is discretized as presented in Equation 3.48.

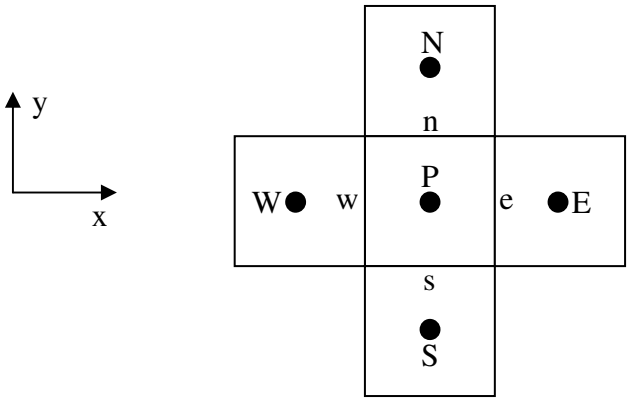

Figure 3.121: Control volume and node layout of discretized domain

$$\frac{1}{\Delta\bar{x}}\left(\phi_x\bar{h}^3\Big|_e\frac{\Phi_E-\Phi_P}{\Delta\bar{x}}-\phi_x\bar{h}^3\Big|_w\frac{\Phi_P-\Phi_W}{\Delta\bar{x}}\right)+\frac{4L^2}{Width^2\Delta\bar{y}}\left(\phi_x\bar{h}^3\Big|_n\frac{\Phi_N-\Phi_P}{\Delta\bar{y}}-\phi_x\bar{h}^3\Big|_s\frac{\Phi_P-\Phi_S}{\Delta\bar{y}}\right)$$
$$=6\beta\frac{U}{U_{ref}}\frac{\bar{h}_T\Big|_e-\bar{h}_T\Big|_w}{\Delta\bar{x}}+6\beta\bar{\sigma}\frac{U}{U_{ref}}\frac{\phi_S\Big|_e-\phi_S\Big|_e}{\Delta\bar{x}}+\Omega\bar{\rho}\frac{\bar{h}_T^3\Big|_e-\bar{h}_T^3\Big|_w}{\Delta\bar{x}}+12\beta\lambda\frac{\bar{h}_T\Big|_P-\bar{h}_T\Big|_{P,pre}}{\Delta\bar{t}} \quad (3.48)$$

Where: $\phi_x\bar{h}^3\Big|_e=\frac{2\phi_x\bar{h}^3\Big|_E*\phi_x\bar{h}^3\Big|_P}{\phi_x\bar{h}^3\Big|_E+\phi_x\bar{h}^3\Big|_P}$, $\phi_x\bar{h}^3\Big|_w=\frac{2\phi_x\bar{h}^3\Big|_W*\phi_x\bar{h}^3\Big|_P}{\phi_x\bar{h}^3\Big|_W+\phi_x\bar{h}^3\Big|_P}$, $\phi_x\bar{h}^3\Big|_n=\frac{2\phi_x\bar{h}^3\Big|_N*\phi_x\bar{h}^3\Big|_P}{\phi_x\bar{h}^3\Big|_N+\phi_x\bar{h}^3\Big|_P}$,

$\phi_x\bar{h}^3\Big|_s=\frac{2\phi_x\bar{h}^3\Big|_S*\phi_x\bar{h}^3\Big|_P}{\phi_x\bar{h}^3\Big|_S+\phi_x\bar{h}^3\Big|_P}$, $\bar{h}_T\Big|_e=\frac{\bar{h}_T\Big|_E+\bar{h}_T\Big|_P}{2}$, and $\bar{h}_T\Big|_w=\frac{\bar{h}_T\Big|_W+\bar{h}_T\Big|_P}{2}$

Equation 3.48 is rearranged and put into a more concise form with Equation 3.49. It was assumed that the film thickness, local film thickness, and gap height was not dependent on the y coordinate, therefore, it can be said that $a_S=a_N$ and $\phi_x\bar{h}^3\Big|_s=\phi_x\bar{h}^3\Big|_n$. Equation 3.49 is solved by employing the Tridiagonal matrix algorithm (TDMA) detailed by Patankar in 1980, where γ is the source term [54]. To speed up the computation the TDMA is applied from south to north in lines going east to west, then from west to east in lines going from north to south for each iteration. The boundary conditions for the

problem are: atmospheric pressure at the most north and south boundaries corresponding to the sides of the armature, magnetic pressure at the most eastern boundary corresponding to the trailing edge of the armature, and the boundary condition on the most western boundary corresponding to the trailing edge of the pocket the pressure is calculated by considering the pressure due to the accelerated column of fluid inside the pocket. If the pocket empties out before the reservoir is empty, the interface leading edge is moved toward the trailing edge as was done for all of the previous armatures except the base case.

$$a_P\Phi_P = a_E\Phi_E + a_W\Phi_W + a_N\Phi_N + a_S\Phi_S + \gamma \tag{3.49}$$

Where: $a_E = \frac{\phi_x \bar{h}^3\big|_e}{\Delta\bar{x}^2}$, $a_W = \frac{\phi_x \bar{h}^3\big|_w}{\Delta\bar{x}^2}$, $a_N = \frac{4L^2}{Width^2}\frac{\phi_x \bar{h}^3\big|_n}{\Delta\bar{y}^2}$, $a_S = \frac{4L^2}{Width^2}\frac{\phi_x \bar{h}^3\big|_s}{\Delta\bar{y}^2}$,

$a_P = a_E + a_W + a_N + a_S$, and

$$\gamma = -\left(6\beta\frac{U}{U_{ref}}\frac{\bar{h}_T\big|_e - \bar{h}_T\big|_w}{\Delta\bar{x}} + 6\beta\bar{\sigma}\frac{U}{U_{ref}}\frac{\phi_S\big|_e - \phi_S\big|_e}{\Delta\bar{x}} + \Omega\bar{\rho}\frac{\bar{h}_T^3\big|_e - \bar{h}_T^3\big|_w}{\Delta\bar{x}} + 12\beta\lambda\frac{\bar{h}_T\big|_P - \bar{h}_T\big|_{P,pre}}{\Delta\bar{t}} \right)$$

The fluid velocity in the x and y directions is calculated using the two dimensional pressure field. The Navier-Stokes Equations can be simplified to Equations 3.50 and 3.51 by using the classical lubrication assumptions. In the simplified Navier-Stokes Equations, the pressure is known at every x and y coordinate as in the armature acceleration.

$$\frac{\partial^2 u}{\partial z^2} = \frac{1}{\mu}\frac{\partial P}{\partial x} - \rho a \tag{3.50}$$

$$\frac{\partial^2 v}{\partial z^2} = \frac{1}{\mu}\frac{\partial P}{\partial y} \tag{3.51}$$

To solve for *u* and *v*, the equations are discretized using the previous notation. Nodes in the z direction must be added because *u* and *v* are three dimensional quantities. The node in the positive z direction in relation to node P is node U, while the node in the negative z direction is node D. The discretized equations are shown in Equations 3.52 and 3.53. These equations are rearranged into Equations 3.54 and 3.55 and the TDMA is employed to find a solution at every x and y node. The boundary conditions applied to the equations are: zero lubricant velocity in the y direction at the rail and the armature, zero lubricant velocity in the x direction at the armature, and the lubricant velocity in the x direction at the rail is set equal to the velocity of the armature using an armature-fixed coordinate system.

$$\frac{u_U + u_D - 2u_P}{\Delta z^2} = \frac{1}{\mu}\frac{P_E - P_W}{2\Delta x} - \rho a \tag{3.52}$$

$$\frac{v_U + v_D - 2v_P}{\Delta z^2} = \frac{1}{\mu}\frac{P_N - P_S}{2\Delta y} \tag{3.53}$$

$$a_P u_P = a_U u_U + a_D u_D + \gamma \tag{3.54}$$

Where: $a_P = 2$, $a_U = 1$, $a_D = 1$, and $\gamma = -\left(\frac{1}{\mu}\frac{P_E - P_W}{2\Delta x} - \rho a\right)$

$$a_P v_P = a_U v_U + a_D v_D + \gamma \tag{3.55}$$

Where: $a_P = 2$, $a_U = 1$, $a_D = 1$, and $\gamma = -\left(\frac{1}{\mu}\frac{P_N - P_S}{2\Delta y}\right)$

Once the lubricant velocities in the x and y directions are found, the mass flow rates of lubricant leaking from any cross section can be calculated. To find the mass flow rate of lubricant in the x direction the lubricant velocity in the x direction is multiplied by the lubricant density and integrated with respect to the y and z coordinates. This can be done to find the mass flow rate at any x coordinate. The mass flow rate in the y direction for a given y coordinate can be found by multiplying the lubricant velocity in the y direction by the density and integrating with respect to the x and z coordinates. The leakage in the y direction at the sides of the armature is added to the leakage in the x direction from the trailing edge of the interface and subtracted from the pocket in the mass balance.

3.5.5 Results and Discussions

The shot is simulated by modifying the Magneto-Elastothermohydrodynamic model used for NRL shot 223 to analyze the IAT GTL-2-4C armature. The major modification made in this model is to consider lubricant leakage from the sides of the interface. The muzzle voltage history from the experimental shot by IAT is displayed in

Figure 3.122. The muzzle voltage is below 100 V until a time of about 2.25 ms. After 2.25 ms the muzzle voltage remains around 100 V until the armature exits the launcher at about 2.9 ms. However, even at the beginning of the shot, the muzzle voltage is approximately 20 V to 50 V.

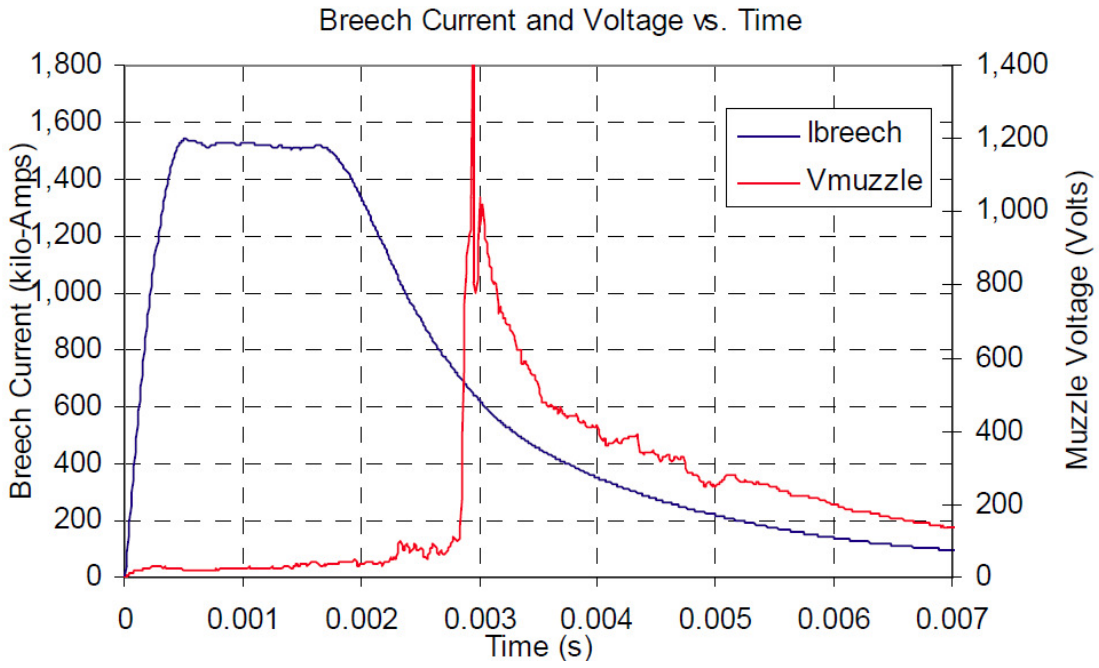

Figure 3.122: Experimental muzzle voltage

The history of the electric current used for GTL-2-4C is shown in Figure 3.123. The general shape of the current profile is similar to those used for previous armatures. It quickly rises and obtains a maximum of about 780 kA at an approximate time of 0.6 ms. After the peak, it levels off with only a slight decrease until about 1.8 ms when it begins to decrease at a fairly steady pace until the end of the shot. When the shot ends the electric current is almost one third of the peak value at about 320 kA.

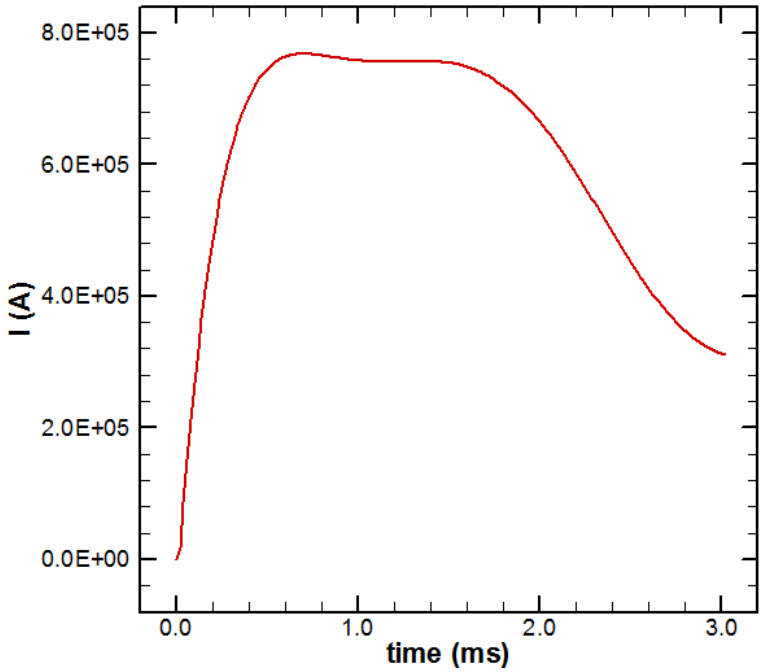

Figure 3.123: Electric current history

Figure 3.124 displays the calculated magnetic flux density in the rail an armature at various times from the beginning of the shot. The magnetic flux concentrates on the trailing edges of the armature as was seen with the previous simulations. The current increases very rapidly for this shot. At a time of 0.1 ms the magnetic flux density has peak values of about 7.1 T. By 0.6 ms the magnetic field is approximately at its peak strength with maxim values around 22 T. The magnetic field remains at approximately its peak strength even at 1.0 ms. By 2.0 ms the magnetic flux density values are beginning to recede as the current slowly falls.

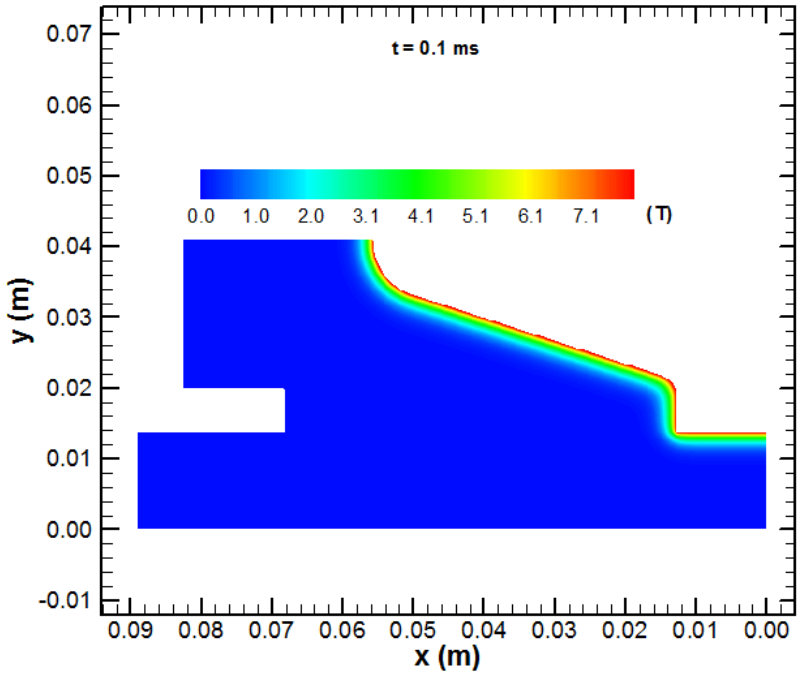

(a)

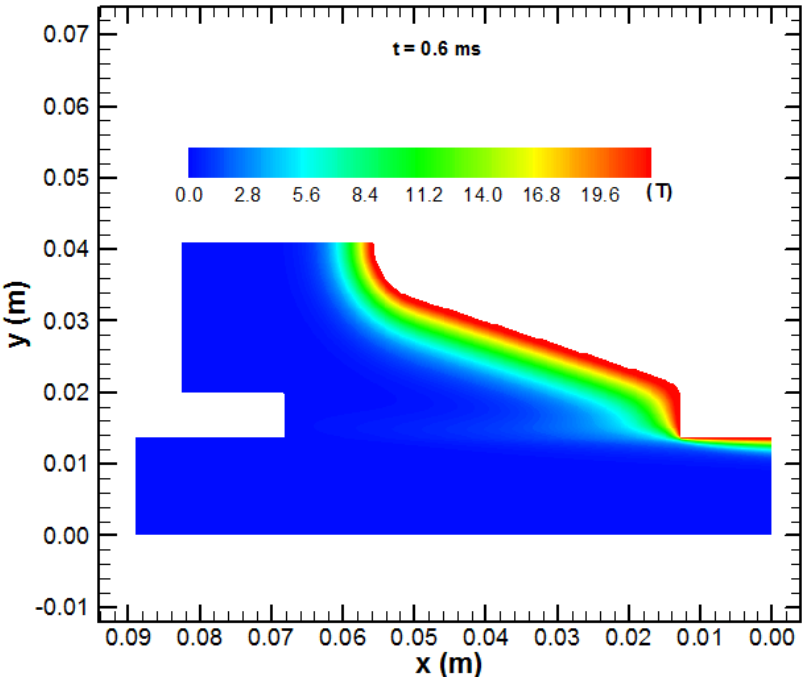

(b)

Figure 3.124: Magnetic flux density distribution at different times

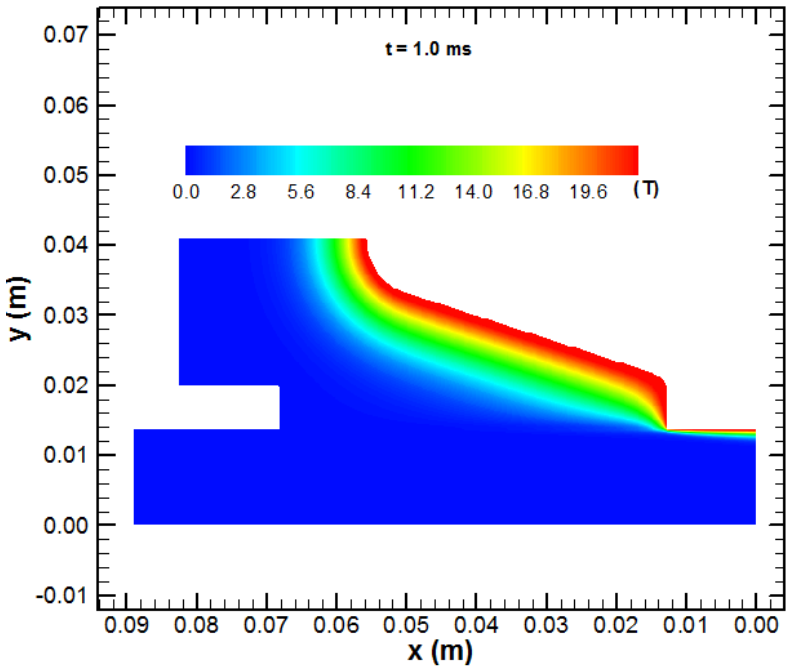

(c)

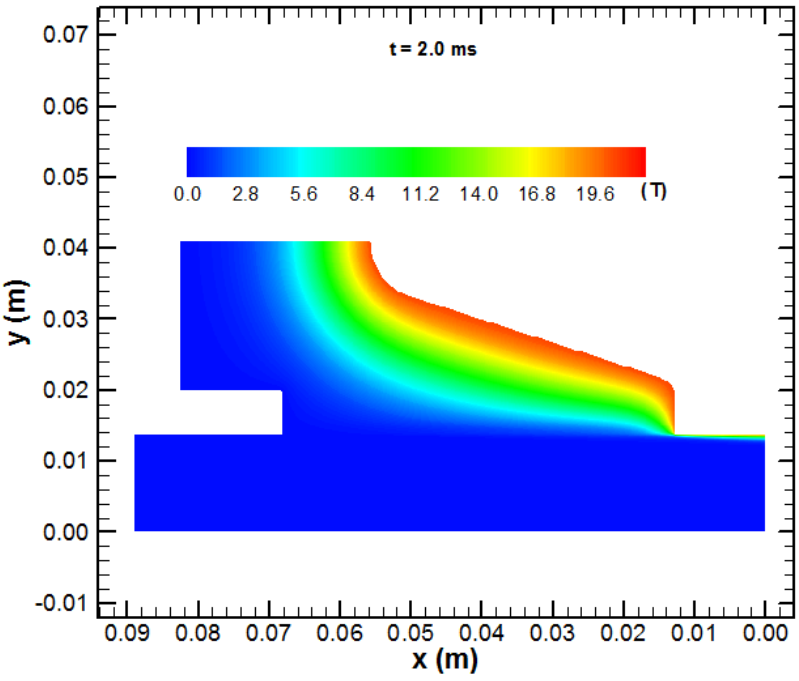

(d)

Figure 3.124 continued

Figure 3.125 shows the electric current distribution at different times for GTL-2-4C. The electric current density is initially concentrated on the trailing edges of the armature. When the armature speeds up, the velocity skin effect pulls the current density toward the trailing edge of the interface. The electric current density in general increases with the electric current. At a time of 0.6 ms the electric current is extremely concentrated at the trailing edge of the interface.

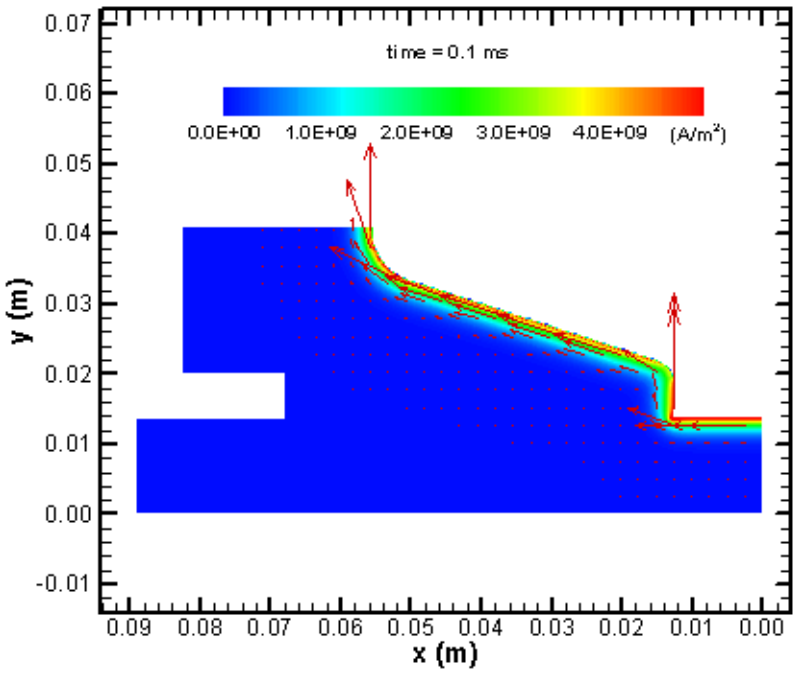

(a)

Figure 3.125: Electric current distribution at different times

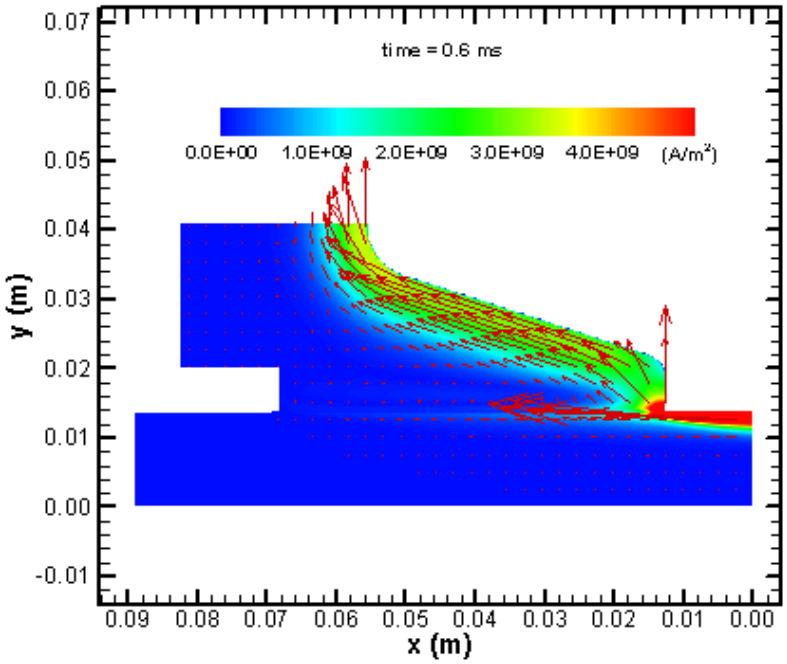

(b)

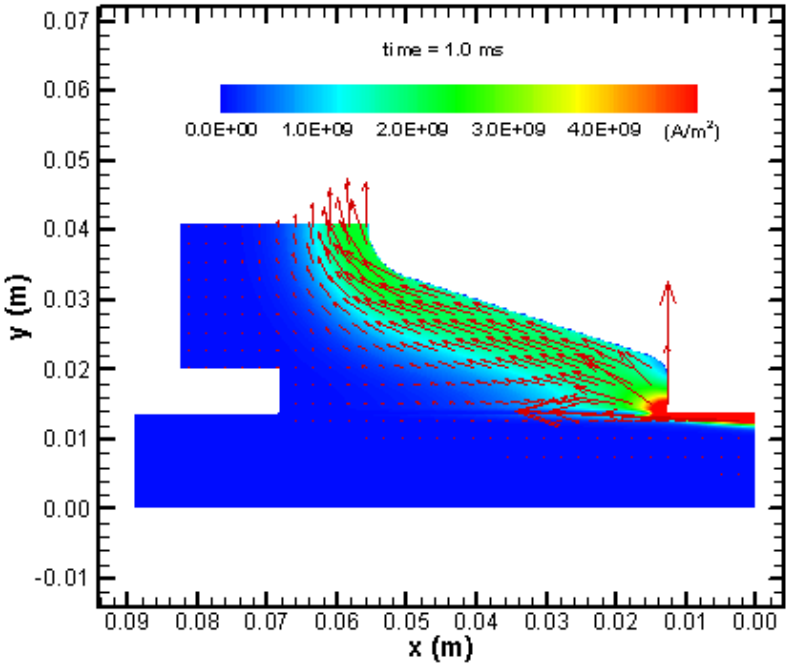

(c)

Figure 3.125 continued

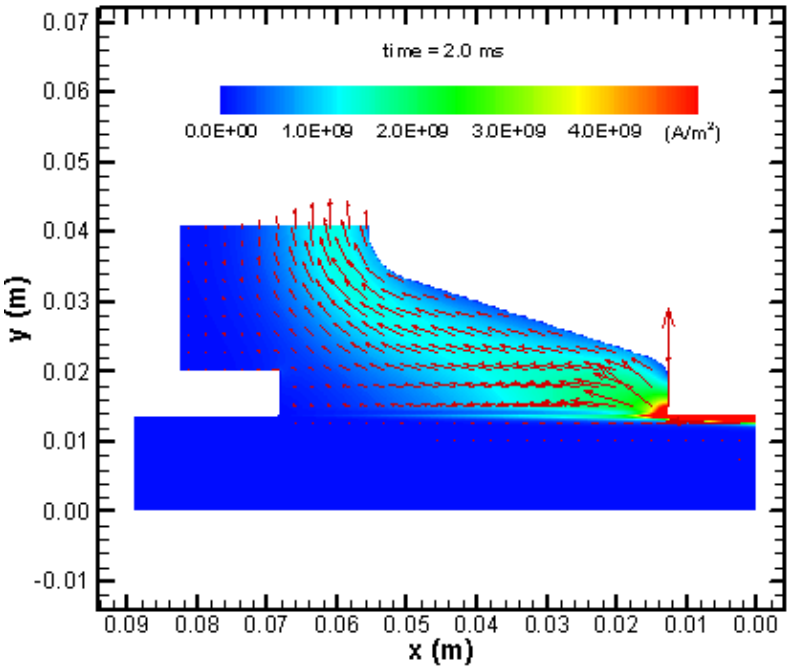

(d)

Figure 3.125 continued

The body forces due to electromagnetic interactions are presented in Figure 3.126. One component of the forces pushes the armature along the rail; the other pushes it into the rail as dictated by the direction of the arrows. The electromagnetic body forces are highest in the places where the current density and magnetic flux densities are also at peak values. Also, in general the magnitude follows the electric current history due to the physical interdependence of electric current, magnetic field, and electromagnetic force.

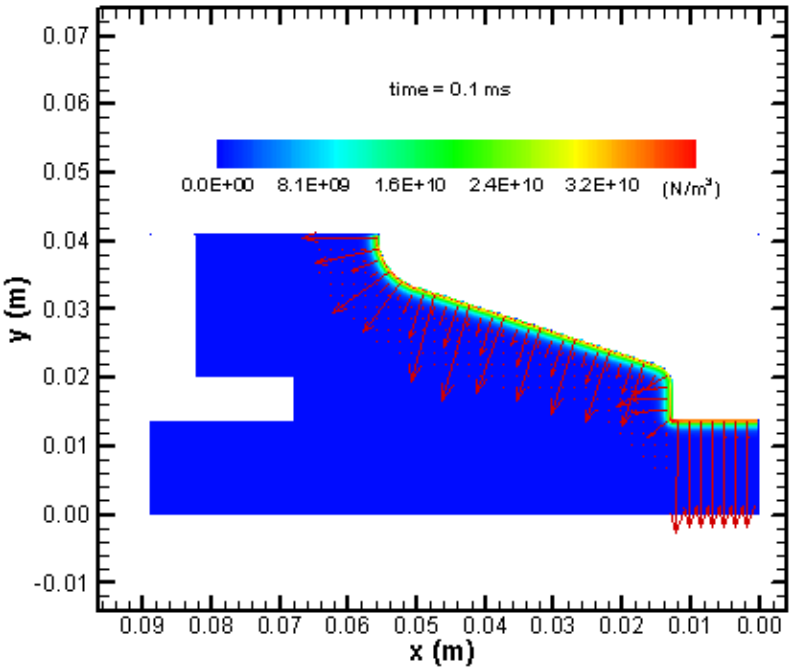

(a)

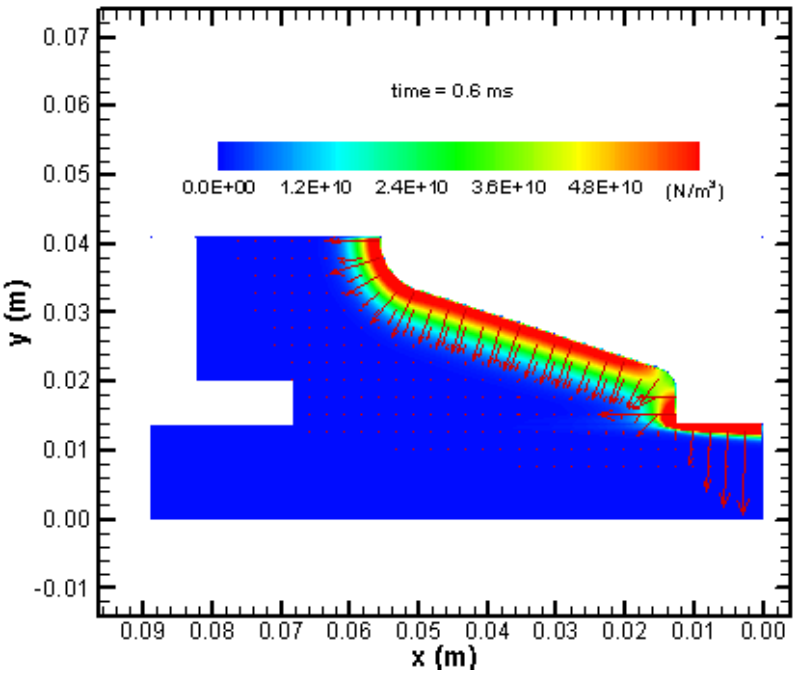

(b)

Figure 3.126: Magnetic body force distribution at different times

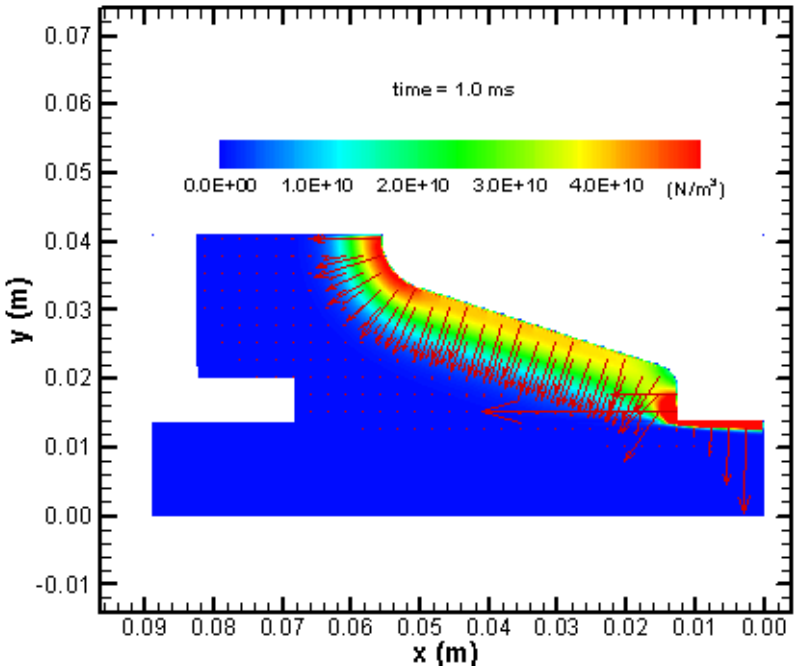

(c)

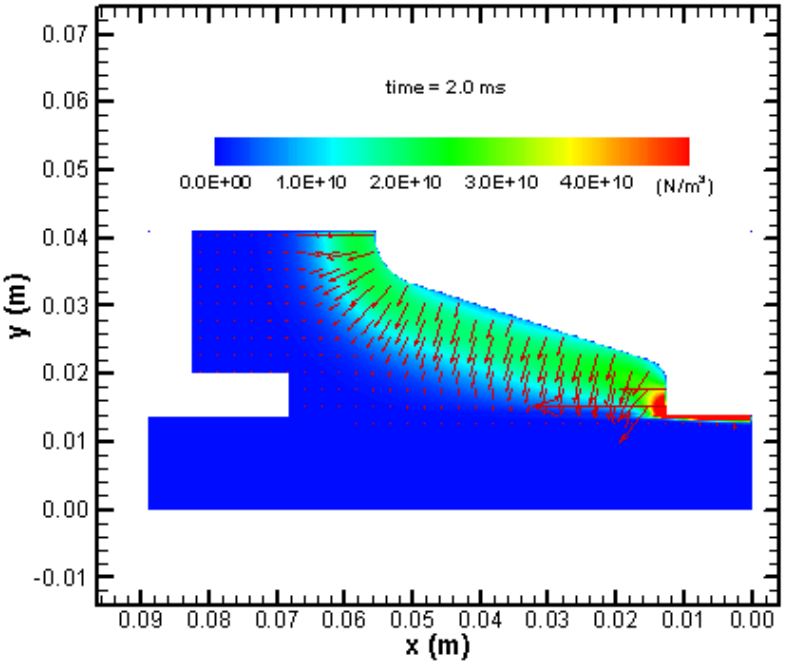

(d)

Figure 3.126 continued

The temperature profile is illustrated in Figure 3.127 for different times. At 0.1 ms the armature is approximately at room temperature. At 0.6 ms there is a considerable amount of heat on the trailing edge of the armature and on a thin strip inside the interface. As the shot progresses, some heat begins to build up on the inside of the trailing edges of the armature. The strip of high temperature material in the interface is small enough to assume that it will not cause melting of the armature. However, as the shot nears 2.0 ms the spot of material at the trailing edge of the armature-rail interface which is at the melting temperature becomes fairly large. In order to melt, this spot has to absorb an amount of energy equal to the latent heat of fusion after it obtains the melting temperature. This analysis assumes that it does not absorb enough energy to melt.

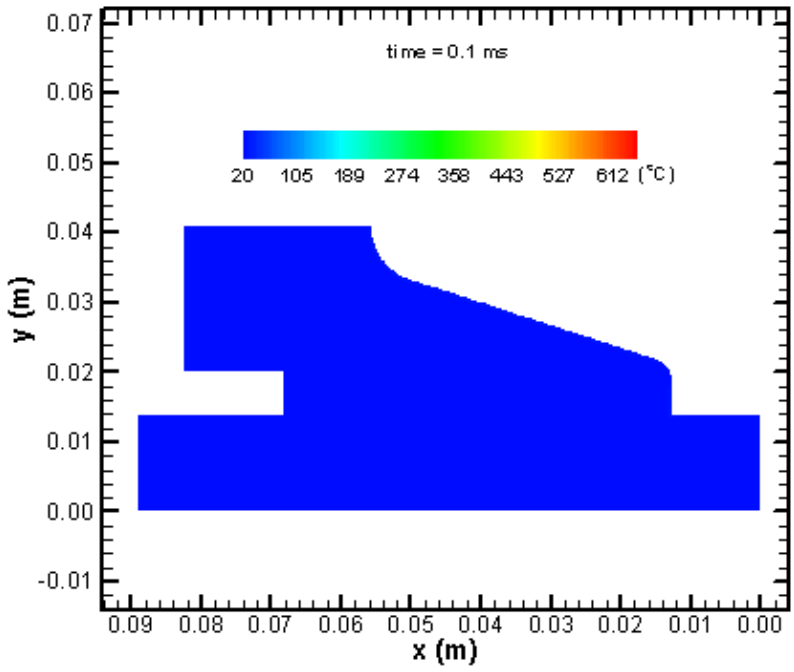

(a)

Figure 3.127: Temperature distribution at different times

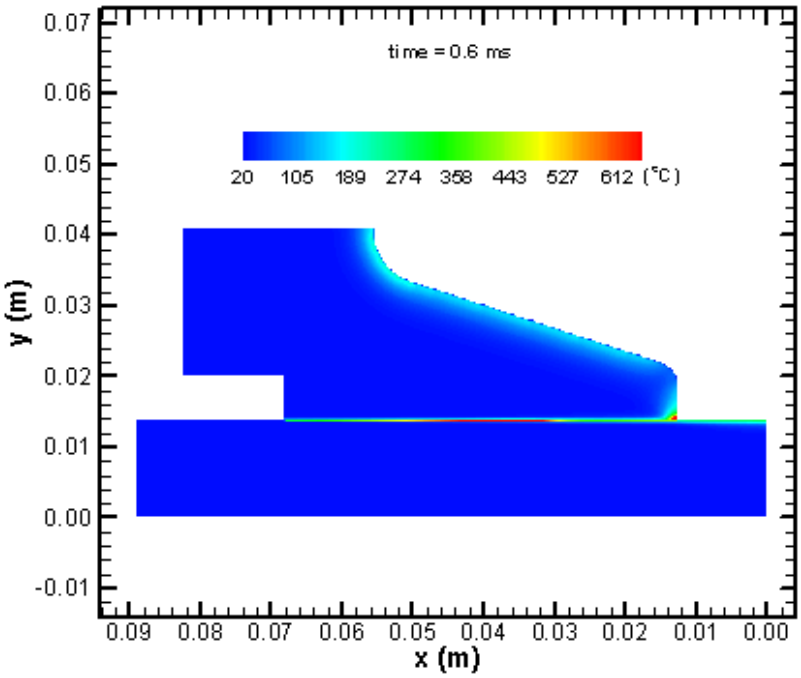

(b)

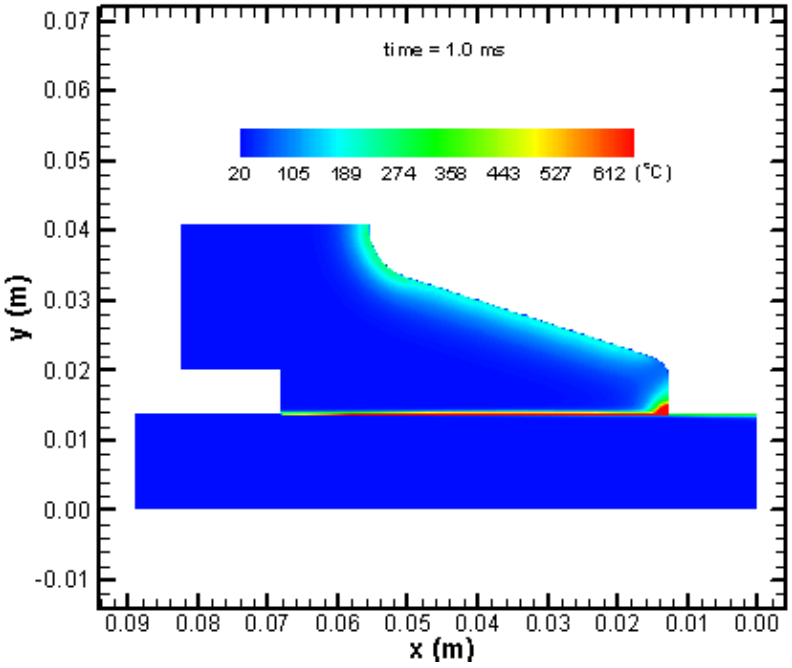

(c)

Figure 3.127 continued

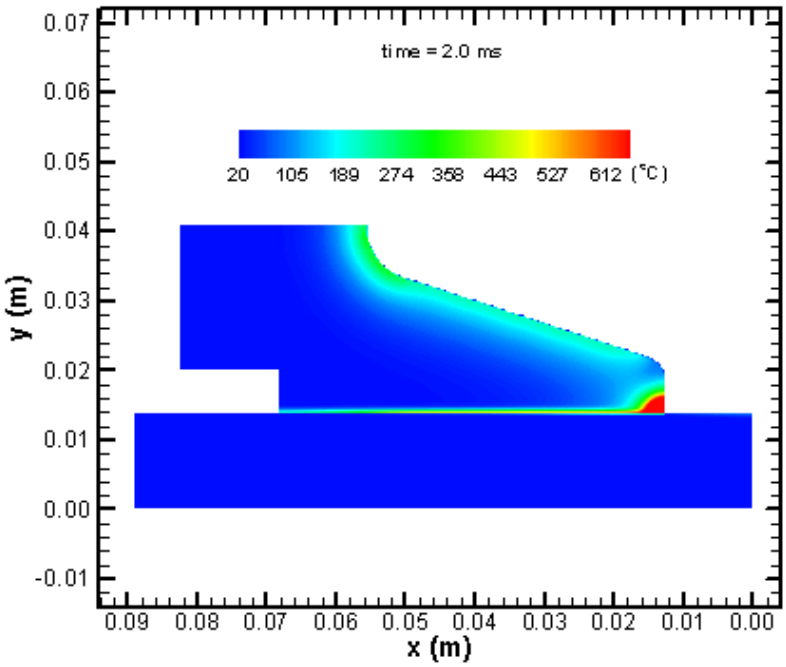

(d)

Figure 3.127 continued

Figure 3.128 shows the net forces acting on the armature in the direction of the rails. The electromagnetic force, $F_{emag,}$ is approximately proportional to the square of the current profile and reaches a maximum of approximately 480 kN at about 0.6 ms around the same time the peak current is reached. The viscous force F_v is small enough that it does not affect the net force on the armature in the x direction. The frictional force, F_f, is less than 10 percent of the total force for the entire shot and negligible for the second half until the transition. When validating the contact pressure it was assumed that values of the correct order of magnitude would yield a close enough estimate. The frictional force is low enough that this assumption can be used with caution. There is a sharp jump in the frictional force at about 2.1 ms, close to the time in which the experimental shot transitioned.

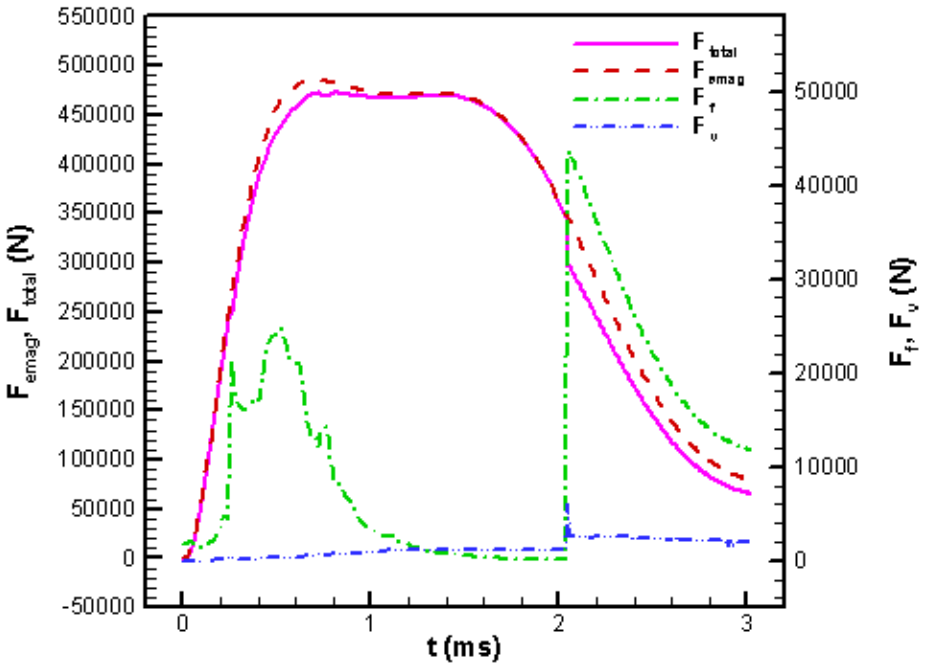

Figure 3.128: *x* direction armature force history

As was the case in the previous armatures the armature acceleration history presented in Figure 3.129 is almost a direct result of the total force shown in the previous figure. The armature acceleration quickly increases to a value of about 1,500 km/s^2 at a time of 0.6 ms. After 0.6 ms the acceleration climbs slightly to a value of about 1,800 km/s^2 at approximately 1.5 ms. After the maximum acceleration is reached, the armature acceleration declines to the value of 880 km/s^2 at the time of the transition.

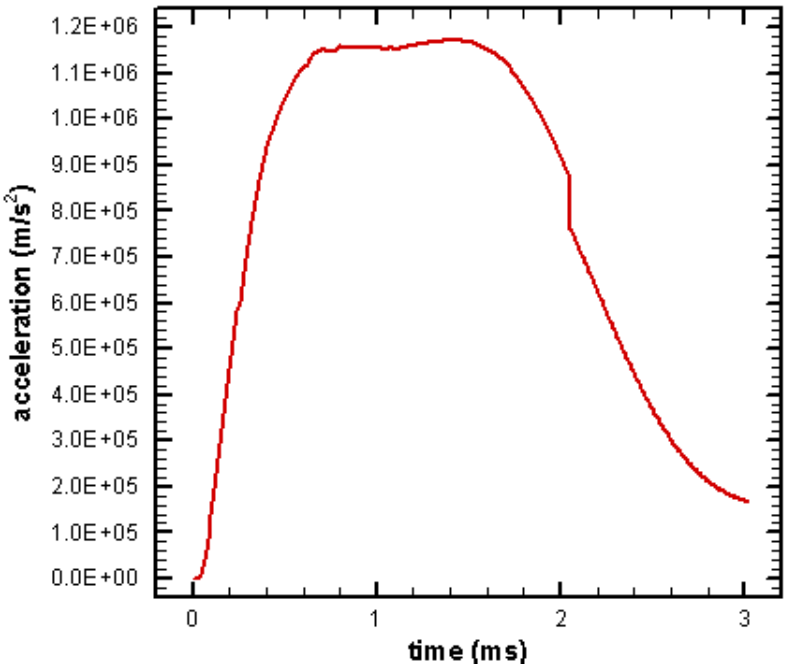

Figure 3.129: Armature acceleration history

The velocity profile predicted with the numerical model is fairly close to the experimentally observed armature velocity as compared in Figure 3.130. The armature is held in place briefly by the frictional force at the beginning of the shot but is quickly accelerated along a nearly smooth line until about 2.0 ms. The velocity at the transition as found in the experiment is about 2100 m/s. The muzzle velocity for GTL-2-4C is around 2400 m/s. The armature position history predicted agrees very well with the experimentally observed armature position as shown in Figure 3.131. The armature exits the muzzle when it gets to a position of about 3.9 m at a time of 3.0 ms.

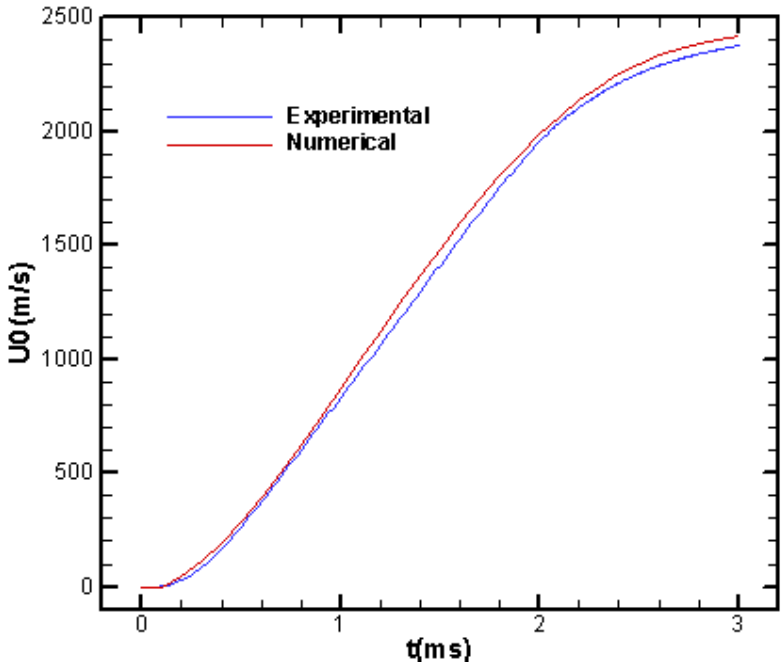

Figure 3.130: Comparison of predicted armature velocity history with experimental measurements

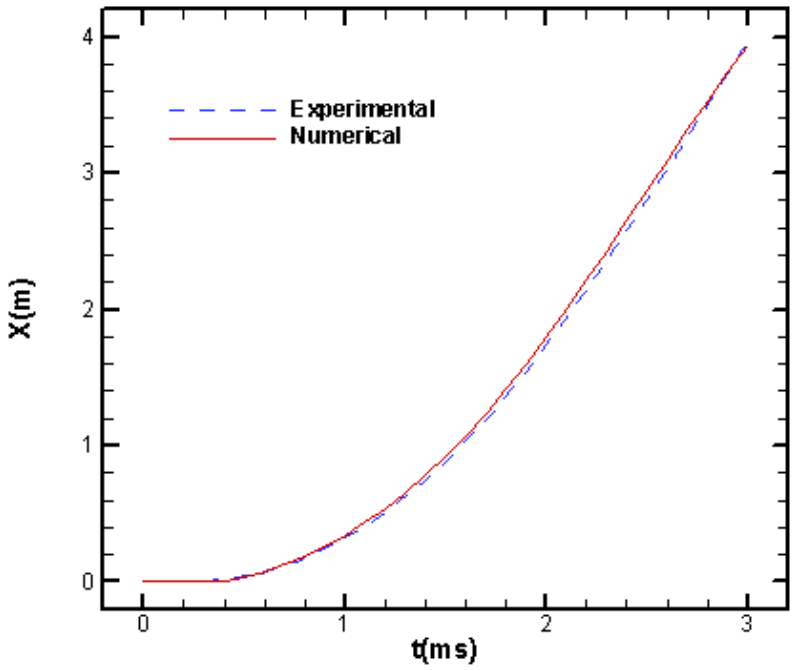

Figure 3.131: Comparison of predicted armature location history with experimental measurements

A history of the amount of lubricant left inside the reservoir, Q_{left}, is shown in Figure 3.132. The reservoir begins with a charge of 6.7 g which is delivered to the pockets through the conduits as the armature accelerates. The lubricant inside the injection conduit is subtracted from the reservoir before the shot begins resulting in a smaller amount of lubricant in the reservoir when the shot begins. This amount of lubricant did not make a noticeable difference in the initial mass of lubricant in the reservoir for the previous armatures. This amount of lubricant is not added back into the pocket when the reservoir empties out because some lubricant may remain inside the injection conduit without more lubricant to push it out. The reservoir completely empties out by 2.1 ms. The lubricant consumption history of one pocket is illustrated in Figure 3.133. Q_{out} is the amount of lubricant delivered to the pocket, Q_l is the amount leaked from the leading edge, Q_r is the amount leaked from the trailing edge of the pocket which is equal to the amount of lubricant leaked from the sides of the armature and the trailing edge of the interface, and Q_{net} is the amount of lubricant inside the pocket. For this shot, the pocket never accumulates a net mass of lubricant. All of the lubricant coming from the reservoir goes straight to the interface. Because the pocket never fills up, no lubricant leaks from the leading edge. When the reservoir empties out at a time of 2.1 ms there is no lubricant being supplied to the interface which is likely to cause the shot to transition. This is close to the experimental time of transition of about 2.25 ms from the beginning of the shot.

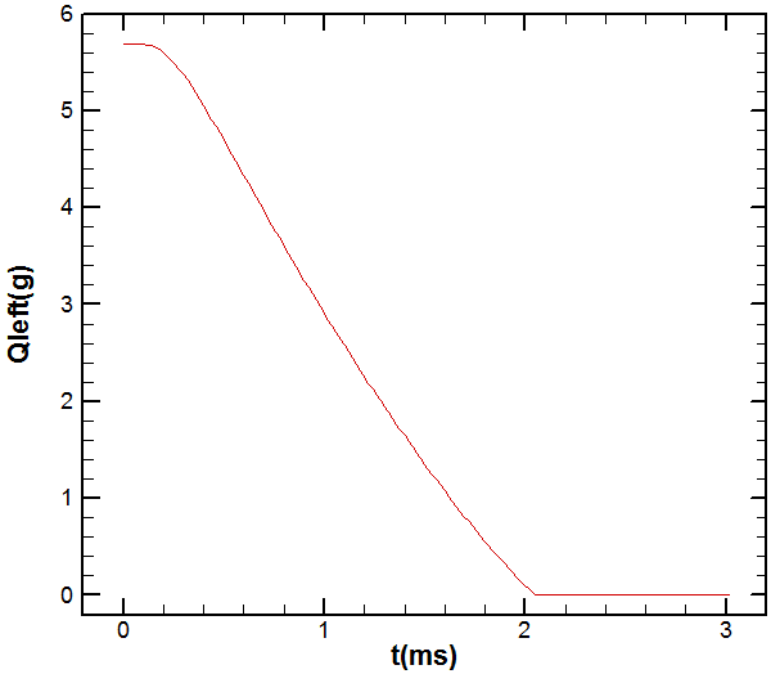

Figure 3.132: History of the amount of lubricant left inside each reservoir.

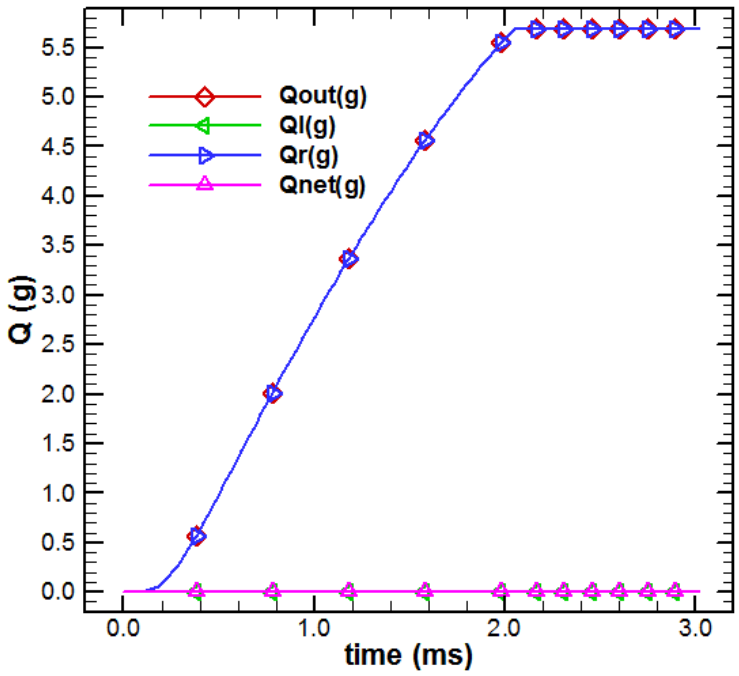

Figure 3.133: Mass flow amount history

The minimum gap height history for the shot is shown in Figure 3.134. The minimum film thickness initially decreases as the magnetic forces push the armature into the rail. As the armature picks up speed the pressure from the lubricant increases the minimum gap height until the reservoir empties out at a time of 2.1 ms. The gap height falls due to a complete lack of lubricant inside the interface when the reservoir empties. The collapse of the interface gap corresponds well with the time of the transition of 2.25 ms found in the experimental shot. The gap heights reported after the transition should be neglected because the model does not include the effects of transition events.

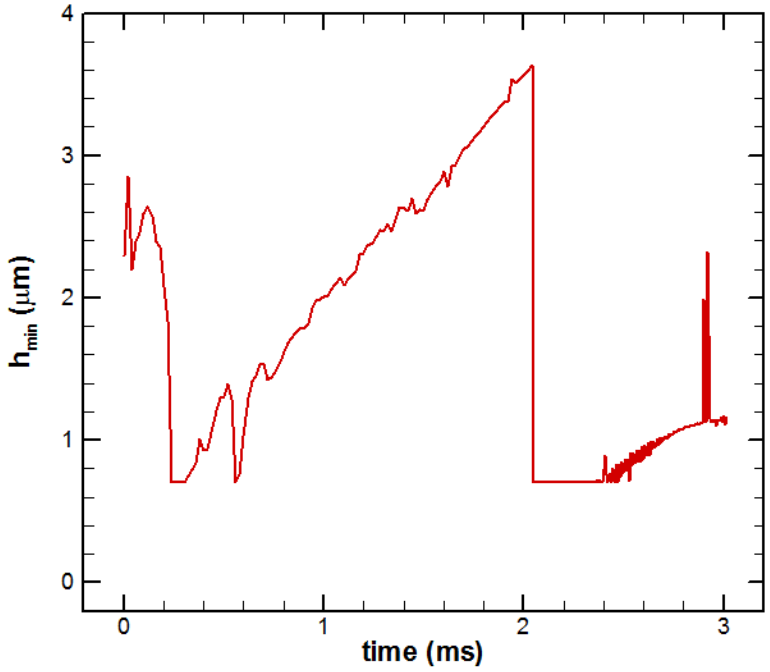

Figure 3.134: Minimum film thickness history

The two dimensional total pressure in the lubricant at different times is displayed in Figure 3.135 with the x and y axis representing the length and width of one of the

armature pads respectively. The pressure profile is approximately parabolic in the y direction due to the assumption of uniform armature deflection in the y direction. The boundaries along the sides of the armature are at atmospheric pressure as well as the leading edge of the interface since the pocket never accumulates a net mass of lubricant. The boundary at the armature trailing edge is equal to the magnetic pressure. Towards the beginning of the shot, there is a small zone of lubricant with a negative total pressure. Cavitation is not considered in this analysis, but the zone of negative pressure is small enough to be neglected for an approximation. At a time of 1.0 ms the negative pressure region disappears but comes back as an even smaller region by 2.0 ms.

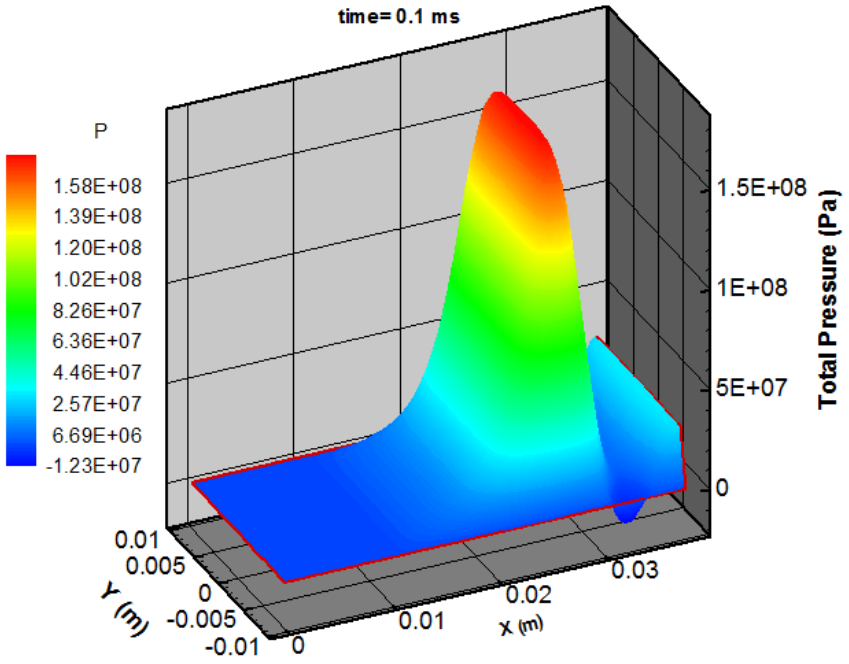

(a)

Figure 3.135: Pressure in the lubricant at different times

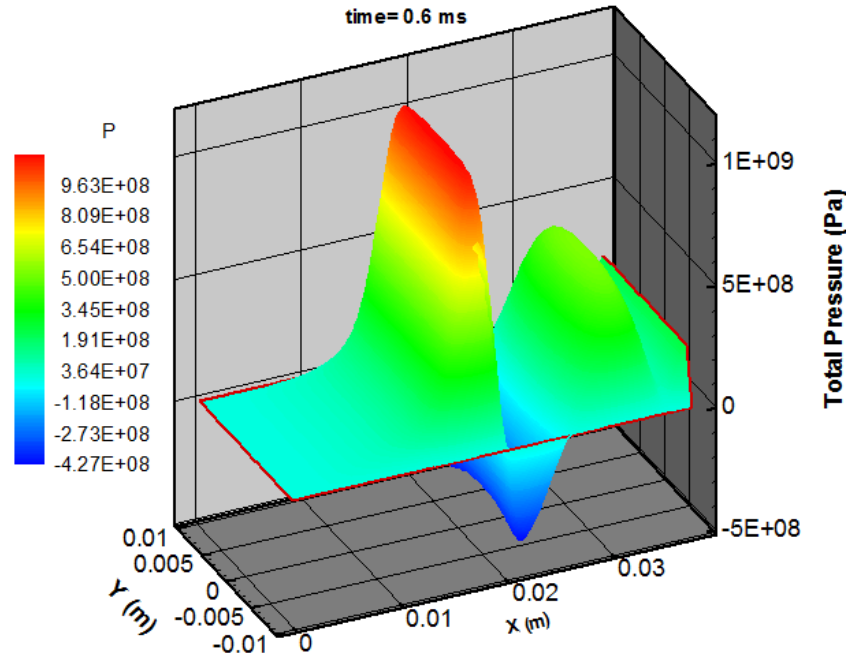

(b)

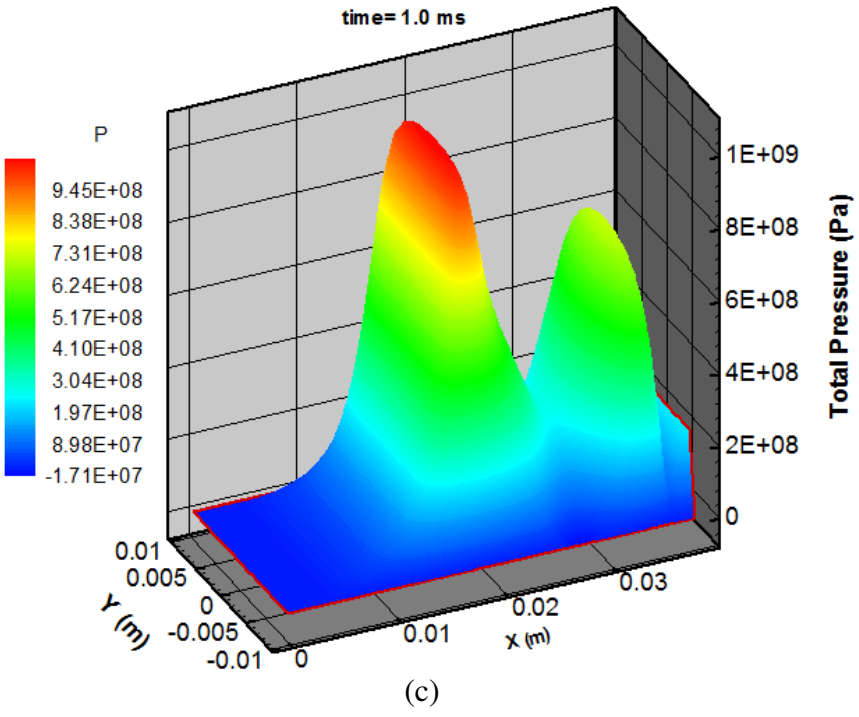

(c)

Figure 3.135 continued

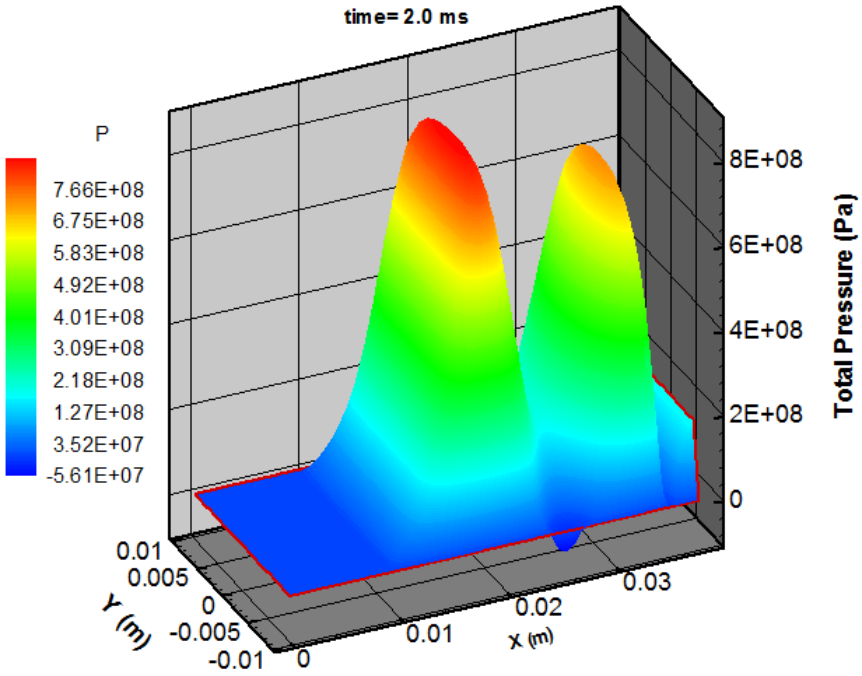

(d)

Figure 3.135 continued

Figure 3.136 shows the distributed forces acting on the armature in the transverse direction. The positive forces push the armature away from the rail, while the negative forces pull it closer. The armature-rail interface does not fill with lubricant at any time for this shot. The approximate position of the empty and full regions of the interface can be seen in the figure. The empty regions can not exert a force on the armature with the lubricant, therefore, the distributed force from the fluid is zero in the figure for the empty regions of the interface. The interface slowly begins to fill as the armature accelerates, but after about 1.0 ms it slowly begins to empty as more lubricant is being leaked from the trailing edges and the sides than is being supplied to the interface.

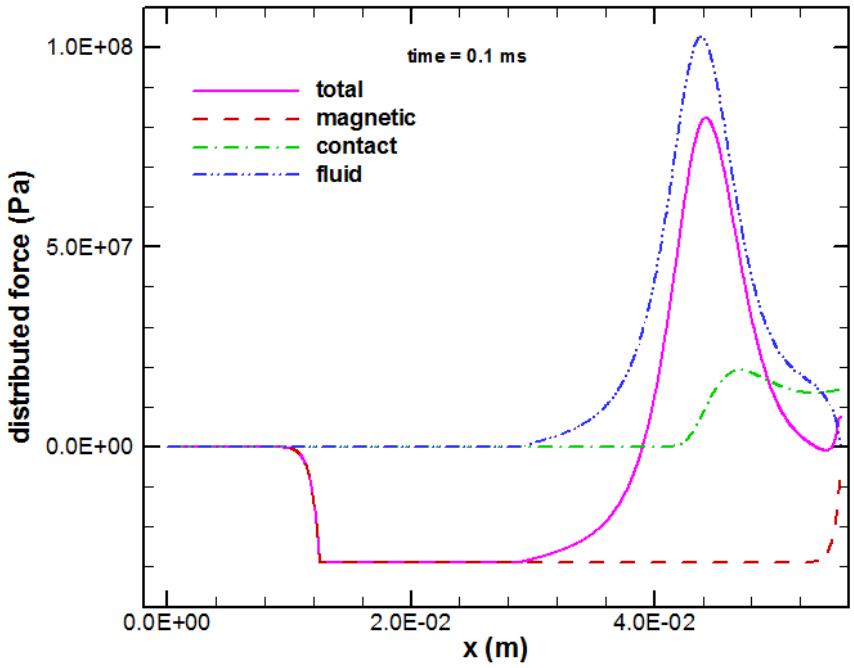

(a)

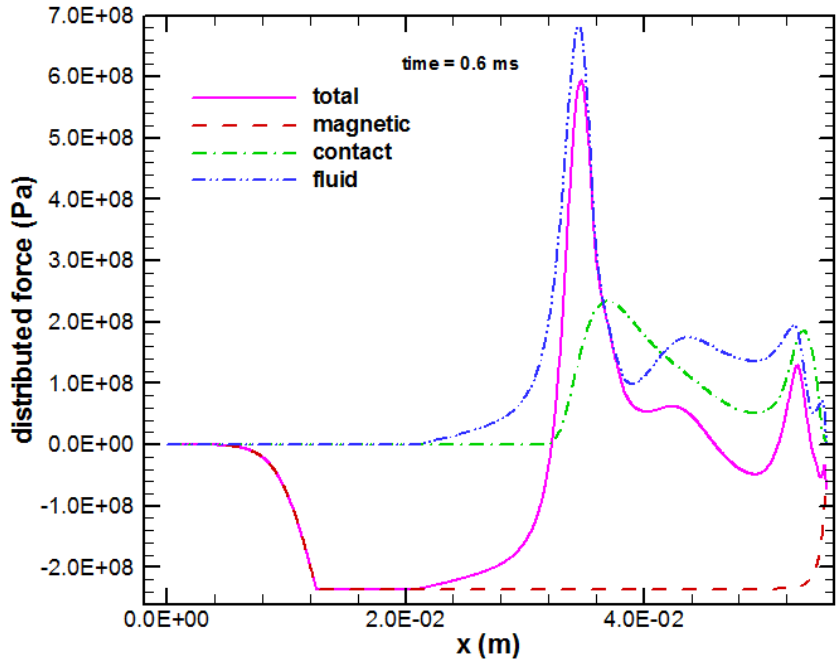

(b)

Figure 3.136: Distributed forces on the armature leg at different times

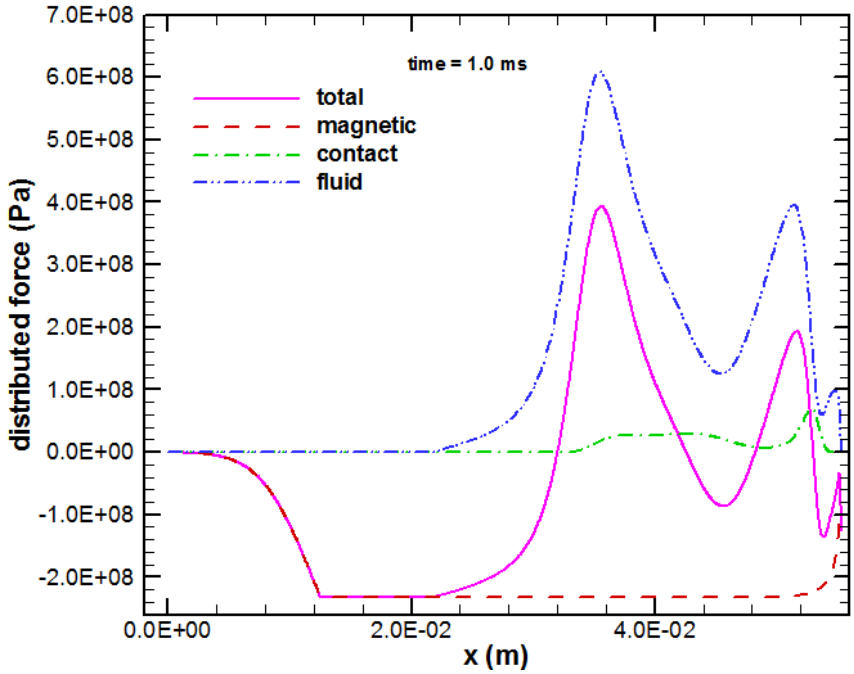

(c)

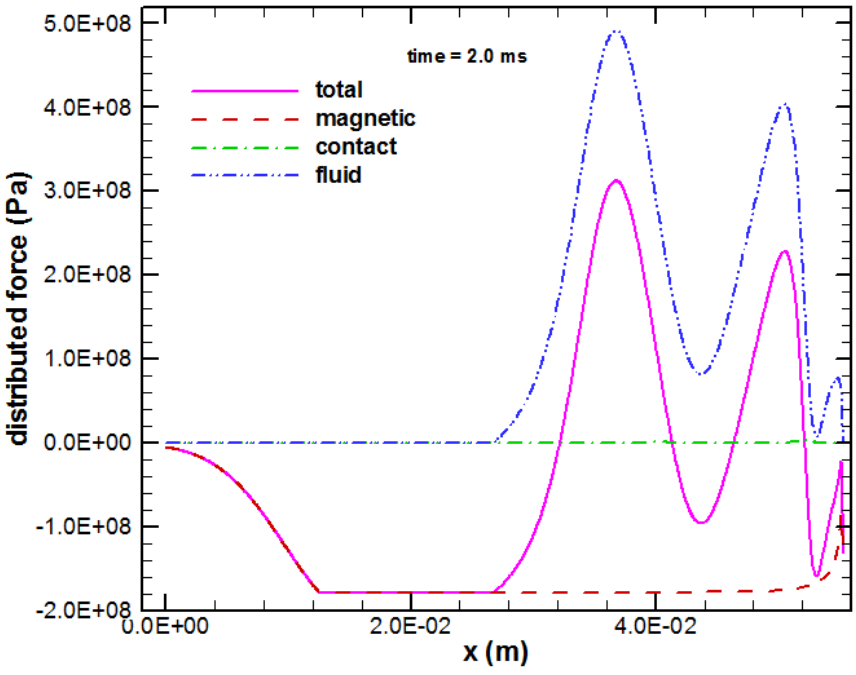

(d)

Figure 3.136 continued

Figure 3.137 displays the nondimensional interface gap profile at different times. One difference in the gap profiles for this armature is the diverging gap at the leading edge. This is found because the armature is initially flat in this region but gets deflected along with the rest of the trailing edges. At a time of 0.0 ms, the contact pressure alone deforms the gap. As the shot proceeds the forces acting on the armature deforme the gap. The gap height at the rear half of the interface is small during most of the shot.

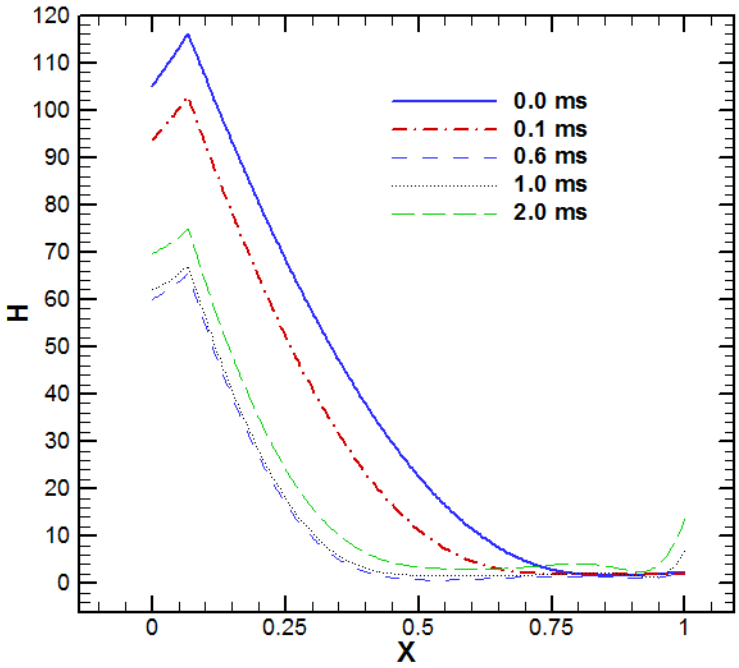

Figure 3.137: Nondimensional interface gap profiles at different times

The magneto-elastothermohydrodynamic model was farther extended to analyze the cylindrical IAT launcher with the GTL-2-4C armature. It was shown that even though the armature is cylindrical, the current path and electromagnetic body force directions are dominantly planar and the magnetic field is dominant in one direction.

Therefore, the armature was approximated as a rectangular bore armature to calculate the thermal and electromagnetic fields. Equivalent cantilever beams were found using the radial displacement of three dimensional models with similar boundary conditions. The lubricant was analyzed by ignoring the curvature of the armature and rail, using a two dimensional pressure field to account for leakage from the side of the armature and through the slit by assuming constant deformation in the direction normal to the slit, and ignoring cavitation. The experimental muzzle voltage indicated a transition at a time of 2.25 ms. The results predict this transition well by showing that the reservoir empties out at a time of 2.1 ms and the pocket never accumulates a net mass of lubricant. The armature-rail interface is predicted to be only partially full for the entire shot. Additionally, the minimum gap heights predicted are small and collapse when the reservoir and interface empty.

3.6 Modified GTL-2-4C

The GTL-2-4C armature in the previous section leaked a lot of lubricant from the trailing edge of the interface as well as the sides of the pad; especially because the slit divided the two interfaces into four each being about half the width. One solution to this problem which was considered was to not cut the slit in the rear of the armature, giving fewer spaces for the lubricant to leak from. The following study is an exploratory analysis of how the modified armature will behave using the current, velocity, and position histories from experimental shot of the original armature. The shot is simulated in the same manner as the previous one except a half armature model is considered so one

complete interface can be analyzed. The thermal and electromagnetic fields will not change due to this extra amount of material. Figure 3.138 shows the original GTL-2-4C armature on the left and the modified GTL-2-4C on the right. The radii on the outsides of the trailing edges of the armature are again neglected.

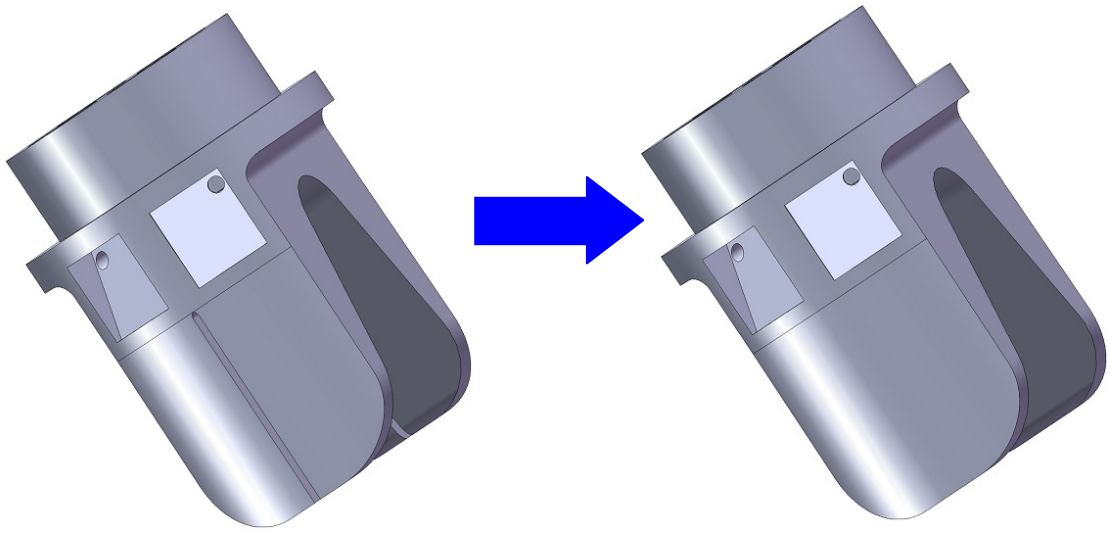

Figure 3.138: Schematic of the original GTL-2-4C armature on the left and the modified GTL-2-4C on the right

3.6.1 Armature Deflection Modeling

The additional material added to the armature does some structural rigidity although there is so little material that the effect is small. The equivalent cantilever beam used for the modified armature is almost identical to the one used for the original. The shear forces used are double those used for the previous armature because a half armature model is being used as opposed to a quarter armature model, so the armature will be about twice as stiff. The comparison of the equivalent Euler-Bernoulli method and the

COMSOL results is displayed in Figure 3.139. The results are almost identical to the results of the previous quarter armature model with half of the force applied.

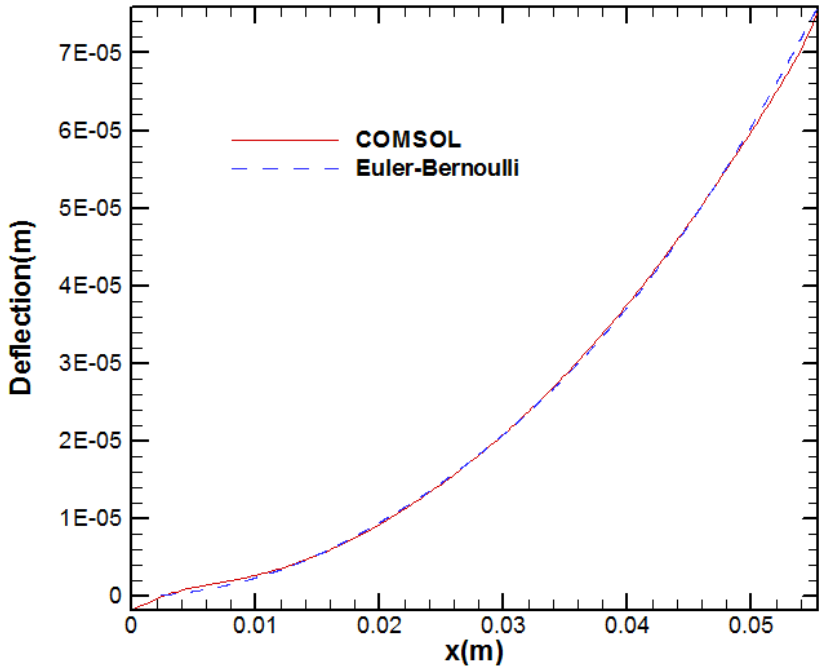

(a)

Figure 3.139: Comparison of armature wing deflection between COMSOL and Euler-Bernoulli models with a shear force of (a) 1000 N, (b) 2000 N, (c) 4000 N, and (d) 8000 N

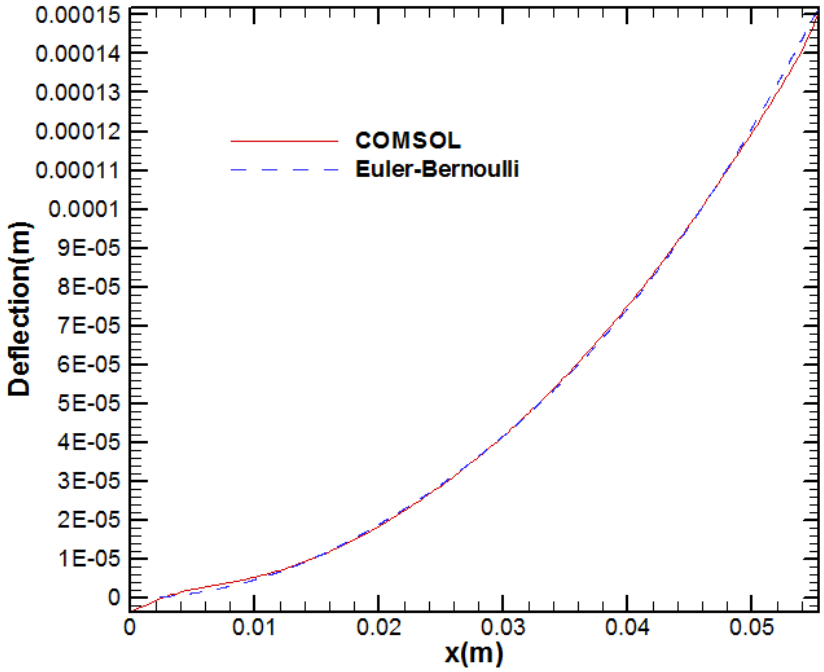

(b)

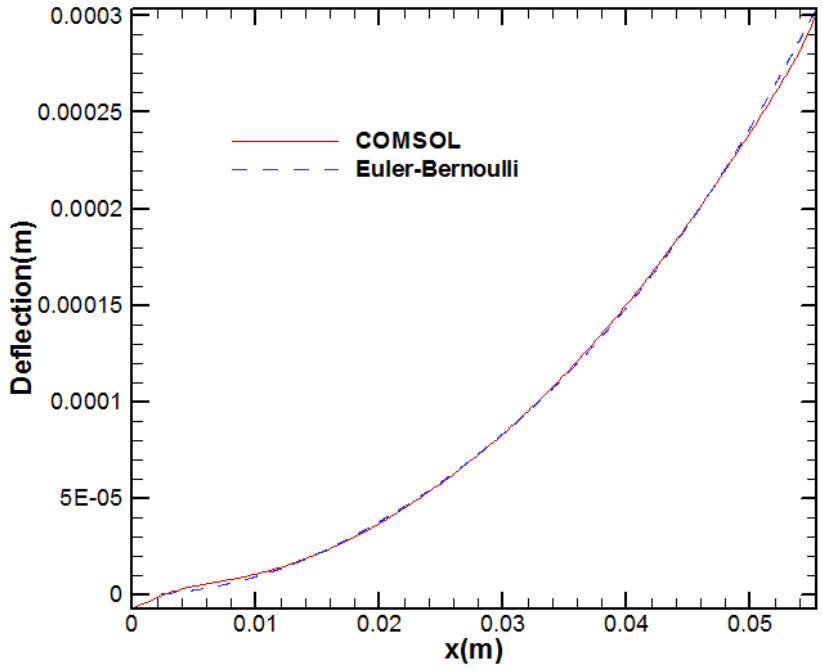

(c)

Figure 3.139 continued

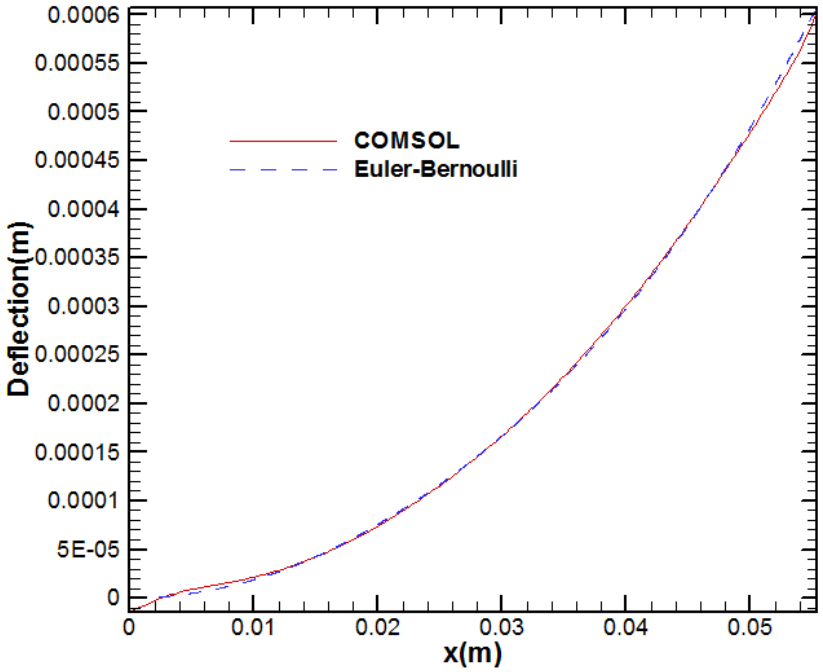

(d)

Figure 3.139 continued

The calculation of the contact pressure is validated for the modified GTL-2-4C armature in the same way as the original. The two dimensional ANSYS approximation is compared to the Greenwood-Williamson calculation using the equivalent cantilever beam in Figure 3.140. The deflections resulting for the two methods are shown in Figure 3.141. The contact pressures and deflections calculated with ANSYS are the same as for the original armature because the two dimensional simplification uses a unit area therefore modeling half of the armature instead of one quarter does not make a difference. The contact pressures calculated with the Greenwood-Williamson method are only slightly closer to the ANSYS pressures than was found with the original armature. The deflections found by the two methods agree fairly well.

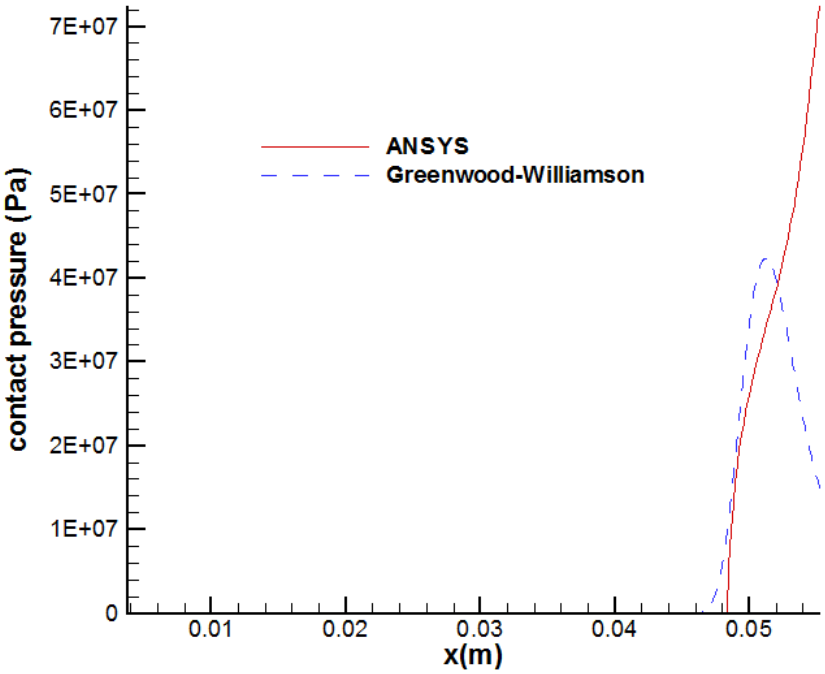

(a)

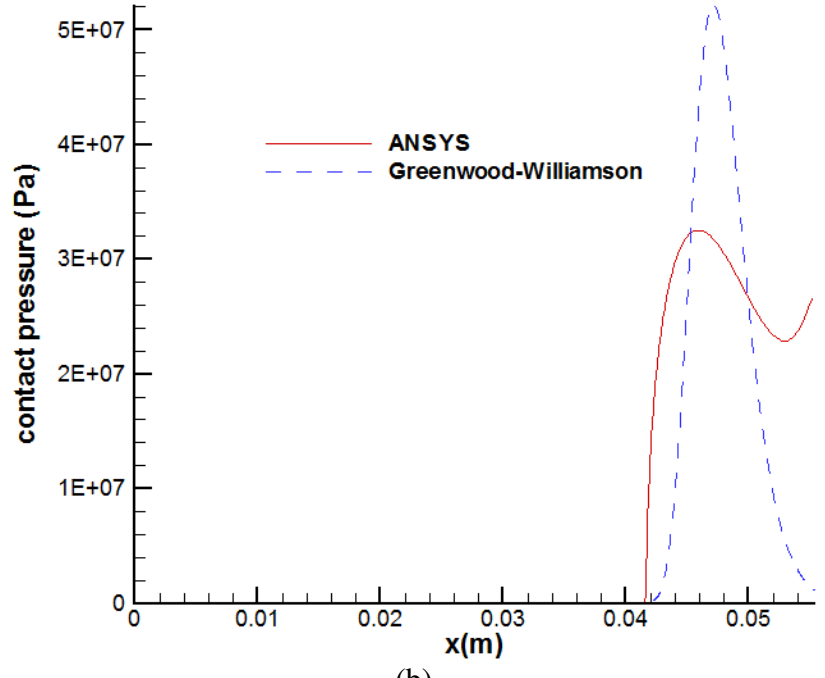

(b)

Figure 3.140: ANSYS and Greenwood-Williamson model contact pressure for an interference of (a) 1.0312 mm and (b) 1.1582 mm

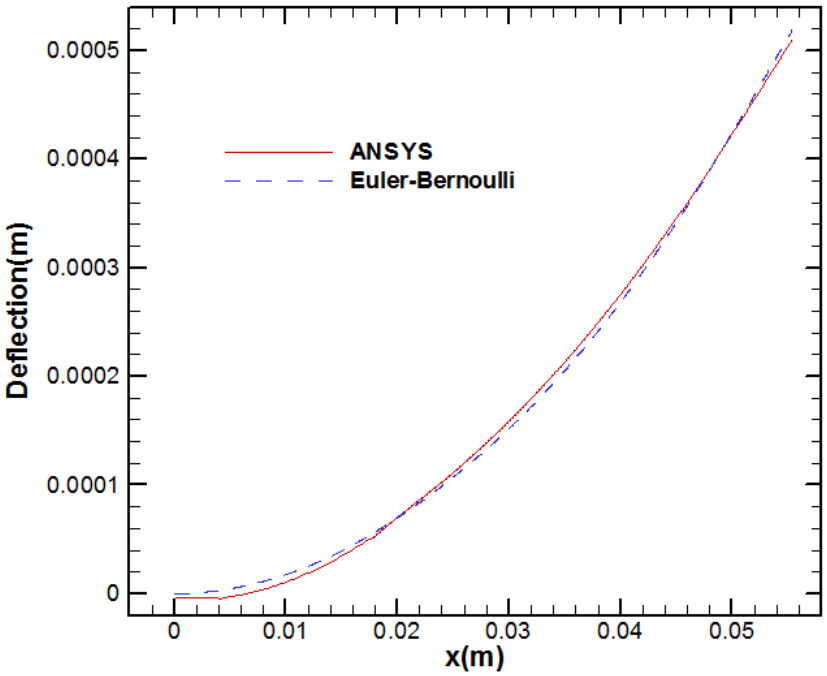

(a)

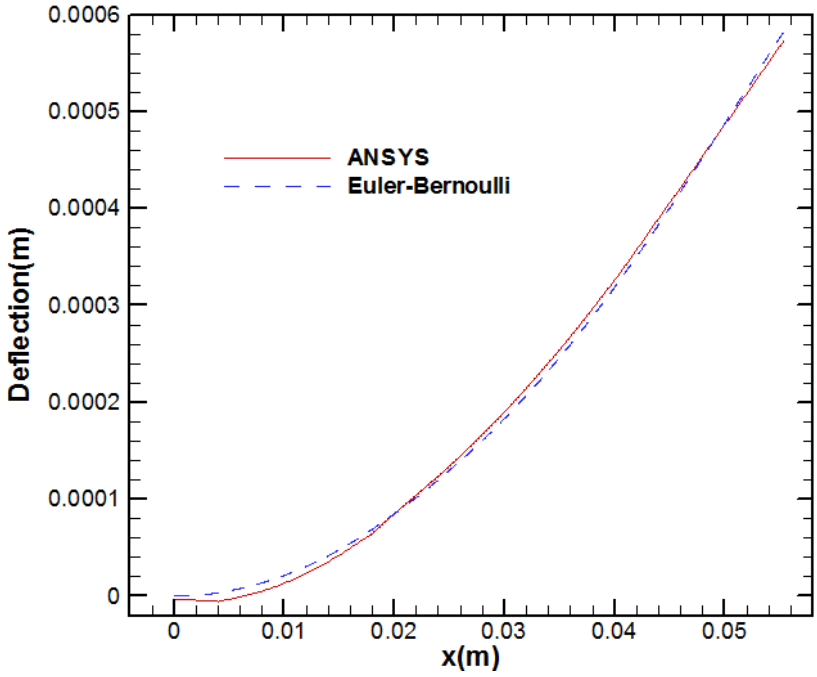

(b)

Figure 3.141: ANSYS and Euler-Bernoulli contact deformation for an interference of (a) 1.0312 mm and (b) 1.1582 mm

Even though the thermal field will be the same for the modified armature, the loads and deflection due to the temperature field may be slightly different due to the added material. As was done for the original armature, A COMSOL model is created with the same boundary conditions with the exception that the boundaries of the slit which were adiabatic do not exist in the model of the modified armature and instead of applying a radial distributed load of 300 N to each pad, a load of 600 N is applied to each wider pad. The results displayed in Figure 3.142 are very similar to those found with the original armature.

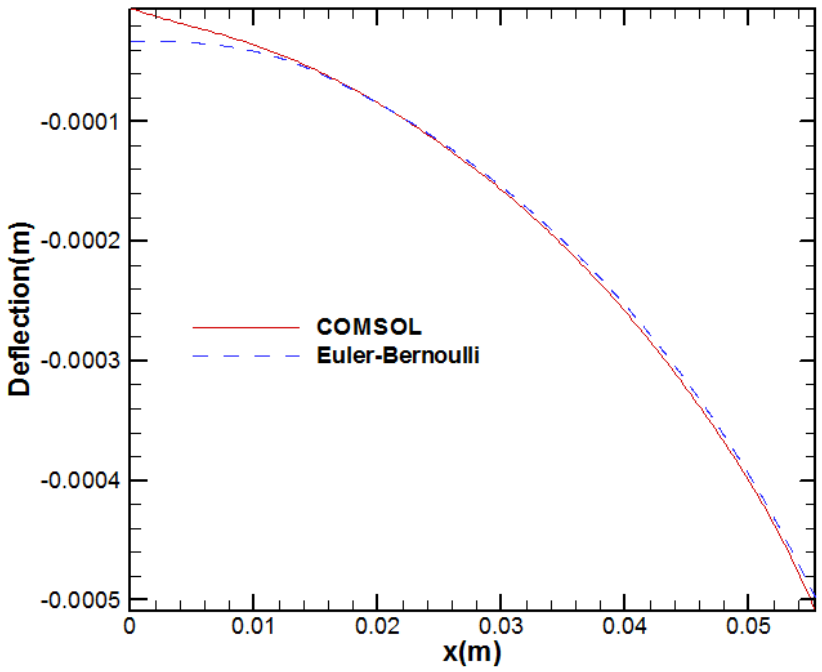

(a)

Figure 3.142: Comparison of armature wing deflection between COMSOL and Euler-Bernoulli models for high boundary temperatures of (a) 200 °C, (b) 300 °C, (c) 400 °C, and (d) 600 °C

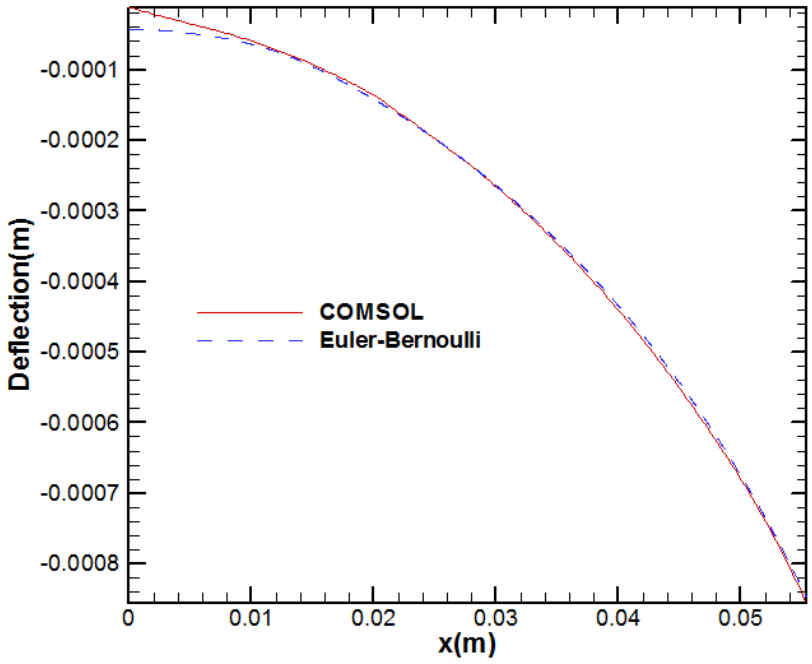

(b)

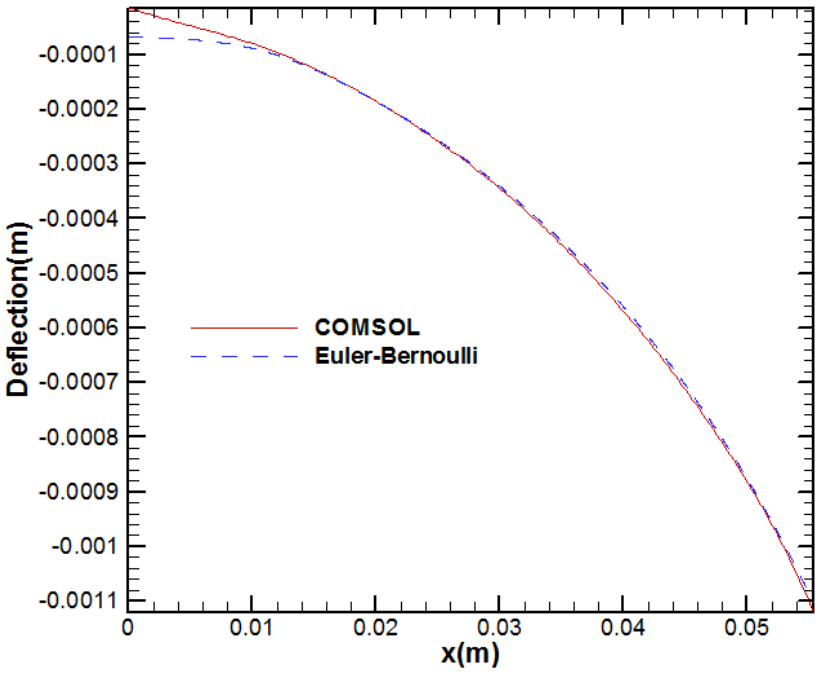

(c)

Figure 3.142 continued

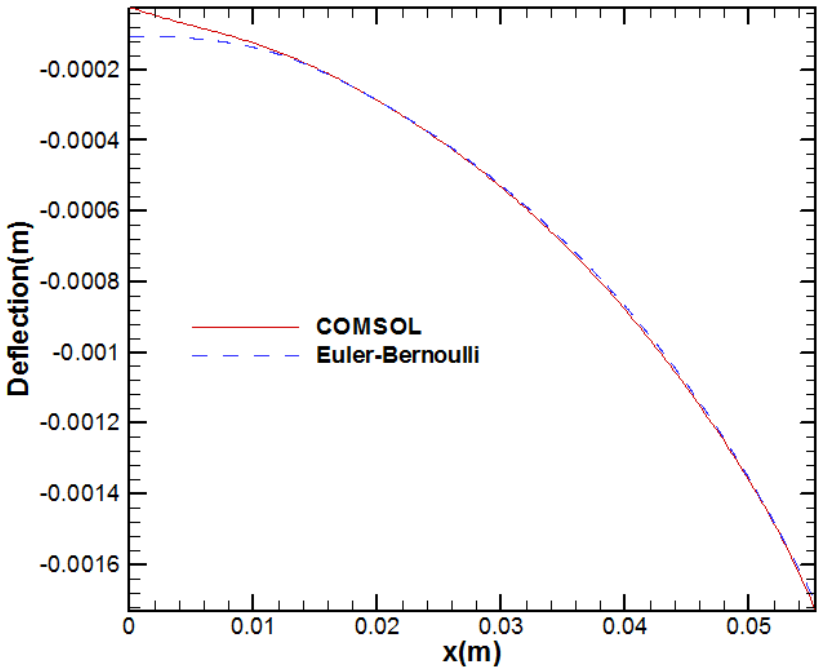

(d)

Figure 3.142 continued

3.6.2 Lubricant Modeling

A few changes are made to the lubrication model. The pad is twice as wide as in the quarter armature model. The two pockets on the half armature model are modeled as one equivalent pocket that is twice the width of a single pocket. The equivalent pocket is supplied by two reservoirs each with its own injection conduit. In the previous model cavitation was neglected in the derivation of the equations used to find the interface pressure. However, if large negative pressures develop, the finite difference code may have difficulty converging or converge on inaccurate solutions. This problem is encountered while analyzing the modified GTL-2-4C armature. To account for cavitation without complicating the problem or slowing down the computational time, the simple cavitation model used by Oh and Goenka in 1985 is employed. Inside the TDMA

iterations, if the fluid pressure is less than zero, it is set to zero [8]. This method does not conserve mass, but is good for a rough approximation as long as the cavitation is light and confined to a small region.

3.6.3 Results and Discussions

The simulation of the modified armature produced results for many physical parameters which were not noticeably different from those presented for the original armature. The main difference in the armature without the slit is the lubrication. Even though the physics are coupled, the effects on some parameters of a different lubricant pressure field are negligible. The same current history is used for both shots, causing similar current densities, magnetic flux densities, and thermal fields. Although the thermal field can be altered by the cooling effect of the lubricant or viscous and frictional heating, the majority of the heating is through joule heating. With similar electric current densities, there will be similar amounts of heating in the same regions.

The net forces in the x direction are displayed in Figure 3.143. The electromagnetic force is approximately the same as was found with the original armature. However, the frictional force is apparent for most of the shot. Although its magnitude is much less than the net force, it does have a small effect. The acceleration is mostly due to the electromagnetic force which is close to the same for both armatures, so the velocity and armature position histories will also be about the same.

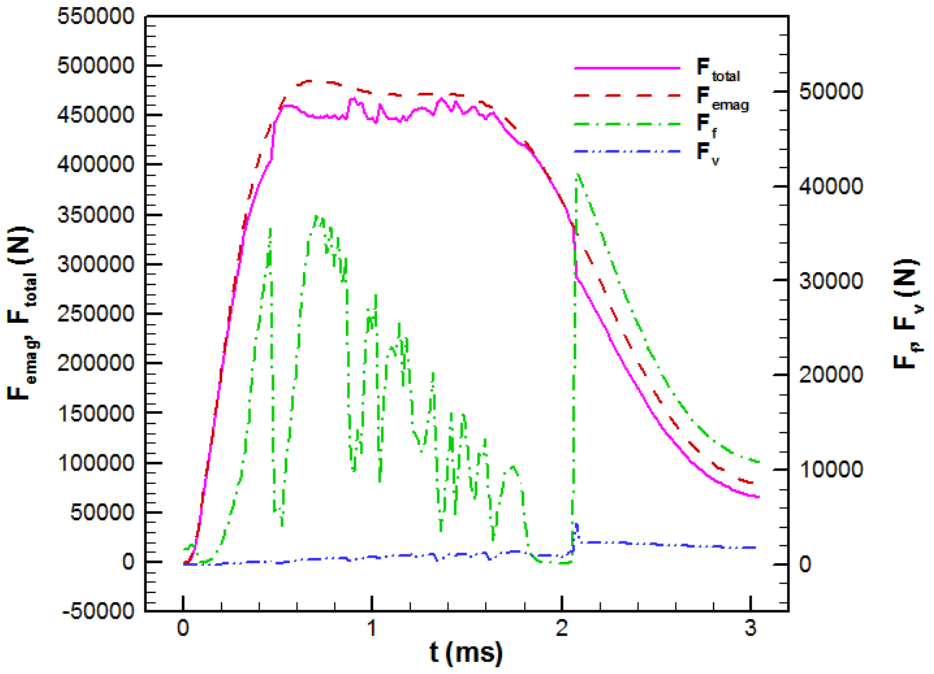

Figure 3.143: *x* direction armature force history

A history of the amount of lubricant left inside one reservoir, Q_{left} is shown in Figure 3.144 and the lubricant consumption history of one pocket is illustrated in Figure 3.145. With the modified armature, the amount of lubricant leaked from the trailing edge of the pocket, Q_r, is less than the amount of lubricant being supplied by the reservoir, Q_{out} for the beginning half of the shot. This allows a net mass of lubricant, Q_{net}, to build up inside the pocket. The original armature with the slit did not allow lubricant to accumulate inside the pocket. However, only a small mass of lubricant accrues in the pocket and it is leaked out by about 1.7 ms. The history of the amount of lubricant left inside each reservoir is not effected by the build up of lubricant inside the pocket unless the pocket fills which does not happen. So the history of Q_{left} is the same as for the original armature. A transition is still likely after the reservoir empties at 2.1 ms because there is no lubricant being supplied to the interface.

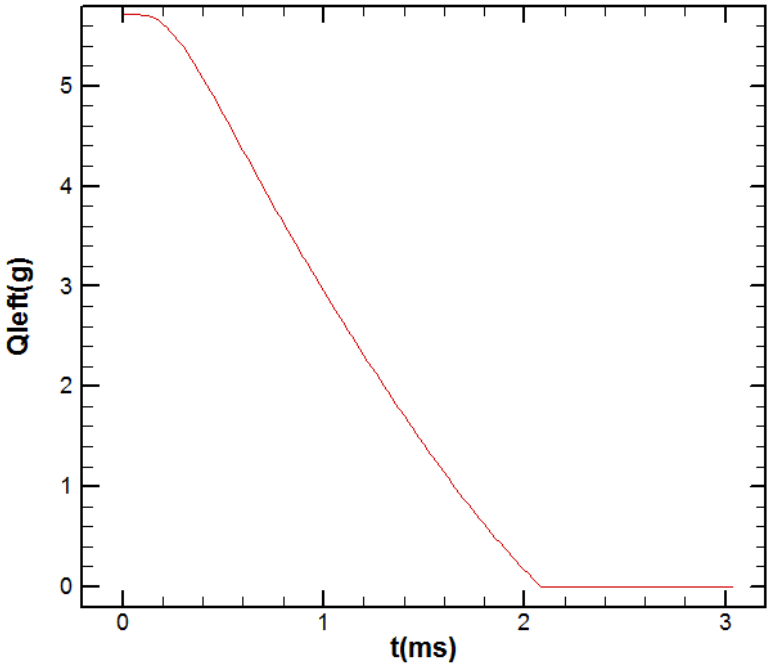

Figure 3.144: History of the amount of lubricant left inside each reservoir.

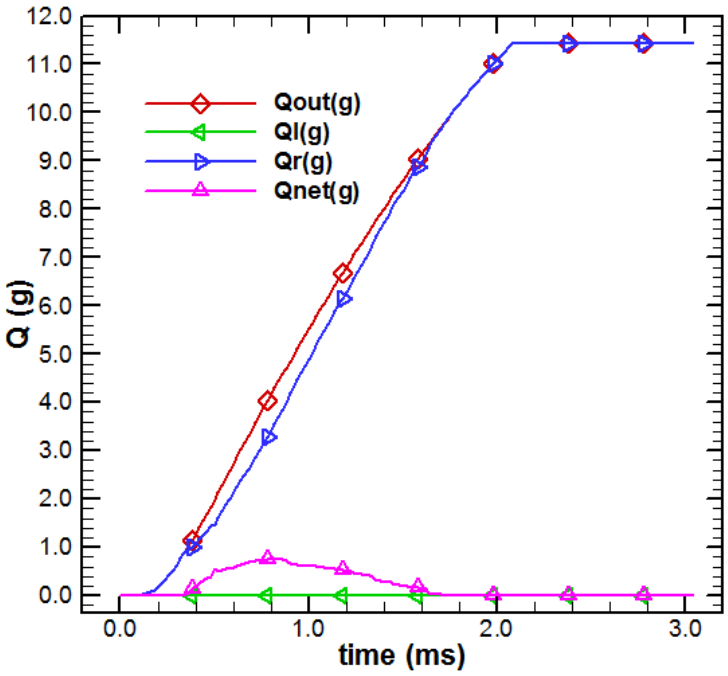

Figure 3.145: Mass flow amount history

The minimum gap height history for the modified armature is shown in Figure 3.146. The minimum film thickness follows a similar pattern to the original armature. The gap height initially decreases, and then builds up as the armature picks up speed. When the reservoir empties at 2.1 ms there is no lubricant being supplied to the interface and the gap collapses making a transition likely.

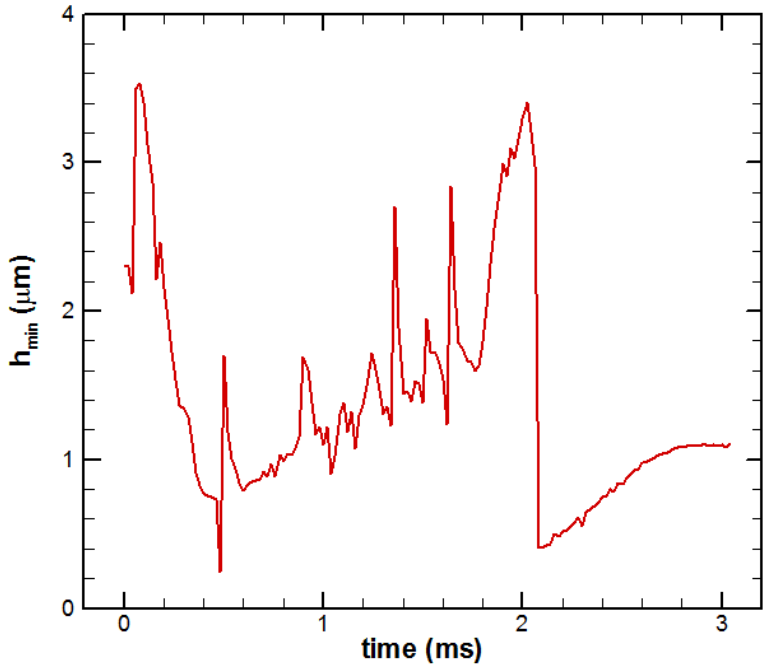

Figure 3.146: Minimum film thickness history

The two dimensional fluid pressure in the lubricant at different times is displayed in Figure 3.147. The profiles are approximately parabolic in the y direction. At 0.1 ms the fluid pressure is low with atmospheric conditions on all boundaries. As the armature deforms and speeds up, the pressure increases and any cavitation zones which appear will have their fluid pressure set to zero.

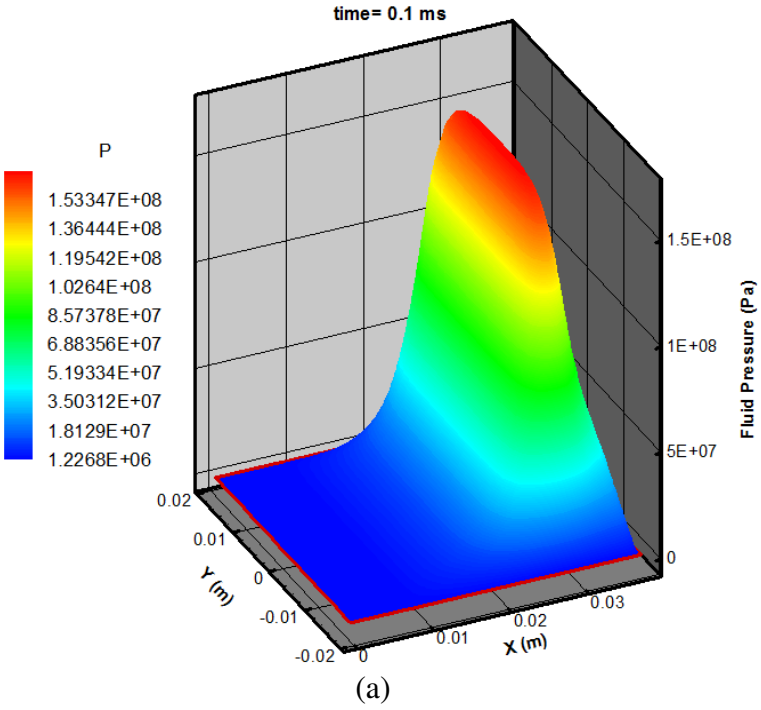

(a)

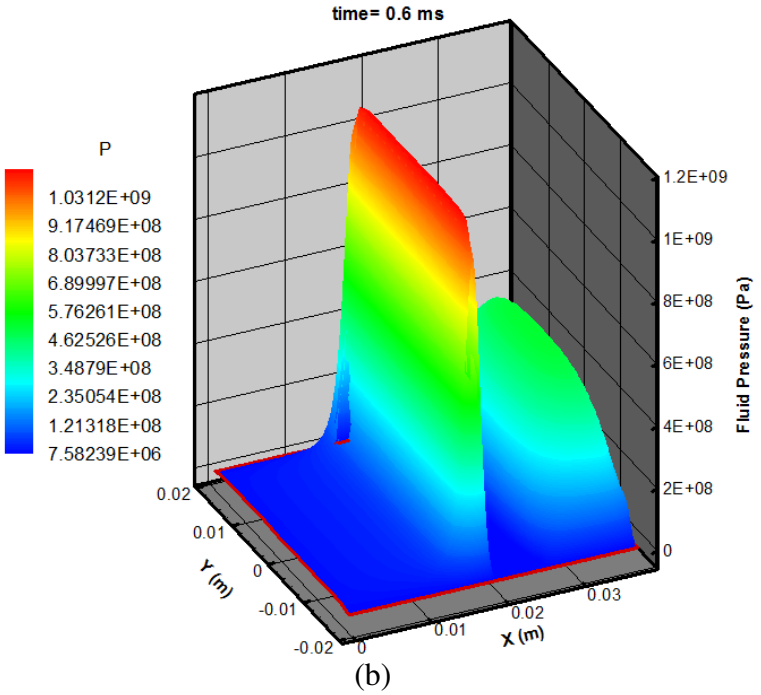

(b)

Figure 3.147: Pressure in the lubricant at different times

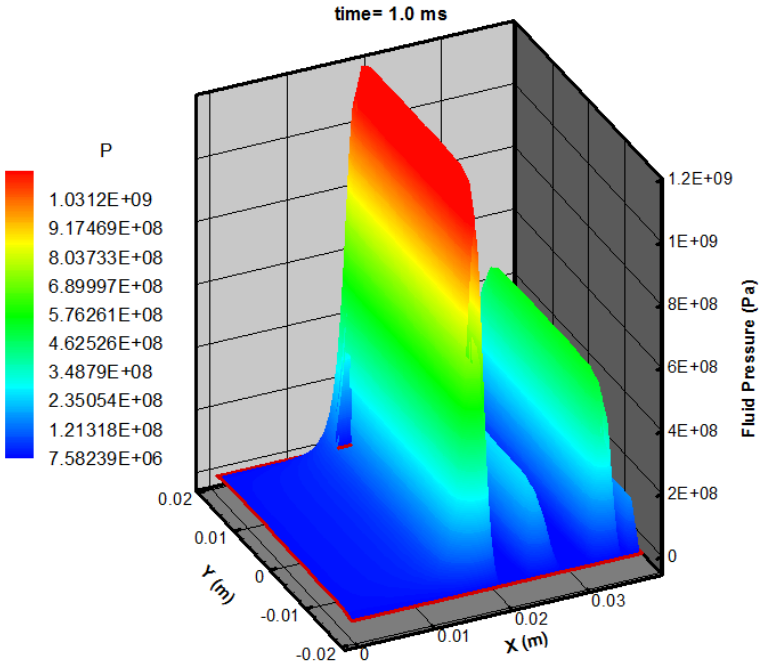

(c)

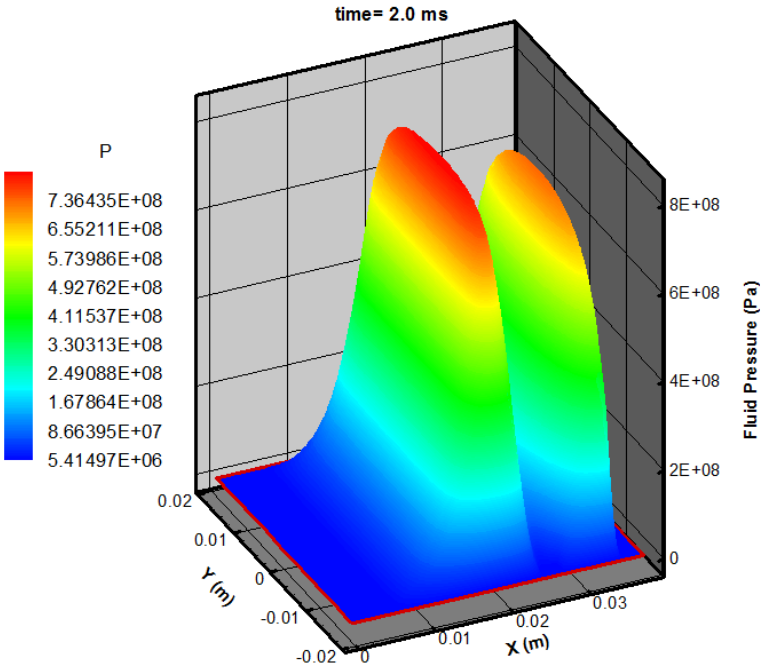

(d)

Figure 3.147 continued

Figure 3.148 presents the distributed forces acting on the armature in the transverse direction. The contact forces are apparent for most of the shot however, they are generally smaller in magnitude than the fluid pressures. The empty and full regions of the interface can be found by locating the regions where the lubricant pressure is zero. From 0.4 ms and 1.6 ms the interface is filled to the pocket, however, there is only a small amount of lubricant inside the pocket so there is not much pressure applied at the trailing edge of the pocket. By 2.0 ms the interface is beginning to empty out as was the case with the original armature.

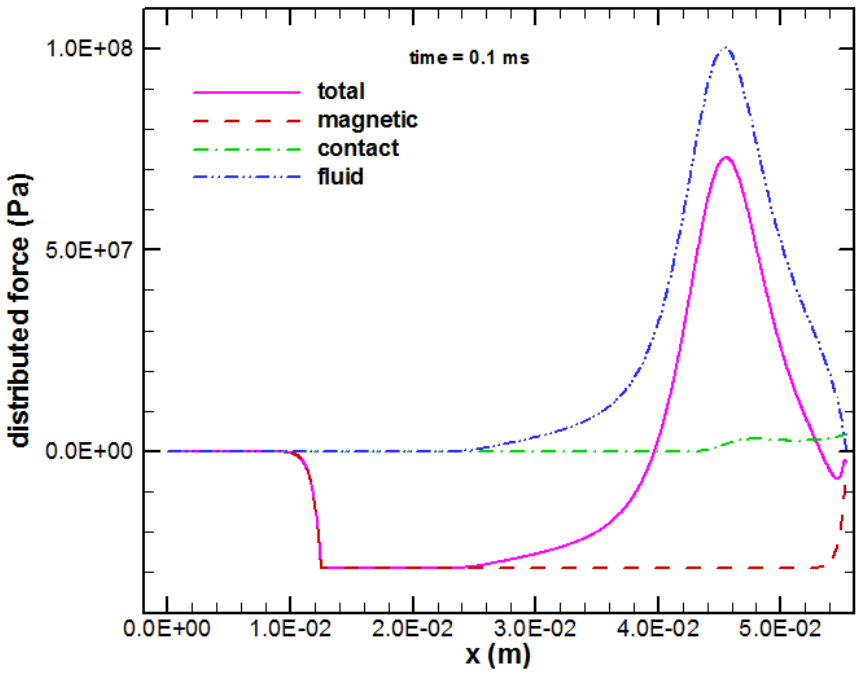

(a)

Figure 3.148: Distributed forces on the armature leg at different times

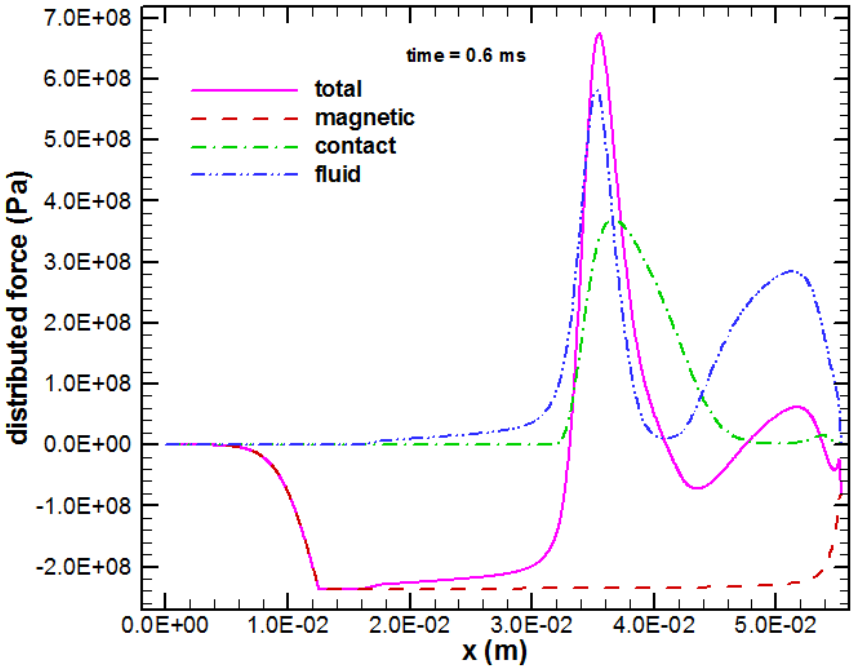

(b)

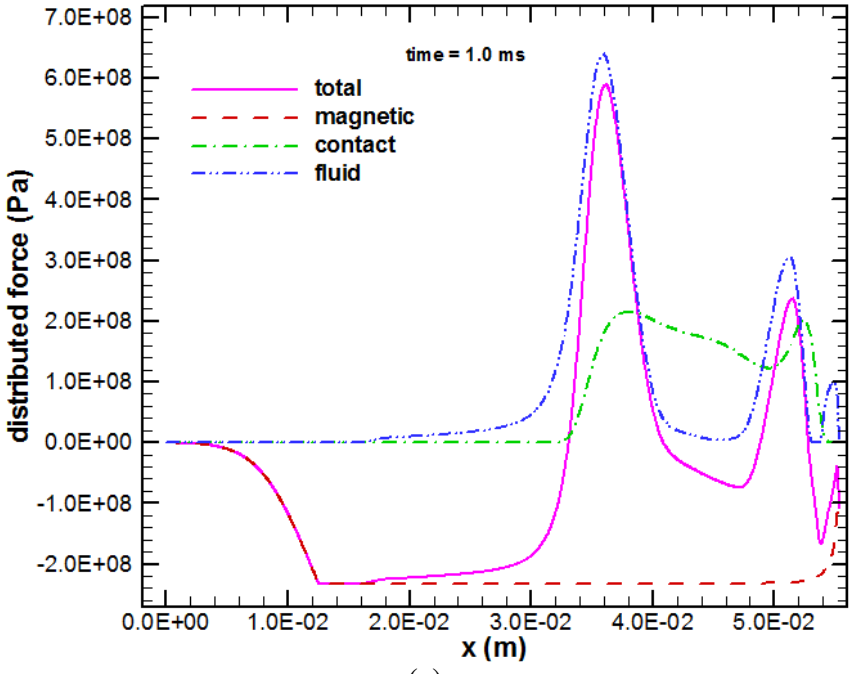

(c)

Figure 3.148 continued

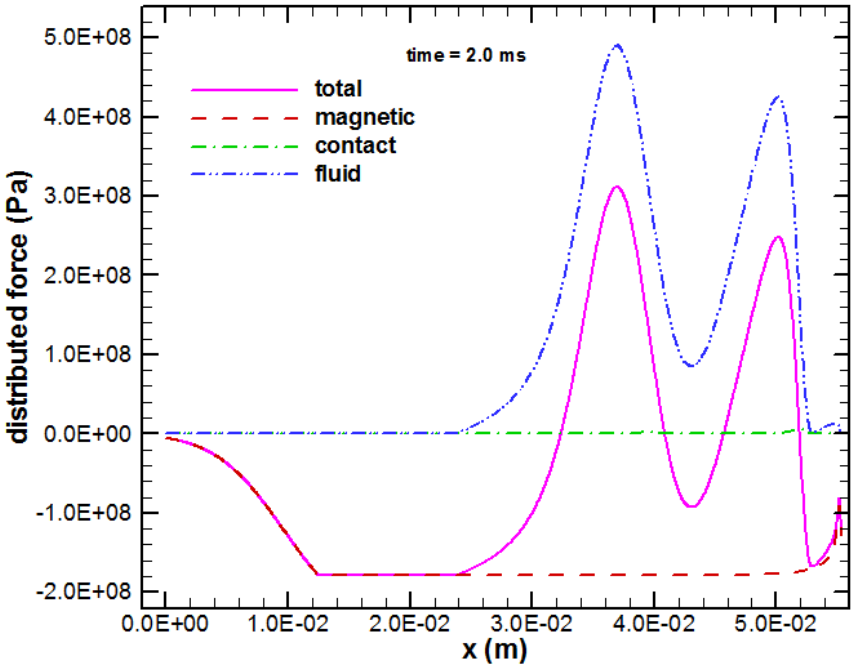

(d)

Figure 3.148 continued

Figure 3.149 shows the nondimensional interface gap profile at different times. At the beginning of the shot the gap profile is governed only by the deflection resulting from the rail and armature contacting. As the current is applied, the electromagnetic forces deform the armature towards the rail and create a sharper converging gap at the leading half of the interface and a more level gap at the trailing half. The general trends in armature-rail interface gap height are the same as were found with the original GTL-2-4C armature.

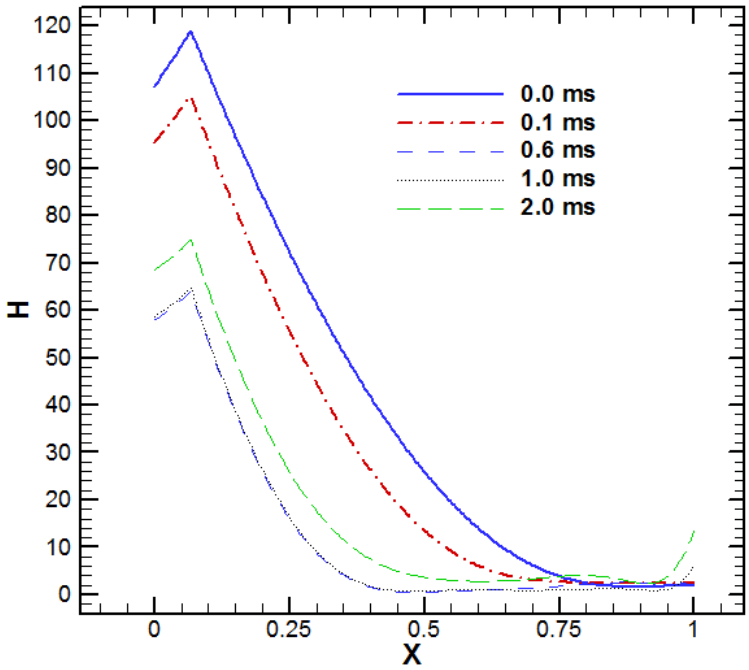

Figure 3.149: Nondimensional interface gap profiles at different times

A modification to the GTL-2-4C armature was proposed in which the slit in the armature trailing edges is not cut, thereby providing fewer places for lubricant to leak from and causing the pads to be more square because they are twice the width. Many physical parameters did not differ due to the modification. There was a slight amount of rigidity added by the material where the slit had been cut in the original armature. To reflect the increased rigidity the equivalent cantilever beams were adjusted. The lubricant in the interface was modeled in the same way as in the original armature accept the pad was twice the width and the effects of cavitation on the fluid pressure were approximated using a simplistic approach. The results predict that there will be no difference in the time of the transition for the modified armature because the pocket does not accrue enough lubricant to slow the drainage of the reservoir.

CHAPTER 4

CONCLUSIONS

For the armatures simulated, a more accurate prediction of the history of the lubricant supplied from the reservoir is obtained by considering the flow inside the injection conduits to be turbulent. Incorporating the major and minor losses into the analysis is successful in showing when too much restriction inside the injection conduits causes the pocket to empty out before the reservoir. However, the shot does not necessarily transition as soon as the pocket empties out because the reservoir is still supplies lubricant to the interface. Simulating the emptying of the armature-rail interface gives more incite into how interface dry-out leads to a transition as well as offers an explanation for the gently increasing muzzle voltage experimentally observed in some of the shots.

For most of the armature designs considered the long bearing assumption was used to analyze the lubricant inside the interface with great success. For other armature designs a two dimensional fluid pressure model was considered in order to account for leakage from the side of the armature. The simulations using a two dimensional fluid pressure model were also successful in predicting the armature-rail interface behavior. The results show that if cavitation exists inside the interface it is limited to a small region, allowing less accurate cavitation models to be used for simplicity and faster computational convergence.

It was shown that the magnetic field in a rectangular bore electromagnetic launcher is dominant in one direction and therefore can be correctly approximated with a two dimensional field. When considering the cylindrical bore launchers, it was shown that the electromagnetic forces lie dominantly in planes similar to those used to analyze the rectangular bore launchers. Also by showing that the magnetic field is dominant in only one direction, the model used for rectangular bore armatures was successfully extended by simplifying the electromagnetic field as a two dimensional quantity to analyze the cylindrical bore launchers.

REFERENCES

[1] Ying, W., Marshall, R., and Shukang, C., Physics of Electric Launch. Beijing, China:Science Press, 2004. pp.1-21.

[2] Wang, L., "Modeling of the Armature-Rail Interface in an Electromagnetic Launcher with Lubrication", PHD Thesis, Georgia Institute of Technology, Atlanta, GA. 2009

[3] Flegontova, E. Yu. and Yuferev, V. S., "Influence of Lubricant on the Motion of a Body in an Electromagnetic Raigun Accelerator. II. Hydrodynamics of a conducting lubricant," Technical Phys., vol. 44, no. 10, 1999, pp. 1226–1233.

[4] Drobyshevski, E., Kolesnikova, E., & Yuferev, V. "Calculating the Liquid Film Effect on Solid Armature Rail-gun Launching". IEEE Transactions on Magnetics, vol 35, no 1, 1999, pp. 53-58.

[5] Drobyshevskii, E. M., Kolesnikova, E. N., and Yuferev, V. S., "Influence of Lubricant on the Motion of a Body in an Electromagnetic Raigun Accelerator. I. Electric Current Distribution in the Accelerated Body and the Rails", Technical Phys., vol. 44, no. 7, 1999, pp. 831–838.

[6] Drobyshevskii, E. M., Kolesnikova, E. N., and Yuferev, V. S., "Influence of Lubricant on the Motion of a Body in an Electromagnetic Raigun Accelerator. III. Temperature Distribution in the Armature, Rail and Liquid Film", Technical Phys., vol. 44, no. 10, 1999, pp. 1234–1241.

[7] Drobyshevski E. M. et al., "Physics of Solid Armature Launch Transition into Arc Mode", IEEE Trans. Magn., vol. 37, no. 1, 2001, pp. 62–66.

[8] Oh, K. P., Goenka, P. K., "The Elastohydrodynamic Solution of Journal Bearings Under Dynamic Loading" Journal of Lubrication Technology, vol. 107, no. 3, 1985, pp. 389–395.

[9] Payvar, P. and Salant, R. F., "A Computational Method for Cavitation in a Wavy Mechanical Seal", J. of Tribology, vol. 114, 1992, pp. 199–204.

[10] Salant, R. F. and Wang, L., “Simulation of Liquid Lubricant Injection in Electromagnetic Launcher Armatures” IEEE Trans. Magn., vol. 43, No. 1, 2007, pp. 364–369.

[11] Ghassemi, M. and Pasandeh R., “Thermal and electromagnetic analysis of an electromagnetic launcher,” IEEE Trans. Magn., vol. 39, no. 3, 2003, pp. 1819–1822.

[12] Ghassemi, M. and Barsi, Y. M., “Effect of liquid film (indium) on thermal and electromagnetic distribution of an electromagnetic launcher with new armature,” IEEE Trans. Magn., vol. 41, no. 1, 2005, pp. 408–413.

[13] Ghassemi, M., Barsi, Y. M., and Hamedi, M. H., “Analysis of force distribution acting upon the rails and the armature and prediction of velocity with time in an electromagnetic launcher with new method,” IEEE Trans. Magn., vol. 43, no. 1, 2007, pp. 132–136.

[14] Patir, N. and Cheng, H. S., “An Average Flow Model for Determining Effects of Three-Dimensional Roughness on Partial Hydrodynamic Lubrication,” J. of Lubrication Technology, vol. 100, 1978, pp. 12–17.

[15] Patir, N. and Cheng, H. S., “Application of Average Flow Model to Lubrication Between Rough Sliding Surfaces,” J. of Lubrication Technology, vol. 101, 1979, pp. 220–229.

[16] Feng, M, and T Kenjo. "Friction and Wear of Spindle Motor Hydrodynamic Bearings for Information Storage Systems During Startup and Shutdown." Microsystem Technologies, vol 13, no 8-10, 2007, pp. 987-997.

[17] Tripp, J. H., “Surface roughness effects in hydrodynamic lubrication: the flow factor method,” J. of Lubrication Technology, vol. 105, 1983, pp. 458–465.

[18] Elrod, H. G. and Ng, C. W., “A Theory for Turbulent Fluid Films and its Application to Bearings” J. of Lubrication Technology, 1967, pp. 346–362.

[19] Brunetiere, N., Tourneie B., and Frene J., “Influence of Fluid Flow Regime on Performances of Non-Contacting Liquid Face Seals,” J. of Tribology, vol. 124, 2002, pp. 515–523.

[20] Brunetiere, N., Tourneie B., and Frene J., “TEHD Lubrication of Mechanical Face Seals in Stable Tracking Mode: Part 1 – Numerical Model and Experiments” J. of Tribology, vol. 125, 2003, pp. 608–616.

[21] Kothmann, R. E. and Stefani, F., “A Thermal Hydraulic Model of Melt-Lubrication in Railgun Armatures” IEEE Trans. Magn., vol. 37, no. 1, 2001, pp. 86–91.

[22] Merril, R. and Stefani F., “Electrodynamics of the current melt-wave erosion boundary in a conducting half-space,” IEEE Trans. Magn., vol. 39, no. 1, 2003, pp. 66–71.

[23] Greenwood, J. A. and Williamson, J. B., ”Contact of Nominally Flat Surfaces” Proceedings of the Royal Society of London Series A-mathematical and Physical Sciences, vol. 295, no. 1442, 1966, pp. 300-3019.

[24] Greenwood, J. A. and Wu, J., “Surface Roughness and Contact: An Apology” MECCANICA, vol. 36, no. 6, 2001, pp. 617-630.

[25] Streator, J. L., “A Model of Mixed Lubrication with Capillary Effects” Proc. 15th Leeds-Lyon Symp. On Tribl., Vienna, Austria, 2001, pp. 121–128.

[26] Rapka, J. R., Hildenbrand, D.J., and Weldon, J.M., “The Determination of Launch Induced Static and Dynamic Rail Deflection of a Benet 50 mm Railgun Barrel” IEEE Trans. Magn., vol. 31, no. 1, 1995, pp. 231–236.

[27] Johnson A. J. and Moon F. C., “Elastic Waves and Solid Armature Contact Pressure in Electromagnetic Launchers” IEEE Trans. Magn., vol. 42, no. 3, 2006, pp. 422–429.

[28] Jerome, T. T., “Dynamic Response of Electromagnetic Railgun Due to Projectile Movement”, IEEE Trans. Magn., vol. 39, no. 1, 2003, pp. 472–475.

[29] Daneshjoo, K., Rahimzadeh, M., Ahmadi, R., and Ghassemi, M., “Dynamic Response and Armature Critical Velocity Studies in an Electromagnetic Railgun” IEEE Trans. Magn., vol. 43, no. 1, 2007, pp. 126–131.

[30] Tzeng, J. T., “Dynamic Response of Electromagnetic Railgun Due to Projectile Movement” IEEE Trans. Magn., vol. 39, no. 1, 2003, pp. 472–475.

[31] James T. E. and James D. C., “Contact Pressure Distribution and Transition in Solid Armatures” IEEE Trans. Magn., vol. 37, no. 1, 2001, pp. 81–85.

[32] Hopkins, D. A., Stefani, F., Hsieh, K., and Kim, B., “Analysis of Startup Behavior in a C-shaped Armature Using Linked EMAP3D/DYNA3D Finite Element Codes” IEEE Trans. Magn., vol. 35, no. 1, 1999, pp. 59–64.

[33] Newill, J. F., Powell J. D., and Zielinski A. E., “Coupled Finite-element Codes for Armature Design” IEEE Trans. Magn., vol. 39, no. 1, 2003, pp. 148–152.

[34] Zielinski,A. E., Newill, J. F., and Powell, J. D., “Experiments to Assess Structural Loads During Solid Armature Contact Transition” IEEE Trans. Magn., vol. 39, no. 1, 2003, pp. 92–96.

[35] Hsieh, K. T., “A Lagrangian Formulation for Mechanically, Thermally Coupled Electromagnetic Diffusive Processes With Moving Conductors” IEEE Trans. Magn., vol. 31, no. 1, 1995, pp. 604–609.

[36] Hsieh, K. T. and Kim, B. K., “3D modeling of Sliding Electrical Contact” IEEE Trans. Magn., vol. 33, no. 1, 1997, pp. 237–239.

[37] Thiagarajan, V. and Hsieh, K. T., “An Algorithm to Couple an External RL Circuit with the Finite-element Code EMAP3D” IEEE Trans. Magn., vol. 43, no. 1, 2007, pp. 376–379.

[38] Brunetiere, N., Tourneie B., and Frene J., “TEHD Lubrication of Mechanical Face Seals in Stable Tracking Mode: Part 1 – Numerical Model and Experiments” J. of Tribology, vol. 125, 2003, pp. 608–616.

[39] Young, F. J. and Hughes, W. F., “Rail and Armature Current Distributions in Electromagnetic Launchers” IEEE Trans. Magn., vol. 18, no. 1, 1982, pp. 33–41.

[40] Barber, J. P. and Dreizin Y. A., “Model of Contact Transitioning with Realistic Armature-Rail Interface” IEEE Trans., vol. 31, no. 1, 1995, pp. 96–100.

[41] Engel, T. G., Neri, J. M., and Veracka, M. J., “Characterization of the Velocity Skin Effect in the Surface Layer of a Railgun Sliding Contact” IEEE Trans. On Magn., vol. 44, no. 7, 2008, pp. 1837–1844.

[42] James, T. E., "Current Wave and Magnetic Saw-Effect Phenomena in Solid Armatures" IEEE Trans. Magn., vol. 31, no. 1, 1995, pp. 622–627.

[43] Woods, L. C., "The Current Melt-Wave Model" IEEE Trans. Magn., vol. 33, no. 1, 1997, pp. 152–156.

[44] Powell, J. D. and Zielinski, A. E., "Current and Heat Transport in the Solid-Armature Railgun" IEEE Trans. Magn., vol. 31, no. 1, 1995, pp. 645–650.

[45] Powell, J. D. and Zielinski, A. E., "Observation and Simulation of Solid-Armature Railgun Performance" IEEE Trans. Magn., vol. 35, no. 1, 1999, pp. 84–89.

[46] Critchley, R., Leyden, C., and Argyle A. P. J., "The Use of Coupled EM-hydro Finite Element Techniques for the Design of Railguns" IEEE Trans. Magn., vol. 35, no. 1, 1995, pp. 576–581.

[47] Hsieh, K. T. and Kim, B. K., "3D Modeling of Sliding Electrical Contact" IEEE Trans. Magn., vol. 33, no. 1, 1997, pp. 237–239.

[48] Kothmann, R. E. and Stefani, F., "A Thermal Hydraulic Model of Melt-Lubrication in Railgun Armatures" IEEE Trans. Magn., vol. 37, no. 1, 2001, pp. 86–91.

[49] Merrill, R. and Stefani, F., "A Turbulent Melt-Lubrication Model of Surface Wear in Railgun Armatures" IEEE Trans. Magn, vol. 41, No. 1, 2005, pp. 414–419.

[50] Bair, S., "Scaling a Delivery System for Lubrication of an Armature/Rail Interface" ONR 352, Georgia Institute of Technology, 2009.

[51] Marshall, R. and Ying, W., Railguns: their Science and Technology. Beijing, China:China Machine Press, 2004. pp.8-12.

[52] ANSYS, Inc., "ANSYS Release 11.0 Documentation" SAS IP, Inc., 2007.

[53] Fox, R., McDonald, A., and Pritchard, P., Introduction to Fluid Mechanics. Hoboken, NJ, John Wiley & Sons, Inc., 2006. 6th ed. pp.334-348.

[54] Patankar, S. V., Numerical Heat Transfer and Fluid Flow, Taylor and Francis, 1980.